Investigation of Cuprate Superconductors by Electron Paramagnetic Resonance (EPR) and Muon-spin Rotation (μSR)

I EPR Study of Relaxation Processes and Phase Separation in Cuprate Superconductors

II Analysis of μSR Line Shapes in the Vortex State of Type-II Superconductors

Dissertation

zur
Erlangung der naturwissenschaftlichen Doktorwürde
(Dr. sc. nat.)

vorgelegt der
Mathematisch-naturwissenschaftlichen Fakultät der
Universität Zürich

von
Alexander Maisuradze
aus Georgien

Promotionskomitee

Prof. Dr. Hugo Keller (Vorsitz)
Prof. Dr. Alexander Shengelaya
Prof. Dr. Dr. h.c. mult. Karl Alex Müller
Prof. Dr. Boris Ivanovich Kochelaev

Zürich, 2008

Contents

Summary

Superconductivity is one of the most fascinating phenomenon in solid state physics. Although it is not the only phenomenon showing quantum effects on a macroscopic scale, the most natural of which is magnetism, it is surely one of the most interesting from a technological point of view. The discovery of high-temperature superconductivity (HTS) in cuprates by Georg Bednorz and Alex Müller [1] stimulated research in this field of physics. Although much has been done to investigate this phenomenon both experimentally and theoretically, the basic questions related to the driving mechanisms are still unanswered. The BCS theory [2], so successful in the description of most of the properties of conventional phonon-mediated superconductors, is not able to describe HTS. Unconventional isotope effects, strong polaronic and magnetic interactions substantially complicate the physics of cuprates [3]. The Jahn Teller (JT) effect, characteristic of Cu^{2+} ions, is one of the most plausible origins of strong electron-phonon coupling observed experimentally and evidence for its involvement has also been detected by Electron Paramagnetic Resonance (EPR) in previous studies [4].

EPR is a powerful microscopic method for investigating the properties of the solid state [5]. Although other experimental techniques have experienced tremendous improvements in the last few decades, there are still fields of application where EPR is the most appropriate method. The principle advantages of EPR in comparison with other magnetic resonance techniques are its high speed of measurement, high sensitivity, and its availability. In this thesis, the whole phase diagram of the cuprate superconductor $Y_{0.98}Yb_{0.02}Ba_2Cu_3O_x$ was investigated by Yb^{3+} EPR. The main subjects of this study were phase separation and relaxation mechanisms. In addition, a few other superconductors were studied for comparison with $YBa_2Cu_3O_x$.

As is known from the classical London and Ginzburg-Landau theories of superconductivity [6], the penetration depth and the coherence length are the basic parameters of a superconductor characterizing the order parameter and the superfluid density. Muon-spin-rotation (μSR) spectroscopy has been shown to be one of the most reliable techniques for measuring the penetration depth and in some cases also the coherence length [7, 8]. The dependence of the fundamental length scales on temperature, pressure, field, etc. can shed light on basic properties of superconductors . For this reason it is very important to develop reliable methods to determine these parameters from experimental measurements based on the existing theories. The second part of this thesis is devoted to these questions.

The thesis is organized as follows: In "Introduction", the generic properties and the universal phase diagram of cuprates are described. In chapter 1, "Experimental techniques", the basics of the EPR and the μSR techniques are given. A simple theory along with the experimental setup are briefly described. The chapter 2, "EPR study of relaxation processes and phase separation in cuprate superconductors", contains a description of the physics of cuprates studied by EPR. In secs. 2.1 and 2.2, investigation of the spin-lattice relaxation mechanisms in $Y_{0.98}Yb_{0.02}Ba_2Cu_3O_x$ using Yb^{3+} EPR is presented. In Sec. 2.3, these investigations are extended to higher temperatures in order to find possible relaxation anomalies related to the onset of the pseudogap state. This is followed by an investiga-

tion (Sec. 2.4) of the insulator-to-superconductor transition in $YBa_2Cu_3O_x$ ($x \simeq 6.4$) near the antiferromagnetic-to-superconducting phase boundary. The electronic phase separation into magnetic and superconducting states is observed and the phase diagram of $YBa_2Cu_3O_x$ at $x \simeq 6.4$ is described. For a comparison with results obtained for $YBa_2Cu_3O_x$, the relaxation mechanisms of the electron-doped superconductor $Sr_{0.9}La_{0.08}Yb_{0.02}CuO_2$ was also studied (Sec. 2.5). In addition, the results of the relaxation measurements in $YBa_2Cu_3O_x$ and $Sr_{0.9}La_{0.08}Yb_{0.02}CuO_2$ were compared with those of $Bi_2Sr_2CaCu_2O_8$ studied in the work of U. Mosele [9] (Sec. 2.6). Finally, at the end of this chapter, an experimental study of the line broadening of Yb^{3+} in $La_{2-x}Sr_xCuO_4$ and possible implications of these results are reported (Sec. 2.7). In chapter 3, "Analysis methods of the field distribution in type-II superconductors", the different methods of μSR-data analysis for superconductors in the vortex state are presented. The following methods of analysis will be discussed (Secs. 3.1-3.2): 1) The second-moment method, 2) the analytical method of London, 3) the analytical Ginzburg-Landau method and 4) the numerical method of Ginzburg-Landau. The last chapter 4 contains the conclusions and outlook for future work along with acknowledgements. In APPENDIX A, the numerical calculation of the crystal-field splitting on the example of the rare earth Yb^{3+} is presented.

Zusammenfassung

Supraleitung ist eines der faszinierenden Phänomene in der aktuellen Festkörperphysik. Obwohl sie nicht das einzige Phänomen ist, bei dem die Quantenphysik makroskopisch in Erscheinung tritt (das bekannteste ist wohl der Magnetismus), ist sie sicherlich technologisch von höchstem Interesse. Die Entdeckung der Hochtemperatur-Supraleitung (HTS) in Kupraten durch Georg Bednorz und Alex Müller [1] stimulierte die Erforschung dieses Bereiches der Physik in hohem Masse. Trotz zahlreicher experimenteller und theoretischer Untersuchungen dieses neuartigen Phänomens sind die Hauptfragen bezüglich des zugrundeliegenden Mechanismuses der HTS noch immer unbeantwortet. Die BCS Theorie [2] die so erfolgreich in der Beschreibung der meisten Eigenschaften der konventionellen, Phonon-vermittelten Supraleitung ist, kann die HTS nicht beschreiben. Unkonventionelle Isotopeneffekte, sowie starke polaronische und magnetische Wechselwirkungen komplizieren die Physik der Kuprate wesentlich [3]. Der Jahn-Teller-Effekt, charakteristisch für Cu^{2+} Ionen, ist eine der plausibelsten Ursachen der starken Elektron-Phonon-Kopplung, die experimentell beobachtet wurde, u.a. mittels elektronparamagnetischer Resonanz (EPR) [4].

EPR ist eine sehr flexible mikroskopische Methode zur Untersuchung von Festkörpereigenschaften [5]. Obwohl in den letzten Jahrzehnten viele neue experimentelle Methoden entwickelt wurden, existieren Anwendungsbereiche, wo EPR die beste Untersuchungsmethode bleibt. Vorteile der EPR, im Vergleich zu anderen magnetischen Resonanztechniken, sind ihre hohe Messgeschwindigkeit und Empfindlichkeit. In der vorliegenden Arbeit wurde das gesamte Phasendiagramm von $Y_{0.98}Yb_{0.02}Ba_2Cu_3O_x$ mittels Yb^{3+} EPR untersucht. Hauptgegenstand unserer EPR-Studie waren Phasenseparation und Relaxationsmechnismen. Zudem wurden weitere Hochtemperatursupraleiter zu Vergleichszwecken hergestellt und gemessen.

Von den klassischen London- und Ginzburg-Landau-Theorien der Supraleitung ist bekannt, dass die Eindringstiefe und die Kohärenzlänge zentrale Parameter sind, um den Ordnungsparameter und die Dichte der Supraflüssigkeit zu charakterisieren [6]. Muon-Spin-Rotations(μSR)-Spektrospkopie hat sich als wichtige Technik zur Bestimmung der Eindringstiefe, und in manchen Fällen auch der Kohärenzlänge, gezeigt [7, 8]. Die Abhängigkeit dieser fundamentalen Längen von Temperatur, Magnetfeld, Druck oder anderen Parametern kann helfen die grundsätzlichen Eigenschaften der Supraleiter aufzeigen. Es ist deshalb wichtig, diese Parameter genauestens aus μSR-Messungen mit Hilfe von etablierten Theorien zu extrahieren. Der zweite Teil dieser Arbeit ist diesen Fragen gewidmet.

Der vorliegende Bericht ist wie folgt gegliedert: In der Einleitung sind einige grundsätzliche Eigenschaften von Kupratsupraleitern beschrieben. Ein allgemein akzeptiertes Phasendiagramm als Funktion der Lochdotierung und der Temperatur wird diskutiert. Im Kapitel 1 "Experimental techniques" werden die Grundlagen der EPR- und μSR-Techniken vorgestellt. Aufbau und Funktionsweise der Apparaturen wird kurz beschrieben. Kapitel 2 "EPR study of relaxation processes and phase separation in cuprate superconductors" behandelt die EPR-Untersuchungen an den Kupratsupraleitern und schliesst den ersten Teil der vorliegenden Arbeit ab. Im Abschnitt 2.1 werden die Untersuchungen der Spin-Gitter-Relaxationsmechanismen in $Y_{0.98}Yb_{0.02}Ba_2Cu_3O_x$ mittels Yb^{3+} EPR Probe präsen-

tiert. Abschnitt 2.3 beschreibt Untersuchungen bei höheren Temperaturen, welche auf das Auffinden von Relaxationszeitanomalien im "Pseudogap"-Zustand gerichtet waren. Desweiteren wurde der Isolator-Supraleiter-Übergang in $Y_{0.98}Yb_{0.02}Ba_2Cu_3O_x$ an der Phasengrenze zwischen Antiferromagnet und Supraleiter für $x \simeq 6.4$ untersucht (Abschnitt 2.4). Es wird die beobachtete elektronische Phasenseparation in magnetische und supraleitende Bereiche, sowie das Phasendiagramm von $Y_{0.98}Yb_{0.02}Ba_2Cu_3O_x$ in der Nähe von $x \simeq 6.4$ beschrieben. Abschnitt 2.5 behandelt die Relaxationsmechanismen im elektronendotierten Supraleiter $Sr_{0.9}La_{0.08}Yb_{0.02}CuO_2$ und vergleicht die Ergebnisse mit denjenigen von $YBa_2Cu_3O_x$. Im weiteren werden die Ergebnisse mit Resultaten der Bachelorarbeit von Urs Mosele [9] an $Bi_2Sr_2CaCu_2O_8$ vergleichend diskutiert (Abschnitt 2.6). Am Ende dieses Kapitels werden die experimentellen Ergebnisse der EPR-Linienbreiten von Yb^{3+} in $La_{2-x}Sr_xCuO_4$ präsentiert und interpretiert (Abschnitt 2.7). Im Kapitel 3 "Analysis methods of the field distribution in type-II superconductors" werden verschiedene Methoden der Analyse von μSR-Daten von Supraleitern im Vortex-Zustand beschrieben. Die analytischen Modelle (Standardisiertes zweites Moment, London, Ginzburg-Landau) und das numerische Ginzburg-Landau-Modell werden diskutiert (Abschnitt 3.1-3.2). Ausblick und Schlussfolgerungen sind in Kapitel 4 zusammengefasst. Im APPENDIX A werden die numerischen Rechnungen der Kristallfeldaufspaltung am Beispiel der seltenen Erde Yb^{3+} dargelegt.

0.1 Introduction

The phenomenon of superconductivity is a remarkable example of quantum effects operating on truly macroscopic scale. In a superconducting material, a finite fraction of the electrons are in real sense condensed into a "macromolecule" (or "superfluid") which extends over the entire volume of the system and is capable of motion as a whole [10]. These sentences of Robert Schrieffer describe well the essence of the superconductivity. Infinite conductivity and perfect diamagnetism are the most exciting properties of the superconductors. Since 1911, when this phenomenon was discovered by Kammerlingh Onnes, physicists did not give up on attempting to understand the physics behind it. It was only in 1957 that Bardeen, Cooper, and Schrieffer created the first microscopic theory describing the mechanism of superconductivity that could be successfully applied to most of the superconductors known at that time [2]. The crucial experiment for developing this theory was evidence of the isotope effect on T_c performed by Reynolds *et al.* and Maxwell [11], which unambiguously indicated the phononic origin of superconductivity. The discovery of the high temperature superconducting (HTS) materials by George Bednorz and Karl Alex Müller made the field of superconductivity much more interesting than before for several reasons: First of all, the belief that superconductivity is "a He temperature phenomenon“ was broken, and later the cuprate superconductors with critical temperatures T_c as high as ~ 150 K were found. Secondly, superconductivity was found in a material where nobody would expect it. The BCS theory, so successful for the low temperature (conventional) superconductors, could not explain the properties of the HTS materials. In addition, unconventional isotope effects, in some cases even stronger than in BCS materials, were observed. A strong electron phonon coupling and magnetic interactions are characteristic of cuprate superconductors. The role of these interactions for superconductivity is still a puzzling question. The aim of the present work is to contribute to the understanding the HTS physics.

0.1.1 Generic phase diagram and properties of cuprate superconductors

Before starting the discussion of different experiments, it is useful to describe general properties of cuprate superconductors, their crystal structure, and their phase diagram. $La_{2-x}Sr_xCuO_4$ (LSCO) belongs to the family of HTS materials first discovered by George Bednorz and Karl Alex Müller in 1986 [1]. The crystal has a layered structure and conducting/superconducting CuO_2 layers are separated by insulating SrO layers as is shown in Fig. 1. $La_{2-x}Sr_xCuO_4$ is a single-plain HTS material, which means that there is single layer of the superconducting CuO_2 plane separated by insulating layers. Although the superconducting transition temperature $T_c = 40$ K is not particularly high, this compound is interesting because of its simple crystal structure (Fig. 1). If there is no Sr doping, this material is an antiferromagnetic (AF) Mott insulator [12]. The Sr^{2+} in this material substitutes for the La^{3+} and induces additional carriers (holes) into the CuO_2 plane. The properties of $La_{2-x}Sr_xCuO_4$ are extremely dependent on the Sr concentration x. With increasing x, the material undergoes a series of phase transitions. In the range of Sr content $x = 0 - 0.02$ $La_{2-x}Sr_xCuO_4$ is AF and insulating. At lower temperatures, it undergoes a cluster-spin glass transition (see Fig. 2). In the range of the Sr doping $x = 0.02 - 0.06$, the material is an insulator with spin-glass transition at low temperatures. Within a Sr concentration between $x = 0.06$ and $x = 0.27$ the material becomes superconducting with a maximal critical temperature $T_c = 40$ K at $x = 0.15$. The material with $0.06 < x < 0.15$ is called an underdoped superconductor; with $0.15 < x < 0.27$ - an overdoped one; and with $x \simeq 0.15$ an optimally doped one. At $x = 0.2$ and zero temperature the $La_{2-x}Sr_xCuO_4$ undergoes a tetragonal-to-orthorombic phase transition as indicated in Fig. 2. In addition, in the underdoped material, besides the superconducting transition at T_c, there is a pseudogap state of the material below the characteristic temperature T* dependent on x as well (Fig. 2). In this state the Fermi surface of the material is partially gapped even above T_c.

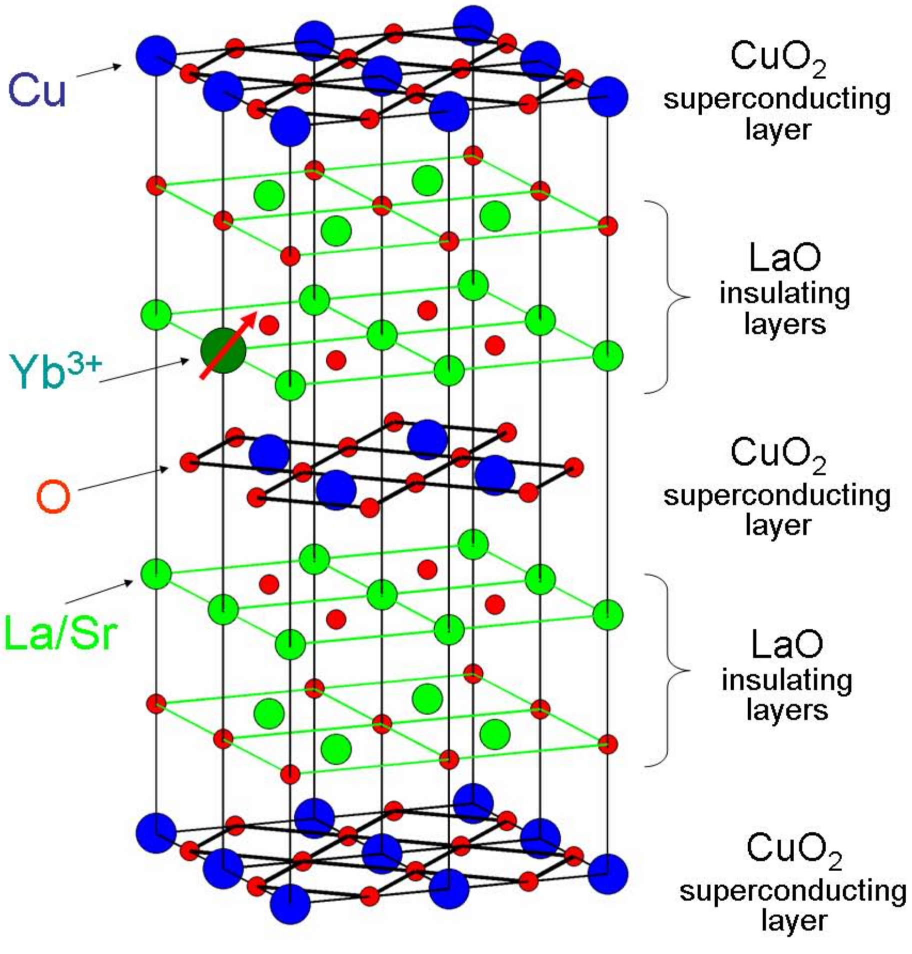

Figure 1: Crystal structure of $La_{2-x}Sr_xCuO_4$. The crystal has a layered structure: superconducting CuO_2 layers are separated by two insulating LaO layers. The site of the EPR probe Yb^{3+} , which will later be used for investigations, is shown as well.

Nanoscale distortions and inhomogeneities, stripe-like arrangement of the carriers and spins are characteristic of the cuprate superconductors. Typically these phenomena are observed in the lightly doped or the underdoped materials [3]. The phase diagram described for the $La_{2-x}Sr_xCuO_4$ material is qualitatively very similar to that of other cuprates with slight modifications. Figure 2(b) shows a qualitative picture of the phase diagram for the $YBa_2Cu_3O_x$ superconductor as a function of oxygen doping x. The carrier doping in this material is not exactly proportional to the oxygen doping x and as a result, this figure is more qualitative than quantitative.

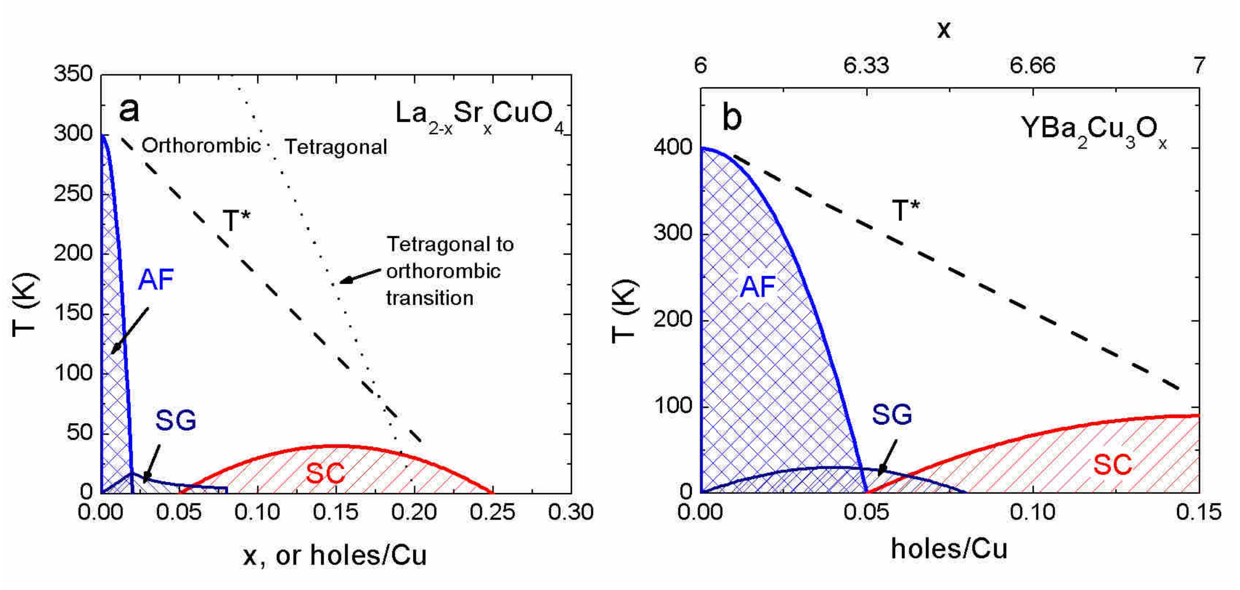

Figure 2: Qualitative picture of the phase diagram of $La_{2-x}Sr_xCuO_4$ (a) and $YBa_2Cu_3O_x$ (b) superconductors as a function of the hole doping (Sr/O doping x). AF, SG, and SC mean antiferromagnetic, spin-glass and superconducting phases, respectively. The dashed line separates the normal and the pseudogap state (below T*) of the material.

Chapter 1

Experimental techniques

1.1 Short overview of the electron paramagnetic resonance technique.

Electron paramagnetic resonance (EPR) is the first magnetic resonance technique invented. This important phenomenon was discovered by Zavoisky in Kazan (Russia) in 1944. This experiment was one of the first big steps in the development of the magnetic resonance technique which now is widely used in everyday life, science, and technology.

1.1.1 The basics of electron paramagnetic resonance

As is known, the energy level representing a paramagnetic ion (in general, this can be any particle with a spin) experiences a Zeeman splitting in an applied external magnetic field **B**. In the simplest case of an isolated ion with spin $S = 1/2$ and without orbital momentum $\mathbf{L} = 0$, there are two possible energy states of the ion depending on whether the orientation of the magnetic momentum of the ion is parallel or antiparallel to the applied field (the quantization axis of the free ion). The Zeeman energy of an ion of spin $S = 1/2$ is expressed by the relation

$$U = -\overrightarrow{\mu}\mathbf{B} = -m_s g \mu_B B \tag{1.1}$$

where $\overrightarrow{\mu}$ is magnetic moment of the particle, g is the g-factor or the spectroscopic splitting factor, m_s is the quantum number (that has two values 1/2 or -1/2 in this case), $\mu_B = eh/2mc$ is the Bohr magneton (the natural unit for measuring the magnetic moments of ions/particles) and **B** is the field applied to the ion/particle. Since in paramagnetic materials, magnetization and hence demagnetization factors are usually small, one treats **B** as the applied field. The quantities e, m, h, and c are the electron charge, the electron mass, Plank's constant and the speed of light, respectively.

In an applied magnetic field, the double-degenerate ground state of the ion can be split and these two states are no longer equivalent. As a result, the ion tends to minimize its energy orienting itself preferably along the applied field. For a macroscopic sample with a large number of such "noninteracting" ions, this leads to a magnetization of the sample. From quantum mechanics, it is known that the z-component of the magnetic moment $\overrightarrow{\mu}$ (the z-axis being parallel to the field direction) is quantized and can equal to $m_s = S, (S-1), ... - S$ in units of $g\mu_B$ ($2S+1$ possibilities). In addition to the energy splitting in the applied magnetic field, the ion experiences a so-called Larmor precession. By definition, an ion with spin S has the mechanical moment $\overrightarrow{G} = \overrightarrow{\mu}/\gamma$, where $\gamma = g\mu_B/h$ is giromagnetic ratio. Classical mechanics leads to the following equation of motion for the ion:

$$d\overrightarrow{\mu}/dt = \gamma\overrightarrow{\mu} \times \mathbf{B}. \tag{1.2}$$

The solution of this equation corresponds to the precession of the ion around the axis along the applied field with a frequency $\overrightarrow{\omega_L} = \gamma\mathbf{B}$, see Fig. 1.1(a). The energy of the ion during the precession does not change and depends only on the z-component of the magnetic moment $\overrightarrow{\mu}$ determined by the quantum number m_s (see Eq. (1.1)). In magnetic resonance experiments, one applies an additional oscillating magnetic field $\mathbf{B_1}$ that is circularly polarized with a frequency $\overrightarrow{\omega} \simeq \overrightarrow{\omega_L}$. The motion of the magnetic moment $\overrightarrow{\mu}$ is more easily described in the rotating coordinate system (x', y', z'), see Fig. 1.1. If we take into account that the vector coordinate $\mathbf{R}$ transforms from the static (x, y, z) to a rotating coordinate system (x', y', z') with frequency $\overrightarrow{\omega}$ as $\mathbf{R}' = \mathbf{R} - \overrightarrow{\omega}$, the equation of motion will have the following form in this coordinate system:

$$d\overrightarrow{\mu}'/dt = \gamma\overrightarrow{\mu}' \times (\mathbf{B} + \mathbf{B_1} - \overrightarrow{\omega}/\gamma) \simeq \gamma\overrightarrow{\mu}' \times \mathbf{B_1}. \tag{1.3}$$

The solution of this equation implies that the magnetic moment in the rotating coordinate system now precesses around two magnetic fields $\mathbf{B}' = \mathbf{B} - \overrightarrow{\omega}/\gamma = (\overrightarrow{\omega_L} - \overrightarrow{\omega})/\gamma$ and $\mathbf{B_1}$ with frequencies $\overrightarrow{\omega}' = \gamma\mathbf{B}'$ and $\overrightarrow{\omega_1} = \gamma\mathbf{B_1}$, respectively. When the frequency $\overrightarrow{\omega}$ of the $\mathbf{B_1}$ field coincides with the Larmor frequency $\overrightarrow{\omega_L}$, the resonance condition is established and the field $\mathbf{B}'$ in the rotating coordinate system is zero. The magnetic moment $\overrightarrow{\mu}$ in the rotating coordinate system precesses only around the applied field $\mathbf{B_1}$. In other words, applying $\mathbf{B_1}$ leads to a change of the z-component of $\overrightarrow{\mu}$ which is related to the change of energy of the ion according to Eq. 1.1. This change of energy at the resonant condition $\omega \simeq \omega_L$ is the essence of Electron Paramagnetic Resonance.

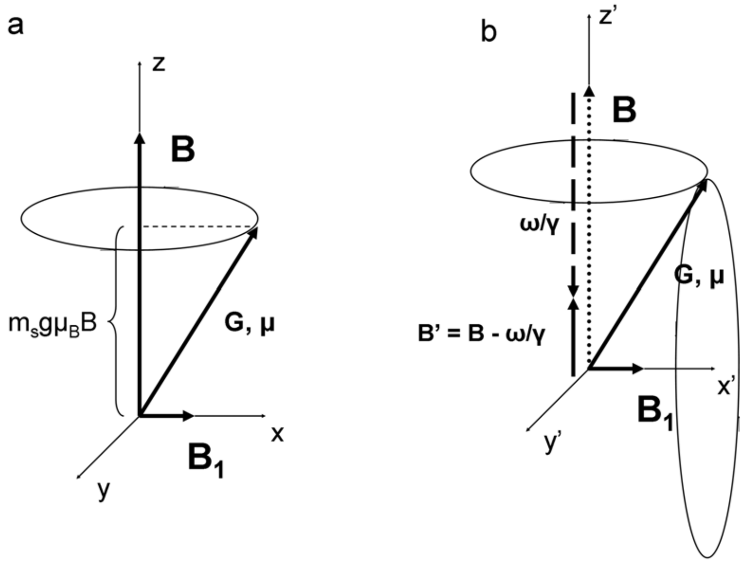

Figure 1.1: (a) The Larmor precession of a paramagnetic ion with magnetic moment μ in an applied magnetic field $\mathbf{B}$. (b) Precession of the paramagnetic ion with the magnetic moment μ in the rotating coordinate system (x', y', z') in the fields $\mathbf{B}'$ and $\mathbf{B_1}$.

In terms of quantum mechanics, this process is described more simply. The energy of a paramagnetic ion in a magnetic field $\mathbf{B}$ is split into $2S+1$ equidistant energy levels according to Eq. (1.1). Then, the application of the electromagnetic wave $\mathbf{B_1}$ or a photon of energy $\hbar\omega = g\mu_B B$ can induce a transition from one energy state to another. The calculation of transition probabilities shows that only transitions with a change of $\Delta m_s = 0$ or 1 are allowed. Therefore, only photons with the Larmor frequency will induce transition. Since in thermal equilibrium, the lower energy states of an ion are populated more than the higher ones, the ion will predominantly absorb the applied electromagnetic wave energy.

In real experiments, the ion additionally has an orbital momentum **L**. If the ions are still isolated, then one can introduce the total momentum $\mathbf{J} = \mathbf{L} + \mathbf{S}$ and all which was mentioned above will be true for **J** instead of **S**.

In practice it is not interesting to study isolated ions. The interaction of paramagnetic ions with its surrounding ligands or electrons allows the possibility of investigating different processes taking place in a material. For a paramagnetic ion in a solid, Abragam and Price [5] introduced a spin-Hamiltonian formalism for the description of its low lying energy levels and wave functions. In general, the spin Hamiltonian can be written as

$$\mathcal{H} = \mu_B(\mathbf{BgS}) + \mathbf{SDS} + \mathbf{SAI}. \tag{1.4}$$

Here **g**, **D**, and **A** are tensors of rank 3 corresponding to the anisotropic g-factor, the fine structure splitting and hyperfine coupling, respectively. The first term of the Hamiltonian represents an anisotropic Zeeman splitting, the second term defines the zero-field, fine structure splitting of the ion and the third term corresponds to the hyperfine interaction of the ion with its nucleus. **I** is the nuclear spin operator and **S** is no longer a simple electron-spin operator as before, but an effective spin operator. Actually, S is determined in such a way that the number of low-lying energy levels of the paramagnetic ion is equal to $2S + 1$.

1.1.2 What can be measured by EPR?

It is difficult to cover all the possibilities of the EPR method in studying solid state, liquid, or gaseous materials. Any physical phenomena that has a detectable influence on the paramagnetic ion can be studied. However, one can take a simple approach and ask the question, what kind of results can be obtained for the simplest case of a paramagnetic center with noninteracting spins $S = 1/2$ (leaving only interactions with its local surrounding)? In this case, there is a signal (absorption peak) that has a Lorentzian line shape. There are then three fit parameters for the signal, namely the intensity $\mathcal{I}$, the resonance field B_r, and the line width ΔB_{pp}. The intensity of the signal has a Curie-Weiss temperature dependence $\mathcal{I} = C/(T - \theta)$ since, like the susceptibility, it is proportional to the difference of the populations of the Zeeman-split energy levels. In addition, $\mathcal{I}$ is proportional to the concentration of the paramagnetic ions. Therefore, one can determine the concentration and the Weiss parameter θ. The advantage of EPR in comparison with a magnetometer is that in many cases different paramagnetic ions resonate at different fields. Therefore, different contributions to the susceptibility may be well separated. The resonant field B_r is determined principally by the g-factor that in turn is determined by the symmetry of the local environment and the ground-state wave function of the ion. In addition, any kind of internal paramagnetic, diamagnetic or exchange field can additionally shift the resonance-field position. Therefore, all these effects influencing the resonant field can be studied. The line width of ideal noninteracting (with each other) ΔB_{pp} ions is determined only by relaxation processes. From the Heisenberg uncertainty principle, the line width of the EPR transition in frequency units is inversely proportional to the lifetime of the ion in one of the Zeeman states $\Delta\omega \sim 1/\tau$. Therefore, relaxation processes can be studied by EPR line-width measurements.

The complexity and variety of physics studied by EPR increases when larger spin values are present and their interactions with nuclear magnetic dipole moments, with electric quadrupole moments, with carriers and with surrounding ligands, etc. are included. For more details on basics and deeper knowledge of EPR, the following classical textbooks are useful: Refs. [5, 13, 14, 15].

1.1.3 Technical description of the EPR spectrometer

The EPR-spectrometer setup/lab is shown in Fig. 1.2. The main components of an EPR instrument are the bridge, the cavity, the console, the magnet together with its power supply and the computer. All the high-frequency components of the spectrometer are located in the bridge. The block diagram of the bridge is shown in Fig. 1.3. The tunable microwave generator (a Gun diode) supplies an electromagnetic wave to the main and the reference arms of the bridge. Both arms are equipped with an attenuator allowing the possibility to vary the microwave power in a 60 dB range. In addition, the reference arm is equipped with a phase shifter (see Fig. 1.3). The electromagnetic wave from the main arm goes further to the circulator. The circulator is a device that controls the flow of microwave power. From input 1, it sends the microwave only to input 2 and from input 2 only to input 3 as is shown by the arrow in Fig. 1.3. The microwave entering input 3 of the circulator usually is completely absorbed. The microwave from the main arm goes through the circulator to the cavity containing the sample. The cavity is optimally coupled to the microwave waveguide by the iris (a small screw, that controls the coupling of the cavity with the waveguide) in order to get a maximum signal. Too strong coupling leads to a reduction of the cavity quality factor Q while too weak coupling reduces the EPR signal. The cavity is placed between the magnet poles as shown in Fig. 1.2. The microwave reflected from the cavity is returned to the circulator and goes further to a detector diode along with the microwave coming from the reference arm after the phase shifter. The aim of the reference arm is to compensate the signal coming from the circulator/cavity when there is no EPR resonance. As long as there is no absorption of the microwave by the sample in the cavity, the signal at the output of the diode is zero. But when the absorption takes place, the quality factor of the cavity drops, the reflected power from the cavity changes and the microwaves from the circulator/cavity and the reference arms no longer compensate each other. As a result, an EPR signal appears at the output of diode. To measure the EPR signal, one scans the external field **B** of the magnet in the region of the EPR resonance and detects the signal as a function of **B**.

This principle of the spectrometer has the disadvantage, that the microwave diode has a high noise level at low frequencies. To solve this problem, one shifts the detection frequency from near zero to a new frequency f_m (typically 100 kHz). To do this, one applies in addition to the external field **B** a small oscillating field $\mathbf{B_m}$ parallel to **B** with a frequency f_m and with a typical amplitude B_{m0} ~3 mT. This additional field modulates the Zeeman splitting with the frequency f_m. As one can easily see from Fig. 1.4, the diode-response signal will have the frequency f_m and an amplitude modulated by the slope of the EPR-absorption curve (or by the derivative of the curve). This signal is further sent to the console where it is detected in a lock-in amplifier. After amplification, filtering, and digitizing, it is sent to the computer for further processing. In addition, the magnet controller, the bridge controller, and the digital interface to the computer are located in the console. For high sensitivity of the spectrometer, it is very important that the cavity have a high Q. For the measurements presented in this thesis, a standard rectangular cavity having a Q of 5000 operating in its TE_{102} mode was used [13]. The sample is located in the center of the cavity where the best conditions for observation of a paramagnetic resonance are to be found, namely, a high magnetic field and the minimum electric field.

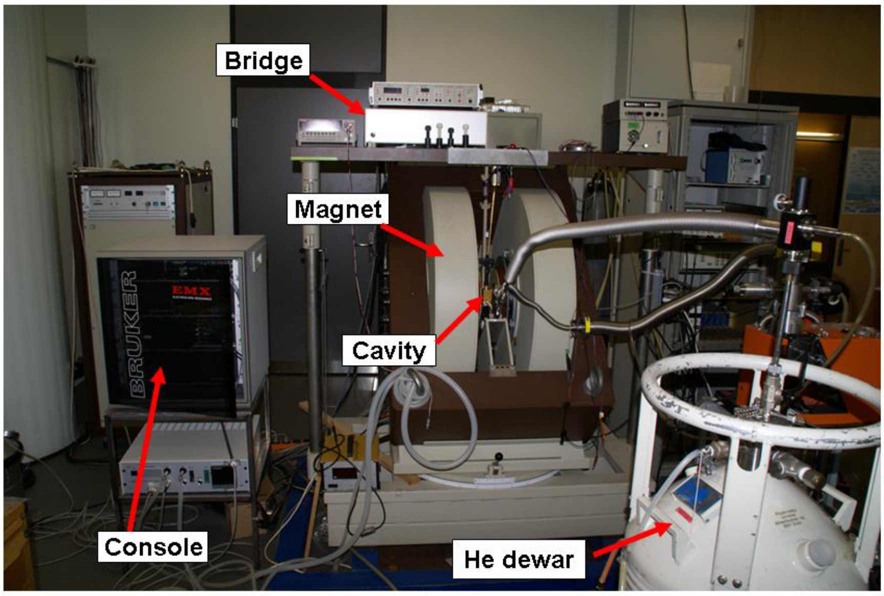

Figure 1.2: EPR spectrometer showing the bridge, the 1.5 T magnet, the console, the cavity between the magnetic poles, He dewar with cryostat and other additional instruments.

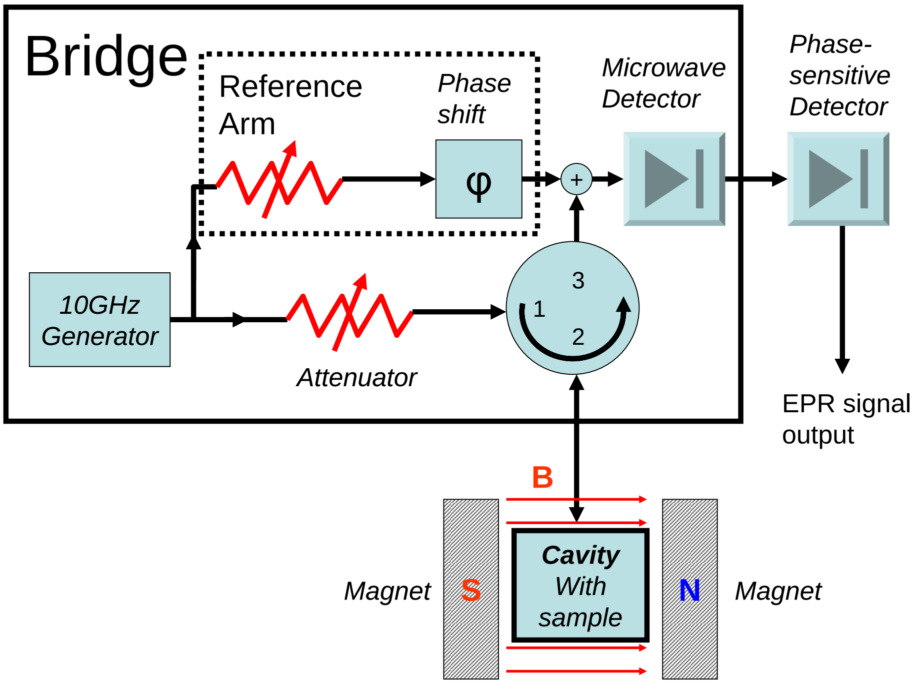

Figure 1.3: Schematic diagram of an EPR spectrometer. The figure shows the basic components of the spectrometer needed for understanding the working principles namely, the bridge, the cavity, the magnet and the detector.

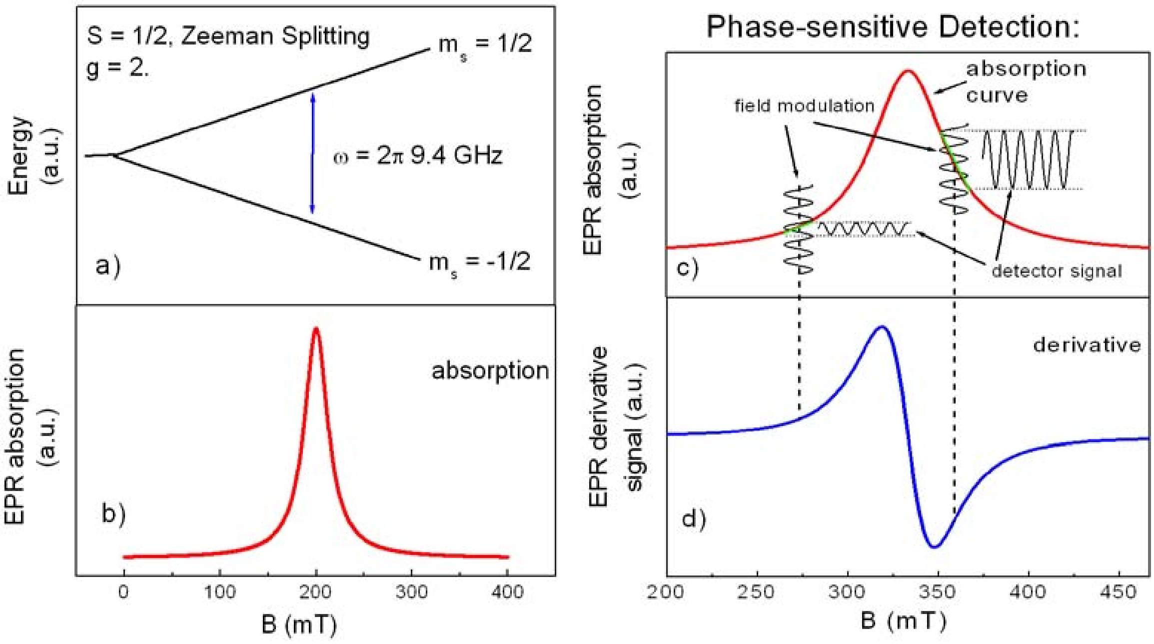

Figure 1.4: (a) The Zeeman splitting of spin degenerate levels in a magnetic field B and (b) the EPR absorption curve as a function of applied magnetic field. (c) Principles of the phase sensitive detection involving the modulated detector signal as a function of the modulated Zeeman field. (d) The EPR signal after the phase sensitive detection.

1.2 Short description of the muon-spin rotation (μSR) technique

The μSR technique has found extremely wide application in condensed matter physics, allowing the study of a variety of problems concerning magnetism, superconductivity, chemical kinetics, diffusion, molecular dynamics and semiconductor physics. It is impossible to cover all the details of its applications for these problems. A good introductory article on muons is Ref. [16] or the review article of Réotier and Yaouanc [8]. More basic knowledge about muons can be found in textbooks (see for example Ref. [7]). Here, the basics of the μSR technique related to the study of superconductors is described, in particular, its application to the study the internal-field distribution in type-II superconductors.

The positive muon μ^+, used to study condensed matter, is an elementary particle. It is a lepton with a mass of approximately 1/9 that of proton, a charge $+e$ and a spin $S = 1/2$. The gyromagnetic ratio of the muon is approximately $\gamma = 2\pi \cdot 135.5$ MHz/T and its lifetime $\tau \approx 2.2$ μs. The muon is produced in the decay of a pion. The pions are obtained by the bombardment of a carbon or a beryllium target with high energy protons [7, 16]. Approximately two microseconds after its production, the muon decays into a positron and two neutrinos. There are two important properties of the muon allowing it to be used as a probe in condensed matter physics. They are 1) the spin of the muon is exactly antiparallel to the momentum of the muon when it is produced from a pion at the rest and 2) due to parity violation in weak interactions, the muon preferably emits a positron in the direction of its magnetic moment $\overrightarrow{\mu}$. The positive muons with an energy of approximately 4 MeV as used at the Paul Scherrer Institute (PSI) are transmitted along a beam line to the secondary target where they are implanted in the sample being investigated. After implantation, the muon quickly thermalizes (in ≈ 1 ns) and stops in an interstitial site of the sample, thus providing the possibility to study the local properties of the sample.

The working principle of a μSR spectrometer is shown in Fig. 1.5. There are two types of spectrometers. The first type uses a continuous beam (CB) of muons and the second one uses a pulsed muon beam (PB). Continuous beam spectrometers are operated at PSI in Switzerland and at TRIUMF in Canada. Pulsed muon beams are used at KEK in Japan and at ISIS in the United Kingdom. In the CB spectrometer, positive, spin-polarized muons, all with roughly the same momentums are incident one at a time on the sample (see Fig. 1.5). At the time of implantation, a special clock triggered by the muon detector is set to zero. In a local magnetic field $\mathbf{B}$, the muon in the sample starts to precess with the Larmor frequency around $\mathbf{B}$ until it decays by emitting a positron. A detected positron e^+ stops the clock and the result of the measured time is used to produce a histogram of detected events for each of the two positron detectors (see Fig. 1.5). Millions of detected positrons are accumulated in the histogram for each of the detectors. At the end of a measurement, one obtains the positron counts as a function of time for the forward $N_F(t)$ and backward $N_B(t)$ detectors. Since the positrons are emitted predominantly in the direction of muon spin which precesses with Larmor frequency, the forward and backward detectors will detect a signal oscillating with the Larmor frequency. In order to get rid of the exponential decay component due to exponential decay of the muons with time, the asymmetry signal as defined by

$$A(t) = \frac{N_F(t) - N_B(t)}{N_F(t) + N_B(t)} \tag{1.5}$$

is introduced. If there is a distribution of the magnetic field $\mathbf{B}(\overrightarrow{r})$ ($\overrightarrow{r}$ is the position vector) in the sample, then each muon will precess with a frequency corresponding to the local field in the sample. The sum of all the asymmetry signals corresponding to the different fields in the sample will produce a somewhat depolarized asymmetry signal. The Fourier transform of this signal will give the internal field distribution in the sample.

In the PB spectrometers, not one but a large number of muons is implanted simultaneously in the sample and again the positron detector counts $N_F(t)$ and $N_B(t)$ as a function of time. One obtains the asymmetry signal using Eq. (1.5). At low fields and a small muon depolarization, the PB spectrometers have an advantage over the CB, since one can obtain high statistical accuracy in a shorter time and one can measure during longer times after implanting the muon. However, at higher fields the PB spectrometers have limitations, since the spread of implantation time due to the muon pulse duration becomes comparable to the Larmor oscillation period of the muon and muons implanted in the sample are no longer polarized.

If the local magnetic field at the muons site $\mathbf{B}(\overrightarrow{r})$ is not oriented normally as is shown in Fig. 1.5 but at the angle θ relative to the muon polarization (spin direction) than the asymmetry signal detected by the forward and the backward detectors can be expressed as [16]:

$$A(t) = A_m[\cos^2\theta + \sin^2\theta\cos(\gamma_\mu Bt)], \tag{1.6}$$

where A_m is the maximal value of the asymmetry, typically between 0.2 and 0.3. This is the starting equation for calculation/modeling of the muon time spectrum $A(t)$ for any spatial field distribution $\mathbf{B}(\overrightarrow{r})$ in a sample.

In a magnetic field above some critical value, type-II supperconductor forms a magnetic vortex structure in which the vortices have a periodic structure. This field is called the first critical field. The periodic structure is referred to as a flux-line lattice (FLL) and typically has a hexagonal or square geometry [17]. Typically, the FLL has a hexagonal or square geometry. The magnetic field around an isolated vortex has a maximum value at the vortex-core center and decreases nearly exponentially with distance from the center. In a FLL, the field has a distribution which depends on the magnetic penetration depth λ and the coherence length ξ. The study of λ and ξ as a function of temperature, field, pressure, chemical substitution, etc. can provide important information about fundamental properties of superconductors. In chapter 3, different models used for the analysis of the internal field distribution of a FLL and the methods used to determine the fit parameters are described.

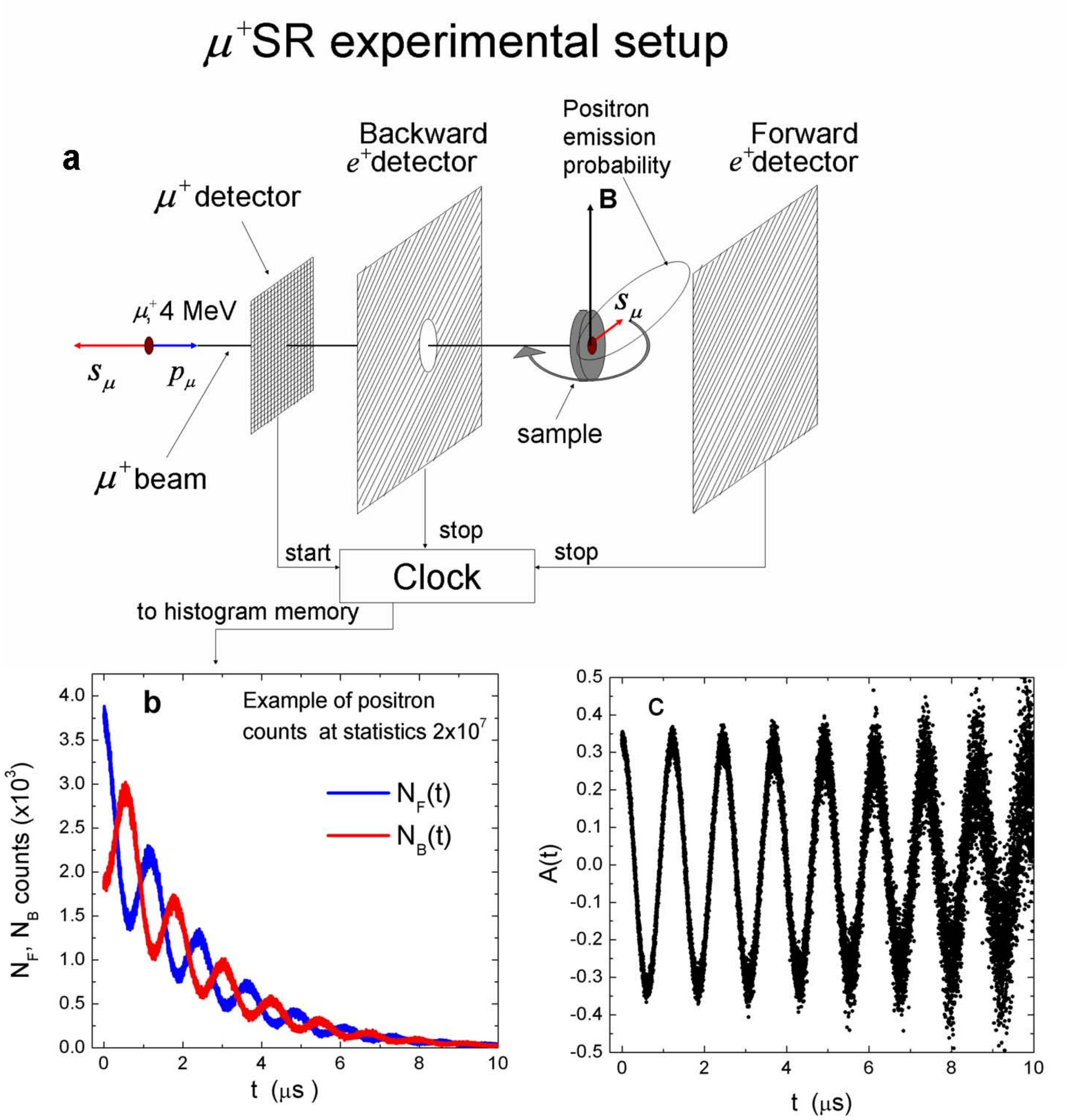

Figure 1.5: The working principle of a μSR spectrometer. (a) The polarized muon μ^+ is implanted in the sample which is located in an external magnetic field B perpendicular to the initial spin direction of the muon. The μ^+ detector sets the clock to zero at the time of implantation. Later, after the decay of a μ^+, a positron detected by either the forward or the backward detector stops the clock. (b) Number of detected positrons as a function of the clock time for the forward and backward detectors stored as histograms in the computer memory. (c) Asymmetry of the μSR signal obtained from the histograms. The asymmetry signal $A(t) = (N_F - N_B)/(N_F + N_B)$ represents the inverse Fourier Transform of the field distribution in the sample.

Chapter 2

EPR study of relaxation processes and phase separation in cuprate superconductors

2.1 The spin-lattice relaxation of Yb^{3+} in $Y_{0.98}Yb_{0.02}Ba_2Cu_3O_x$

2.1.1 Introduction

Relaxation of the rare earth (RE) magnetic moments provides important information about fluctuating electric and magnetic fields in cuprate superconductors. The interaction of the paramagnetic ion with the lattice and the carriers limits the lifetime of the crystal-field (CF) excitations and leads to the broadening of the observed CF transitions. Inelastic neutron scattering (INS) is widely used to study the relaxation of the RE ions in cuprate superconductors by measuring the line width of the observed CF transitions [18]. However, the mechanism for the relaxation of RE ions in cuprates has become an issue of hot debate [19, 20].

Most authors consider an interaction of $4f$ spins with charge-carrier spins (Korringa mechanism) as the dominant channel of the relaxation [21, 22, 23, 24]. Other authors conclude that the interaction of RE spins with charge carriers are negligible and that the interactions with lattice vibrations are responsible for the relaxation behavior of the $4f$ electrons in cuprates [25, 26, 27]. At present, there is no consensus on this subject and therefore it is important to disentangle the electronic and phononic sources of relaxation. Moreover, this study can give additional information concerning the behavior of carriers and phonons related to the CuO_2 planes.

Relaxation of the $4f$ magnetic moments can also be studied by measuring the line width of the Electron Paramagnetic Resonance (EPR) signal of RE ions [28]. There have been only a few EPR studies of the RE ions with nonzero orbital momentum (Er and Yb) doped cuprates [29, 30, 31, 32, 33, 34, 35, 36]. Paramagnetic signals of Nd^{3+} and Sm^{3+} in $YBa_2Cu_3O_x$ are unobservable [37]. Dy^{3+} has low lying CF levels and already relaxes at low temperatures [38, 39]. Again as in the INS studies, the situation in EPR is contradictory. Some groups have observed both electronic (Korringa) and phononic (Orbach) contributions to the EPR relaxation [29, 32, 33] while others conclude that the Korringa contribution is negligible and the interaction with only the lattice vibrations is sufficient to explain the temperature dependence of the EPR line width in cuprates [34, 35].

In the following sections, a detailed EPR study is presented of the Yb^{3+} relaxation in $YBa_2Cu_3O_x$ from the undoped insulating to the optimally doped superconducting region ($6 < x < 7$). By measuring the temperature dependence of the Yb^{3+} EPR line width in the superconducting and the normal state, it was found that both electronic and phononic mechanisms contribute to the relaxation. As expected, the electronic contribution decreases with decreasing oxygen doping while the phonon contribution is nearly doping independent. Comparison of the EPR line width in samples with and without Zn doping allowed for the first time a clear separation of the electronic and phononic contributions to the Yb relaxation. The phononic contribution to the relaxation has an exponential character with an activation energy $\Delta/k_B \simeq 500$ K. Analysis of experimental results allows one to conclude that the phononic relaxation originates from an optical phonon or Jahn-Teller fluctuations involving

CuO_6 complexes.

2.1.2 Sample preparation and EPR spectra

The polycrystalline samples of $YBa_2Cu_3O_x$ with $x = 6.1$, 6.2, 6.3, 6.4, 6.5, 6.6, 6.7 and 6.98 were prepared by the standard solid-state reaction using Y_2O_3, Yb_2O_3, $BaCO_3$ and CuO. A typical spectrum of Yb^{3+} in powdered polycrystalline $YBa_2Cu_3O_x$ samples at low temperatures is shown in Fig. 2.1 as a solid black line. The spectrum is asymmetric and has characteristic features of an EPR spectrum with spin $S = 1/2$ and an anisotropic g-factor. To get rid of the anisotropy, the sample was c-axis oriented. To obtain the orientation, the powdered sample was suspended in epoxy resin (or paraffine) and placed in a 9 T magnetic field until the epoxy (or paraffine) was hardened [40]. The result of the orientation is shown in Fig. 2.1. It is seen that the degree of the orientation is high and one can easily determine principal values of the anisotropic g-factor. For an oxygen doping of $x = 6.4$, there are two principal g-factor values ($g_\perp = g_x = g_y$ and $g_\| = g_z$). With increasing doping, the anisotropy of the g-factor increases in agreement with the tetragonal-to-orthorombic phase-transition at $x = 6.4$ in $YBa_2Cu_3O_x$ [41] and $g_\perp$ splits into two different values (g_x and g_y) as is evident from the splitting of the EPR signal measured in the $B \perp c$-axis orientation (see Fig. 2.1). Using the equation $g^2 = g_x^2 \cos^2\phi + g_y^2 \sin^2\phi$, the distribution of the g-factors for an applied field $B \perp c$-axis and a randomly oriented a-axis is

$$P(g)dg = \frac{1}{\pi}\frac{g}{\sqrt{(g^2 - g_x^2)(g_y^2 - g^2)}}dg. \tag{2.1}$$

This distribution has singularities for $g = g_x$ or g_y. As a result, there are pronounced peaks of the EPR signal for fields corresponding to these g-factors as is seen in Fig. 2.1.

A small unresolved peak near the main signal comes from the hyperfine splitting of the Yb^{3+} line. In natural Yb, there are 3 isotopes for which 14% is ^{171}Yb having a nuclear moment $I = 1/2$, 16% is ^{173}Yb having $I = 5/2$ and 70% is the spinless isotope ^{174}Yb. Both odd isotopes give rise to nuclear hyperfine interactions.

In further investigations, the orientation of B was chosen perpendicular to the c-axis in order to study the relaxation mechanisms for the following reasons: 1) Yb^{3+} in this orientation has a larger g-factor and the Yb^{3+} signal in the perpendicular orientation overlaps with the Cu^{2+} signal at higher temperatures. Therefore, measurements can be performed in a broader temperature range. 2) For the same relaxation rate, the line width is proportional to the inverse g-factor (see Eq. (2.24)). Therefore, the signal is narrower and can be measured at higher temperatures. 3) In the superconducting state, nonresonant microwave absorption (NMA) is less nonlinear for the perpendicular orientation and the signal is less distorted. The only disadvantage is that the line shape is somewhat more complicated than in the $B \parallel c$ orientation.

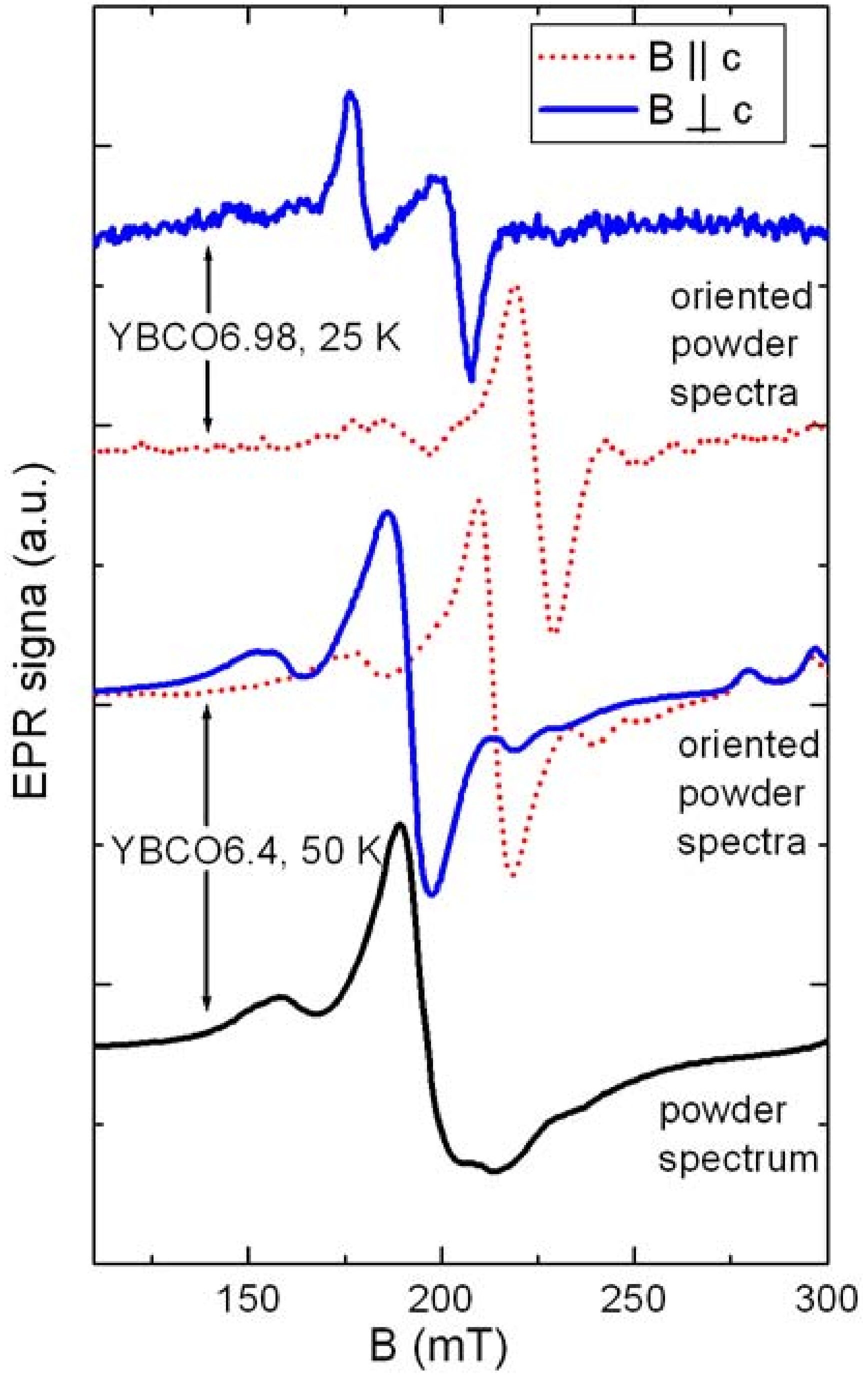

Figure 2.1: Examples of Yb^{3+} spectra in $Y_{0.98}Yb_{0.02}Ba_2Cu_3O_x$. The lower spectrum (black line) corresponds to the nonoriented powder spectrum for $x = 6.4$ (YBCO6.4). The solid blue and dotted red lines in the middle correspond to the spectra of Yb^{3+} after orientating the sample with B perpendicular and parallel to the c-axis, respectively. The degree of orientation is sufficient to resolve the two principal values of the Yb^{3+} g-factor in the tetragonal enviroment of $Y_{0.98}Yb_{0.02}Ba_2Cu_3O_{6.4}$. The upper solid blue and dotted red lines belong to the Yb^{3+} spectra of $Y_{0.98}Yb_{0.02}Ba_2Cu_3O_{7-\delta}$ in the superconducting state for B perpendicular to and parallel to the c-axis, respectively (YBCO6.98). Two peaks in B perpendicular to the c-axis correspond to signals at g_x and g_y (g_a, g_b). Splitting of the $g_\perp$ into g_x and g_y is in agreement with the orthorombic symmetry of Yb^{3+} for $x = 6.98$. Note that the anisotropy in the x and y directions is comparable to that in z direction.

2.1.3 Crystal-field splitting and the ground-state doublet of Yb^{3+} in $\mathrm{Y}_{0.98}\mathrm{Yb}_{0.02}\mathrm{Ba}_2\mathrm{Cu}_3\mathrm{O}_x$

Yb belongs to the rare earth elements for which the electronic shell results in a magnetic moment due to an internal $4f$ shell hidden behind a $6s^2$ shell. For this reason, coupling to the surrounding ions - ligands is relatively weak and Hund's rules [42] valid for isolated ions works well for the rare earth elements. According to Hund's rules the ground state of the $4f^{13}$ shell is an 8-fold degenerate state $^2\mathrm{F}_{7/2}$. However, the Yb^{3+} ion is in the orthorombic surrounding of $\mathrm{Y}_{0.98}\mathrm{Yb}_{0.02}\mathrm{Ba}_2\mathrm{Cu}_3\mathrm{O}_x$ and one should take into account the crystal-field splitting (Stark effect) induced by electrostatic fields of ligand ions. The hamiltonian for the crystal-field splitting in the tetragonal approximation is written in the following way [43]:

$$\mathcal{H} = B_{20}\hat{O}_{20} + B_{40}\hat{O}_{40} + B_{44}\hat{O}_{44} + B_{60}\hat{O}_{60} + B_{64}\hat{O}_{64} \tag{2.2}$$

where B_{20}, B_{40}, B_{44}, B_{60}, B_{64} are coefficients, $\hat{O}_{20} - \hat{O}_{64}$ are Stevens operators expressed as a polynomial of (raising $\hat{J}_+$), lowering ($\hat{J}_-$), and $\hat{J}_z$ operators (see APPENDIX B for details). Each of these operators can be expressed as an 8×8 matrix (since $J = 7/2$ for Yb^{3+} and $2J + 1 = 8$). To find the crystal field, the eigenvalues and the eigenvectors, one has to diagonalize this 8×8 matrix of Hamiltonians thereby obtaining 8 eigenvalues. This problem was solved analytically by Kutuzov *et al.* [43] who obtained the 4 eigenvalues corresponding to the 4 Kramers doublets

$$E_1 = 3B_{20} + 480B_{40} - 2520B_{60} + K_a \tag{2.3}$$

$$E_2 = 3B_{20} + 480B_{40} - 2520B_{60} - K_a \tag{2.4}$$

$$E_3 = -3B_{20} - 480B_{40} + 2520B_{60} + K_c \tag{2.5}$$

$$E_3 = -3B_{20} - 480B_{40} + 2520B_{60} - K_c \tag{2.6}$$

where K_a and K_c are

$$K_a^2 = (A_1 - A_2)^2 + A_3^2 \tag{2.7}$$

$$K_c^2 = (C_1 - C_2)^2 + C_3^2 \tag{2.8}$$

and A_1, A_2, A_3, C_1, C_2, and C_3 are

$$A_1 = 21/2B_{20} + 210B_{40} + 630B_{60}, \qquad C_1 = 3/2B_{20} - 390B_{40} - 315B_{60} \tag{2.9}$$

$$A_2 = -15/2B_{20} + 270B_{40} - 3150B_{60}, \qquad C_2 = -9/2B_{20} - 90B_{40} + 5670B_{60} \tag{2.10}$$

$$A_3 = 12\sqrt{35}B_{44} + 180\sqrt{35}B_{64}, \qquad C_3 = 60\sqrt{3}B_{44} - 420\sqrt{3}B_{64}. \tag{2.11}$$

The eight eigenfunctions are

$$|1,\uparrow\rangle = a_1|-7/2\rangle + a_2|1/2\rangle, \qquad |1,\downarrow\rangle = -a_1|7/2\rangle - a_2|-1/2\rangle \tag{2.12}$$

$$|2,\uparrow\rangle = a_2|-7/2\rangle - a_1|1/2\rangle, \qquad |2,\downarrow\rangle = -a_2|7/2\rangle + a_1|-1/2\rangle \tag{2.13}$$

$$|3,\uparrow\rangle = c_1|5/2\rangle + c_2|-3/2\rangle, \qquad |3,\downarrow\rangle = -c_1|-5/2\rangle - c_2|3/2\rangle \tag{2.14}$$

$$|4,\uparrow\rangle = c_2|5/2\rangle - c_1|-3/2\rangle, \qquad |4,\downarrow\rangle = -c_2|-5/2\rangle + c_1|3/2\rangle \tag{2.15}$$

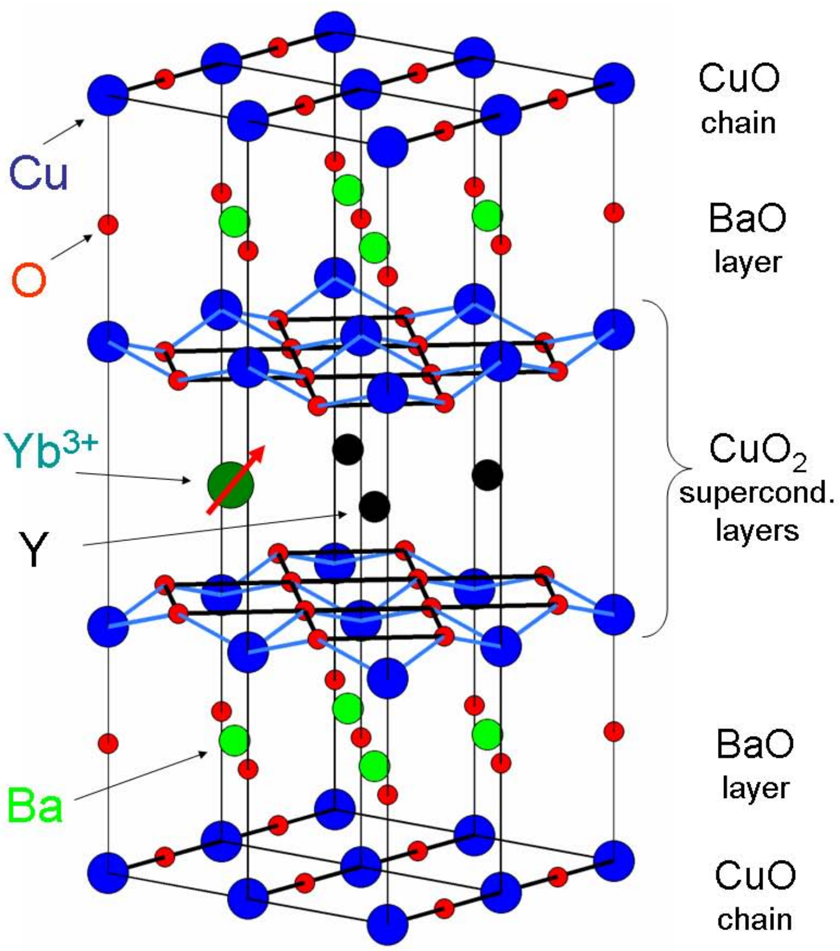

Figure 2.2: Crystal structure of optimally doped $YBa_2Cu_3O_x$. The Yb^{3+} EPR probe occupies a Y^{3+} site sandwiched between the superconducting CuO_2 planes.

where

$$a_1 = [2K_a(K_a + A_1 - A_2)]^{-1/2}(K_a + A_1 - A_2) \tag{2.16}$$

$$a_2 = [2K_a(K_a + A_1 - A_2)]^{-1/2}A_3 \tag{2.17}$$

$$c_1 = [2K_c(K_c + C_1 - C_2)]^{-1/2}(K_c + C_1 - C_2) \tag{2.18}$$

$$c_2 = [2K_c(K_c + C_1 - C_2)]^{-1/2}C_3. \tag{2.19}$$

The ground state is a Γ^7 doublet which is given by Eq. (2.15). The principal values of the g-factor for this doublet are

$$g_{\parallel} = g_J(5c_2^2 - 3c_1^2) \tag{2.20}$$

$$g_{\perp} = 4\sqrt{3}g_J c_1 c_2 \tag{2.21}$$

where $g_J = 8/7$ is the Lande g-factor (or free-ion g-factor).

2.1.4 Analysis of the EPR spectra

The anisotropic nature of the Yb^{3+} signal, the partially resolved hyperfine structure and the nonideal grain alignment of the polycrystalline samples, make it very difficult to accurately model the complex shape of the Yb^{3+} EPR spectra and their evolution with temperature. In order to extract the line width related to the relaxation, we have used an approach similar to the one used in inelastic neutron-scattering studies of rare-earth relaxation in cuprates [23]. The line shape of the EPR signal $g(B)$ at low temperatures ($T \simeq 40$ K) represents a temperature-independent, inhomogeneous broadening. With increasing temperature the function $g(B)$ is additionally broadened due to relaxation processes. The resulting signal $f(x)$ can be expressed as the convolution of $g(B)$ with a Lorentzian, the width of which is proportional to the relaxation rate of Yb^{3+}

$$f(x|A, B_r, \Delta B_{pp}) = \int g(y)L(x-y|A, B_r, \Delta B_{pp})dy. \tag{2.22}$$

Here, the vertical line separates independent variables on the left side from the fit parameters on the right side. x is the field and A, B_r and ΔB_{pp} are fit parameters corresponding to the amplitude, the resonant field and the peak-to-peak line width of a Lorentzian-derivative, respectively. $L(x|A, B_r, \Delta B_{pp})$ is the derivative of the Lorentzian function [13]:

$$L(x|A, B_r, \Delta B_{pp}) = 16A\frac{x - Br}{0.5\Delta B_{pp}} \cdot \left[3 + \left(\frac{x - Br}{0.5\Delta B_{pp}}\right)^2\right]^{-2}. \tag{2.23}$$

The parameter ΔB_{pp} is the subject of our interest and corresponds to the broadening of the line with the given structure $g(B)$ due to the relaxation. The absolute value of spin-lattice relaxation is related to this parameter by the relation [28]:

$$T_2^{-1} = \sqrt{3}/2\gamma\Delta B_{pp} = 7.62 \cdot 10^6 g\Delta B_{pp}. \tag{2.24}$$

2.1.5 Summary of results and discussion

A neutron scattering experimental study of $YbBa_2Cu_3O_{7-\delta}$ has shown that the $^2F_{7/2}$ multiplet of Yb^{3+} splits into 4 doublets with a ground-state doublet and three other doublets lying more than 1000 K above the ground state (88.5, 92.8, and 98.5 meV respectively) [44]. Below room temperature, the EPR signal is observed only for the ground-state doublet which can be described in an effective $S = 1/2$ notation. Experimental values of the g-factors for the optimal doping are $g_x = 3.00$, $g_y = 3.29$, and $g_z = 3.76$. The average value $g_{av} = (g_x + g_y + g_z)/3 = 3.35$ is close to $g = 3.43$ expected for a Γ^7 ground-state doublet in the cubic crystal-field approximation [5].

Fig. 2.3 shows typical EPR spectra in $Y_{0.98}Yb_{0.02}Ba_2Cu_3O_{6.4}$ at different temperatures with the magnetic field perpendicular to the c-axis. The EPR lines in the $g \approx 2$ region are due to the defect Cu^{2+} centers which are always present in $YBa_2Cu_3O_x$ [45]. The Yb EPR spectrum at 40 K broadens with increasing temperature. This broadening is due to the Yb^{3+} relaxation and is a subject of the present study.

Phononic part of the relaxation

Generally, in conducting samples, local magnetic $4f$ moments of RE ions can interact with phonons as well as with charge carriers. Fig. 2.4 shows the temperature dependence of the width ΔB_{pp} of the broadening function [see Eq. (2.22)] in $Y_{0.98}Yb_{0.02}Ba_2Cu_3O_x$ for different oxygen contents x. In the sample with $x = 6.1$, which is antiferromagnetic and insulating with practically no charge carriers, the relaxation rate is comparable to those samples with much higher hole contents. Consequently, this suggests that the phonon contribution to the RE relaxation rate is significant at all oxygen doping levels since at $x = 6.1$ the electronic contribution is expected to be negligible.

It was observed that the temperature dependence of the relaxation rate follows closely the exponential function $C\exp(-\Delta/T)$ for the $x = 6.1$ and 6.4 samples with $\Delta/k_B \sim 500(50)$ K. This is demonstrated in Fig. 2.5 for the $Y_{0.98}Yb_{0.02}Ba_2Cu_3O_{6.4}$ sample, where the relaxation rate is plotted on a logarithmic scale versus inverse temperature. Such an exponential dependence is expected for the Orbach relaxation process via an excited intermediate energy level [48]. However, the first excited states of Yb^{3+} is about 1000 K above the ground state. Therefore, the traditional Orbach relaxation mechanism can be excluded, since there is no excited CF energy level with $\Delta/k_B \sim 500$ K.

Another possible relaxation mechanism is the Raman two-phonon process involving acoustic phonons with the following temperature dependence for the case of the Kramers doublet [5]:

$$T_1^{-1}(T) = CT^9 \int_0^{\Theta_D/T} z^8 e^z/(e^z - 1)^2 dz. \tag{2.25}$$

This expression fits the temperature dependence of the relaxation rate quite well as shown by the dashed line in Fig. 2.5. However, the Debye temperature $\Theta_D = 650(20)$ K obtained from the fit is too large compared with $\Theta_D = 300$ K reported for low-doped $YBa_2Cu_3O_x$ [49]. The dotted line in Fig. 2.5, calculated with $\Theta_D = 300$ K, clearly does not fit the data

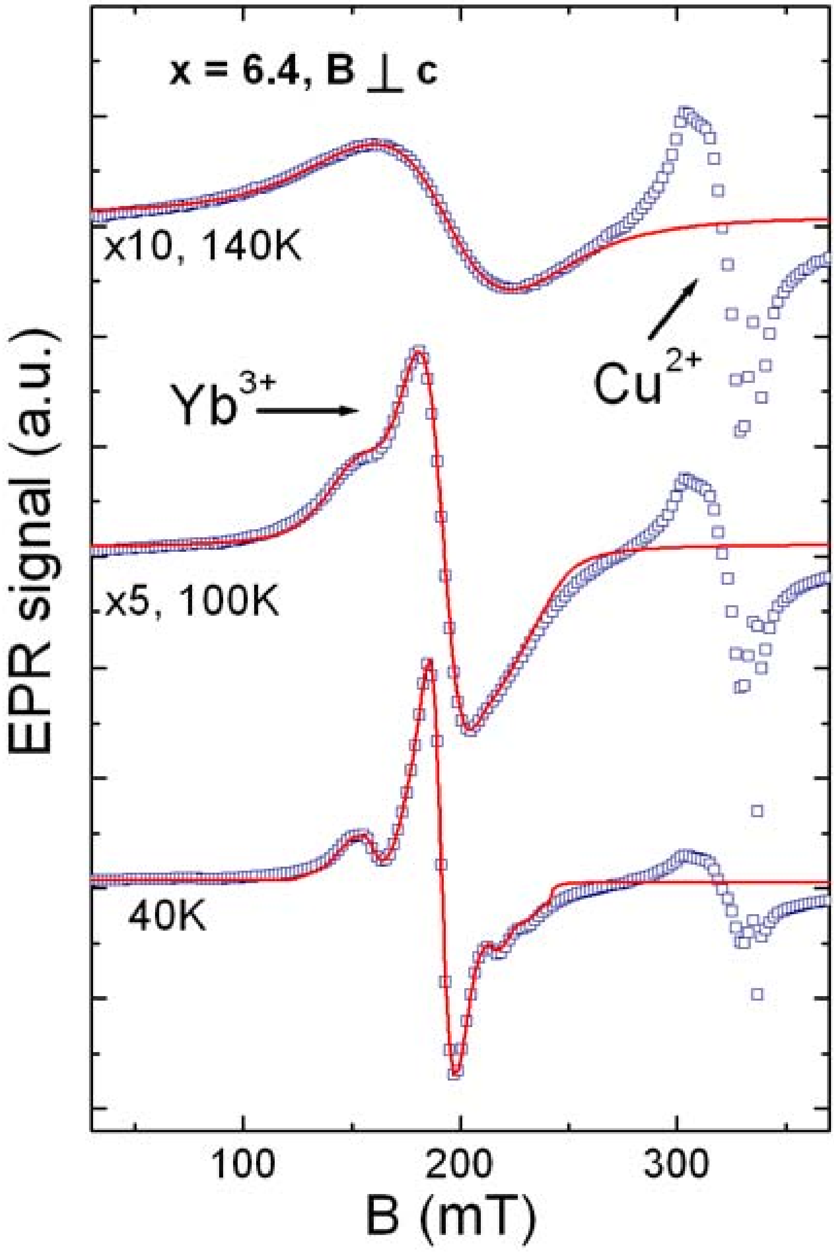

Figure 2.3: EPR spectra in grain oriented $Y_{0.98}Yb_{0.02}Ba_2Cu_3O_{6.4}$ at different temperatures for a magnetic field direction perpendicular to the crystal c-axis. The solid lines are fits to the data and include relaxation as described in the text. The spectrum around 330 mT belongs to the Cu^{2+} always observable in cuprate superconductors [45, 46, 47].

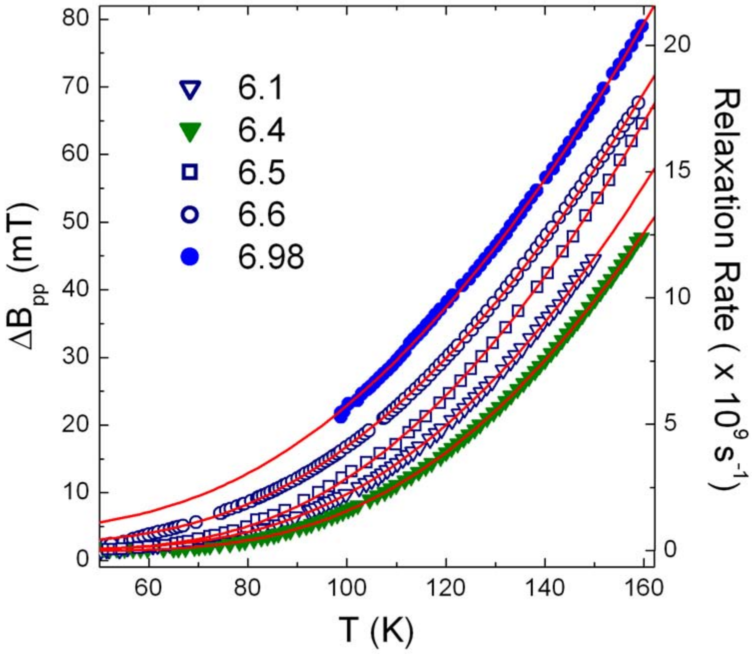

Figure 2.4: Temperature dependence of the width of the broadening function ΔB_{pp} in $Y_{0.98}Yb_{0.02}Ba_2Cu_3O_x$ with different oxygen content x. The solid lines represent the best fit to the data using Eq. (2.27).

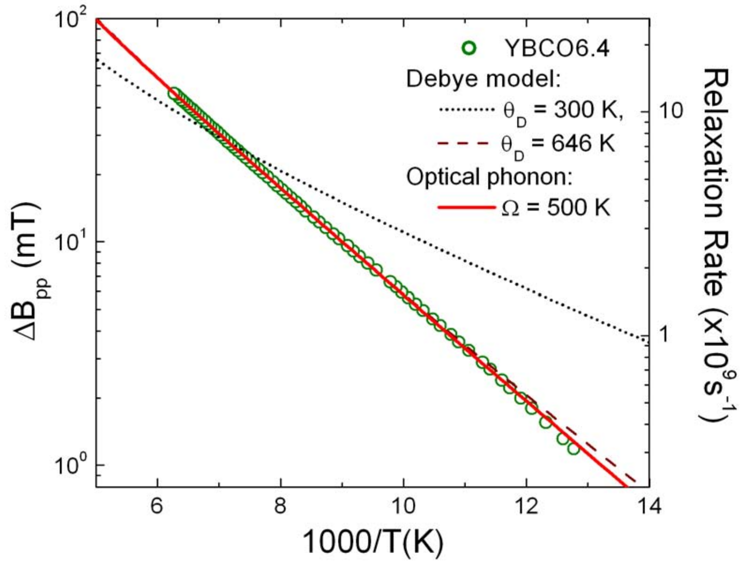

Figure 2.5: Spin-lattice relaxation rate and line width of the broadening function ΔB_{pp} as a function of inverse temperature $(1000/T)$ in $Y_{0.98}Yb_{0.02}Ba_2Cu_3O_{6.4}$ (green circles). The dashed line is the best fit to the data by the Debye model (see text), with $\theta_D = 650$ K. With the dotted line is shown the best fit by the Debye model with fixed $\theta_D = 300$ K. The solid line represents the fit with the optical phonon model with $\Omega = 500(50)$ K as described in the text.

and shows that a conventional Raman process involving acoustic phonons cannot explain the temperature dependence of the Yb^{3+} relaxation rate in $YBa_2Cu_3O_x$. The optical modes in the Debye model are taken into account only by extending the acoustical modes beyond the Brillouin zone with the Debye temperature Θ_D defined by the total degrees of freedom of the lattice (see Fig. 2.6). The dashed line in Fig. 2.5 shows that in principle it is possible to fit the experimental results with such a model; however Θ_D obtained from this fit has nothing to do with the real Debye temperature of the material. Therefore, although the Debye model can reasonably describe the heat capacity properties, our results show that it is not valid for the spin-lattice relaxation at relatively high temperatures.

Since the exponential character of relaxation can not be explained by the traditional Orbach or Raman relaxation models, the only remaining possibility is relaxation via the Raman process with phonons having an energy $\Omega \simeq 500(50)$ K. That is, the distribution of the phonon density as a function of energy, sensed by Yb^{3+} , must behave as shown in Fig. 2.6. Note that Yb^{3+} is sensitive to the planar nearest oxygens creating the crystal field, whereas the specific-heat technique is sensitive to the vibrations of all the ions in $YBa_2Cu_3O_x$. This agrees well with the general phonon density of states (PDOS) measured by neutron scattering shown in Fig. 2.6. The peak near $\simeq$ 44 meV ($\simeq$ 480 K) corresponds to phonons involving the oxygen ions. The other peaks at lower energies probably correspond to the vibrations of heavier ions to which Yb^{3+} is less sensitive. The difference of the PDOS sensed by Yb^{3+} in EPR and other techniques is the reason for the discrepancy between Θ_D obtained by these methods and Θ_D obtained by EPR. For a Raman process with the participation of some local vibrations or optical phonons, one finds

$$T_1^{-1}(T) = C\frac{\exp(\Omega/T)}{[\exp(\Omega/T)-1]^2}, \tag{2.26}$$

where Ω is local/optical phonon frequency [51, 52]. The solid line in Fig. 2.5 represents the best fit to the data using Eq. (2.26) with $\Omega \simeq 500(50)$ K. Optical phonons with this energy range exist in $YBa_2Cu_3O_x$ which are due to (i) in-plane bond-bending (500-560 K) and (ii) out of plane B_{1g} (470 K) phonons [53]. Preliminary theoretical calculations show that the optical phonon contribution to the relaxation in the temperature range 60-140 K is at least one order of magnitude larger than the contribution from acoustical phonons [43].

It is interesting to note that an exponential temperature dependence of the spin relaxation rate was also observed in the EPR study of crystals containing Jahn-Teller (JT) transition-metal ions [54, 55]. In this case, relaxation takes place due to Orbach-like process via the excited vibronic levels of the JT ion. In our case, such a scenario is also possible if the Yb^{3+} spin relaxation occurs due to coupling to the vibrations of surrounding CuO_6 complexes since Cu^{2+} is a strong JT ion. There are no reports on the JT splitting of Cu^{2+} in $SrTiO_3$ or similar perovskites, but in MgO and CaO, there is a splitting at approximately 1500 K [55] which is much larger than the 500 K found in the present work. However, it was observed that for Ni^{3+}, the JT splitting in $SrTiO_3$ is reduced by a factor of 2-4 compared with that in MgO, CaO or Al_2O_3 structures [54, 55]. Similar reduction of JT splitting can also be expected for Cu^{2+} in perovskites which could agree with the energy we observe. It would be interesting

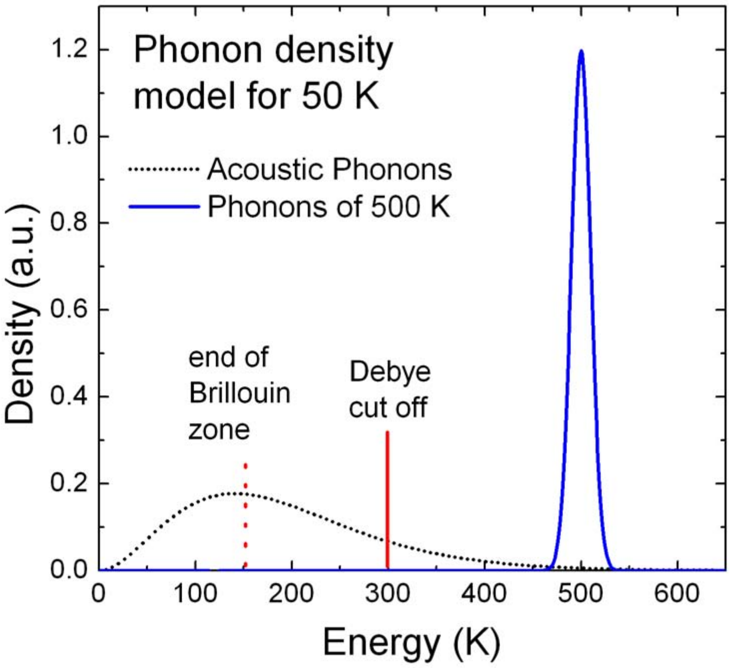

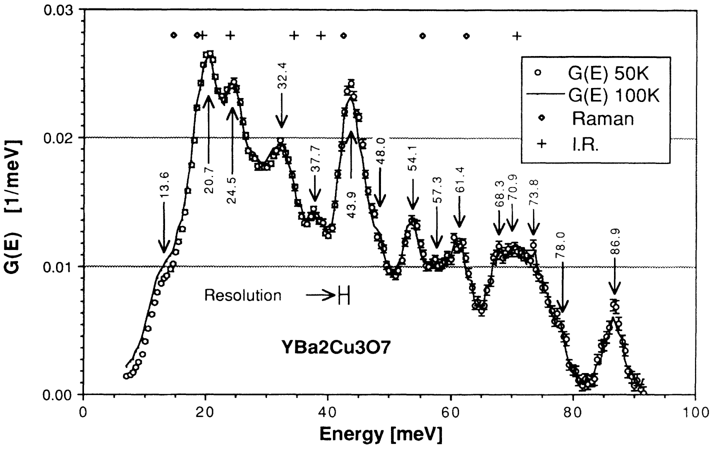

FIG. 1. Generalized phonon density of states (PDOS) at 50 and 100 K for $E_i = 130$ meV.

Figure 2.6: Qualitative description of the phonon density as a function of an energy calculated for $T = 50$ K (top). The black dots describe the acoustic phonon distribution (Planck's distribution) with a cut off at the end of the Brillouin zone. In order to account for the optical phonon modes (solid blue line) of the specific heat measurements or the EPR relaxation, the Debye model is used where the cut off is extended up to the Debye energy/temperature. The lower figure shows the general phonon density of states as measured for $YBa_2Cu_3O_{7-\delta}$ with neutron scattering by Arai *et al.*(bottom) [50]. The intense peak around 44 meV ($\simeq$ 480 K) corresponds to local phonons presumably responsible for the relaxation of Yb^{3+} .

to search for localized vibronic levels in cuprates using inelastic neutron scattering.

Yb^{3+} relaxation due to coupling with charge carriers

For an oxygen content $x > 6.4$, Eq. (2.26) does not describe the relaxation data well. It was necessary to add a term bT linear (Korringa) in temperature. The parameter b of this term is proportional to the product $[J_{sf}N_F]^2$ where J_{sf} is the exchange integral between Yb^{3+} moments and holes and N_F is a density of states at the Fermi energy. The solid lines in Fig. 2.4 correspond to fits to the data using a sum of phononic and electronic contributions having the form

$$T_1^{-1}(T) = C\frac{\exp(\Omega/T)}{[\exp(\Omega/T) - 1]^2} + bT. \tag{2.27}$$

It was found that $\Omega \simeq 500(50)$ K is almost independent of the oxygen content x. This is in agreement with neutron scattering and Raman data which show no dependence of the bond-bending and B_{1g} phonon energies on x [53]. Therefore, $\Omega = 500$ K was fixed during the fit. It was found that b is approximately 0 for $x \leq 6.4$ and increases rapidly with oxygen doping above $x = 6.5$ ($b = 0.6(1)$ G/K for $x = 6.6$ and $b = 1.27(10)$ G/K for $x = 6.98$).

Yb^{3+} relaxation in the superconducting state

Eq. (2.27) describes the data well in the normal state of the superconducting samples. However, in the superconducting state, deviations are observed (see Fig. 2.7(a)). It is natural to attribute the anomaly in the relaxation to the opening of the superconducting gap. However, there is another possibility to explain the anomaly, and that is a softening of phonons below T_c [56]. In order to check these possibilities, the relaxation of Yb^{3+} in $YBa_2(Cu_{0.97}Zn_{0.03})_3O_{6.95}$ was measured for which Zn doping reduces T_c to 57 K. The relaxation rates obtained in samples with and without Zn doping are shown in Fig. 2.7(b). It is expected that the 3% Zn doping should not modify the phonon spectra and the electronic density of states. In fact, above ~90 K, the relaxation rates are the same for both samples. However, below 90 K the behavior of relaxation is quite different in the two samples. While the relaxation rate of the sample without Zn doping sharply decreases below this temperature due to the onset of superconductivity, in the Zn-doped sample, the relaxation continues to decrease monotonically until $T_c^{Zn} = 57$ K where a small decrease in the relaxation rate is seen. This result, together with an increase of relaxation with increased doping, unambiguously shows that the superconducting-gap opening is responsible for the sharp decrease of Yb^{3+} relaxation in $YBa_2Cu_3O_x$. Moreover, it proves the presence of the electronic channel of relaxation described by the Korringa term bT in Eq. (2.26) since such an anomaly cannot be produced by phonon relaxation.

Having extracted the electronic part of the Yb^{3+} relaxation rate, it is interesting to investigate its temperature dependence in the superconducting state where relaxation drops due to the opening of the superconducting gap. In Fig. 2.8 is plotted the electronic part of $1/T_1T$ versus the reduced temperature T/T_c in the x=6.98 sample together with the corresponding quantity obtained from NMR measurements for oxygen [57] and copper [58]

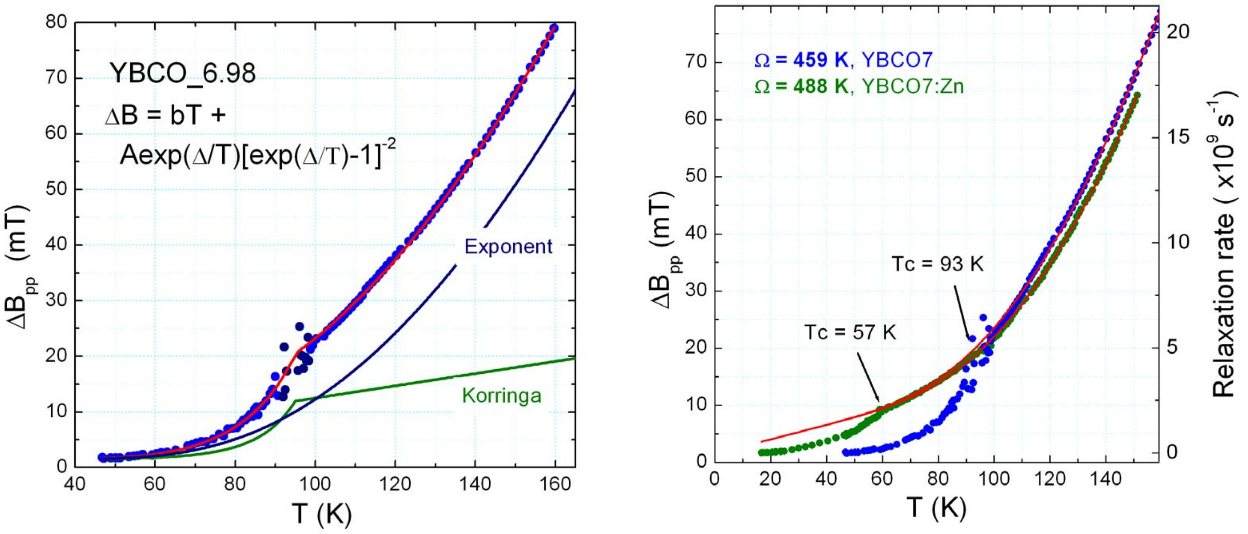

(a) The spin-lattice relaxation rate of Yb^{3+} for optimally doped $Y_{0.98}Yb_{0.02}Ba_2Cu_3O_{6.98}$. The solid red line above T_c is a fit to the data with Eq. (2.27). Below T_c, the coefficient b was taken to be temperature dependent of the form $b_{sc} = b\exp(-\Delta_{sc}(T)/T)$ where $\Delta_{sc}(T) = \Delta_0[1-(T/T_c)^4]$ is the superconducting gap and $\Delta_0 \simeq 220$ K which gives $2\Delta/T_c \simeq 4.8$. The solid blue and green lines correspond to the phononic and the electronic contributions to the relaxation, respectively.

(b) The spin-lattice relaxation rate of Yb^{3+} for optimally doped $Y_{0.98}Yb_{0.02}Ba_2Cu_3O_{6.98}$ (YBCO7) and $Y_{0.98}Yb_{0.02}Ba_2Cu_{2.91}Zn_{0.09}O_{6.98}$ (YBCO7:Zn). The figure shows an anomaly in the relaxation is observed in both cases at the superconducting transition which supports the idea of an electronic origin of relaxation anomaly as explained in text.

Figure 2.7: Description of spin-lattice relaxation rate in $Y_{0.98}Yb_{0.02}Ba_2Cu_3O_{7-\delta}$ and relaxation in $Y_{0.98}Yb_{0.02}Ba_2Cu_3O_{7-\delta}$:Zn.

nuclei. It is remarkable that ($1/T_1T$) has a very similar temperature dependence for Yb^{3+} spins and ^{63}Cu and ^{17}O nuclei despite a huge (10^6) difference between the electron and nuclear relaxation rates.

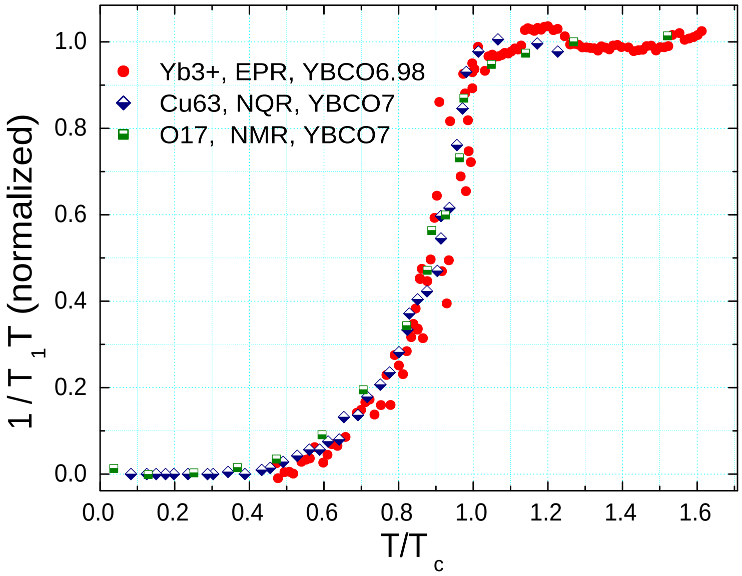

Figure 2.8: $1/T_1T$ of Yb^{3+} in the superconducting state normalized by its value at 100 K in $Y_{0.98}Yb_{0.02}Ba_2Cu_3O_{6.98}$ versus reduced temperature T/T_c, compared with those of ^{17}O NMR and ^{63}Cu NQR in $Y_{0.98}Yb_{0.02}Ba_2Cu_3O_{7-\delta}$ [58].

2.1.6 Conclusions

To summarize, the detailed study of the temperature dependence of Yb^{3+} EPR line width was performed, i.e., the relaxation in $YBa_2Cu_3O_x$ from the undoped insulating to optimally doped superconducting region ($6 < x < 7$). It was found that both electronic and phononic processes contribute to Yb^{3+} relaxation. It was possible to separate these processes and study their relative contributions to relaxation as a function of oxygen doping. As expected, the electronic contribution decreases with decreasing oxygen doping while the phonon contribution is practically doping independent. It was found that traditional Raman and Orbach mechanisms involving acoustic phonons can not explain the temperature dependence of the Yb^{3+} EPR line width. Instead, a Raman process via the coupling to high-energy (∼500 K) phonons is responsible for the phononic part of Yb^{3+} relaxation in $YBa_2Cu_3O_x$. The kind of local phonon is still under question. Possible candidates are any optical phonon related to the planar-oxygen vibration or Jahn-Teller fluctuations of the CuO_6 complexes with energy ∼500 K.

In the sample with the maximum oxygen doping $x = 6.98$, a sharp drop of the relaxation rate is observed below T_c. Comparison of the EPR line width in samples with and without Zn doping allowed us to prove that the opening of the superconducting gap is responsible for the sharp decrease of Yb^{3+} relaxation in $YBa_2Cu_3O_{6.98}$. It was shown that the electronic part of the Yb^{3+} relaxation rate in superconducting state follows the same temperature dependence as the ^{63}Cu and ^{17}O nuclear relaxations despite the six orders of magnitudes difference between corresponding electronic and nuclear relaxation rates.

The results obtained showed that Yb^{3+} can serve as a very effective microscopic spin probe to study electronic, magnetic, and lattice properties of $YBa_2Cu_3O_x$.

2.2 Related publication

Probing the Yb^{3+} *spin relaxation in* $Y_{0.98}Yb_{0.02}Ba_2Cu_3O_x$ *by electron paramagnetic resonance*
A. Maisuradze, A. Shengelaya, B.I. Kochelaev, E. Pomjakushina, K. Conder, H. Keller, and K.A. Müller
Phys. Rev. B **79**, 054519 (2009).

PHYSICAL REVIEW B **79**, 054519 (2009)

Probing the Yb^{3+} spin relaxation in $Y_{0.98}Yb_{0.02}Ba_2Cu_3O_x$ by electron paramagnetic resonance

A. Maisuradze,[1] A. Shengelaya,[2] B. I. Kochelaev,[3] E. Pomjakushina,[4,5] K. Conder,[4] H. Keller,[1] and K. A. Müller[1]
[1]*Physik-Institut der Universität Zürich, Winterthurerstrasse 190, CH-8057 Zürich, Switzerland*
[2]*Institute of Physics, Tbilisi State University, Chavchavadze av. 3, GE-0128 Tbilisi, Georgia*
[3]*Department of Physics, Kazan State University, Kremlyovskaya st. 18, 420008, Russia*
[4]*Laboratory for Developments and Methods, Paul Scherrer Institut, CH-5232 Villigen PSI, Switzerland*
[5]*Laboratory for Neutron Scattering, Paul Scherrer Institut and ETH Zürich, CH-5232 Villigen PSI, Switzerland*

(Received 2 April 2008; revised manuscript received 14 November 2008; published 18 February 2009)

The relaxation of Yb^{3+} in $YBa_2Cu_3O_x$ $(6<x<7)$ was studied using electron paramagnetic resonance. It was found that both electronic and phononic processes contribute to the Yb^{3+} relaxation. The phononic part of the relaxation has an exponential temperature dependence, which can be explained by a Raman process via the coupling to high-energy (~500 K) optical phonons or an Orbach-type process via the excited vibronic levels of the Cu^{2+} ions (localized Slonczewski-modes). In a sample with a maximum oxygen doping $x=6.98$, the electronic part of the relaxation follows a Korringa law in the normal state and strongly decreases below T_c. Comparison of the samples with and without Zn doping proved that the superconducting gap opening is responsible for the sharp decrease of Yb^{3+} relaxation in $YBa_2Cu_3O_{6.98}$. It was shown that the electronic part of the Yb^{3+} relaxation in the superconducting state follows the same temperature dependence as ^{63}Cu and ^{17}O nuclear relaxations despite the huge difference between the corresponding electronic and nuclear relaxation rates.

DOI: 10.1103/PhysRevB.79.054519 PACS number(s): 74.72.−h, 76.75.+i, 74.25.Dw, 74.25.Ha

I. INTRODUCTION

It is well known that in the high-T_c superconductor $YBa_2Cu_3O_x$ the substitution of yttrium by isovalent rare-earth (RE) ions, having local magnetic 4*f* moments, does not change the critical temperature T_c considerably.[1] This makes it possible to use these local moments as useful paramagnetic probes of the electronic states within the CuO_2 planes without seriously perturbing them. Relaxation of the RE magnetic moments provides important information about fluctuating electric and magnetic fields in cuprate superconductors. In the normal state, RE ions with nonzero orbital moment can interact with phonons, spin fluctuations, and charge carriers. These interactions limit the lifetime of the crystal-field (CF) excitations and lead to broadening of the observed CF transitions. Inelastic neutron scattering (INS) is widely used to study the relaxation of the RE magnetic moments in cuprates superconductors by measuring the linewidths of the observed CF transitions.[2] However, the mechanism of the relaxation of RE ions in cuprates is the issue of hot debates.[3,4] Most of the authors consider an interaction of 4*f* spins with charge-carrier spins (Korringa mechanism) as a dominant channel of relaxation.[5–8] Other authors, in opposite, conclude that the interactions of RE spins with charge carriers are negligible and that the interactions with lattice vibrations are only responsible for the relaxation behavior of the 4*f* spins in cuprates.[9–11] At the moment there is no consensus on this subject and therefore it is important to disentangle the electronic and phononic sources of relaxation.

Relaxation of the 4*f* magnetic moments can be studied also by measuring the linewidth of the electron paramagnetic resonance (EPR) signal of the RE ions.[12] There have been a few EPR studies of the RE ions with nonzero orbital moment (Er and Yb) doped in cuprates.[13–20] Again, the situation with EPR is similarly contradictory as in INS studies. Some groups observed both electronic (Korringa) and phononic (Orbach) contributions to EPR relaxation.[13,16,17] While others conclude that the Korringa contribution is negligible and the interaction with lattice vibrations only is sufficient to explain the temperature dependence of the EPR linewidth in cuprates.[18–20]

In this work we report a detailed EPR study of the Yb^{3+} relaxation in $YBa_2Cu_3O_x$ samples with oxygen content x covering the whole doping range $(6<x<7)$. By measuring the temperature dependence of the Yb^{3+} EPR linewidth in a broad temperature range, it was found that *both* phononic and electronic mechanisms contribute to the relaxation. The electronic contribution decreases with decreasing oxygen content x, while the phononic contribution is practically doping independent and has an exponential temperature dependence. In a sample with a maximum oxygen doping $x=6.98$, the electronic part of the relaxation follows a Korringa law in the normal state, and a sharp drop of the relaxation rate is observed below T_c. In the superconducting state the electronic part of the Yb^{3+} relaxation rate follows the same temperature dependence as ^{63}Cu and ^{17}O nuclear relaxations.

This paper is organized as follows: sample preparation and experimental details are described in Sec. II. The EPR spectra and the procedure of their analysis are discussed in Sec. III. Section IV presents the temperature and doping dependence of the Yb^{3+} relaxation rate in the normal and superconducting states. In Sec. V we summarize our results and the conclusions of this study.

II. EXPERIMENTAL DETAILS

The polycrystalline samples of $Y_{1-y}Yb_yBa_2Cu_3O_x$ were prepared by the standard solid-state reaction by using Y_2O_3, Yb_2O_3, $BaCO_3$, and CuO of a minimum purity of 99.99%.

Appropriate amounts of starting reagents were mixed and calcinated at temperatures 800–920 °C during at least 150 h in air, with several intermediate grindings. Finally, the as-prepared sample was oxidized in oxygen atmosphere (1 bar of O_2) at 500 °C. After the oxidation the sample had oxygen content close to 7 (6.98). The required oxygen content in the samples was adjusted by gettering in a closed ampoule with metallic copper (850 °C, 10 h; cooling 10 °C/h). The oxygen content in the reduced samples was checked by comparing theoretical and real mass changes of the oxidized getter and the reduced sample. For all the samples phase purity was checked with a conventional x-ray diffractometer (SIEMENS D500).

The dilute level of the Yb doping ($y=0.02$) was chosen in order to minimize broadening effects from Yb-Yb interactions and at the same time to obtain a sufficiently strong EPR signal. The EPR measurements were performed with an *X*-band BRUKER EMX spectrometer equipped with an Oxford Instruments helium flow cryostat. In order to avoid a signal distortion due to skin effects, the samples were ground and the powder was suspended in epoxy. The *c*-axes grain orientation was obtained by placing the samples in a 9 T magnetic field until the epoxy hardened. As a result of the orientation procedure the *c* axes of the grains were preferentially aligned along the magnetic field direction.[21]

EPR spectra were measured in five samples $Y_{0.98}Yb_{0.02}Ba_2Cu_3O_x$ with $x=6.1$, 6.4, 6.5, 6.6, and 6.98 and critical temperatures T_c of 0, 12(1), 51(1), 60(1), and 93(1) K, respectively. In addition, one Zn-doped sample $Y_{0.98}Yb_{0.02}Ba_2(Cu_{0.97}Zn_{0.03})_3O_{6.95}$ was measured with $T_c=57(1)$ K.

III. ANALYSIS OF THE YTTERBIUM EPR SPECTRA

In the $YBa_2Cu_3O_x$ structure, the rare-earth site is eightfold coordinated by oxygens lying in the CuO_2 bilayers. Group theoretical considerations show that the eightfold degeneracy of the ground-state multiplet $^2F_{7/2}$ of the Yb^{3+} ions ($4f^{13}$) is split by the crystal electric field of orthorhombic symmetry into four Kramers doublets.[22] Generally, this splitting is large enough so that only the lowest lying doublet is appreciably populated at low temperatures. In fact, inelastic neutron-scattering measurements showed that in $YbBa_2Cu_3O_7$ the first-excited doublet lies 1000 K above the ground doublet.[23] So, EPR signals would be observed only for this doublet, which can be described in an effective $S=1/2$ notation.

Figure 1(a) shows Yb^{3+} EPR spectra of $Y_{0.98}Yb_{0.02}Ba_2Cu_3O_{6.4}$ at $T=40$ K with the external magnetic field along and perpendicular to the crystal *c* axis. The spectra correspond to Yb^{3+} with an effective spin $S=1/2$ with g values $g_{\parallel}=3.13(3)$ and $g_{\perp}=3.49(3)$. The average value $g_{\mathrm{av}}=3.37$ is close to $g=3.43$ expected for the isolated Γ_7 ground doublet.[22] Figure 1(b) shows Yb^{3+} EPR spectra for the optimally doped sample $x=6.98$ at $T=25$ K. Note that the EPR line splits into two components for the $H\perp c$ orientation. This reflects the transition from tetragonal to orthorhombic crystal symmetry in $YBa_2Cu_3O_x$ with increasing oxygen content. Enhanced noise seen in these spectra is related to the superconducting state. It is known that in the superconducting state the strong noise is generated due to vortex motion in the modulating magnetic field used in standard EPR spectrometers.

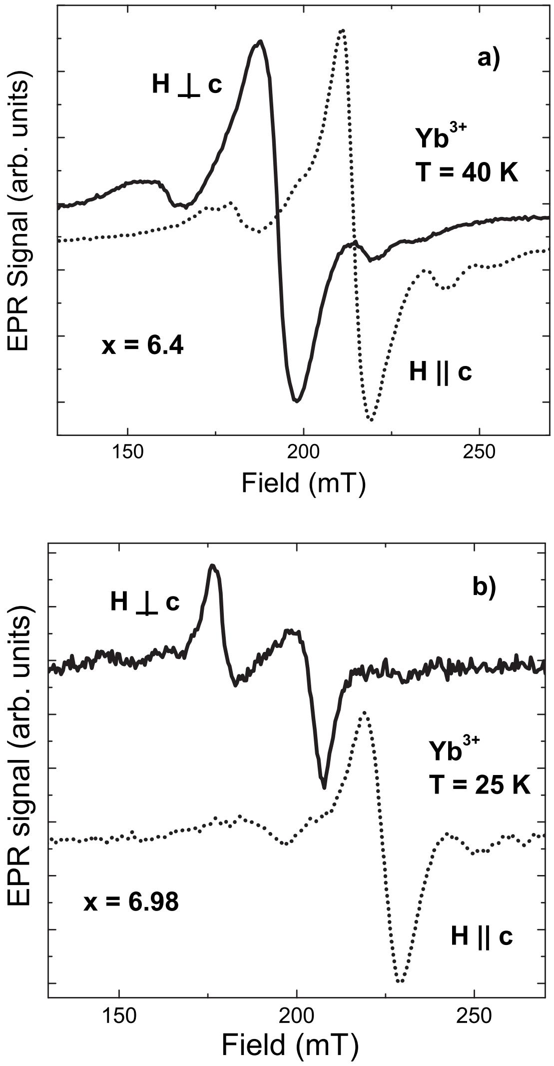

FIG. 1. EPR spectra of Yb^{3+} in grain oriented $Y_{0.98}Yb_{0.02}Ba_2Cu_3O_x$ with different oxygen contents: (a) $x=6.4$; (b) $x=6.98$. Two orientations correspond to the external magnetic field along and perpendicular to the crystal *c* axis.

Figure 2 shows typical EPR spectra for the $x=6.4$ sample at different temperatures with the magnetic field applied perpendicular to the *c* axis. The EPR lines in the $g\approx 2$ region are due to Cu^{2+} defect centers, which are always present in $YBa_2Cu_3O_{6+x}$.[24] The concentration of the Cu^{2+} defect centers in our samples correspond to 1–2% of the total copper content, as determined from the Cu^{2+} EPR signal intensity. The Yb^{3+} EPR spectrum at 40 K is rather complex, with a dominant central line and shoulders on each side. The shoulders are due to partially resolved hyperfine components. Natural ytterbium has 69% even-mass isotopes with nuclear spin $I=0$ 14% ^{171}Yb with $I=1/2$, and 16% ^{173}Yb with $I=5/2$. Both odd isotopes give rise to nuclear hyperfine interactions. In Fig. 2 one can see that with increasing temperature the

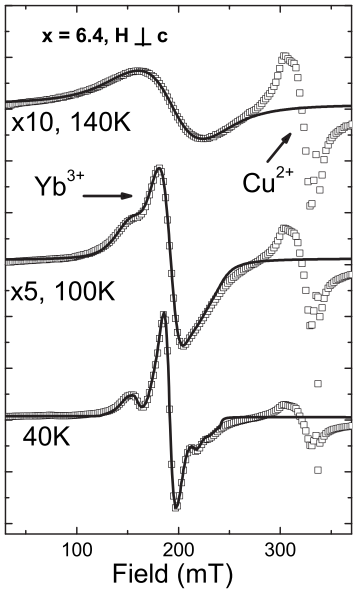

FIG. 2. EPR spectra in grain oriented $Y_{0.98}Yb_{0.02}Ba_2Cu_3O_{6.4}$ at different temperatures for a magnetic field direction perpendicular to the crystal *c* axis. The solid lines are fits to the data, including relaxation as described in the text.

Yb^{3+} EPR line broadens and the multiple-line structure of the Yb spectra gradually merges into one line which continues to broaden with temperature. This broadening is due to the Yb relaxation and is the subject of the present study.

The observed line shape can be interpreted in the following way: a temperature-independent residual function due to inhomogeneous broadening which is further broadened by a temperature dependent relaxation. The method by which the relaxation-induced peak-to-peak derivative linewidth ΔB^r_{pp} is extracted from the total peak-to-peak linewidth of the EPR signal ΔB^t_{pp} depends upon the line shapes associated with inhomogeneous and homogeneous broadening mechanisms. The homogeneous broadening leads to Lorentzian line shape while the inhomogeneous low-temperature line shape is usually approximated as either Lorentzian or Gaussian. For a Lorentzian-Lorentzian convolution there is a simple relation: $\Delta B^r_{pp}(T)=\Delta B^t_{pp}(T)-\Delta B^0_{pp}$, where ΔB^0_{pp} is a residual, temperature-independent linewidth. The result of a Lorentzian-Gaussian convolution is called a Voigt function, which cannot be expressed in closed form.

In our case the low-temperature line shape is neither Lorentzian nor Gaussian. The anisotropic nature of the Yb^{3+} signal, the partially resolved hyperfine structure, and the nonideal grain alignment, make it very difficult to accurately model the complex shape of the Yb EPR spectra and its evolution with temperature. Therefore, in order to extract the linewidth related to relaxation, we used an approach similar to one used in inelastic neutron-scattering studies of rare-earth relaxation in cuprates.[7]

The inhomogeneous broadening of an EPR line is due to the spread of the resonance frequencies of an assembly of electronic spins. The width of the single spin packet contributes to homogeneous broadening. This situation can be described by a convolution integral,[25]

$$I(B)=\int p(B')f(B-B')dB' = p(B)*f(B), \qquad (1)$$

where $*$ is the convolution symbol, $p(B)$ is the inhomogeneous line shape, and $f(B)$ is the resonance line profile of the spin packet given by a Lorentzian line function. EPR spectra are usually detected in the form of a first derivative, $I'(B) = \partial I(B)/\partial B$. In this case $I'(B)=p(B)*f'(B)$, where $f'(B)$ is the first derivative of a Lorentzian with amplitude A, center at B_0 and the peak-to-peak width ΔB^r_{pp} related with relaxation,

$$f'(B)=A\frac{2(B-B_0)}{\Delta B^r_{pp}}\left[3+\left(\frac{2(B-B_0)}{\Delta B^r_{pp}}\right)^2\right]^{-2}. \qquad (2)$$

In order to describe the inhomogeneous line shape $p(B)$, we divided Yb EPR spectra in 120 points with a step of $\delta B = 1$ mT in the interval of 120–240 mT. In this case an integral is replaced by a sum of 120 Lorentzians,

$$I'(B)=\sum_{i=1}^{120} p_i(B_i)\cdot f'(B-B_i)\delta B. \qquad (3)$$

The residual function $p_i(B_i)$, characterizing the inhomogeneous line shape was obtained at low temperatures where relaxational broadening is negligible. We found that in all samples measured in the present work, except one Zn-doped sample, the relaxational broadening was absent below 40 K. Therefore, this temperature was used to determine the inhomogeneous line shape for samples without Zn doping. In Zn-doped sample the linewidth continues to decrease down to 15 K and therefore the inhomogeneous line shape was determined at this temperature. As an example, the line drawn through the 40 K data in Fig. 2 represents the residual function for $x=6.4$ sample. Having established the residual function, we kept the coefficients p_i fixed at all temperatures and fitted the data at high temperatures by convolving the residual function with the broadening function of Lorentzian shape. The center B_0, width ΔB^r_{pp}, and amplitude A of the broadening function were the only variable parameters. The resulting fits are shown in Fig. 2.

The peak-to-peak linewidth ΔB^r_{pp} is related to the transverse relaxation rate T_2^{-1} as follows:[26]

$$T_2^{-1}=\frac{\sqrt{3}g\mu_B\Delta B^r_{pp}}{2\hbar}=7.62\times 10^6 g\Delta B^r_{pp}. \qquad (4)$$

For paramagnetic relaxation of RE ions in cuprates T_2^{-1} is equal to the spin-lattice relaxation rate T_1^{-1}, as was shown for Gd^{3+} in $Y_{0.99}Gd_{0.01}Ba_2Cu_4O_8$.[27]

IV. TEMPERATURE AND DOPING DEPENDENCE OF THE YTTERBIUM RELAXATION

A. Yb^{3+} relaxation in the normal state

Figure 3 shows the temperature dependence of the peak-to-peak width ΔB^r_{pp} related with relaxation and corresponding relaxation rate $1/T_1$ of Yb^{3+} in $Y_{0.98}Yb_{0.02}Ba_2Cu_3O_x$ for different oxygen contents. In order to distinguish between electronic and phononic contributions to relaxation, let us

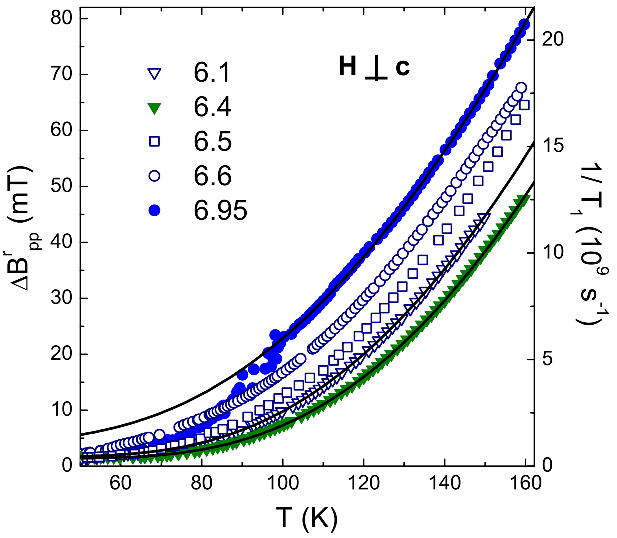

FIG. 3. (Color online) Temperature dependence of the width of the broadening function ΔB^r_{pp} and the corresponding spin-lattice relaxation rate T_1^{-1} of Yb^{3+} in $Y_{0.98}Yb_{0.02}Ba_2Cu_3O_x$ with different oxygen content x for $H \perp c$. The solid lines represent the best fit to Eq. (6).

first consider the sample with the lowest oxygen content ($x=6.1$). One can see in Fig. 3 that in this sample, which is antiferromagnetic and insulating with practically no charge carriers, the relaxation rate is comparable to those of samples with much higher oxygen contents. Consequently, this suggests that the phonon contribution to the rare-earth relaxation rate is significant at all oxygen doping levels since in the $x=6.1$ sample the electronic contribution is expected to be negligible.

We observed that the temperature dependence of the relaxation rate follows closely the exponential function $C\exp(-\Delta/T)$ with $\Delta=520(30)$ and $570(30)$ K, for $x=6.1$ and 6.4 respectively. This is demonstrated in Fig. 4, where the relaxation rates as a function of inverse temperature are plotted on a semilogarithmic scale. Such an exponential dependence is expected for the Orbach relaxation process via an excited intermediate energy level.[28] In this case Δ corresponds to the separation between the ground-state doublet and the excited level. According to inelastic neutron-scattering experiments the first-excited energy level of Yb in $YBa_2Cu_3O_7$ is about 1000 K above the ground-state doublet.[23] Since there is no excited crystal-field energy level with $\Delta \sim 500$ K, the traditional Orbach relaxation mechanism can be excluded.

An exponential temperature dependence of the relaxation rate is also expected for the Raman two-phonon process involving optical phonons or local vibrations.[29,30] In this case the relaxation rate is

$$1/T_1 = C\exp(\Omega/T)/[\exp(\Omega/T)-1]^2, \qquad (5)$$

where Ω is the optical phonon frequency.[29,30] The solid lines in Fig. 4 represent a best fit to the data using Eq. (5). It is obvious that the Raman process involving optical phonons can explain the phonon contribution to the Yb^{3+} spin-lattice relaxation. Optical phonons within the energy range 500(50) K exist in $YBa_2Cu_3O_x$. These are: (i) the in-plane bond-bending (500–560 K) and (ii) the out-of-plane B_{1g} (470 K) phonons.[31] Theoretical calculations are necessary in order to determine which of the two optical phonon modes (in-plane bond bending or out-of-plane B_{1g}) mostly contributes to Yb^{3+} spin-lattice relaxation.

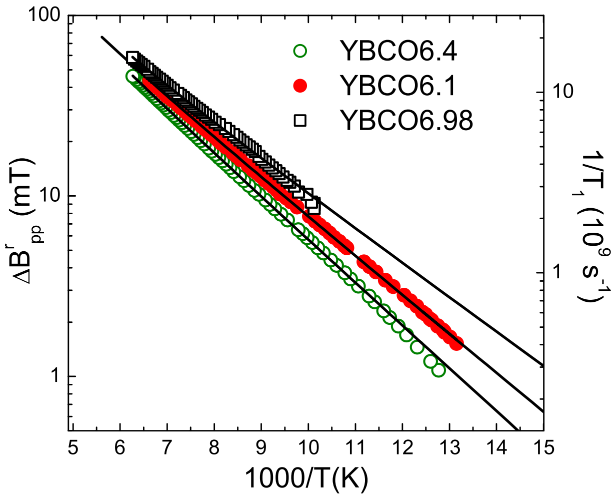

FIG. 4. (Color online) The width of the broadening function ΔB^r_{pp} and the corresponding spin-lattice relaxation rate T_1^{-1} of Yb^{3+} in $Y_{0.98}Yb_{0.02}Ba_2Cu_3O_x$ with $x=6.1$, 6.4, and 6.98 versus inverse temperature plotted on a semilogarithmic scale. For $x=6.98$ sample only phononic contribution to relaxation is plotted. The solid lines represent the best fit to Eq. (5).

It is interesting to note that an exponential temperature dependence of the spin-relaxation rate was observed in a previous EPR study of crystals containing Jahn-Teller (JT) transition metal ions.[32,33] In this case relaxation takes place due to an Orbach-type process via the excited vibronic levels of the JT ion (localized Slonczewski modes).[34] In our case such a scenario is also possible if Yb^{3+} spin relaxation occurs due to coupling to the vibrations of surrounding CuO_6 complexes since Cu^{2+} is a strong JT ion. There are no reports on JT splitting of Cu^{2+} in $SrTiO_3$ or similar perovskites, but in MgO and CaO it is approximately 1500 K,[33] which is much larger than 500 K found in the present work. However, it was observed that for Ni^{3+} the JT splitting in $SrTiO_3$ is two to four times reduced compared to MgO, CaO, or Al_2O_3.[33] A similar reduction in the JT splitting can be expected also for Cu^{2+} in perovskites. In addition, in cuprates the Cu^{2+} ions are situated next to each other. In such a cooperative situation the energy of the Slonczewski mode will be lower compared to the isolated Cu^{2+} ions. It would be interesting to search for localized vibronic modes in cuprates using inelastic neutron scattering.

For an oxygen content $x>6.4$, Eq. (5) cannot describe the relaxation data well, and it was necessary to take into account the Korringa relaxation mechanism where localized Yb^{3+} moments couple to mobile charge carriers in the CuO_2 planes through an exchange interaction. In normal metals the Korringa relaxation has a linear temperature dependence bT.[12] The parameter b is proportional to the product

TABLE I. The fitting parameters of the Yb^{3+} relaxation in $Y_{0.98}Yb_{0.02}Ba_2Cu_3O_x$ using Eq. (6).

x	T_c (K)	C (G)	Ω (K)	b (G/K)
6.1		10800(500)	500(30)	0
6.4	12(1)	13190(500)	540(30)	0
6.98	93(1)	9090(400)	460(30)	1.27(10)
6.95(Zn)	57(1)	10160(400)	490(30)	1.27(10)

$[J_{sf}N(E_F)]^2$, where J_{sf} is the exchange integral between Yb^{3+} moments and holes, and $N(E_F)$ is the density of states at the Fermi energy. In underdoped cuprates the density of states at the Fermi level is temperature dependent due to the pseudogap opening. This leads to the nonlinear temperature dependence of the relaxation rate as demonstrated by ^{89}Y NMR (Ref. 35) and Gd EPR (Ref. 36) experiments in $YBa_2Cu_3O_x$. No exact formula exists to describe this nonlinear temperature dependence. Therefore we did not fit the data for underdoped samples ($6.4<x<6.98$). However, the use of the Korringa law is justified in our optimally doped sample $x=6.98$, where the pseudogap is absent.[35] The solid lines in Fig. 3 correspond to fits of the data using a sum of phononic and electronic contributions,

$$1/T_1 = C\exp(\Omega/T)/[\exp(\Omega/T)-1]^2 + bT. \qquad (6)$$

The obtained parameters C, Ω, and b are summarized in Table I. It is interesting to compare the value of the Korringa constant $b=1.27(10)$ G/K for $x=6.98$ with the values obtained from EPR measurements of Gd-doped $YBa_2Cu_3O_x$. In contrast to Yb^{3+}, the Gd^{3+} ion has zero orbital moment ($L=0$) and interacts very weakly with lattice vibrations. Therefore, the Korringa relaxation due to interaction with charge carriers is the dominant process and the Korringa constant can be obtained directly from the temperature dependence of the EPR linewidth. Indeed, EPR measurements on a Gd-doped $EuBa_2Cu_3O_{6.85}$ single crystal[37] showed a linear broadening of the EPR line in the temperature range 90–300 K with the Korringa constant $b=0.5$ G/K. This value of b is comparable, but smaller than our value of b. This is expected due to the smaller oxygen content ($x=6.85$) and consequently smaller density of states at the Fermi level $N(E_F)$ compared to our sample ($x=6.98$).

The comparable values of Korringa constants b for Gd^{3+} and Yb^{3+} in YBCO show that they have similar exchange coupling J_{sf} with charge carriers. The observed Korringa constants of RE ions in YBCO are at least 1 order of magnitude smaller than the corresponding quantities found for RE ions in conventional metals.[12] The small value of b for RE ions in $YBa_2Cu_3O_x$ is due to the weak coupling J_{sf} between the RE moments and the holes in the CuO_2 planes. This explains naturally the small effect of RE magnetic moments on T_c in $YBa_2Cu_3O_x$.[38]

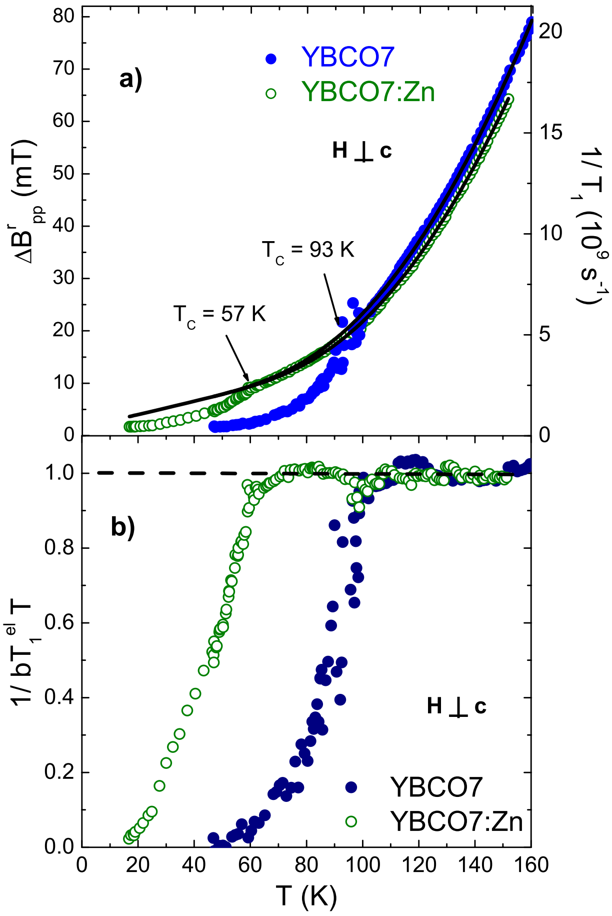

FIG. 5. (Color online) (a) Temperature dependence of the width of the broadening function ΔB^r_{pp} and the corresponding spin-lattice relaxation rate T_1^{-1} of Yb^{3+} in $Y_{0.98}Yb_{0.02}Ba_2Cu_3O_{6.98}$ (YBCO7) and $Y_{0.98}Yb_{0.02}Ba_2(Cu_{0.97}Zn_{0.03})_3O_{6.95}$ (YBCO7:Zn) for $H\perp c$. The solid lines represent the best fit to Eq. (6) of the YBCO7 and YBCO7:Zn data above their superconducting transition temperatures $T_c=93$ and 57 K, respectively. (b) Temperature dependence of the electronic part of the Yb^{3+} relaxation $1/bT_1^{el}T$ in YBCO7 and YBCO7:Zn. The dashed line represents the normal-state relaxation expected by the Korringa law.

B. Yb^{3+} relaxation in the superconducting state

Generally, it is difficult to measure EPR in the superconducting state because of the strong microwave absorption and the noise due to vortex motion in the modulating magnetic field used in standard EPR spectrometers. Nevertheless, in grain-aligned samples with small grain size it was possible to observe an Yb^{3+} EPR signal below T_c [see Fig. 1(b)]. This allowed us to study the temperature dependence of the Yb^{3+} relaxation in the superconducting state. We observed a strong reduction in the Yb^{3+} relaxation rate below T_c. This is clearly seen in Fig. 3 for $x=6.98$, where the relaxation rate falls below the theoretical line given by Eq. (6). It is natural to attribute the drop of the relaxation to the opening of the superconducting gap.

In order to check this possibility, we measured the relaxation of Yb^{3+} in $Y_{0.98}Yb_{0.02}Ba_2(Cu_{0.97}Zn_{0.03})_3O_{6.95}$ where Zn doping reduces T_c to 57 K. Figure 5(a) shows the temperature dependence of the peak-to-peak width ΔB^r_{pp} related with relaxation and corresponding relaxation rate $1/T_1$ in samples with and without Zn doping. It is expected that 3% Zn doping should not change strongly the phonon spectra and the electronic density of states. In fact, above ~90 K the relaxation rates are very close for both samples. However, below ~90 K the behavior of relaxation is different. While the relaxation rate of the sample without Zn doping sharply decreases below this temperature due to the onset of superconductivity, in the Zn-doped sample relaxation continues to decrease gradually until $T_c^{\mathrm{Zn}}=57$ K, where a similar sharp turn is observed. This result unambiguously shows that the superconducting gap opening is responsible for the drop of Yb^{3+} relaxation in $\mathrm{YBa_2Cu_3O_{6.98}}$. Moreover, it proves the presence of the electronic channel of relaxation described by the Korringa term bT in Eq. (6). Zn doping helps to reveal the Korringa term, which is masked at high temperatures by phonon relaxation due to the much stronger temperature dependence, and below T_c by opening of the superconducting gap. Figure 5(b) shows the electronic part of the Yb^{3+} relaxation after subtracting the phonon contribution in pure and Zn-doped samples. The linear temperature dependence in the normal state and a sharp decrease below T_c are clearly seen.

In superconducting samples at low temperatures extra broadening could be present due to the distribution of the diamagnetic shifts related to the irregular shape of the powder grains. However, we observed no additional broadening even in optimally doped superconducting sample down to 40 K. In fact, the superconducting and nonsuperconducting samples had the same inhomogeneous linewidth at this temperature. This is in agreement with the estimations of the diamagnetic shift ~3 mT at 10 K in $H \perp c$ orientation in $\mathrm{YBa_2Cu_3O_7}$, which further decreases with increasing temperature.[36] Therefore, extra broadening from the distribution of this diamagnetic shift in our optimally doped sample at 40 K is estimated to be about 1 mT, which is much smaller than the observed inhomogeneous linewidth $\Delta B_{\mathrm{pp}}=11$ mT.

It is expected that the electronic part of the relaxation of the 4*f* magnetic moments on the yttrium site in YBCO measured by EPR has the same temperature dependence as $^{89}\mathrm{Y}$ nuclear relaxation, since in both cases the relaxation is proportional to the imaginary part of the dynamic spin susceptibility.[39] This was confirmed by EPR measurements of Gd^{3+} spin relaxation in $\mathrm{YBa_2Cu_3O_x}$ in normal state.[36,40] Also, in the present work, the electronic part of the Yb^{3+} spin relaxation in optimally doped YBCO above T_c shows a linear temperature dependence (Korringa behavior) such as $^{89}\mathrm{Y}$ nuclear relaxation.[35] Note, however, that there is a huge difference between the magnitudes (more than a factor 10^9) of the electron and nuclear relaxation rates due to the large difference between the corresponding coupling constants.

It would be interesting to compare the temperature dependences of the electron and nuclear spin-relaxation rates on the yttrium site in the superconducting state, where relaxation drops due to the opening of the superconducting gap. Unfortunately, no detailed $^{89}\mathrm{Y}$ nuclear relaxation data exists for $\mathrm{YBa_2Cu_3O_x}$ in the superconducting state. A very small coupling between the yttrium nuclei and the charge carriers leads to very long relaxation times and makes $^{89}\mathrm{Y}$ NMR measurements in the superconducting state extremely difficult. Therefore, we plot in Fig. 6 the electronic part of $1/T_1T$ versus reduced temperature T/T_c for Yb^{3+} in $x=6.98$ sample together with the corresponding quantities from NMR measurements for $^{17}\mathrm{O}$ and $^{63}\mathrm{Cu}$ nuclei in $\mathrm{YBa_2Cu_3O_7}$.[41,42] The relaxation rates are plotted for $H \perp c$ orientation, and $^{63}\mathrm{Cu}$ NMR relaxation data are plotted for weak magnetic field $H=0.45$ T where the fluxoid core contribution to relaxation is small.[42] The electron and nuclear relaxation rates were normalized to their values above T_c at $T=100$ K. As is evident from Fig. 6, $(1/T_1T)$ shows a very similar temperature dependence for the Yb^{3+} electronic spins and the $^{63}\mathrm{Cu}$ and $^{17}\mathrm{O}$ nuclei.

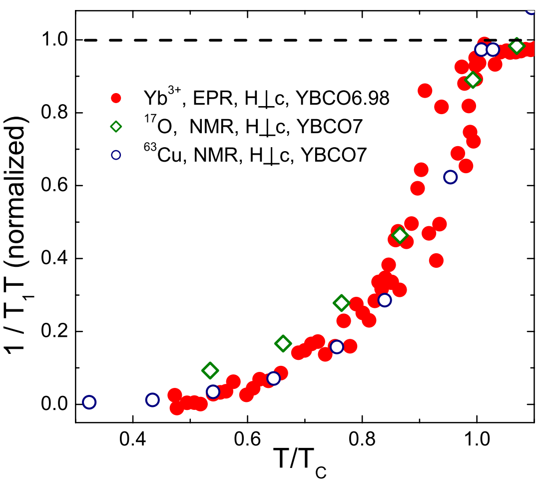

FIG. 6. (Color online) $(1/T_1T)$ of Yb^{3+} in the superconducting state normalized by its value at 100 K in $\mathrm{Y_{0.98}Yb_{0.02}Ba_2Cu_3O_{6.98}}$ versus reduced temperature T/T_c, compared with those of $^{17}\mathrm{O}$ NMR (Ref. 41) and $^{63}\mathrm{Cu}$ NMR (Ref. 42) in $\mathrm{YBa_2Cu_3O_{7-\delta}}$.

Previously, the relaxation rate $1/T_1$ of Yb^{3+} in the superconducting state of optimally doped $\mathrm{YBa_2Cu_3O_7}$ was extracted from $^{170}\mathrm{Yb}$ Mössbauer spectra.[43] The temperature dependence of $1/T_1$ was followed only up to 90 K limited by the decrease in the intensity of the Mössbauer effect. Therefore, a sharp decrease in the relaxation rate at transition from normal to superconducting state was not observed. Nevertheless, it is interesting to compare the absolute values of the relaxation rates of Yb^{3+} obtained by Mössbauer and EPR techniques. Such a comparison is shown in Table II. The excellent quantitative agreement of the relaxation rates obtained by two different experimental techniques is remarkable and provides strong support of the methods of extracting relaxation rates from Mössbauer spectroscopy[43] and from EPR spectra presented in this work.

Relaxation measurements at low temperatures ($T \ll T_c$) can provide information about the superconducting gap

TABLE II. The relaxation rates of Yb^{3+} in $\mathrm{YBa_2Cu_3O_7}$ at different temperatures obtained by Mössbauer technique ($1/T_1^{\mathrm{MS}}$, Ref. 43) and by EPR in the present work ($1/T_1^{\mathrm{EPR}}$).

T (K)	$1/T_1^{\mathrm{MS}}$ (10^9 s^{-1})	$1/T_1^{\mathrm{EPR}}$ (10^9 s^{-1})
60	0.5(1)	0.6(1)
70	1.3(1)	1.2(1)
80	2.5(1)	1.8(1)
90	4.0(1)	4.4(1)

symmetry.[44] However, in the present EPR experiments we could not detect relaxation broadening at $T \ll T_c$ since it becomes much smaller than the inhomogeneous residual linewidth. This prevents a reliable measurement of the relaxation rate below $T=0.5T_c$. It is expected that at low temperatures in the superconducting state the Yb^{3+} relaxation rate will decrease below 10^7 s^{-1}. In this case T_1 can be measured directly using the pulse EPR techniques. It would be interesting to perform such experiments at low temperatures.

V. SUMMARY AND CONCLUSIONS

To summarize, we performed a detailed study of the temperature dependence of the Yb^{3+} EPR linewidth, i.e., the relaxation in $YBa_2Cu_3O_x$ from the undoped insulating to the optimally doped superconducting region ($6 \leq x \leq 7$). It was found that both electronic and phononic processes contribute to Yb^{3+} relaxation. We were able to separate these processes and studied their relative contributions to relaxation as a function of oxygen doping. As expected, the electronic contribution decreases with decreasing oxygen doping, while the phonon contribution is practically doping independent. It was found that the phononic part of relaxation has an exponential temperature dependence, which cannot be explained by a traditional mechanism involving acoustic phonons. Instead, a Raman process via the coupling to high-energy (~500 K) optical phonons or an Orbach-type process via the excited vibronic levels of the Cu^{2+} ions (localized Slonczewski modes) is responsible for the phononic part of the Yb^{3+} relaxation in $YBa_2Cu_3O_{6+x}$.

In a sample with maximum oxygen doping $x=6.98$, the electronic part of relaxation follows the Korringa law in the normal state, and a sharp drop of the relaxation rate was observed below T_c. Comparison of the EPR linewidths in samples with and without Zn doping allowed us to prove that the superconducting gap opening is responsible for the sharp decrease in Yb^{3+} relaxation in $YBa_2Cu_3O_{6.98}$. It was shown that the electronic part of the Yb^{3+} relaxation rate in the superconducting state follows a very similar temperature dependence as the ^{63}Cu and the ^{17}O nuclear relaxation rates, despite the huge difference between the corresponding electronic and nuclear relaxation rates.

There is an excellent quantitative agreement between relaxation rates of Yb^{3+} in $YBa_2Cu_3O_7$ obtained previously by Mössbauer spectroscopy and in the present work by EPR. This provides strong support of the methods of extracting relaxation rates from Mössbauer spectroscopy and from EPR spectra. One should note however, that the EPR signal from Yb^{3+} in $YBa_2Cu_3O_x$ can be followed up to at least 160 K, while Mössbauer measurements in the same compound using ^{170}Yb are limited by 90 K due to the decrease in the intensity of the Mössbauer effect with temperature.

The present results demonstrate that Yb^{3+} can serve as a very effective microscopic spin probe to study electronic, magnetic and lattice properties of $YBa_2Cu_3O_x$.

ACKNOWLEDGMENTS

This work was supported by the Swiss National Science Foundation, the SCOPES grant No. IB7420-110784, and the NCCR program MaNEP.

---

[1] P. H. Hor, R. L. Meng, Y. Q. Wang, L. Gao, Z. J. Huang, J. Bechtold, K. Forster, and C. W. Chu, Phys. Rev. Lett. **58**, 1891 (1987).

[2] J. Mesot and A. Furrer, J. Supercond. **10**, 623 (1997).

[3] A. T. Boothroyd, Phys. Rev. B **64**, 066501 (2001).

[4] S. W. Lovesey and U. Staub, Phys. Rev. B **64**, 066502 (2001).

[5] U. Walter, S. Fahy, A. Zettl, S. G. Louie, M. L. Cohen, P. Tejedor, and A. M. Stacy, Phys. Rev. B **36**, 8899 (1987).

[6] G. Amoretti, R. Caciuffo, P. Santini, O. Francescangeli, E. A. Goremychkin, R. Osborn, G. Calestani, M. Sparpaglione, and L. Bonoldi, Physica C **221**, 227 (1994).

[7] A. Mukherjee, A. T. Boothroyd, D. M. K. Paul, M. P. Sridhar Kumar, and M. A. Adams, Phys. Rev. B **49**, 13089 (1994); A. T. Boothroyd, A. Mukherjee, and A. P. Murani, Phys. Rev. Lett. **77**, 1600 (1996).

[8] J. Mesot, G. Böttger, H. Mutka, and A. Furrer, Europhys. Lett. **44**, 498 (1998).

[9] U. Staub, M. Gutmann, F. Fauth, and W. Kagunya, J. Phys.: Condens. Matter **11**, L59 (1999).

[10] S. W. Lovesey and U. Staub, Phys. Rev. B **61**, 9130 (2000).

[11] M. Roepke, E. Holland-Moritz, B. Büchner, H. Berg, R. E. Lechner, S. Longeville, J. Fitter, R. Kahn, G. Coddens, and M. Ferrand, Phys. Rev. B **60**, 9793 (1999).

[12] S. E. Barnes, Adv. Phys. **30**, 801 (1981).

[13] L. Kan, S. Elschner, and B. Elschner, Solid State Commun. **79**, 61 (1991).

[14] M. V. Eremin, I. N. Kurkin, M. P. Rodionova, I. H. Salikhov, and L. R. Tagirov, Supercond., Phys. Chem. Technol. **4**, 716 (1991).

[15] I. N. Kurkin, I. Kh. Salikhov, L. L. Sedov, M. A. Teplov, and R. Sh. Zhdanov, JETP **76**, 657 (1993).

[16] H. Shimizu, K. Fujiwara, and K. Hatada, Physica C **288**, 190 (1997).

[17] H. Shimizu, K. Fujiwara, and K. Hatada, Physica C **299**, 169 (1998).

[18] V. A. Ivanshin, M. R. Gafurov, I. N. Kurkin, S. P. Kurzin, A. Shengelaya, H. Keller, and M. Gutmann, Physica C **307**, 61 (1998).

[19] L. K. Aminov, V. A. Ivanshin, I. N. Kurkin, M. R. Gafurov, I. Kh. Salikhov, H. Keller, and M. Gutmann, Physica C **349**, 30 (2001).

[20] M. R. Gafurov, L. K. Aminov, I. N. Kurkin, and V. V. Izotov, Supercond. Sci. Technol. **18**, 352 (2005).

[21] D. E. Farrell, B. S. Chandrasekhar, M. R. DeGuire, M. M. Fang, V. G. Kogan, J. R. Clem, and D. K. Finnemore, Phys. Rev. B **36**, 4025 (1987).

[22] A. Abragam and B. Bleaney, *Electron Paramagnetic Resonance of Transition Ions* (Clarendon, Oxford, 1970).

[23] M. Guillaume, P. Allenspach, J. Mesot, U. Staub, A. Furrer, R. Osborn, A. D. Taylor, F. Stucki, and P. Unternährer, Solid State Commun. **81**, 999 (1992).

[24] J. Sichelschmidt, B. Elschner, A. Loidl, and B. I. Kochelaev, Phys. Rev. B **51**, 9199 (1995).
[25] A. I. Smirnov and R. L. Belford, J. Magn. Reson., Ser. A **113**, 65 (1995).
[26] Gh. Cristea, T. L. Bohan, and H. J. Stapleton, Phys. Rev. B **4**, 2081 (1971).
[27] V. A. Atsarkin, V. V. Demidov, G. A. Vasneva, T. Feher, A. Jánossy, and B. Dabrowski, Phys. Rev. B **61**, R14944 (2000).
[28] S. A. Dodds, J. Sanny, and R. Orbach, Phys. Rev. B **18**, 1016 (1978).
[29] B. I. Kochelaev, Sov. Phys. JETP **10**, 171 (1960).
[30] Chao-Yuan Huang, Phys. Rev. **154**, 215 (1967).
[31] L. Pintschovius, W. Reichardt, M. Klaser, T. Wolf, and H. v. Lohneysen, Phys. Rev. Lett. **89**, 037001 (2002); M. Opel, R. Hackl, T. P. Devereaux, A. Virosztek, A. Zawadowski, A. Erb, E. Walker, H. Berger, and L. Forro, Phys. Rev. B **60**, 9836 (1999).
[32] U. Höchli and K. A. Müller, Phys. Rev. Lett. **12**, 730 (1964).
[33] U. Höchli, K. A. Müller, and P. Wysling, Phys. Lett. **15**, 5 (1965).
[34] K. A. Müller, in *Magnetic Resonance and Relaxation*, edited by R. Blinc (North-Holland Publishing Company, Amsterdam, 1967), pp. 192–208.
[35] H. Alloul, T. Ohno, and P. Mendels, Phys. Rev. Lett. **63**, 1700 (1989).
[36] A. Jánossy, L. C. Brunel, and J. R. Cooper, Phys. Rev. B **54**, 10186 (1996).
[37] D. Shaltiel, C. Noble, J. Pilbrow, D. Hutton, and E. Walker, Phys. Rev. B **53**, 12430 (1996).
[38] N. E. Alekseevskii, A. V. Mitin, V. I. Nizhankovskii, I. A. Garifullin, N. N. Garifyanov, G. G. Khaliullin, E. P. Khlybov, B. I. Kochelaev, and L. R. Tagirov, J. Low Temp. Phys. **77**, 87 (1989).
[39] B. I. Kochelaev and G. B. Teitelbaum, *Superconductivity in Complex Systems* (Springer, Berlin, 2005), pp. 205–266.
[40] V. A. Atsarkin, V. V. Demidov, and G. A. Vasneva, Phys. Rev. B **52**, 1290 (1995).
[41] J. A. Martindale, P. C. Hammel, W. L. Hults, and J. L. Smith, Phys. Rev. B **57**, 11769 (1998).
[42] J. A. Martindale, S. E. Barrett, C. A. Klug, K. E. O'Hara, S. M. DeSoto, C. P. Slichter, T. A. Friedmann, and D. M. Ginsberg, Phys. Rev. Lett. **68**, 702 (1992).
[43] J. A. Hodges, P. Bonville, P. Imbert, and G. Jéhanno, Physica C **184**, 259 (1991).
[44] For a review, see K. Asayama, Y. Kitaoka, G. Q. Zheng, and K. Ishida, Prog. Nucl. Magn. Reson. Spectrosc. **28**, 221 (1996).

2.3 Relaxation mechanisms of Yb^{3+} in $YbBa_2Cu_3O_{7-\delta}$ at high temperatures

2.3.1 Introduction

The spin-lattice relaxation rate of paramagnetic ions is one of the important parameters characterizing a material. The relaxation rate of a paramagnetic probe is sensitive to the dynamics of the lattice and to the electronic or magnetic systems. Any kind of phase transition related to these systems influences the relaxation rate [59]. By applying the appropriate theory, one can extract valuable information related to the mechanisms of relaxation and processes taking place in the sample. In the previous section, we investigated the mechanisms of the spin-lattice relaxation of a Yb^{3+} probe in $Y_{0.98}Yb_{0.02}Ba_2Cu_3O_x$ (YBCO) from a lightly doped sample with $x = 6.1$ to an optimally doped sample with $x = 6.98$. The concentration of Yb^{3+} in these samples was small and the interaction between the Yb^{3+} spins could be neglected. The mechanisms of the Yb^{3+} relaxation in these samples are of phononic and electronic origin. The electronic (Korringa) component in the relaxation is proportional to the carrier doping in the sample. The phononic contribution to the relaxation has an exponential temperature dependence with an activation energy $\sim$ 500 K. There have been few EPR studies of the rare earth ions with nonzero orbital moment (Er and Yb) doped in cuprates [29, 30, 31, 32, 33, 34, 35, 36]; however, the studies were performed at temperatures less than about 100-150 K above which there is a substantial broadening of the line. On the other hand, there are reports [23, 24] of neutron experiments in which observations of a pseudogap opening in the region near 180 - 200 K with a sharp transition. This fact seems to contradict the investigation of the relaxation mechanisms of Yb^{3+} in $Y_{0.98}Yb_{0.02}Ba_2Cu_3O_x$, since at such high temperatures, there is only a phononic contribution to the relaxation and a decrease of the relaxation rate would be related to the electronic system. However, this could be a very interesting fact indicating a substantial change of the phononic spectrum if indeed there is such a change of the relaxation at the pseudogap-opening temperature. Another interesting phenomena taking place in HTS is an electronic phase-separation process. It was shown in Ref. [60] that in lightly doped $La_{2-x}Sr_xCuO_4$ for $x = 0.01$ to 0.06, there is an electronic phase separation characterized by a temperature $T' \simeq 150$ K below which carriers in the CuO_2 plane of $La_{2-x}Sr_xCuO_4$ arrange themselves in hole rich and hole deficient regions. This was observed with a Mn^{2+} EPR measurement and with other techniques [61, 62, 63, 64, 65, 66]. In the $YBa_2Cu_3O_x$ system, there were some indications of, but no clear observation of this phenomenon [63, 66, 67, 68]. This could be explained by the relatively fast motion of hole rich or hole-poor regions at high temperatures. But at low temperatures, this motion is assumed to slow down. In this case, when the characteristic frequency of this motion at certain temperature close to the Larmor precession frequency of Yb^{3+}, one should observe an increase of the Yb^{3+} relaxation rate characterized by a spike of the temperature dependence of the relaxation. In order to investigate these possibilities, the study of the relaxation mechanisms was extended to higher temperatures by using $YbBa_2Cu_3O_x$ samples that result in a 50 times larger intensity of the EPR signal, thereby allowing measurements at higher temperatures.

2.3.2 Experimental details

The polycystalline samples were prepared by the standard solid-state reaction at Paul Scherrer Institut, Switzerland. Oxides of Yb_2O_3, CuO and the carbonate $BaCO_3$ were mixed in their proper molar concentrations and calcined at 900^{o}C. Then the samples were ground several times, pressed into pellets and sintered at 887^{o}C. It was found empirically that at this temperature, the Cu^{2+} signal existing in all HTC cuprate materials has a minimum intensity. In addition, it was found that for the samples annealed at temperatures less that 860^{o}C, there is an increase of the signal near a g-factor value of 2 at low temperatures ($\sim$20 K). Using X-ray spectroscopy, the signal was associated with the Yb_2CuBaO_5 (green) phase of the sample that orders magnetically below 18 K [69]. Details of the sample preparation are described in Ref. [70]. Note that the possible green phase Yb_2BaCuO_5 existing in small concentrations as an impurity phase has no Yb^{3+} EPR signal [69] and therefore, can not influence the results. The required oxygen content in the samples was adjusted by gettering in a closed ampoule with metallic copper at 850^{o}C for 10 h and then cooled at a rate of 10^{o}C/h). Six samples of $YbBa_2Cu_3O_x$ were prepared with oxygen dopings $x = 6.2$, 6.3, 6.4, 6.6, 6.8, and 6.95. T_c-s of the samples were measured with a Quantum Design SQUID magnetometer and were found to be 0, 0, 0, 30, 62, and 92 K, respectively. For EPR measurements, a standard X-band (9.4 GHz) Bruker EMX spectrometer was used. The spectrometer was equipped with a ^{4}He-flow cryostat form Oxford Instruments that allowed measurements between 4 K and 300 K.

2.3.3 Results and discussion

Fig. 2.9 shows typical EPR spectra of $YbBa_2Cu_3O_{6.95}$ at different temperatures. Below 30 K, a strong EPR signal is observed with a g-factor of approximately 2 coming from the green phase. Since the EPR measurements with an Yb doping of 2% are performed at low temperatures (see Sec. 2.1), the measurements were extended to temperatures above 100 K. The large amplitude, broad signal corresponds to the Yb^{3+} absorption line with $g = 3.4$ in agreement with previous reports of the eight-fold coordinated orthogonal/tetragonal symmetry [5, 35]. The Yb^{3+} ion is very convenient, since the crystal field splits most of the degeneracy of the $^2F_{7/2}$ multiplet leaving only the ground-state doublet Γ^7 which is well described by an $S = 1/2$ Hamiltonian. The first excited states of the multiplet lies at about 1000 K above the ground state and one can exclude additional channels of the spin-lattice relaxation by CF-split levels which could complicate the analysis. The nonzero orbital momentum of Yb^{3+} that couples the spin to the lattice is important as well.

At 100 K, the peak-to-peak line width ΔB_{pp} of the signal is comparable to the resonant field B_r due to the strong dipole-dipole broadening. The broadening of the line due to the g-factor anisotropy is negligible in this case and the relaxation broadening is relatively small at 100 K (see Sec. 2.1). Calculations of the dipole-dipole broadening performed by

Likodimos *et al.* [71] gives for a powder sample, an average square root of the Van Vleck [72] second moment $B_d \simeq 0.13$ T. At 100 K, the measured ΔB_{pp} is in the range of 0.12 - 0.17 T for different oxygen dopings. This is approximately a factor of 2 smaller than expected (since $B_d = 0.5\Delta B_{pp}$ for a Gaussian signal). This is explained by an exchange coupling J between the Yb^{3+} spins of the order of ~0.3 K [71, 73] what is comparable with the dipole interaction energies $g\mu_B B_d \sim 0.34$ K (μ_B is the Bohr magneton). This means that the EPR signal is exchange narrowed by approximately a factor of two at 100 K. As one can see from Fig. 2.10 with a reduction of doping to $x = 6.4$, there is an increase of the ΔB_{pp} at 100 K that corresponds to the small reduction of the exchange coupling and narrowing in agreement with experimental reports on the doping dependence of T_N for Er^{3+} [74]. The doping dependence of $\Delta B_{pp,T=100K}$ implies that, besides dipolar interactions, the carriers are participating in the total exchange coupling J. For an oxygen dopings less than 6.4, there is an abrupt strong increase of the EPR line width at 100 K. This is associated with an additional increase of the internal field at the Yb^{3+} site produced by defects of antiferromagnetically (AF) ordered Cu^{2+} spins.

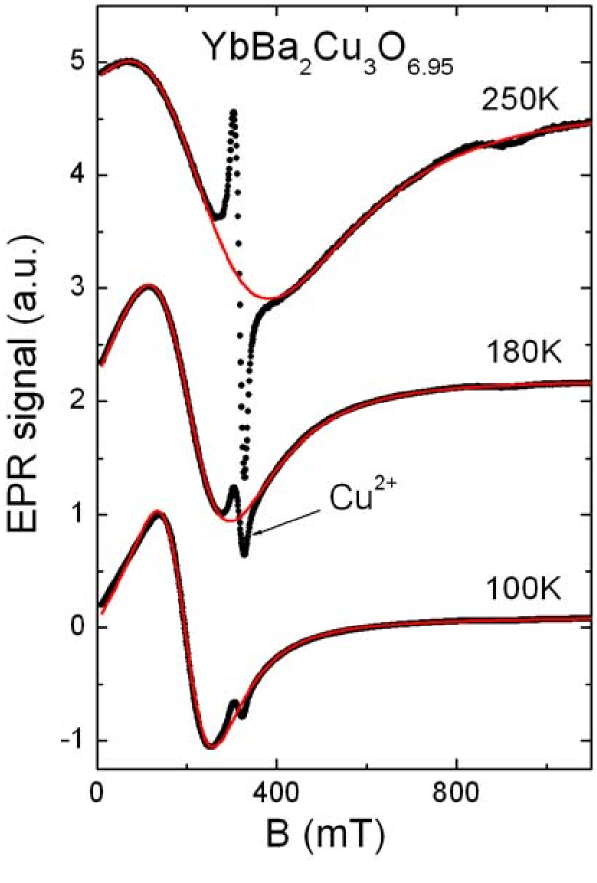

Figure 2.9: Temperature dependence of the EPR signal for an $YbBa_2Cu_3O_{7-\delta}$ sample. The red curve is a fit of the data with a Lorentzian. The narrow signal at 330 mT comes from Cu^{2+} defects.

Fig. 2.10 shows the temperature dependence of the peak-to-peak line width ΔB_{pp} for different oxygen dopings x. There is a very slow temperature dependence of ΔB_{pp} below

150 K and a faster increase of the linewidth above that temperature. As mentioned above, at low temperatures, the line shape and the line width are predominantly determined by the exchange-narrowed, dipole-dipole broadening. With rising temperature, the relaxation processes play an increasing role in the line width of the signal. At ~250 K the spin-lattice relaxation dominates the broadening of the signal. Note that, for all the samples with different dopings, the line widths are different at low temperatures than at high temperatures where they follow the same curve. This could mean that the substantial dipolar broadening of the EPR signal at 100 K is additionally "narrowed" at higher temperatures. The reason for the stronger exchange narrowing at high temperatures, e.g. increase of J with increasing temperature, is not known. However, as mentioned above, J increases with increasing carrier concentration. Therefore, one can speculate that the exchange integral J increases with temperature due to the closing of the pseudogap for the underdoped samples which increases the carrier concentration. This in turn will increase the exchange narrowing of J and B_d. The relation between ΔB_{pp} and the relaxation rate T_2^{-1} is [75]:

$$T_2^{-1} = \sqrt{3}/2\gamma\Delta B_{pp} = 7.62 \cdot 10^6 g\Delta B_{pp}, \tag{2.28}$$

where γ is the gyromagnetic ratio.

The line-shape and line-width behavior for the exchange-coupled concentrated paramagnetic system has already been calculated by Anderson and Weiss [76]. They showed that the EPR line shape for the system of dipoles with the isotropic exchange coupling $J = \hbar\omega_e$ can be well described by the Fourier Transform (FT) of the function [76]

$$\phi(\tau) = \exp\{-A\frac{\omega_d^2\tau}{\omega_e}\int_0^{\omega_e\tau} e^{(\pi/4)x^2}dx + \frac{2\omega_d^2}{\pi\omega_e^2}\left[1 - \exp\left(-\frac{\pi}{4}\omega_e^2\tau^2\right)\right]\}, \tag{2.29}$$

where $A = 1$, $\omega_d = B_d/\gamma$ is the square root of the secular second moment and $\omega_e \simeq J/\hbar$ is the frequency of Yb^{3+} spin fluctuations due to the exchange coupling. Two extreme cases of the FT for this function are a Lorentzian when $\omega_e \gg \omega_d$ and a Gaussian when $\omega_e \ll \omega_d$. Calculations of the exchange frequency using Eq. (2.29) for the given square root of the secular moment $\gamma\omega_d \simeq 130$ mT [71] gives $\omega_e \simeq 80$ GHz. The Zeeman frequency in the present case is $\omega_0 = 9.4 \times 2\pi \simeq 59$ GHz. From this estimate, it is clear that the fluctuation frequency of Yb^{3+} ions due to exchange interaction ω_e are just slightly above the Larmor-precession frequency ω_0. This means that the function Eq. (2.29), derived in the adiabatic approximation ($\omega_e \ll \omega_0$), can not be applied to this case. In the extreme case, when $\omega_e \gg \omega_0$ Eq. 2.29 is again correct; however, the coefficient in the subexponential function should be $A = 10/3$. That is, the line width increases by a factor of 10/3 in the nonadiabatic case [14]. In the present case where we have neither an adiabatic nor a completely nonadiabatic case, the coefficient A should be somewhere between 1 and 10/3. As was mentioned above, experimental results indicate that the exchange integral J increases with temperature. In this case, the situation becomes more complicated, since with increasing $\omega_e \simeq J/\hbar$, one slowly goes to a completely nonadiabatic case ($\omega_e \gg \omega_0$). As a result, the coefficient A in Eq. (2.29) gradually varies from X to 10/3, where $1 < X < 10/3$. A relatively simple analytical model for the line shape when $\omega_e \simeq \omega_d \simeq \omega_0$, does not exist and an exact solution is much too complicated [77] to be useful. Although it is impossible to describe the properties of the line in the full temperature range, the high relaxation rate at high temperatures practically determines the line shape and line width of the signal. In addition, the sharp and abrupt changes in the relaxation will also be correspondingly reflected in the temperature dependence of the line width.

In Fig. 2.10, the dashed red line shows the extrapolation of the relaxation rate of Yb^{3+} in $Y_{0.98}Yb_{0.02}Ba_2Cu_3O_x$ (the diluted case) expressed in the line width units [T]. The Korringa contribution at high temperatures is negligible and this line is practically doping independent. There is a clear discrepancy between the present result obtained at high temperatures and the previous result. The reason for such a difference is due to circumstances encountered basically in EPR. In the highly concentrated systems [78] when the dipole-dipole field/energy B_d is comparable to the Zeeman field/energy B_r, there is expected an additional increase of the relaxation. In this case, the local field of the Yb^{3+} ion is no longer dominated by the external field B but the dipolar field from a neighboring Yb^{3+} is comparable or even stronger. If the Yb^{3+} ion "flips" due to the relaxation process, then the dipolar field of a neighboring Yb^{3+} ion will also change its direction (assuming the external field to be negligible). This is equivalent to an additional relaxation of the neighboring Yb^{3+} ion. T_1^{-1} due to this effect is increasing according to the relation [14, 79]

$$T_1^{-1} = T_{1K}^{-1} \frac{B_r^2 + \delta(10/3)\langle \Delta B_d^2 \rangle}{B_r^2 + (10/3)\langle \Delta B_d^2 \rangle}, \tag{2.30}$$

where T_{1K}^{-1} is the relaxation rate at high resonant fields, B_r is the resonant field and $\delta = 2$.

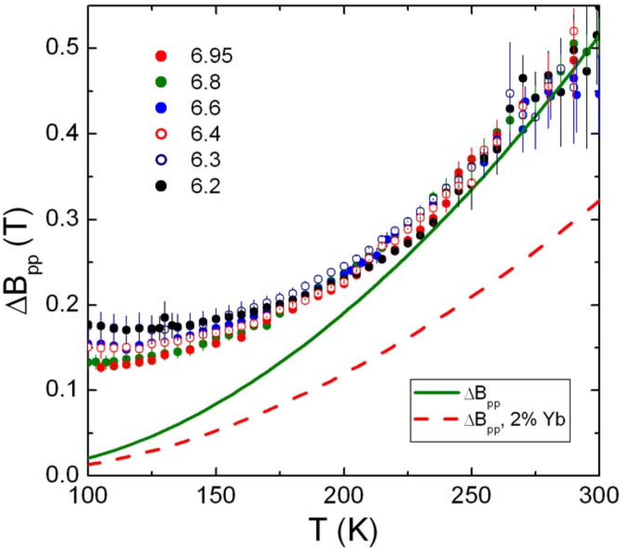

Figure 2.10: Temperature dependence of the peak-to-peak line width of the EPR signal for dopings x = 6.2, 6.3, 6.4, 6.6, 6.8, 6.95. The dashed red line is the previously reported one for the relaxation rate. The solid green line is the relaxation after corrections described in the text.

In the extreme case when $B_d \gg B_r$, there is an increase of a factor of two in the relaxation.

In the present case, $B_d = 0.13$ T and $B_r = 0.2$ T. If we put these numbers in Eq. (2.30), we find that the relaxation in the present case should be 1.6 times as strong as in a dilute case where the distance between the Yb^{3+} ions is large and dipolar interaction is negligible. The relaxation increased by the factor of 1.6 is shown in Fig. 2.10 by the green line. It agrees well with the line width at high temperatures. In the concentrated magnetic system with a strong exchange coupling between the ions in the nonadiabatic limit, the following equation is valid for the transverse relaxation rate [14]:

$$\frac{1}{T_2} = \frac{1}{T_2'} + \frac{7}{10}\frac{1}{T_1}, \tag{2.31}$$

where $T_2'^{-1}$ is the relaxation rate in the adiabatic limit $\omega_e \ll \omega_0$ and T_1^{-1} is the longitudinal relaxation rate. If we take into account $T_1 \simeq T_2'$, then one gets $T_2^{-1} \simeq 1.7T_1^{-1}$ which also agrees well with present results.

From Fig. 2.10, one can clearly see that there is no anomaly of the relaxation near the expected value of the pseudogap temperature T^*. For the samples with oxygen doping $x = 6.3$, 6.4, and 6.6, this temperature should be around 180-220 K. In Ref. [23, 24], the drop of relaxation observed around 200 K is 20% and 70% for the Ho and Er crystal-field transitions, respectively. This amount of change could easily have been detected in the EPR experiment and is definitely not present. However, one can assume that the drop of the relaxation is very small and it may be within the statistical scatter of the points. This scattering is mostly due to an uncertainty of the temperature measured within a few Kelvin (up to 3 K, according to information from Oxford Instruments). In order to improve the results, a special sample holder was designed with a small resistive cernox-temperature sensor attached within ~ 1 mm of the sample. The linear size of the sensor is $\simeq 1$ mm. For the resistance measurements, the standard four-point technique with very thin wires (diameter $d = 0.05$ mm) was used. The samples with all oxygen dopings were measured with this sample holder and analysis showed that there is no abrupt change of the Yb^{3+} relaxation around the expected T^* temperatures (170-240 K). The data are much smoother as a function of temperature than shown in Fig. 2.10, but there is an additional systematic deviation in this results related to the temperature-dependent broad spectrum of the sample holder (plexiglass). From this experiment, it was possible to detect a relative change of the line width better than a few mT, or 1% of ΔB_{pp}. However, nothing was detected. Therefore, one can conclude that there is either a very small undetected change or no change of the relaxation at T^* within the accuracy of the experiment. There is no detectable anomaly related to the possible phase-separation process in the whole doping range above 100 K. Although the results obtained in the present work seem to contradict the results obtained by the neutron spectroscopy [23, 24], there is an interesting systematic trend. The larger the energy of the Zeeman or the crystal-field (CF) transitions, the more pronounced is this effect. The energies of the Zeeman, the Ho CF and the Er CF transitions are 0.03, 1, and 10 meV, respectively. For Er^{3+} CF transition, a relaxation change of $\sim 70\%$ of that around 200 K. For Ho CF transition, the change was $\sim 20\%$ and, in the case of the Zeeman EPR transition, nothing was detected within the precision of the experiment (~ 1 %).

2.3.4 Conclusions

In conclusion, detailed measurements of the line width for $YbBa_2Cu_33O_x$ at $x = 6.2$, 6.3, 6.4, 6.6, 6.8 and 6.95 were performed. There are two mechanisms for the Yb^{3+} EPR-line broadening. The first is the exchange-narrowed, dipole-dipole broadening at low temperatures that further narrows at high temperatures due presumably to an increase of J with increasing temperature [14]. At higher temperatures, the line width is predominantly determined by the spin-lattice relaxation process that is $\simeq 1.6$ times larger than in the dilute case reported in Sec. 2.1 which is in full agreement with the predictions of Ref. [14, 79]. No anomalies were found in the temperature dependence of the relaxation rate related either to an onset of the pseudogap state as reported in Ref. [23, 24] or to the phase-separation process in the temperature range 100 to 300 K and in the oxygen doping range $x = 6.2$ to 6.95. The absence of a relaxation drop due to the transition to the pseudogap state is in agreement with previous conclusions that at high temperatures, the dominant relaxation mechanism is phononic. Comparison of the detection energies for the neutron and the EPR experiments and the strength of the relaxation drop of the pseudogap transition leads us to conclude that with increasing detection energy, this effect becomes more pronounced.

2.4 Antiferromagnetic to superconducting phase transition in $Y_{0.98}Yb_{0.02}Ba_2Cu_3O_x$ for $x \simeq 6.4$ investigated by Yb^{3+} EPR

2.4.1 Introduction

Electrons in cuprates adopt a remarkable sequence of ground states as one varies the density of charge carriers. When the electron density in the CuO_2 planes of a cuprate material is exactly 1.0 per Cu atom in the plane, the material is a Mott insulator [12] with static long-range antiferromagnetic order, and the electrons are localized on their sites by strong Coulomb repulsion. This electronic gridlock can be relaxed by removing electrons from the planes, a charge-transfer process induced by chemical substitution away from the planes. This doping process adds holes to the planes and at high carrier density yields a normal metal with the basic signatures of a Fermi liquid. At intermediate density, it is a superconductor, but the nature of the underdoped phase, which lies between the insulator and the superconductor, is one of the central puzzles of the field. For the $YBa_2Cu_3O_x$ compound, this carrier doping corresponds to $x \simeq 6.4$. Whereas superconductivity in $La_{2-x}Sr_xCuO_4$ emerges from a nonmetallic phase (Fig. 2), the precursor phase for $YBa_2Cu_3O_x$ still remains controversial [80, 81, 82, 83]. A detailed study in the vicinity of boundaries of antiferromagnetic (AF) and superconducting (SC) phases is needed in order to understand whether the AF and the SC phases coexist, compete or are separated by a novel phase.

Investigations of $YBa_2Cu_3O_x$ for the hole doping $x \simeq 6.4$ was the subject of recent studies by various techniques [84, 85]. In the paper of Stock *et al.* [85], a single crystal of $YBa_2Cu_3O_x$ with $x = 6.353$ with $T_c = 18$ K was investigated. They conclude that there are coexisting SC and AF phases and that these phases are simultaneously and homogeneously distributed in the sample.The Cu spin dynamics show the appearance with decreasing temperature of a "central mode" with $E < 0.08$ meV and a broad mode at $E \simeq 2$ meV. The coherence length of the Cu-spin dynamics is short. On the other hand, the recent investigations of Sanna *et al.* [84] on a similar material indicate that there are two phases, a superconducting and a magnetic one, presumably ordered/separated in a stripe-like geometry. They conclude that the insensitivity of the superconducting-order parameter to the magnetic one excludes a magnetic origin of SC.

EPR is a very sensitive tool to detect different phases in the oxygen doping range $6.35 \lesssim x \lesssim 6.45$. The dynamics of Cu spins found by neutron measurements is close to the EPR frequency $\nu_0 = 9.4$ GHz. EPR measurements are fast, as required for the experiments described below. Our experimental observations show that there is a very drastic change of the EPR signal over the AF-to-SC transition at low temperatures in agreement with previous observations [33]. In the vicinity of the AF-to-SC transition in the AF state, the EPR line width of Yb^{3+} in $Y_{0.98}Yb_{0.02}Ba_2Cu_3O_x$ is very broad ~ 120 mT whereas in the SC state, besides a nonresonant microwave absorption, a narrow Yb^{3+} signal is observed with a peak-to-peak line width $\Delta B_{pp} \simeq 10$ mT. The drastic broadening in the AF state is due to uncompensated/disordered AF Cu spins, produced by slowly hopping carriers or slowly fluctuating Cu spins. Slow means that no motional narrowing of the signal is present or that it is negligible, e.g. the dynamics of the field created by the Cu spins is slower that the line width of the Yb^{3+} signal. In order to study this effect more carefully, it was decided to vary the doping in the vicinity of $x \simeq 6.4$. To do so, the well known effect of the hole-doping dependence in the CuO_2 planes on the oxygen order in the chain was used (besides its dependence on the oxygen content x. It is known that, by applying pressure or by quickly quenching the $YBa_2Cu_3O_x$ sample, one can change the oxygen order in the chain without changing the total oxygen content in the sample [86, 87, 88]. In the present experiments the the sample quenching and annealing technique was used to vary hole doping.

It was found that the time dependence of the hole-doping relaxation in the CuO_2 planes is in agreement with previous studies of this effect on the magnetization [86, 87, 88]. Based on simple argumentations, it was possible to determine the hole-doping distribution in the samples. The coexistence of the magnetic and the superconducting phase in the region of oxygen doping $x \simeq 6.4-6.45$ is clearly demonstrated. For the first time, it was unambiguously shown that these phases are spatially separated in agreement with the assumption made by Sanna *et al.* [84]. By comparing the present results with the results of Stock *et al.* [85], it was found that the central and the $\sim$ 2meV mode observed by neutron spectroscopy correspond to separated magnetic and superconducting phases detected by EPR.

2.4.2 Sample preparation and experimental details

The polycrystalline sample $Y_{0.98}Yb_{0.02}Ba_2Cu_3O_{7-\delta}$ was prepared by a standard solid-state reaction from oxides of Y_2O_3, Yb_2O_3, $BaCO_3$, and CuO at the Paul Scherrer Institute. The starting oxides were mixed in the proper proportions and calcinated at 900^{o}C. Afterwards, the sample was ground several times and sintered at 920^{o}C. The as-prepared sample was then oxidized in an oxygen atmosphere at 500^{o}C. After the oxidation, the sample had an oxygen content $x = 6.98$. The required oxygen contents $x = 6.1$, 6.2, 6.3, 6.4, and 6.5 were obtained by gettering the samples with metallic copper in a closed ampoule at 850^{o}C for 10 h and then cooling at a rate of 10^{o}C/h. The magnetization measurements performed with a Quantum Design SQUID magnetometer showed that the samples with $x = 6.1$, 6.2, 6.3, 6.4, and 6.5 had superconducting-transition temperatures of $T_c = 0$, 0, 0, 12(1), and 52 K, respectively. The starting sample A of $Y_{0.98}Yb_{0.02}Ba_2Cu_3O_{6.4}$ was used to obtain two other samples, B and C for the experiments described below. The powdered EPR samples A, B, and C were placed in a quartz capillary which was open on one side. They were not suspended in paraffin or epoxy in order to allow annealing at high temperatures. The EPR spectra of these samples showed no difference from the ones suspended in paraffin or epoxy. No noticeable signs of a Dysonian shape were detected as would be characteristic of conducting samples. The sample B was obtained by annealing sample A in an N_2 atmosphere at 520^{o}C for 40 hours. The sample was then quickly quenched in liquid nitrogen at 77 K. The quenching time was approximately 1 second, being close to the time constant of sample thermalization. The annealing was performed in order to reduce the oxygen doping slightly below $x = 6.4$

where the Cu spins in the sample order antiferromagnetically. The sample C was obtained by quenching part of the starting sample A from 300^oC in air to 77 K using liquid nitrogen. The sample was kept at 300^oC for 30 minutes. It is well known that the dynamics of the chain oxygen above this temperature is very fast and therefore it does matter whether the sample is quenched from 520^oC or from 300^oC [88] since the quenching time ($\sim 1-3$ seconds) is much longer than the time constant for chain-oxygen diffusion at these temperatures. On the other hand, at 300^oC no oxygen escape from or absorption into sample takes place and thus the total oxygen content remains unchanged [89]. The quenched samples B and C were then annealed at room temperature for different periods of time and after each annealing they were measured at low temperatures using the EPR spectrometer. It is known that as a function of time, a quenched $YBa_2Cu_3O_x$ sample starts to relax to the ordered chain-oxygen state with a time constant depending on temperature according to the Arrhenius law [86, 87]. At temperatures below 100 K, one can neglect the change of the chain-oxygen order during a measurement time $\lesssim$ 3 hours [86, 87, 88]. In addition to the samples B and C, a sample D was prepared by quenching $Y_{0.98}Yb_{0.02}Ba_2Cu_3O_{6.5}$ from 300^oC (30 min), similar to the sample C. The EPR measurements were performed with an X-band BRUKER EMX spectrometer equipped with a helium-flow cryostat of Oxford Instruments. EPR is practically the only magnetic-resonance technique that has the possibility to perform such fast measurements thereby allowing such experiments. The temperature after each annealing was swept from 40 to ~140 K within 2 hours while simultaneously the EPR measurements were performed. A single EPR spectrum over the entire field range was measured in 40 seconds, producing up to 100 spectra/points for each temperature scan. Nine temperature scans for different annealing times were performed for each of the samples B and C.

2.4.3 Discussion of the Yb^{3+} EPR signal in $Y_{0.98}Yb_{0.02}Ba_2Cu_3O_x$ for $6.0 < x \lesssim 6.4$

As was mentioned in the introduction, the Yb^{3+} EPR signal of $Y_{0.98}Yb_{0.02}Ba_2Cu_3O_x$ at $x \simeq 6.4$ and $6.0 < x \lesssim 6.3$ is split into two lines, a broad and a narrow one with line widths $\simeq$120 and 10 mT (at $T \simeq 50$ K), respectively. Across the SC-to-AF and the normal conducting (NC)-to-AF state transitions (see Fig. 2), the line is drastically broadened in the AF state. With increasing temperature, both signals broaden additionally due to the relaxation processes described in Sec. 2.1. Fig. 2.11 shows the oxygen-doping dependence of the broad component of the Yb^{3+} EPR signal C_{broad} measured at 70 K. The narrow component of the signal has an intensity proportional to $C_{nar} = (1 - C_{broad})$. The peak-to-peak line width of Yb^{3+} $\Delta B_{pp} \simeq 10$ mT at high oxygen dopings abruptly increases below $x = 6.4$. On further reduction of the doping x, the line narrows again. The points at x=6.0 which are shown as open circles in Fig. 2.11 are not measured points. In Fig.2.11, the value C_{broad} at x=6.0 is zero by definition due to the chemical composition of the sample. The point for ΔB_{pp} at x=6.0 was obtained by a linear extrapolation from the measured points at x=6.1, 6.2, and 6.3. The fraction of the broad Yb^{3+} signal C_{broad} abruptly increases below $x = 6.4$ from 0 to 1. With a further reduction of x, the fraction again gradually decreases from 1 to 0. This picture suggests that the mechanisms of the broadening and the increase of the broad Yb^{3+} signal fraction is related to the charge-carrier concentration. At low doping $x \simeq 6.0$, there are no free carriers, and thus, the dipolar fields of the AF ordered Cu^{2+} moments on Yb^{3+} site are completely compensated. As a result, only the narrow signal is observed. With increasing hole-doping, the volume occupied by carriers increases and the Yb^{3+} ions in this volume fraction experience additional dipolar fields produced by the carriers which locally destroy the AF order. As a result, the EPR signal from the Yb^{3+} in this volume is broad. Therefore, the broad Yb^{3+} signal intensity is proportional to the fraction of the volume containing the carriers. Above $x \simeq 6.3$, almost the whole area of the CuO$_2$ planes is filled with holes and only the broad Yb^{3+} EPR signal is observed. With a further increase of the hole doping, at $x = 6.4$ the dynamics of the AF ordered Cu^{2+} spins becomes fast and the dipolar fields, created by carriers and Cu^{2+} spins, are motionally averaged. As a result, the dipolar fields sensed by the Yb^{3+} EPR probe are again reduced to zero and the Yb^{3+} signal becomes narrow. Note that the resistance and the mobility of the carriers around $x = 6.4$ at 70 K do not change abruptly [90]. Therefore, the motional narrowing of the Yb^{3+} signal is due to the increased Cu^{2+} spin fluctuations and not to the increased charge-hopping rate.

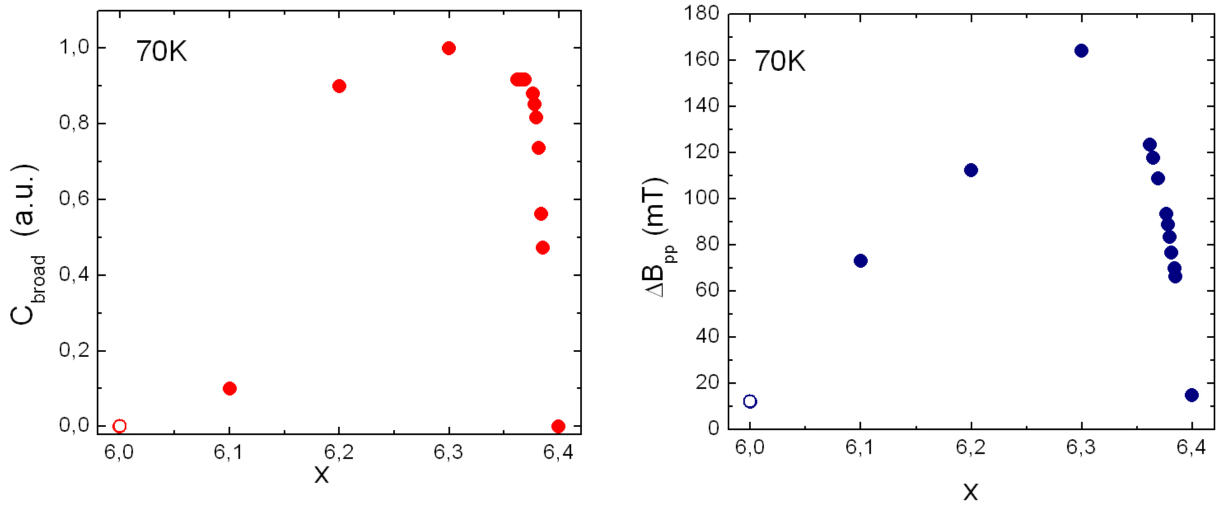

Figure 2.11: The broad Yb^{3+} signal fraction (left) and its peak-to-peak line width (right) as a function of oxygen doping x in $Y_{0.98}Yb_{0.02}Ba_2Cu_3O_x$ at $T = 70$ K. The open circles are not measured points. The value of C_{broad} at x=6.0 is by definition equal to zero. The value of ΔB_{pp} at x=6.0 was obtained by linear extrapolation from the measured values at x=6.1, 6.2, and 6.3.

2.4.4 Results and discussion

The ground state of Yb^{3+} is a Γ^7 doublet with an average g-factor of 3.43 and a small axial anisotropy for tetragonal $Y_{0.98}Yb_{0.02}Ba_2Cu_3O_x$ with $6.0 < x \lesssim 6.4$. The first excited state of

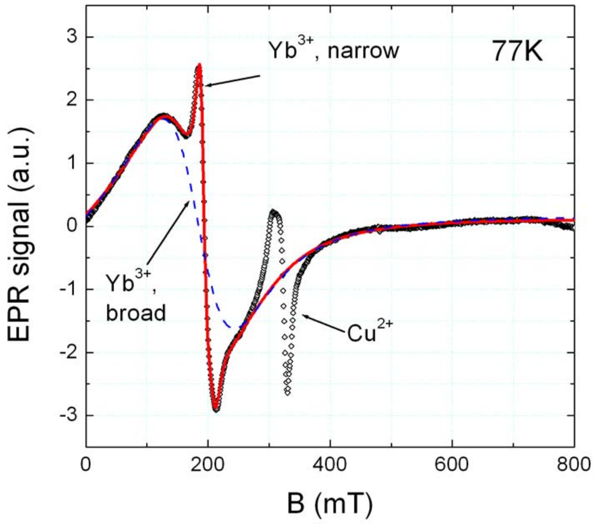

Figure 2.12: Example of the EPR signal at 77 K for sample B just after quenching. The broad and narrow signals correspond to the magnetic and nonmagnetic fractions of the sample, respectively. The red line is the fit to the data using Eq. (2.32).

the Yb^{3+} Γ^7 multiplet is about 1000 K above the ground state, therefore, only the ground-state doublet is populated at temperatures below 140 K. A typical example of an EPR signal at 77 K for the B sample measured just after quenching is shown in Fig. 2.12. The EPR spectrum consists of three signals, namely, a narrow and a broad Yb^{3+} signal corresponding to nonmagnetic and magnetic fractions of the sample as described in Sec. 2.4.3, and a Cu^{2+} signal which is always present in $YBa_2Cu_3O_x$ samples [45, 46, 47].

The temperature dependence of a paramagnetic signal intensity for a Kramers doublet follows the Curie-Weiss law, namely, $I \propto C/(T-\theta)$ [5]. This inverse temperature dependence reflects an increase of the population difference of the Zeeman-split doublet with decreasing temperature and the θ indicates the interaction of the Yb^{3+} ions with each other. We are interested in the parameter C which is proportional to the concentration of Yb^{3+} in the sample. If the signal is split into a broad and a narrow component, then $C_{nar}(T)$ will show the temperature dependence of the nonmagnetic volume fraction and $C_{broad}(T)$ will be due to the magnetic one. Furthermore, $C \equiv C_{nar} + C_{broad}$ is a constant, i.e. the total Yb^{3+} concentration does not change with temperature.

Fig. 2.13 is useful in understanding the origin of the broad and the narrow signals and their temperature dependence. It is assumed that there is a distribution of hole doping in different grains of the powdered sample or even gradients of hole doping within a grain. This distribution is taken to be a Gaussian function as is shown in Fig. 2.13. At low temperatures, all the grains of the sample will be in the magnetic state. With increasing temperature, the grains which are more strongly doped will be the first to undergo the magnetic-to-normal/superconducting state transition. At sufficiently high temperatures, all of the grains of the sample will be in the nonmagnetic state. Correspondingly, at low temperature, the Yb^{3+} signal of all grains will be broadened. However, at a certain temperature, the narrow

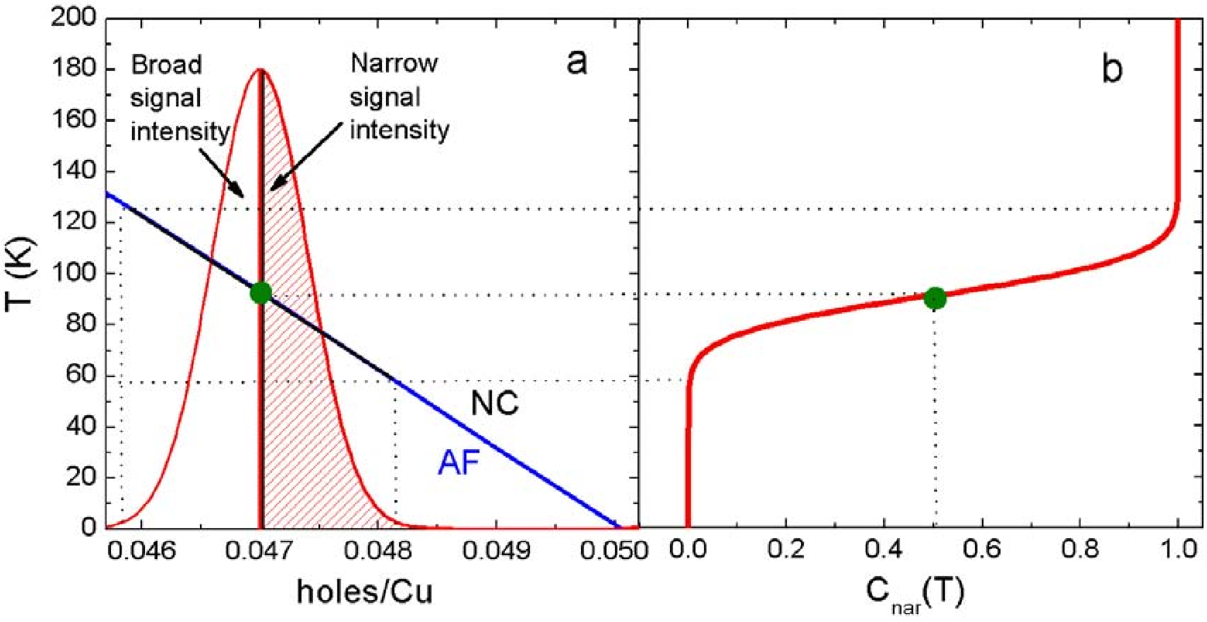

Figure 2.13: (a) Qualitative description of the origin of the narrow and the broad signals and (b) temperature dependence of the narrow signal. The Gaussian distribution of (a) represents the hole-doping distribution in the sample. The blue line is the AF-to-NC phase border. The filled area of the Gaussian is proportional to the intensity of the narrow signal at $\simeq$ 90 K. In (b), C_{nar} is plotted as a function of temperature corresponding to the doping distribution shown in (a).

component will appear and at high temperatures, only the narrow component of the signal will remain. In Fig. 2.13(a), the case for $T \simeq 90$ K and a hole doping $h = 0.047$ holes/CuO_2[1] is illustrated (where the broad and narrow signal have approximately the same intensity). In Fig. 2.13(b), the temperature dependence of C_{nar} is plotted for doping distribution shown in Fig. 2.13(a). The transition-temperature width depends on the steepness of the AF-to-NC phase border and on the doping-distribution width δh.

The data were fit with a model having two components, namely, a narrow and a broad signal. For the fit of the broad signal, a Lorentzian was used. It fits the data well as is shown by the blue dashed line in Fig. 2.12. The model for the narrow signal is more complicated, being the convolution of a Lorentzian, representing the relaxation component of the signal (as described in Sec. 2.1), with the inhomogeneous broadening of the signal measured at 50 K where it has its narrowest width. The width of the convoluted Lorentzian was taken equal to the one obtained from the relaxation studies at $x = 6.4$ in order to avoid additional fit parameters. Finally, the data were fitted according to the following equation:

$$\begin{aligned} F(x|A_n, Br_n, W_n, A_b, Br_b, W_b) &= L(x|A_b, Br_b, W_b) + L(x|A_b, -Br_b, W_b) \\ &\quad + \int_0^\infty g(y)L(x-y|A_n, Br_n, W_n)dy \end{aligned} \tag{2.32}$$

where

$$L(x|A, B_r, \Delta B_{pp}) = 16A\frac{x - Br}{0.5\Delta B_{pp}} \cdot \left[3 + \left(\frac{x - Br}{0.5\Delta B_{pp}}\right)^2\right]^{-2}, \tag{2.33}$$

is the derivative of the Lorentzian and $g(y)$ is a function representing the structure of the spectrum at 50 K where it is not substantially broadened due to relaxation effects. Two Lorentzians with resonant fields B_r and $-B_r$ are used to take into account the two different circular polarizations of the linearly polarized microwave field [78] which is essential for broad signals. The parameters A_b/A_n, Br_b/Br_n, and W_b/W_n are the amplitudes, the resonance fields and the line widths of the broad and the narrow EPR signals, respectively. The physical quantity in which we are most interested is the intensity of the narrow signal $I_n \propto A_n \cdot W_n^2$ since it is fit very precisely. The volume fraction of the NC or SC states is then proportional to $C_{nar} = I_n \cdot (T - \theta)$.

Shown in Fig. 2.14 is $C_{nar}(T)$ of sample B for different room-temperature annealing times. The black circles show C_{nar} just after quenching the sample. It is obvious that the sample is completely magnetic since the fraction of the narrow signal is temperature independent and very small. This small temperature-independent fraction corresponds to a small superconducting part of the sample which remained after quenching. For a given temperature, the fraction of the nonmagnetic part of the sample increases with increasing annealing time. After a long annealing time, practically all of the sample is nonmagnetic for temperatures above 100 K. The numbers in the Fig. 2.14 identify measurements for various annealing time at room temperature. Each of the curves in the figure is an integral of the hole-distribution function shown in Fig. 2.13. If one shifts all curves in Fig. 2.14 by the

---

[1] We assume that the oxygen doping $x = 6.4$ corresponds to a hole doping 0.05 holes/CuO_2 where the onset of superconductivity occurs. Different authors report slightly different values.

appropriate amount along the x-axis, they will then all collapse onto a single curve as shown in Fig. 2.15. The red line is a fit to this curve by the integral of Gaussian-distribution function

$$C_{nar}(x|a, y_0, w) = a \int_0^x \exp\left(\frac{1}{2}\frac{(y-y_0)^2}{w^2}\right) dy, \tag{2.34}$$

where a, y_0 and w are the amplitude, the center and the width of the Gaussian, respectively. The vertical line in $C_{nar}(x|a, y_0, w)$ separates the argument x from the fit parameters a, y_0, and w. The excellent fit justifies the assumption of a Gaussian distribution for the hole doping. In reality, the width of the transition in Fig. 2.13(b) for $C_{nar}(T)$ is composed of the two components as shown in the equation

$$C_{nar}(T) = \int_{T-x>0}^{\infty} \left(\int_0^x D(y)dy\right) S(T-x)dx, \tag{2.35}$$

where the first component $D(x)$ is the real doping distribution and the second one $S(T)$ is the width of the transition for an ideal sample with a doping distribution expressed by the delta function $D(x) = \delta(x)$. At the AF-to-NC phase border, enhanced fluctuations of the order parameter, or Cu^{2+} spins, are expected. The frequency of the spin fluctuaions cannot change abruptly from a high value (corresponding to the narrow signal) to approximately zero (corresponding to the broad signal). Therefore, the function $S(T)$ cannot be a step function as was assumed in Eq. (2.34) for an ideal sample but instead, it must have a certain width. Thus, the line width of the hole distribution δh is in reality smaller than $\delta h_m \propto w$ obtained from Eq. (2.34). Most important in Fig. 2.15 is the estimate of the maximum width of the doping distribution δh_m where 80% of the sample is concentrated. As shown in Fig. 2.15, δh_m corresponds to a ∼60 K change of the temperature for a fixed average doping h. (see also Fig. 2.13). The total change of the position of the inflection point Δh corresponds to ∼120 K. That is, the change of the peak of the doping distribution Δh is a factor of two larger than δh_m. This is the principle information that we have obtained from sample B since it did not cross the phase boundary into the superconducting region due to the strong underdoping. An approximate estimate of the hole-doping change expressed in oxygen concentration units is $\Delta h \simeq 0.04$ and therefore, $\delta h_m \simeq 0.02$ or approximately a factor of 7 smaller in units of holes/CuO_2).

The inflection points of the curves shown in Fig. 2.14, where the C's reach half their maximum value, correspond to the peak of the Gaussian-distribution of Eq. (2.34). In the process of room-temperature annealing, the distribution shifts to higher hole-doping levels. In Fig. 2.16, the relative change of this Gaussian peak as a function of the time is shown on a semi-logarithmic scale. The time dependence of the peak, reflects a two-step process of oxygen ordering. The first process dominates during approximately the first 6 hours and has a time constant $\tau_1 = 6.0(1)$ hours. Afterwards, the ordering process continues with the time constant $\tau_2 = 23(1.5)$ hours. Alternatively, this process can be described by the so-called "stretched exponential" function with a time constant $\tau \sim 5$ hours in agreement with previous studies on magnetization [86, 87].

Sample B was annealed in a nitrogen atmosphere at a temperature of 520^{o}C which slightly reduced the oxygen content compared to sample A. Thus, the hole doping after a long

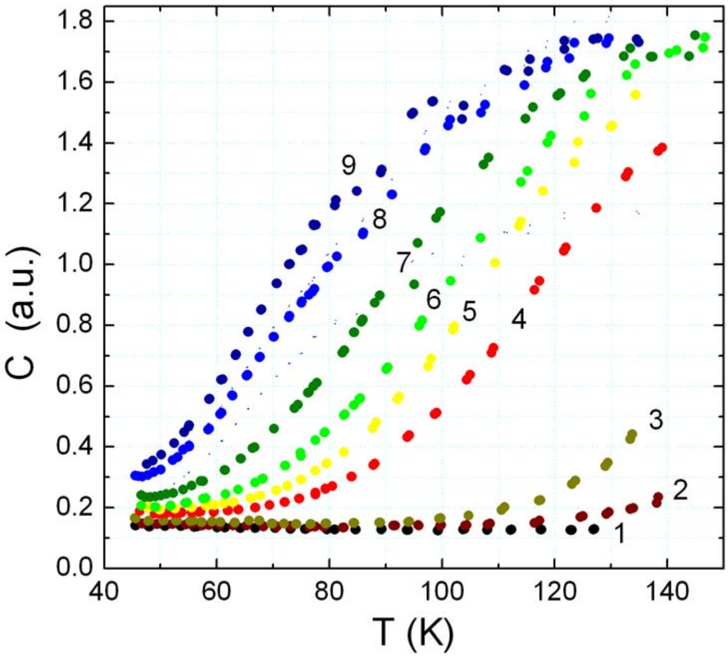

Figure 2.14: Intensity of the narrow EPR signal as a function of temperature for the sample B annealed at room temperature for different times. With an increase of the experiment number (1 to 9 in the figure), the annealing time and the hole-doping increase according to the time dependence shown in Fig 2.16.

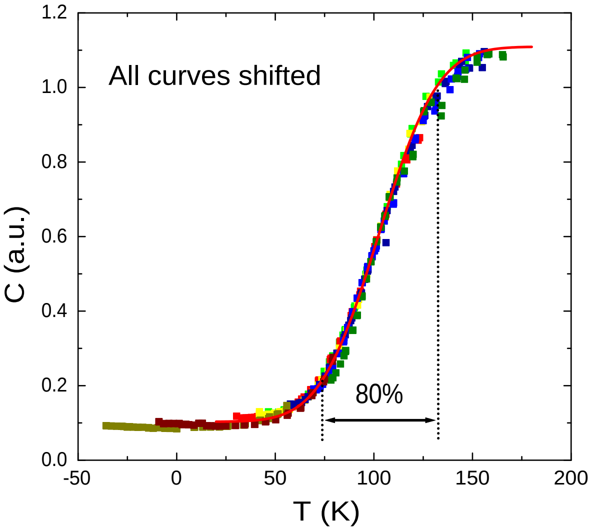

Figure 2.15: The temperature dependence of the transition from the AF to the NC state obtained from the curves of Fig. 2.14. They collapse onto a single curve when shifted along the x-axis. The red line is a fit to this curve by the integral of a Gaussian function as described in the text. The dotted lines show the temperature interval where 80% of sample undergoes the magnetic to normal-state transition.

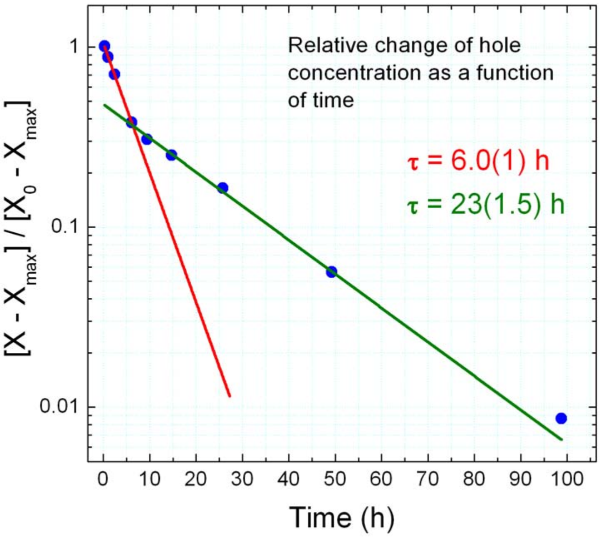

Figure 2.16: The time dependence of the mean hole doping (or inflection point of the curves in Fig. 2.14). There is a two-step process of the chain-oxygen relaxation to the equilibrium state (ordering) with time constants $\tau_1 = 6.0(1)$ h and $\tau_2 = 23(1.5)$ h. Alternatively, the relaxation process can be described by a stretched exponential function in agreement with Ref. [86, 87]. The total change of the peak position of the doping distribution Δh is twice the maximum width of the doping distribution representing 80% of the sample δh_m (see Fig. 2.15).

annealing time did not return to that of sample A and the sample did not cross the NC-to-SC boundary. As was shown in a previous study [88], the hole-doping change Δh above $\sim 300^oC$ is the same independent of the quenching temperature. This is because the sample thermalization time ~ 1 s is long compared to the fast dynamics of the chain-oxygen hopping at temperatures above $\sim 300^oC$. On the other hand, heating the sample to 300^oC for a short period of time (30 min), does not change the oxygen content in the sample [89]. For this reason, samples C and D were prepared and quenched in air from 300 ^oC. For sample C, the fraction of magnetic and nonmagnetic signal as a function of temperature and annealing time was measured in the same manner as for the sample B. For sample D, only a measurement immediately after ($\sim 5-10$ min) the fast quench was performed. The results of these experiments are shown in Fig. 2.17. On the left side of the figure, the result for sample C is shown as a contour plot. On the right side, the result for sample D is shown. The dashed black and red lines between the contour plot of the sample C and the two points of the sample D are interpolated values. The fraction of the magnetic phase is obtained from the narrow-line intensity, expressed as $1 - C_{nar}$ since the statistical accuracy for C_{broad} is larger. For sample C, the superconducting fraction is obtained from the amplitude of the nonresonant microwave absorption at zero field in the EPR spectrum. As is obvious from the figure, there are coexisting superconducting and magnetic phases in the region of the doping filled by diagonal lines. Coexistence of SC and magnetic phases is supported by measurement of the maximum possible width of the hole-doping distribution $\delta h < \delta h_m \simeq 0.02$ (expressed

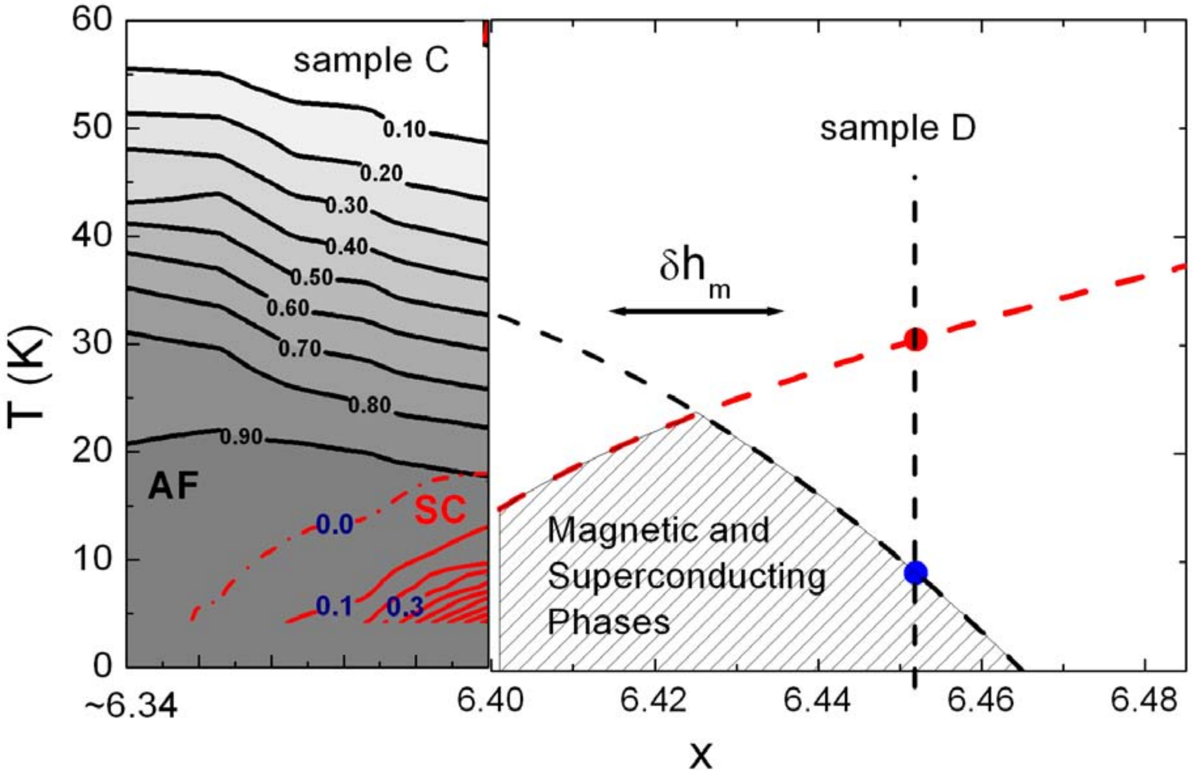

Figure 2.17: Contour plot of the magnetic and the superconducting phase as a function of oxygen/hole doping and temperature. The left side of the figure shows a measurement of sample C. The two points on the right side include the superconducting and the magnetic transition temperature and are obtained from sample D immediately after a quick quench. The dashed black and red lines between the samples C and D is an interpolation. The black lines denote the magnetic phase and the red ones the superconducting phase. The maximum change of the hole doping after a quick quench of the sample is assumed to be $\Delta h \simeq 0.04$ in oxygen doping units. The steepness of the magnetic phase as a function of doping is less than in Fig. 2.14, implying that the magnetic phase is closer to the spin-glass transition than to the AF transition. The maximum width of the doping distribution δh_m representing 80% of the sample is also shown.

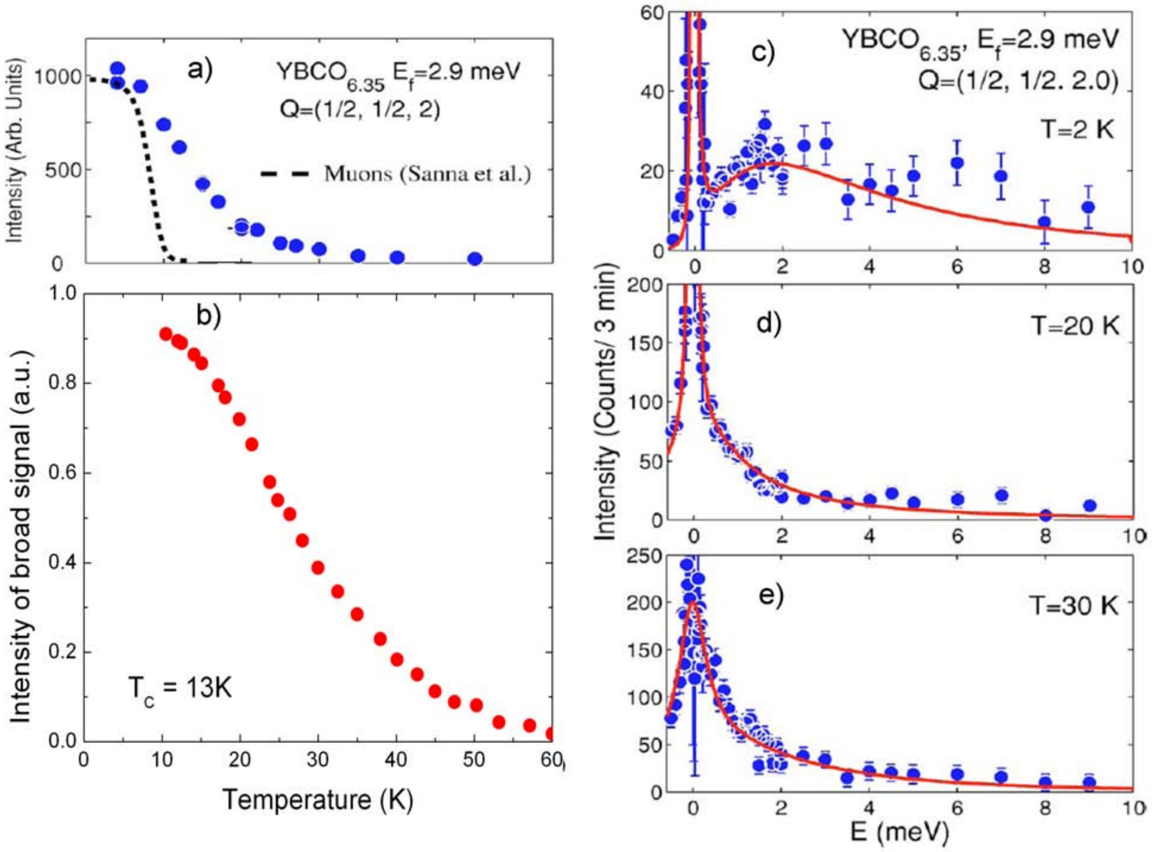

Figure 2.18: (a) Temperature dependence of the central mode (circles) and the temperature dependence of the magnetic phase (dashed lines) as reported in Refs. [84, 85]. (b) Temperature dependence of the broad EPR signal. Note that the T_c's of the samples used in neutron, μSR and EPR measurements are 18(1), 18, and 12(1) K, respectively. (c)-(e) Temperature dependence of the neutron-energy scans with its "central mode" (sharp peak) near 0 energy. Data in panels (a), (c)-(e) are from Ref. [85].

in units of oxygen doping) indicated by arrows in Fig. 2.17.

A similar phase diagram was recently obtained by Sanna *et al.* [84] using μSR spectroscopy. μSR spectroscopy provides the possibility to study magnetic and superconducting properties of a sample and it is possible to measure fractions of the magnetic and superconducting phases microscopically. In their studies they conclude that at low temperatures there are simultaneously 100% of both magnetic and superconducting fractions of the signal. This striking effect can have different theoretical interpretations, namely, either it can be due to a similar nature of the magnetic and superconducting-order parameters (since 100% of both volume fractions coexist simultaneously) or that these two order parameters are insensitive to each other since there is no change in the SC order parameter over the magnetic transition [84]. It should be stressed, that in the present case, the signal of Yb^{3+} is split into broad and narrow components, corresponding to the two different phases and one can trace the volume fraction of each of the phases as a function of doping and temperature, unlike the μSR experiment where 100% of both the superconducting and the magnetic phase

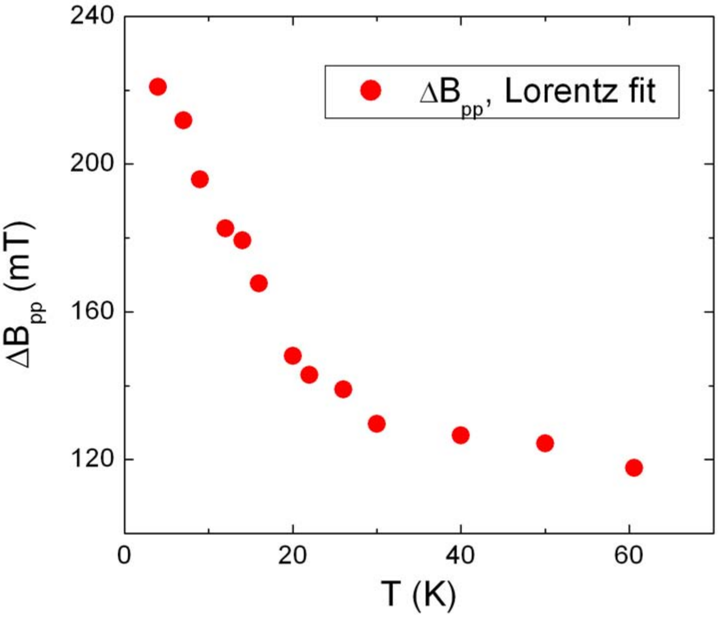

Figure 2.19: Temperature dependence of the peak-to-peak line width ΔB_{pp} of the broad signal for sample C immediately after the quench. The reduction of the line width with increasing temperature implies a motional narrowing of the signal. Note, that the magnetic fraction for this sample appears below ∼ 40 K, whereas there is additional broadening of the signal below ∼20 K implying that the transition from the AF to the spin-glass state occurs at this temperature (∼20 K).

are simultaneously observed. Alternatively, the μSR result can be interpreted as evidence for a homogeneous distribution of these phases as argued by Stack *et al.* [85]. The present results clearly indicate that the sample is spatially inhomogeneous. The reason that two different signals are observed in the case of EPR while only one is observed in μSR , might be due to the shorter range sensitivity of the EPR technique as compared to that of μSR. In addition, the EPR probe Yb^{3+} at the Y site perturbs the local microscopic properties of the sample much less than the muon near the apical or chain-oxygen site. In a recent neutron-spectroscopy study, Stock *et al.* [85] conclude that there is no phase separation as reported by Sanna *et al.*. It is argued that the sample is spatially homogeneous and there are two different energy scales corresponding to modes of the Cu^{2+} spin dynamics, namely, a "damped mode" of $E \sim 2$ meV and a "central mode" of $E < 0.08$ meV. The result of their investigations is shown in Fig. 2.18. In Fig. 2.18(a), the intensity of the central mode as a function of temperature measured by neutron spectroscopy is shown together with the magnetic fraction of the sample as a function of temperature obtained using μSR [84]. In Fig. 2.18(b), the intensity of the broad signal is plotted as a function of temperature measured in the EPR experiment for the sample A ($Y_{0.98}Yb_{0.02}Ba_2Cu_3O_{6.4}$, not quenched). Note that the hole dopings of the samples are slightly different. The T_c's for the samples studied by Stock *et al.*, Sanna *et al.* and in the present work are 18 K, 18 K and 12 K, respectively.

From Fig. 2.18(b), it is clear that the broad EPR signal originates from regions of the sample corresponding to the central mode with slow dynamics of the Cu^{2+} spins. If the dynamics of the Cu^{2+} spins is slowed down or frozen, the line width is no longer motionally narrowed [14] whereas the narrow EPR signal corresponds to regions of the sample where the Cu^{2+} -spin dynamics is fast and therefore strongly motionally narrowed. It is possible to estimate the frequency of the central mode dynamics if one looks at the temperature dependence of the line width for the broad Yb^{3+} signal of sample C immediately after quenching (left side of Fig. 2.17). This line width is plotted in Fig. 2.19. At low temperatures where the dynamics of the spin fluctuations slow down [after the transition to the cluster spin-glass phase (SG)], the line width is a maximal; however, with increasing temperature the spins start to fluctuate and motional narrowing takes place. This transition is presumably the transition from the SG phase to the AF phase since it takes place below $\sim$ 20 K (see Fig. 2.19), whereas 50% of the AF order is observed at $\sim$ 40 K . The fit of the signal at 4 K with a Gaussian function yields 260 mT for the peak-to-peak line width which corresponds to the square root of the second moment $B_d = 130$ mT (the square root of the second moment for a Gaussian is a factor of two smaller than the peak-to-peak width). As is evident from Fig. 2.19, the frequency of the Cu^{2+}-spin fluctuations at temperatures above 30 K do not increase further and the line exhibits a Lorentzian shape with a peak-to-peak line width $\Delta B_{pp} = 124$ mT. This corresponds to approximately twice the exchange-narrowed line width of the signal (from 260 to 124 mT). Calculations using Eq. (2.29) show that in this case, the well known formula for exchange narrowing of the fluctuation field B_{fluct}

$$B_{fluct} = B_d^2/(\sqrt{3}/2 \cdot \Delta B_{pp}) \tag{2.36}$$

can be used [14, 76]: If one inserts $\Delta B_{pp} = 124$ mT and $B_d = 130$ mT, one obtains $B_{fluct} =$ 157.5 mT corresponding to $\nu_{fluct} = 7.4$ GHz for the EPR frequency $\nu_0 = 9.4$ GHz and a resonant field of $\simeq$200 mT. The frequency ν_{fluct} corresponds to an energy of 0.03 meV in good agreement with the neutron result < 0.08 meV obtained by Stock *et al.*. The frequency of the spin fluctuations is close to the EPR frequency and therefore nonadiabatic effects can take place [14]. This means that the result for the fluctuation frequency is a lower limit and it should be multiplied by a factor slightly larger than but of the order of unity [14].

2.4.5 Conclusions

To conclude, it was possible to scan the hole doping of $Y_{0.98}Yb_{0.02}Ba_2Cu_3O_x$ around $x \simeq 6.4$ and perform EPR measurements of Yb^{3+}. The oxygen ordering (hole-doping) was studied as a function of the room temperature annealing time. This reordering process proceeds in two steps, the first six hours having a time constant $\tau_1 = 6.0(1)$ h and later times having a time constant $\tau_2 = 23(1.5)$ h. This is in complete agreement with previous results obtained in Refs. [86, 87]. In addition, the hole distribution in powdered samples was estimated and it was found that the mean value of the carrier-doping changes during the scan by approximately $\Delta h \simeq 0.05$ (in equivalent oxygen doping units). This value is twice the upper limit for the doping-distribution width δh_m corresponding to 80% of the sample, e.g.

$\delta h_m \simeq \Delta h/2$. Experiments clearly show the simultaneous presence of a magnetic and a superconducting phase. For the first time, it was unambiguously demonstrated that these two phases are spatially separated. The existence of a narrow and a broad line corresponding to the superconducting and the magnetic phase of the sample was clearly demonstrated. By comparison with the neutron results of Stock *et al.*, it was shown that the broad Yb^{3+} signal corresponds to regions of the sample where the central mode of Cu^{2+} spin dynamics originates, hence, the narrow line is related to the damped mode. By measuring the temperature dependence of the line width and using the standard motional narrowing equations, it was possible to estimate the fluctuation frequency of the central mode $\hbar\nu_{fluct} \simeq 0.03$ meV or $\nu_{fluct} = 7.4$ GHz (without nonadiabatic corrections). Combining all of the above arguments, the present findings support the conclusion made by Sanna *et al.* that the magnetic phase can not be a precursor state of the superconducting one since there is no influence of the superconducting-order parameter on the magnetic transition and these two phases are spatially separated and most probably compete with each other.

2.5 Relaxation mechanisms of the Yb^{3+} in the infinite-layer compound

2.5.1 Introduction

The infinite-layer $Sr_{1-x}La_xCuO_2$ is very special among the different families of cuprate superconductors. In comparison to $YBa_2Cu_3O_x$, $Bi_2Sr_2CaCu_2O_8$, and $La_{2-x}Sr_xCuO_4$ discussed in this thesis the infinite layer system belongs to 3-dimensional superconductors [91], since the CuO_2 layers are not separated by insulating charge reservoirs but by metallic Sr layers [92, 93]. The second-critical field of this materials is approximately 14 T [91] which gives $\xi_{ab} \simeq 50$ Å for the coherence length in the Ginzburl-Landau approximation. The c-axis coherence length $\xi_c = \xi_{ab}/\gamma = 5.2$ $\AA$ is considerably larger than half of the distance between the plains $3.41/2$ $\AA$ [91, 94]. Since its structure is so simple, this compound provides a unique opportunity to explore the fundamental nature of high-temperature superconductors. In addition it is an electron-doped superconductor and it is therefore interesting to compare its properties with hole-doped superconductors. The infinite-layer superconductor is also well suited for measurements using electron paramagnetic resonance (EPR), since the La^{3+} ion is easily replaced with any isovalent Rare-Earth (RE) element with no substantial influence of its superconducting properties [95]. In the present study, the RE element Yb^{3+} was chosen since it has a simple spectrum described by an effective spin $S = 1/2$ and a g-factor typically different from 2 where the Cu^{2+} signal is present. In addition, it has an orbital momentum that couples the Yb^{3+} spin to the lattice. Spin-lattice relaxation of a RE element can provide valuable information about fluctuating electric and magnetic fields. In previous studies of $Y_{0.98}Yb_{0.02}Ba_2Cu_3O_x$, it was shown that the relaxation of Yb^{3+} has two dominant contributions, namely, 1) the relaxation of Yb^{3+} by the system of carriers (Korringa) that is proportional to the hole-doping and 2) the relaxation by the narrow band of phonons with an energy of 500(50) K. In addition it was shown that acoustic phonons have a negligible contribution to the relaxation. The aim of present study is to investigate the relaxation mechanisms in the superconductor $Sr_{0.9}La_{0.08}Yb_{0.02}CuO_2$ and compare this with results found in the hole-doped $YBa_2Cu_3O_x$ and $Bi_2Sr_2CaCu_2O_8$ systems.

2.5.2 Experimental details

A high quality polycrystalline sample $Sr_{0.9}La_{0.08}Yb_{0.02}CuO_2$ was prepared under high pressure in the multi-anvil-type press [94]. La_2O_3, Yb_2O_3, $SrCO_3$ and CuO were mixed to form the nominal composition of $Sr_{0.9}La_{0.08}Yb_{0.02}CuO_2$. The mixture was then calcined at 950^oC for 36 h with several intermediate grindings. The pelletized sample was then sandwiched between Ti oxygen getters and put in a gold capsule to be used in the high-pressure cell. The sample was compressed to 4 GPa and heat treated at 1000^oC during 2 h. The sample was then quenched to room temperature after an additional postannealing at 500-600^oC for 4 h. The magnetization measured using a standard Quantum Design SQUID magnetometer showed a sharp onset of superconductivity at T_c=43 K. The EPR signal was measured with the standard BRUKER X-Band (9.4 GHz) spectrometer. The temperature was varied using the He-flow cryostat of Oxford Instruments. The polycrystalline sample was ground to avoid Dysonian-like distortions of the EPR signal. To reduce the line width of the signal due to a g-factor anisotropy, the sample was suspended in paraffin and oriented in a 1.2 T magnetic field.

2.5.3 Results and discussion

Yb^{3+} in the $Sr_{0.9}La_{0.08}Yb_{0.02}CuO_2$ compound is sandwiched between the CuO_2 layers and allows the study of processes taking place in these layers. It occupies the eightfold coordinated cite of La^{3+} with tetragonal symmetry. Therefore, like $YBa_2Cu_3O_x$, it is expected that the ground state and the crystal-field splitting will be similar. The spectroscopic splitting factor g has axial symmetry with principal values $g_{||} = 2.50(3)$ and $g_{\perp} = 3.75(3)$. The average value $g = 1/3 \cdot g_{||} + 2/3 \cdot g_{\perp} = 3.33$ is close to $g = 3.43$ observed for Γ^7 doublet [5]. The EPR spectra for the $Sr_{0.9}La_{0.08}Yb_{0.02}CuO_2$ sample at 45 K are shown in two different orientations of crystal c-axis relative to the applied field B in Fig. 2.20. A high degree of sample orientation is found, especially for the spectrum with parallel orientation of the sample where only a negligible trace of the signal from the perpendicular orientation is observed that is dominate for unoriented samples. The signal at 330 mT is due to Cu^{2+} impurities observed in all cuprate superconductors [45, 46, 47].

The difference of the resonant field between parallel ($B \parallel c-$axis) and perpendicular ($B \perp c-$axis) orientations is much greater than in the case of $Y_{0.98}Yb_{0.02}Ba_2Cu_3O_x$ which indicates a larger degree of anisotropy of the local surroundings (CuO_2 planes) of the Yb^{3+}. On the other hand, the main peak of the spectrum of the perpendicular orientation is not split as was the case for $Y_{0.98}Yb_{0.02}Ba_2Cu_3O_x$ which means that the system is tetragonal, unlike the orthorombic $Y_{0.98}Yb_{0.02}Ba_2Cu_3O_{7-\delta}$. To my knowledge, there are no experimental reports on crystal-field splitting of Yb in $Sr_{0.9}La_{0.08}Yb_{0.02}CuO_2$; however, similar to a higher degree of g-factor anisotropy, the crystal-field splitting is also expected to be higher than in $Y_{0.98}Yb_{0.02}Ba_2Cu_3O_x$.

The line width of the Yb^{3+} EPR signal is determined from the spectra as described in Section 2.1. The technique is simple. First, one finds the residual line shape at low temperatures by measuring and integrating the EPR spectrum since the relaxation processes at low temperatures are negligible. Then, the high temperature spectra are fit by the convolution of this shape-function with a Lorentzian. The line width of the Lorentzian is the parameter which is proportional to the relaxation rate. Fig. 2.20 shows the spectrum with the perpendicular orientation that was used for calculating the shape function.

The result for the line width and relaxation time obtained in this way with the $B \perp$c-axis orientation is shown in Fig. 2.21(a) and Fig. 2.21(b). The relaxation rate (or line width) is well described by the equation

$$T_1^{-1} = A\frac{\exp(\Delta/T)}{(\exp(\Delta/T)-1)^2} + bT. \qquad (2.37)$$

The first term of this equation corresponds to the phononic part of the relaxation and the

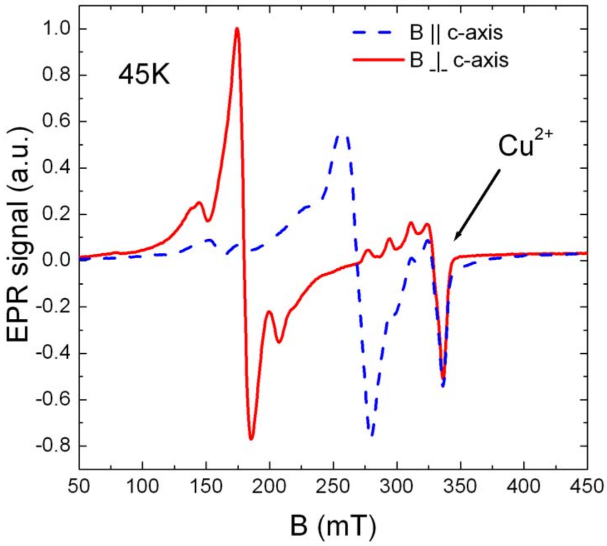

Figure 2.20: The EPR spectrum of $Sr_{0.9}La_{0.08}Yb_{0.02}CuO_2$ at 45 K as measured in the parallel and perpendicular orientations of the c-axis relative to applied field B . At these temperatures, the relaxation processes are weak and the line shape represents the so-called inhomogeneous broadening caused by a distribution of g-factors, dipolar interaction of neighboring Yb^{3+} ions, hyperfine splitting, ect.

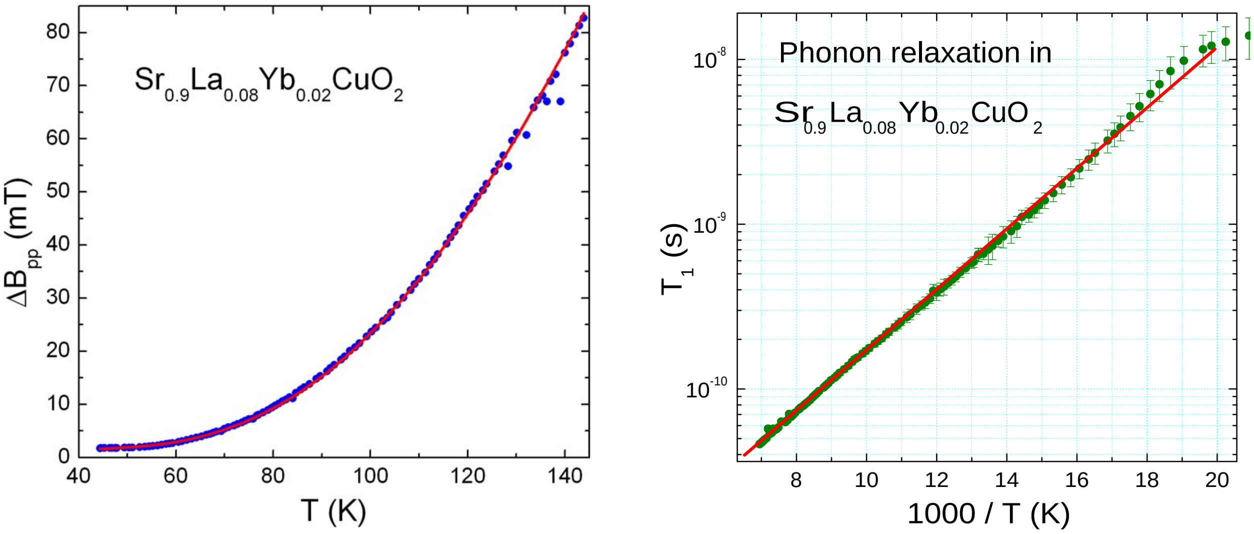

(a) The line width of the experimental EPR signal as a function of temperature. The red line is a fit to the data using Eq. (2.37).

(b) The phononic contribution to the spin-lattice relaxation time as a function of temperature. The linear dependence of lgT$_1$ vs 1/T indicates that the relaxation rate has an exponential character. The activation energy is $\Delta = 410(30)$ K.

Figure 2.21: ΔB_{pp} and T_1 for $Sr_{0.9}La_{0.08}Yb_{0.02}CuO_2$ as a function of temperature.

second one, linear in temperature, to the electronic (Korringa) relaxation. The fit result for Δ is 410(30) K which is close to that observed for $Y_{0.98}Yb_{0.02}Ba_2Cu_3O_x$ $\Delta = 500(50)$ K. As mentioned above, it is expected that the crystal-field splitting for the Yb^{3+} Γ^7 multiplet is as large as in $Y_{0.98}Yb_{0.02}Ba_2Cu_3O_x$ where the first excited state is about 1000 K above the ground-state doublet . Therefore, one can exclude the Orbach type of relaxation since crystal-field levels are not excited. The Debye temperature estimated from specific heat measurements of Ref. [96] is approximately $\Theta_D \simeq 250$ K (according to the relation $A = 12\pi^2 N_A k_B/5\Theta_D^3$, where N_A is Avogadro constant, k_B is Boltzmann constant and A is the coefficient of the phononic part to the specific heat). The fit to the relaxation using the Debye model gives $\Theta_D \simeq 550$ K which is substantially larger than the specific-heat result. Therefore, one can conclude that in this case, similar to that of $Y_{0.98}Yb_{0.02}Ba_2Cu_3O_x$, one has a relaxation of Yb^{3+} in a narrow band of phonons with an energy of 410(30) K close to that detected in $Y_{0.98}Yb_{0.02}Ba_2Cu_3O_x$. In contrast to $Y_{0.98}Yb_{0.02}Ba_2Cu_3O_x$, a very small reduction of the relaxation rate was detected below T_c. The electronic (Korringa) contribution to the relaxation rate for this material was found to be less than 0.01 mT/K. This result is more than a factor of 10 smaller than that of optimally doped $Y_{0.98}Yb_{0.02}Ba_2Cu_3O_{7-\delta}$ in agreement with the more than four times smaller value of the density of states at the Fermi level N_F observed in NMR (Korringa relaxation is proportional to N_F^2) [97]. Note that the superfluid density, in contrast to the density of states, is a factor of four larger than in $YBa_2Cu_3O_x$ or $La_{2-x}Sr_xCuO_4$ at the same T_c [98]. Therefore, one can say with good approximation that the relaxation mechanisms in this material are phononic at all temperatures above T_c.

2.5.4 Conclusions

The relaxation mechanisms of Yb^{3+} in $Sr_{0.9}La_{0.08}Yb_{0.02}CuO_2$ were investigated. The relaxation mechanisms are of phononic and electronic origin similar to that of $Y_{0.98}Yb_{0.02}Ba_2Cu_3O_x$. The electronic contribution to the relaxation is small and is less than 0.01 mT/K in agreement with a smaller density of states at the Fermi level in this material. Interestingly, this is in contrast to the 4 times larger superfluid density in the hole-doped cuprates at the same T_c. The phononic contribution is dominant and has an exponential character. It was found that, similar to the case of $Y_{0.98}Yb_{0.02}Ba_2Cu_3O_x$, the two-phonon Raman process involving phonons within a narrow band of energies near 410(30) K dominates the Yb^{3+} relaxation in $Sr_{0.9}La_{0.08}Yb_{0.02}CuO_2$. Similar to the case of $YBa_2Cu_3O_x$, the possible phonons inducing the relaxation of Yb^{3+} are either optical phonons or Jahn-Teller fluctuations of CuO_6 complexes.

2.6 Comparison of relaxation mechanisms of Yb^{3+} in $YBa_2Cu_3O_x$ and $Bi_2Sr_2CaCu_2O_8$

Investigation of relaxation mechanisms of rare earth (RE) elements in $YBa_2Cu_3O_x$ performed on Yb^{3+} revealed two components for the relaxation mechanism, namely, the electronic (Korringa) and the phononic components. The electronic one is doping dependent as expected and increases with increased carrier doping. The phononic part is dominated by phonons within a narrow energy range near 500 K. A schematic picture of the phonon distribution as a function of energy is shown in Fig. 2.6. It is interesting to check whether a similar picture of phonon distribution is observed for other cuprate superconductors and what are the electronic components of the relaxation. Recently, Urs Moselle [9] has performed such investigations. Similar to $YBa_2Cu_3O_x$. he doped Yb^{3+} into the Ca cite of the $Bi_2Sr_2CaCu_2O_8$. The Ca has approximately the same local symmetry as Y in $YBa_2Cu_3O_x$ and therefore, it is expected that Yb^{3+} will have a similar ground state and crystal-field splitting as observed in $Y_{0.98}Yb_{0.02}Ba_2Cu_3O_x$. It was found that Yb^{3+} in $Bi_2Sr_2CaCu_2O_8$ has very similar relaxation mechanisms as $YBa_2Cu_3O_x$. He found that there are two components of Yb^{3+} relaxation, the electronic and the phononic. The electronic component increases with the hole-doping and the phononic part displays an exponential behavior with an activation energy $\sim$480(50) K which is quite similar to that of $YBa_2Cu_3O_x$. Similarly, a decrease of the relaxation below T_c was observed indicating an electronic nature for this part of the relaxation.

This comparison allows one to conclude that the relaxation mechanisms of these two hole-doped families of cuprates are similar. The electronic component of relaxation has approximately the same order of magnitude and hole-doping dependence as in $YBa_2Cu_3O_x$. The planar phonons that are most active in the relaxation process of Yb^{3+} in $YBa_2Cu_3O_x$ are also active in $Bi_2Sr_2CaCu_2O_8$ and have approximately the same energy.

2.7 Line broadening and relaxation of Yb^{3+} in $La_{2-x}Sr_xCuO_4$

In the section 2.1, the relaxation mechanisms of Yb^{3+} in various HTS cuprate materials, such as $YBa_2Cu_3O_x$, $Bi_2Sr_2CaCu_2O_8$, and $Sr_{0.9}La_{0.08}Yb_{0.02}CuO_2$ were studied. Despite the fact that they belong to the different families, they have very similar relaxation mechanisms . The electronic component of relaxation was found to be completely different for the hole-doped cuprates $YBa_2Cu_3O_x$ and $Bi_2Sr_2CaCu_2O_8$ as compared with the electron doped $Sr_{0.9}La_{0.08}Yb_{0.02}CuO_2$. However, the temperature dependence of the Yb^{3+} relaxation rate for the phononic component of the relaxation was very similar in these materials. All three materials have a similar exponential increase of relaxation with an activation energy in the range of 450-500 K. This similarity is very interesting. In order to check the relaxation mechanisms and other interesting phenomena taking place in $La_{2-x}Sr_xCuO_4$, we decided to study this material again with the Yb^{3+} ion. Small amounts of Yb^{3+} can be isovalently substituted as La^{3+} into $La_{2-x}Sr_xCuO_4$ and thereby serve as an EPR probe.

For this study, the following four samples were prepared: $La_{1.89}Yb_{0.01}Sr_{0.1}CuO_4$, $La_{1.88}Yb_{0.02}Sr_{0.1}CuO_4$, $La_{1.98}Yb_{0.02}CuO_4$, and $La_{1.73}Yb_{0.02}Sr_{0.25}CuO_4$. The samples were prepared by the standard solid-state reaction starting from the oxides La_2O_3, Yb_2O_3, CuO and the carbonate $SrCO_3$. The starting reagents were mixed, calcinated at 900^{o}C, ground several times, pressed into pellets and then annealed at 1050^{o}C. The EPR spectra were measured using the standard X-band BRUKER EMX spectrometer equipped with the Oxfor-Instruments temperature controller and He-flow cryostat.

The narrowest and best spectrum was measured for the sample $La_{1.88}Yb_{0.02}Sr_{0.1}CuO_4$ which is shown in Fig. 2.22. The residual line width of Yb^{3+} EPR signal at low temperatures was large for all samples and could not be explained by dipolar interactions of the Yb^{3+} ions. Previous investigations of the local fields in La_2CuO_4 and Eu_2CuO_4 systems [99, 100] showed that the line broadening due to the internal magnetic fields of Gd^{3+} are of the order of 100-300 G which can not explain the minimal line width of 1500 G observed for Yb^{3+} . The spectroscopic-splitting factor of the line is $g = 2.15$ which is unusual for an Yb^{3+} signal. According to Ref. [5], the g-factor of Yb^{3+} can have two different values depending on the local crystal symmetry. They are $g = 3.43$ for the Γ^7 ground-state doublet observed typically in an eightfold coordinated systems and $g = 2.5$ for the Γ^6 ground-state doublet observed in the case of an octahedral coordination. The value observed in the present case is close to 2.5, characteristic of the octahedral coordination. Indeed, if the electrostatic field of the four nearest Yb^{3+} plain-oxygens in LSCO are represented/averaged by the one in their centrum, then the local coordination of Yb^{3+} will be octahederal (see Fig. 1). The cubic term of the crystal field (CF) usually has the strongest splitting and this splitting in the cubic approximation for rare earths has been investigated in detail by Lea *et al.* [101]. For Yb^{3+}, they showed that the qualitative dependence of the ground and excited states was a function of the single parameter characterizing the cubic CF. In a certain range of this parameter, there is a transition of the ground state from Γ^6 to Γ^7. It is known that a characteristic feature of cuprates is an intrinsic local inhomogeneity [3]. As a consequence, the CF felt by Yb^{3+} can also vary from site to site. If the CF parameters are close to the value where the transition from the Γ^7 to the Γ^6 ground state occurs, then one should include the parameter **D** in the spin Hamiltonian shown in Eq. (1.4). Since the parameter **D** is very sensitive to local inhomogeneities, this could be the reason for the strong broadening of the Yb^{3+} line at low temperatures. The samples with three different carrier dopings $x = 0$, 0.1 and 0.25 (Sr concentration) were prepared in an attempt to reduce the local inhomogeneities possibly related to the carriers. However, the experiment showed that for all cases, namely, the undoped, underdoped and overdoped materials, the width of the Yb^{3+} signal at low temperatures is large ($\simeq$ 2000 G) and only barely detectable. Whether the EPR signal of Yb^{3+} was actually detected was checked by employing the samples $La_{1.89}Yb_{0.01}Sr_{0.1}CuO_4$ and $La_{1.88}Yb_{0.02}Sr_{0.1}CuO_4$. It was found that with increasing Yb^{3+} concentration, the EPR signal was proportional to the increase, which indicated that the signal belonged to Yb^{3+} . The strongest and the narrowest signal was detected for the sample $La_{1.88}Yb_{0.02}Sr_{0.1}CuO_4$. The line width of only this sample will be considered in the following.

Fig. 2.22 shows the EPR signal detected at 55 K where it is narrowest. The spike near 330 mT is the Cu^{2+} signal which is always present in cuprate superconductors [45, 46, 47]. As is seen from the integrated EPR signal, the intensity of the Cu^{2+} signal is negligible. A single Lorentzian or a Gaussian fit did not describe the experimental data well, therefore, the signals were analyzed statistically. First the signal was integrated as shown in Fig. 2.22 and then various moments and the integral of the signals were determined. Fig. 2.23 shows the standard deviation of the signal as a function of temperature. The standard deviation is the quantity proportional to the width of the Gaussian line. The temperature dependence of the line width is weak and unusual. It is unclear whether it is due to relaxation processes or whether there are other processes influencing the EPR line width. Note that there are two kinds of relaxation processes having similar temperature dependence. The first was observed by Rettori *et al.* [102] in Pr_2CuO_4:Gd and Mehran *et al.* in other materials [103]. The relaxation mechanisms obtained in these references are explained either as being due to fluctuating magnetic fields in Gd^{3+} induced by the crystal-field transitions from the ground to the excited state of Pr or else to the Jahn-Teller effect induced dynamical random strains [103]. Another possibility for the observed Yb^{3+} broadening is its interaction with carriers. The spectrum of three-spin polarons was observed for the first time by Kochelaev *et al.* [104]. The temperature dependence of the line width of the three-spin polarons is very similar to that observed here. If one assume that Yb^{3+} relaxes due to the polarons, then both will have a similar temperature dependence.

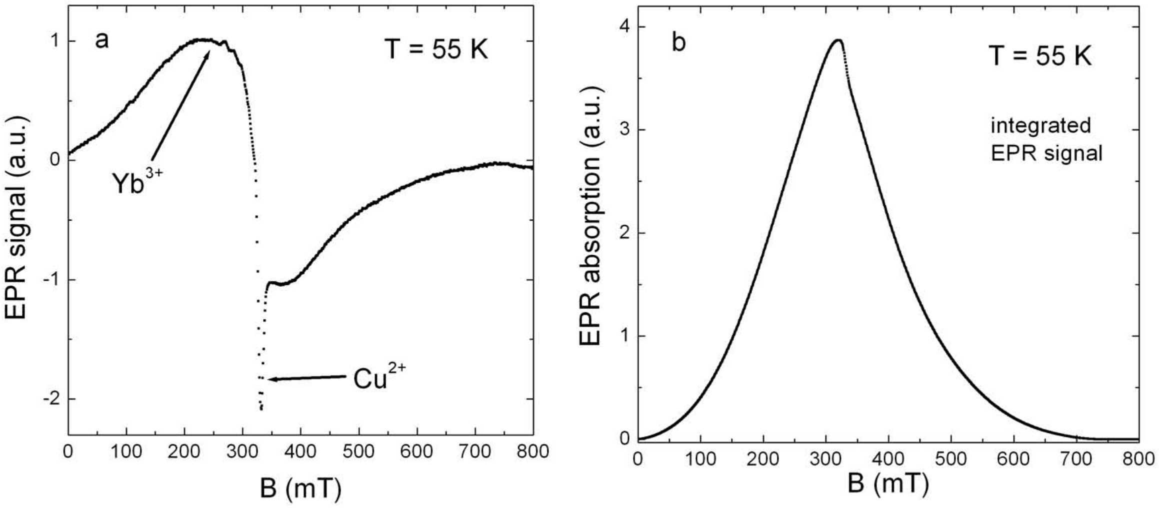

Figure 2.22: (a) EPR signal of Yb^{3+} in $La_{1.88}Yb_{0.02}Sr_{0.1}CuO_4$ at 55 K where the line width is minimal. A very broad inhomogeneous broadening is evident. (b) The EPR spectrum after integration.

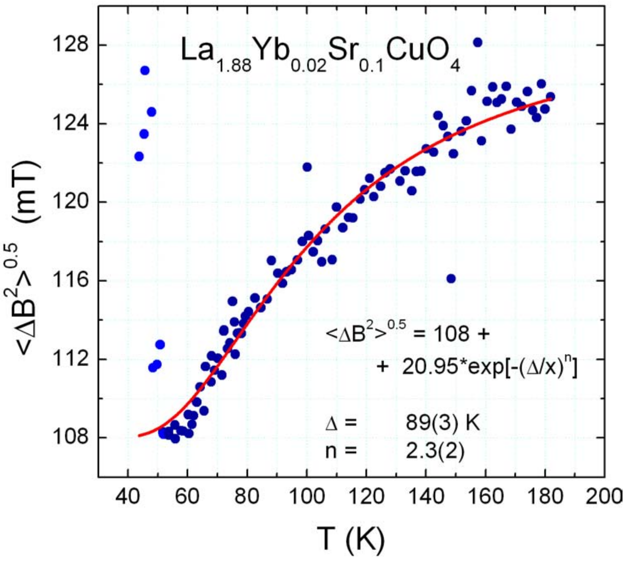

Figure 2.23: Temperature dependence of the standard deviation of the Yb^{3+} EPR signal in $La_{1.88}Yb_{0.02}Sr_{0.1}CuO_4$. The red line represents a fit using the phenomenological equation shown in the figure.

Chapter 3

Analysis methods of the field distribution in type-II superconductors

The muon-spin rotation (μSR) technique is one of the most powerful and unique tool used to study the internal magnetic field distribution $P(B)$ associated with the vortex lattice in type-II superconductors (see, e.g. Refs. [7, 8, 105]). In the vortex state for an applied magnetic field $H > H_{c1}$ or $0 < B$ (H_{c1} and B are the first critical field and the magnetic induction in a sample, respectively), the energy of the surface separating normal and superconducting fractions of the sample becomes negative and the field penetrates the sample in the form of quantized flux lines called vortices each containing an elementary flux quantum ($\Phi_0 = h/2e \simeq 2.0678 \cdot 10^{-15}$ Wb) [17]. In the case of small pinning, these vortices arrange themselves in a regular vortex lattice called a flux-line lattice (FLL) [17]. The distribution of the internal magnetic fields $P(B)$ inside the superconducting sample in the vortex state is uniquely determined by two characteristic lengths, the magnetic field penetration depth λ and the coherence length ξ.

The magnetic field penetration depth λ and the coherence length ξ are two of the most important parameters characterizing a superconductor. For a static magnetic field B applied parallel to a planar vacuum-to-superconducting interface, λ is defined as [106]:

$$\lambda = \frac{1}{B}\int_0^\infty B(r)dr, \tag{3.1}$$

where r is distance into the superconductor measured from the surface and $B(r)$ is a function describing the decay of the magnetic field into the superconducting region. According to the London theory, $1/\lambda^2$ is proportional to the superfluid density n_s of the superconductor as described by

$$\frac{1}{\lambda_i^2} = \frac{\mu_0 e^2 n_s}{m_i^*}, \tag{3.2}$$

where μ_0, e, and m_i^* are the magnetic permeability of vacuum, the elementary charge, and the effective mass of a Cooper pair, respectively. i denotes the x, y or z component of λ or m^*. By measuring the penetration depth as a function of temperature, isotope substitution, pressure, etc., one can obtain important information about the variation of the superfluid density as a function of these parameters. On the other hand, this information may provide constraints to the theory of superconductivity.

Another important parameter characterizing a superconducting state is the coherence length ξ. This parameter was first introduced in the Ginzburg-Landau theory of superconductivity as a measure of the spatial variation of the complex order parameter $\psi = Ae^{-\phi}$ describing the superconducting state. The superfluid density is expressed as $n_s = \psi\psi^*$. The Ginzburg-Landau, free-energy density in the superconducting state is expressed as follows [107]:

$$F_s \simeq F_n + \frac{1}{V}\int d\mathbf{r}^3 \left[\frac{1}{2m^*}|(i\hbar\nabla + e^*\mathbf{A})\psi|^2 + \frac{1}{2\mu_0}B^2(\mathbf{r}) - \mu_0\mathbf{H}(\mathbf{r})\cdot\mathbf{M}(\mathbf{r}) + \alpha(T)|\psi|^2 + \frac{\beta(T)}{2}|\psi|^4\right], \tag{3.3}$$

where F_n is the free energy of the system in the normal state. The first term in the square brackets corresponds to the kinetic energy of a Cooper pair in the magnetic field $\mathbf{B}(\mathbf{r})$ described by the vector potential $\mathbf{A}$ ($\mathbf{B} = [\nabla \times \mathbf{A}]$). The second and third terms describe the energies associated with the magnetic field $\mathbf{B}(\mathbf{r})$ and magnetization $\mathbf{M}$ of the superconductor. The forth and fifth terms are the energies corresponding to the order parameter. In order to have a superconducting transition, e.g. $F_s < F_n$ for a certain $|\psi|^2$, the temperature dependent parameter $\alpha(T)$ must be negative. To have a finite value of $|\psi|^2$ in the superconducting state, $\beta(T)$ must be positive. Minimization of the Ginzburg-Landau free energy for a given $\alpha(T)$ and $\beta(T)$ allows one to obtain the spatial variation of $\mathbf{B}(\mathbf{r})$ and $\psi(\mathbf{r})$. For a coherence length ξ characterizing the spatial variation of ψ, the theory predicts the following expression [106]:

$$\xi(T) = \frac{\hbar}{|2m^*\alpha(T)|^{1/2}}. \tag{3.4}$$

The microscopic BCS theory gives for the coherence length of a cooper pair [2]

$$\xi = \frac{\hbar v_F}{k_B T_c}, \tag{3.5}$$

where v_F, k_B, and T_c are the Fermi velocity, the Boltzmann constant, and the superconducting transition temperature, respectively. As was shown by Gor'kov [108], these two absolutely different ways of defining the coherence lengths coincide for clean superconductors at low temperatures ($\mathrm{T} \ll \mathrm{T}_c$).

The determination of λ and ξ are necessary for understanding the basic properties of superconductivity. As mentioned above, the internal magnetic field distribution $P(B)$ in a type-II superconductor in the vortex state is a function of λ and ξ. From μSR experiments, $P(B)$ profiles are obtained by performing a Fourier transformation of the μSR time spectra.

There are different approaches used to analyze the μSR time spectra. Uusally, the magnetic field penetration depth λ is determined from the second moment $\langle \Delta B^2 \rangle$ of the internal field distribution $P(B)$ [109, 110, 111, 112, 113, 114, 115]. For an isotropic extreme type-II superconductor ($\lambda \gg \xi$), it was shown that $\langle \Delta B^2 \rangle \propto \lambda^{-4}$ [116]. The more advanced approaches that allows one to obtain not only λ but also the coherence length ξ, require a theoretical model for the spatial variation of the internal magnetic field $B(\mathbf{r})$ ($\mathbf{r}$ is the spatial coordinate). An essential requirement of the model is that it must account for the finite size of the vortex cores. So far, the internal magnetic field distribution $P(B)$ measured by μSR was analyzed assuming analytical models for $B(\mathbf{r})$ based on the London and the Ginzburg-Landau (GL) theories.

The London and the GL models were widely applied to determine values of λ and ξ from the measured μSR time spectra taken in the mixed state of type-II superconductors [105, 117, 118, 119, 120, 121, 122, 123, 124, 125, 126, 127, 128, 129, 130, 131, 132]. We should emphasize, however, that despite the broad usage, the limits of validity of these models and the reliability of the parameters extracted from the fits are not discussed in detail in the literature. The main purpose of this thesis is to address these basic questions.

In order to study various methods of analysis of the μSR time spectra in type-II superconductors in the vortex state, a special program was developed in Matlab. Matlab provides a powerful basis for modelling and analysis of various scientific and technical problems. In addition, a program written in Matlab is independent of a platform that can be used with Linux, Windows, Mac, etc. without need of changes. Description of the program is given in

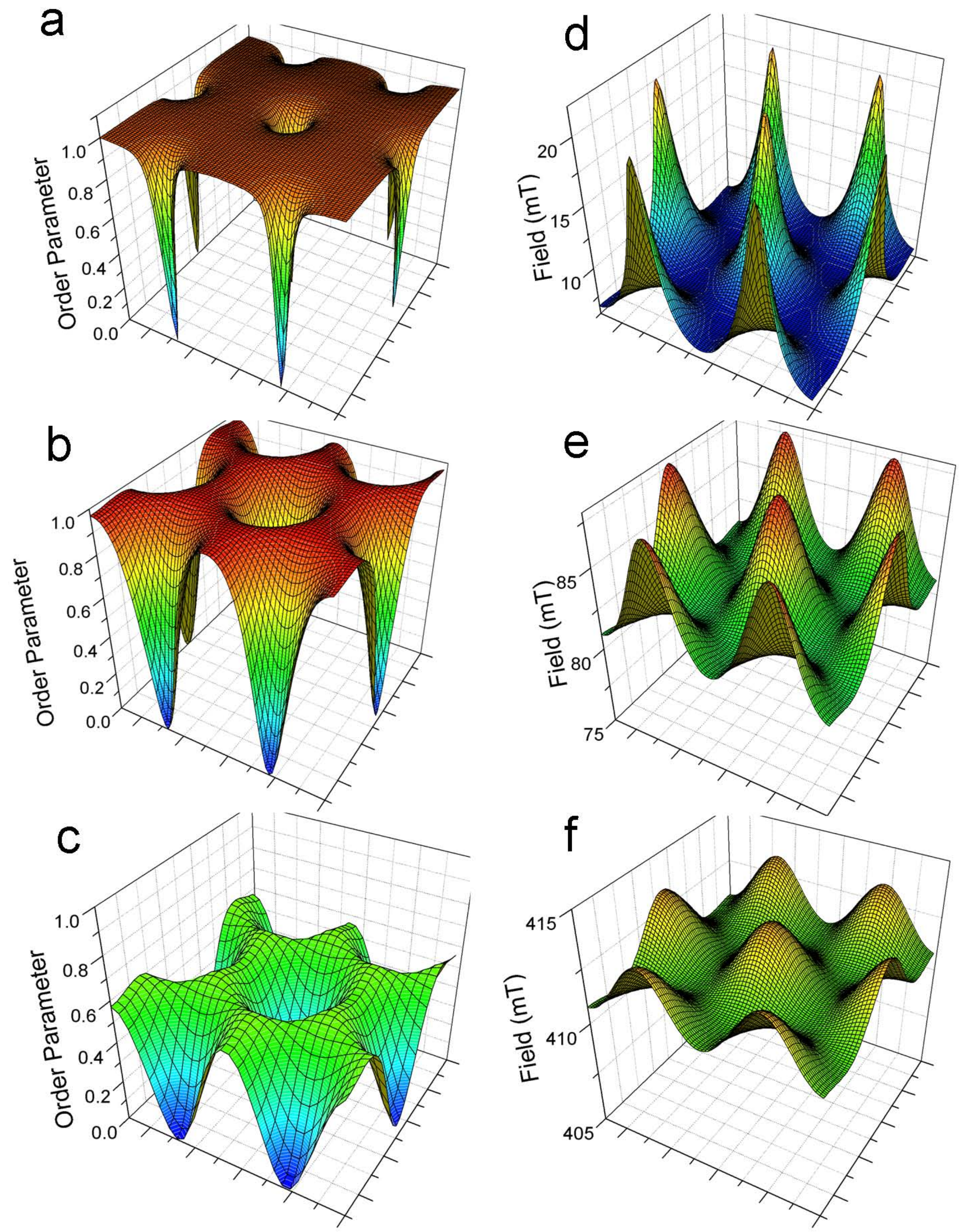

Figure 3.1: Examples of the spatial variation of the order parameter $\psi^*\psi$ (a-c) and the field (d-f) in a type-II superconductor calculated by the minimization of the Ginzburg-Landau free energy [cf. Eq. (3.3)] with the Matlab program developed in this project. The following parameters were used for the calculation: $\lambda = 200$ nm, $\xi = 20$ nm, and 3 different fields $0.01 \cdot B_{c2}$ (a,d), $0.1 \cdot B_{c2}$ (b,e), $0.5 \cdot B_{c2}$ (a,d). The second critical field $B_{c2} \simeq 822.83$ mT was employed.

the corresponding manual. Fig. 3.1 shows examples of the spatial distribution of the magnetic field and the order parameter $\psi^*\psi$ for a superconductor with $\lambda = 200$ nm , $\xi = 20$ nm, in different applied magnetic fields $B = 0.01 \cdot B_{c2}$, $0.1 \cdot B_{c2}$ and $0.5 \cdot B_{c2}$ ($B_{c2} \simeq 822.83$ mT) as calculated using this program (minimization of Ginzburg-Landau free-energy given by Eq. (3.3) was performed, as described in Ref. [133]).

3.1 Models for data analysis

As mentioned in the introduction, the simplest and the most widely used approach for analyzing μSR data is based on the relation between the magnetic penetration depth λ and the second moment $\langle \Delta B^2 \rangle$ of the internal field distribution $P_{id}(B)$ of the ideal FLL [116, 133, 134] as given by

$$\lambda^{-4} = C \cdot \langle \Delta B^2 \rangle. \tag{3.6}$$

Here, C is the proportionality coefficient depending on the value of the reduced magnetic field $b = \langle B \rangle / B_{c2}$ [$\langle B \rangle$ is the first moment of $P_{id}(B)$] and the Ginzburg-Landau parameter κ [116, 133, 134]. In order to estimate $\langle \Delta B^2 \rangle$, one often assumes that $P_{id}(B)$ is a sum of N Gaussian distributions (usually, $N = 1, 2, 3$) [135, 136]:

$$P_{id}(B) = \frac{\gamma_\mu}{\sqrt{2\pi}(A_1 + ... + A_N)} \sum_{i=1}^{N} (A_i/\sigma_i) \, \exp[(B - B_i)^2/2(\sigma_i/\gamma_\mu)^2] \,, \tag{3.7}$$

where A_i, B_i, and σ_i/γ_μ are the weight factor, the first moment, and the standard deviation of the $i-$th Gaussian component, respectively. $\gamma_\mu = 2\pi \times 135.5342$ MHz/T is the muon gyromagnetic ratio. The first and second moment of $P_{id}(B)$ are then readily obtained [135, 136] from

$$\langle B \rangle = \sum_{i=1}^{N} \frac{A_i \, B_i}{A_1 + ... + A_N} \,, \tag{3.8}$$

and

$$\langle \Delta B^2 \rangle = \sum_{i=1}^{N} \frac{A_i}{A_1 + ... + A_N} \left[(\sigma_i/\gamma_\mu)^2 + [B_i - \langle B \rangle]^2 \right] \,. \tag{3.9}$$

With modern computers, it became possible to develop models that allow the calculation of $P_{id}(B)$ for a FLL as a function of various parameters such as magnetic penetration depth, coherence length, applied magnetic field, and FLL geometry (rectangular or hexagonal) [105, 117, 133, 137]. The London models (with different cut-off factors) provide the simplest and fastest way to calculate $P_{id}(B)$ for the analysis of μSR data for $\kappa \gg 1$ [105]. Better approximations of $P_{id}(B)$ for small values of κ and fields closer to B_{c2} can be obtained by the analytic Gingburg-Landau (AGL) model [118, 138]. Strictly speaking, the Ginzburg-Landau theory is only valid in the neighborhood of $T_c(B)$ of the phase diagram of a type-II superconductor. However, it is generally assumed that the Ginzburg-Landau models are also good approximations for any field and temperature. The results obtained by the numerical Ginzburg-Landau (NGL) model correspond to the minimum of the Ginzburg-Landau free energy, whereas other models described in this thesis are approximations to the NGL model. Therefore, the NGL model will be used as a reference for comparison with the AGL model, the modified London (ML) model and the London model with Gaussian cut off (LG). A relatively simple method to calculate $P_{id}(B)$ within the framework of the NGL model was proposed by Brandt [133, 139].

In the LG, ML, AGL, and NGL approximation, the spatial distribution of the magnetic field in the mixed state of a type-II superconductor is described by the Fourier expansion given by

$$B(\mathbf{r}) = \langle B \rangle \sum_{\mathbf{G}} \exp(-i\mathbf{G}\mathbf{r})\, B_{\mathbf{G}}(\lambda, \xi)\,. \tag{3.10}$$

Here, $\mathbf{r}$ is the vector coordinate in a plane perpendicular to the applied field. The origin of the coordinate system is in the center of a vortex core (see, e.g. Ref. [130]), $\mathbf{G} = 4\pi/\sqrt{3}a(m\sqrt{3}/2, n + m/2)$ are the reciprocal lattice vectors for the hexagonal FLL, a is intervortex distance, $B_{\mathbf{G}}$ are the Fourier components and m, n are integer numbers.
For the LG model, the Fourier components $B_{\mathbf{G}}$ are [105, 137]

$$B_{\mathbf{G}} = \frac{e^{-\xi^2 G^2/2}}{1 + G^2\lambda^2}\,. \tag{3.11}$$

For the ML model, the Fourier components $B_{\mathbf{G}}$ are given by [105, 117]

$$B_{\mathbf{G}} = \frac{e^{-\xi^2 G^2/2(1-b)}}{1 + G^2\lambda^2/(1-b)}, \tag{3.12}$$

For the AGL model, the Fourier components $B_{\mathbf{G}}$ are [118, 138]

$$B_{\mathbf{G}} = \frac{\Phi_0}{S} \frac{f_\infty K_1[\frac{\xi_v}{\lambda}(f_\infty^2 + \lambda^2 G^2)^{1/2}]}{(f_\infty^2 + \lambda^2 G^2)^{1/2} K_1(\frac{\xi_v}{\lambda} f_\infty)}, \tag{3.13}$$

where $f_\infty = 1 - b^4$, and

$$\xi_v = \xi(\sqrt{2} - \frac{0.75}{\kappa})(1 + b^4)^{1/2}[1 - 2b(1 - b)^2]^{1/2}.$$

Here, $K_1(x)$ is the modified Bessel function. For applied magnetic fields $H \gg H_{c1}$, the relation $\mu_0 H \simeq \langle B \rangle$ holds [139]. Finally, for the NGL model, no analytical solution for the Fourier components $B_{\mathbf{G}}$ exists. They are determined numerically [133, 139].

From the known spatial distribution of the magnetic field $B(\mathbf{r})$ in the mixed state, one can extract the internal magnetic field distribution $P_{id}(B)$ for an ideal FLL by means of the following equation:

$$P_{id}(B) = \frac{\int \delta(B - B')dA(B')}{\int dA(B')} \tag{3.14}$$

where $dA(B')$ is the elementary area of the FLL with a field B' inside it and the integration is over a quarter of the FLL unit cell [130]. In order to take into account possible random deviations of the flux-core positions from their ideal ones (vortex disorder) and/or possible

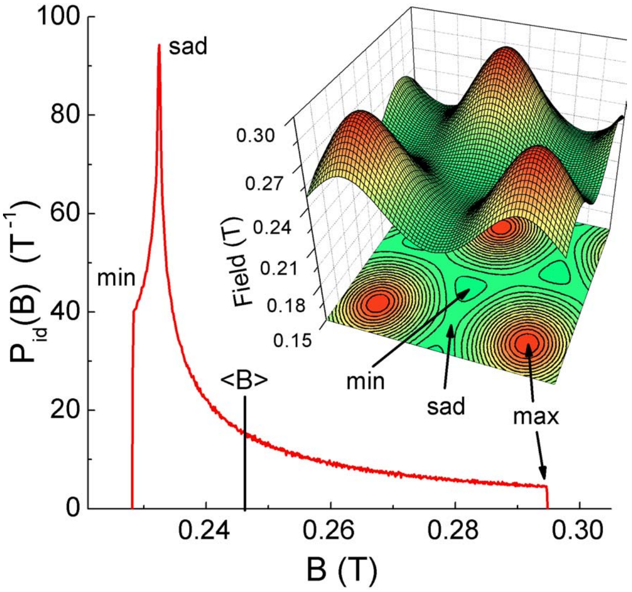

Figure 3.2: Example of a spatial distribution of the magnetic field $B(\mathbf{r})$ and the corresponding local magnetic field distribution $P_{id}(B)$ for an ideal hexagonal FLL determined by the NGL method. The parameters used for the calculations are $\lambda = 50$ nm, $\xi = 20$ nm, $\langle B\rangle = 0.3B_{c2} \simeq 246.8$ mT, and an intervortex distance $a = 69.5$ nm.

broadening of the μSR spectra due to nuclear depolarization, one may convolute the ideal distribution $P_{id}(B)$ with a Gaussian distribution [137]

$$P(B) = \frac{1}{\sqrt{2\pi}\sigma_g} \int P_{id}(B') \exp\left[-\frac{1}{2}\left(\frac{B-B'}{\sigma_g}\right)^2\right] dB' \tag{3.15}$$

where σ_g is the width of the Gaussian distribution. The relation between σ_g, vortex disorder, and nuclear depolarization is described in Sec. 3.2.1.

The μSR time spectra can be further simulated by performing a fourier transform of $P(B)$ convoluted with the Gaussian function given in Eq. (3.15) giving

$$\tilde{P}(t) = Ae^{i\phi} \int P(B) e^{i\gamma_\mu B t} dB\,, \tag{3.16}$$

where A and ϕ are the initial asymmetry and the phase of the μSR time spectra, respectively. For the calculations of the spatial magnetic field distribution $B(\mathbf{r})$ in the FLL, 31×31 Fourier components of the magnetic field and the reciprocal vector $\mathbf{G}$ were used. This allows one to calculate the second moment of $P(B)$ with a precision of better than 10^{-6}. The integral in Eq. (3.14) was calculated numerically over a quarter of the FLL unit cell divided into approximately 100x100 equal pixels depending on the mean magnetic field $\langle B\rangle$ (see Fig. 1 of Ref. [130]).

Equations (3.10 - 3.13) are only valid for isotropic superconductors or superconductors with axial symmetry with the external magnetic field applied along the symmetry axis. In the present study, we concentrate principally on the case of extreme type-II superconductors

($\kappa \gg 1$) such as the cuprate high-temperature superconductors. Since the qualitative behavior of $P_{id}(B)$ as a function of various parameters is essentially the same for a hexagonal and a square FFL, we will consider here only the hexagonal case.

In Fig. 3.2, we plot the spatial distribution of the magnetic field $B(\mathbf{r})$ in the mixed state and the corresponding local magnetic field distribution $P_{id}(B)$ for $\lambda = 50$ nm, $\xi = 20$ nm, and $\langle B \rangle = 0.3B_{c2} \simeq 246.8$ mT as determined by the NGL model. The ideal FLL has three characteristic fields, namely, (i) the maximal field B_{max} corresponding to the field in the vortex core, (ii) the field at the peak of $P_{id}(B)$ which is the saddle point field B_{sad} (located midway between neighboring vortices), and (iii) the minimal field B_{min} which is in the center of the triangle of vortices forming the hexagonal FLL [140]. Instead of the full local magnetic field distribution $P_{id}(B)$, we will use these characteristic fields to discuss the dependence of the shape of $P_{id}(B)$ on different parameters.

3.2 Summary of the analysis of μSR line shapes in the vortex state of type-II superconductors

The magnetic penetration depth λ has often been measured by our group in order to determine fundamental properties of superconductors. The basic experimental method for measurements of the λ in the bulk of a superconductor is the muon spin-rotation (μSR) technique. The μSR time spectra are measured in the vortex state of the superconductor and by Fourier transformation of the spectra, one can directly obtain the internal magnetic field distribution $P(B)$. In general, $P(B)$ depends on λ, ξ, the mean internal field $\langle B \rangle$, and the Gaussian smearing σ_g.

As described above, there are different methods for modelling $P(B)$ and for extracting the values of λ, ξ, $\langle B \rangle$, and σ_g. The theoretical background for these models is well established and described in Refs. [116, 118, 137, 138]. However, how these models work in practice, and the reliability of the extracted parameters λ and ξ is still an open question. Therefore, it is important to study these models in more detail. To do this (i) first, the dependence of $P(B)$ for an ideal FLL on the various parameters was studied, (ii) then, various models of analysis were compared with each other and (iii) finally, these models were investigated in "virtual experiments" on simulated μSR spectra for which the results were obtained and analyzed.

3.2.1 Dependence of $P(B)$ on λ, ξ, $\langle B \rangle$, and σ_g

In order to analyze $P(B)$ as a function of λ, ξ, $\langle B \rangle$, and σ_g, it is convenient to work with the differences between the characteristic fields and the mean field $\langle B \rangle$ (see Fig. 3.2) instead of the entire $P(B)$ curve. These differences are defined as follows:

$$\delta B_{min} = B_{min} - \langle B \rangle, \tag{3.17}$$

$$\delta B_{sad} = B_{sad} - \langle B \rangle, \tag{3.18}$$

$$\delta B_{max} = B_{max} - \langle B \rangle. \tag{3.19}$$

Later on these differences will be called characteristic fields.

Dependence of $P(B)$ on λ, ξ, and $\langle B \rangle$

As is shown by Brandt [133], the internal magnetic field distribution $P_{id}(B)$ of the ideal FLL depends on the reduced field $b = \langle B \rangle / B_{c2}$ (B_{c2} is the second critical field) and the Ginzburg-Landau parameter $\kappa = \lambda/\xi$. Fig. 3.3 shows the most general dependence of the characteristic fields δB_α ($\alpha =$ min, sad, max) of $P_{id}(B)$ as a function of λ, ξ, and $\langle B \rangle$. On the y-axis are given the characteristic fields δB_α normalized to $\Phi_0/4\pi\lambda^2$. That means that the characteristic fields depend on λ as $1/\lambda^2$, and therefore strongly depend on λ. On the x-axis is given the reduced field $b = \langle B \rangle / B_{c2} = 2\pi \langle B \rangle \xi^2/\Phi_0$ (Φ_0 is the flux quantum). Therefore, in the limit of $\kappa \to \infty$, the dependence of the characteristic fields on $\langle B \rangle$ and ξ^2 is identical (see Fig. 3.3). However, in the case of finite κ, there is a difference in their dependence. For fixed λ and ξ, when $\langle B \rangle \to 0$ and therefore $b \to 0$, then $\delta B_\alpha = [B_\alpha - \langle B \rangle] \to 0$, since $0 < B_\alpha < \langle B \rangle$ ($\alpha =$ min, sad). However, for fixed values of λ and $\langle B \rangle$ and at high enough κ, the reduction of $\xi \to 0$ will cause only the reduction of the vortex-core size ($\kappa \to \infty$, $B_{c2} \to \infty$). In this case, δB_α ($\alpha =$ min, sad) will saturate at a finite value as for the case of $\kappa = \infty$ (provided $\langle B \rangle > |\delta B_{min}|$, e.g. $\langle B \rangle$ is not extremely small) and $P(B)$ is practically independent of ξ. Note that the region between δB_{min} and 0 is most important, because the high field tail at δB_{max} is usually below the noise level of experimental μSR spectra and is generally not observed, especially at low fields and for $\kappa \gg 1$ (see Fig. 3.2). The saturation of the characteristic fields below a certain value of b in Fig. 3.3 implies that there is a certain value of $\langle B \rangle$ below which the μSR spectra are *independent* of ξ. For cuprate superconductors, for instance, with typical values of $\xi = 2 - 3$ nm, this critical field is $B_{appl.} \simeq \langle B \rangle \simeq 300$ mT.

Dependence of $P(B)$ on σ_g

In order to take into account the influence of vortex disorder and nuclear broadening, the ideal internal field distribution $P_{id}(B)$ is convoluted with a Gaussian distribution of width [see Eq. (3.15)] [117, 137] given by

$$\sigma_g = \sqrt{\sigma_{VD}^2 + \sigma_N^2}, \tag{3.20}$$

where σ_{VD} and σ_N are the contributions to the Gaussian broadening of $P_{id}(B)$ due to vortex disorder and nuclear depolarization, respectively. The vortex disorder is described by the standard deviation of the vortex-core positions from that of the ideal FLL $\langle s^2 \rangle^{1/2}$ and $\sigma_{VD} \propto \langle s^2 \rangle^{1/2}$.

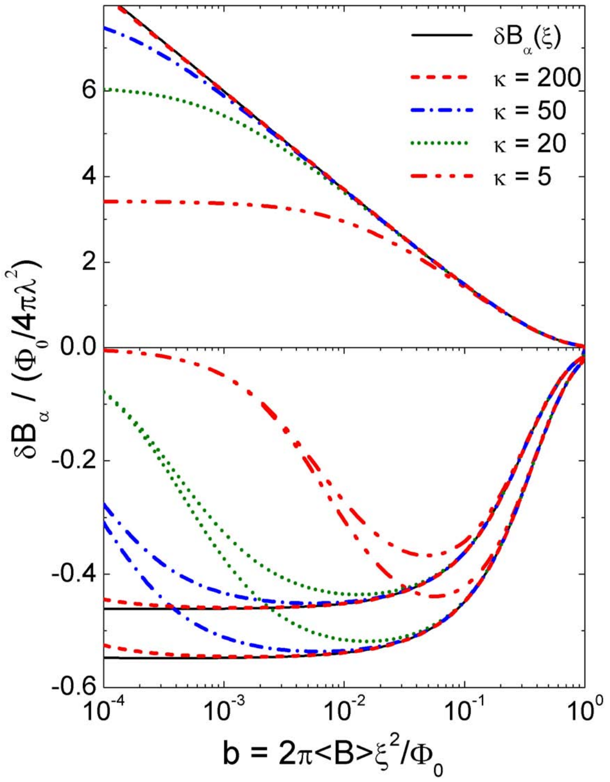

Figure 3.3: Characteristic fields δB_α (α = min, sad, max) calculated by the LG model as a function of the reduced field b (dashed, dotted, and dash-dotted lines) for different values of κ.

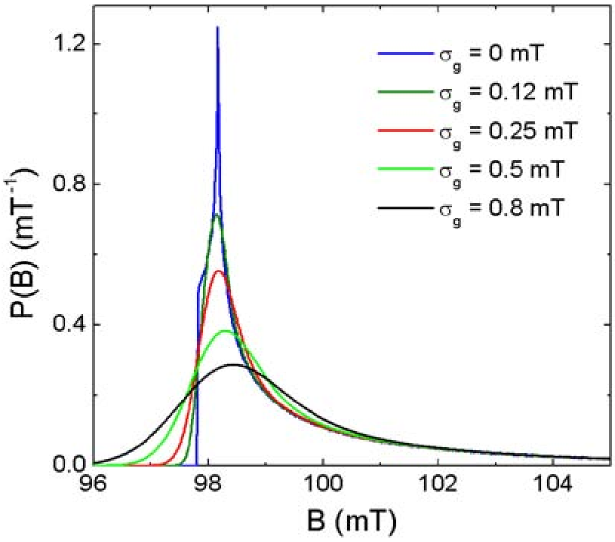

Figure 3.4: Change of the local magnetic field distribution $P_{id}(B)$ for an ideal FLL after convolution with a Gaussian distribution of various widths σ_g. The following parameters were used to generate $P_{id}(B)$ with the LG model: $\lambda = 200$ nm, $\xi = 4$ nm, and $\langle B\rangle = 100$ mT.

Figure 3.4 shows examples of $P(B)$ for $\lambda = 200$ nm, $\xi = 4$ nm, $\langle B\rangle = 100$ mT, and for various values of σ_g calculated by means of the LG model. It is obvious that with an

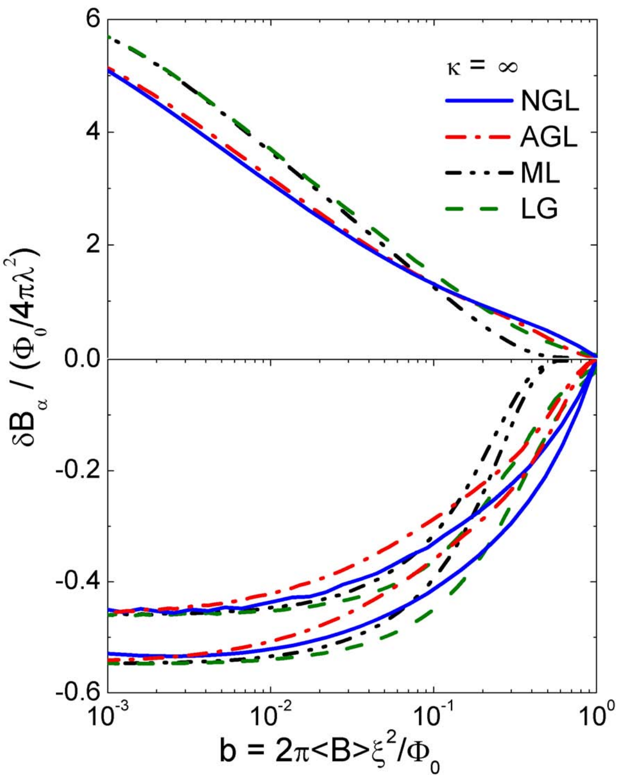

Figure 3.5: Characteristic fields δB_α (α = min, sad, max) as a function of the reduced field $b = 2\pi\langle B\rangle\xi^2/\Phi_0$ for $\kappa = \infty$, as calculated by the LG, ML, AGL, and NGL models.

increasing degree of disorder, the Van Hoove singularities in the ideal internal field distribution $P_{id}(B)$ are smeared out. Note that the low-field part of $P_{id}(B)$ is mainly truncated by the Gaussian smearing, whereas the high-field tail is nearly not affected.

3.2.2 Comparison of different models with the NGL model

In Sec. 3.2.1, it was shown that the characteristic fields δB_α for $\kappa \gg 1$ may be represented by single curves (see Fig. 3.3). Figure 3.5 shows the characteristic fields δB_α as a function of the reduced magnetic field $b = \langle B\rangle/B_{c2}$ in the limit of $\kappa \to \infty$ as calculated by the LG, ML, AGL, and NGL models. For small b values, $\delta B_{min}(b)$ and $\delta B_{sad}(b)$ coincide for all models. The AGL and LG models systematically deviate from the NGL model above $b \approx 0.01$. Of all the models, the ML model approximates best the NGL model up to about $b \simeq 0.1$. However, at higher fields, this model deviates substantially from the NGL model and cannot be used for analysis.

3.2.3 Simulation and fitting of μSR spectra

In order to check the reliability of fit results ”experimentally”, μSR time spectra with known parameters ($\langle B\rangle$, λ, ξ, σ_g) were simulated using the LG and the NGL models describing the internal magnetic field distribution $P(B)$. A typical example of a μSR time spectrum simulated by means of the NGL model is shown in Fig. 3.6.

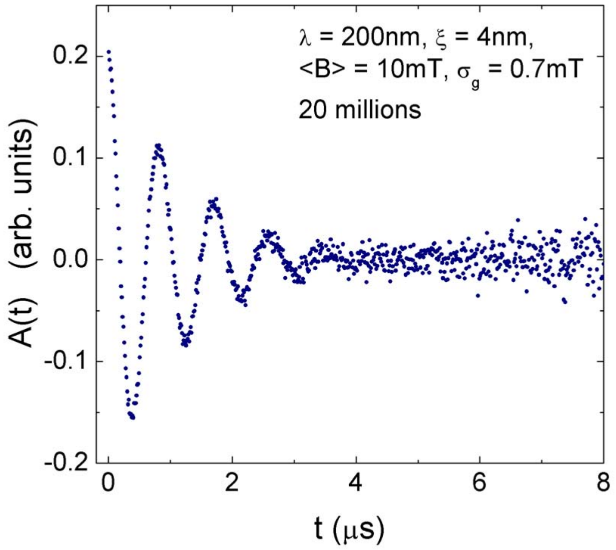

Figure 3.6: μSR time spectrum (20 million events) calculated by the NGL model for $\lambda =$ 200 nm, $\xi = 4$ nm, $\langle B \rangle = 10$ mT, and $\sigma_g = 0.7$ mT.

The simulated μSR time spectra were then analyzed as follows:
(1) The μSR spectra simulated by the NGL model were analyzed by the second-moment (SM) method.
(2) The μSR spectra simulated by the LG model were analyzed by a fitting procedure based on the LG model.

According to the discussions made in the previous section, the following important questions should be answered:
(1) How reliable is the second moment obtained by a multi-Gaussian fit of the μSR spectra (see Eq. (3.21)) and the penetration depth λ extracted from the second moment?
(2) Is there a correlation between σ_g and $1/\lambda^2$, since both influence the second moment of the μSR spectrum?
(3) Is it possible to extract reliable values of ξ from μSR spectra at low magnetic fields $b \simeq 10^{-3}$?
(4) Is there a correlation between λ and ξ at high fields, since for $b \approx 0.1 - 0.9$, both parameters strongly influence the characteristic fields δB_α?

3.2.4 Test of the second-moment method

In this section, the second-moment (SM) method is tested by analyzing μSR time spectra simulated with the NGL model employing well defined parameters ($\langle B \rangle$, λ, ξ, σ_g). Within the framework of this method, the μSR time spectra were usually fit to a sum of N Gaussian components [135, 136] of the form

$$P(t) = \sum_{i=1}^{N} A_i \exp(-\sigma_i^2 t^2/2) \cos(\gamma_\mu B_i t + \phi). \tag{3.21}$$

Here, ϕ is the initial phase of the muon beam, and A_i, σ_i, and B_i are the asymmetry, the relaxation rate and the first moment of the $i-$th Gaussian component, respectively. From the fit parameters A_i, σ_i and B_i, one readily obtains the first and the second moments of $P(B)$, and from the known second moment one finds the penetration depth λ.

In order to investigate this question, μSR time spectra were simulated by the NGL model for an extreme type-II superconductor (such as the cuprate superconductors) with a Ginzburg-Landau parameter $\kappa = 50 \gg 1$. The temperature dependence of λ was assumed to follow the relation (two-fluid model), namely, $\lambda(T)^{-2}/\lambda(0)^{-2} = [1-(T/T_c)^4]$ with $T_c = 22.5$ K and $\lambda(0) = 200$ nm (zero-temperature penetration depth). According to Eq. (3.20), σ_g is composed of two components, $\sigma_g = (\sigma_N^2 + \sigma_{VD}^2)^{1/2}$, where σ_N is the temperature independent smearing due to nuclear depolarization, and $\sigma_{VD} = \beta/\lambda^2$ denotes the temperature dependent smearing due to vortex disorder. The simulations were performed for three different magnetic fields $\langle B\rangle = 50$ mT, 0.5T, and 5 T [141]. For the technical parameters, the following typical values were used: $20 \cdot 10^6$ events, asymmetry $A = 0.2$, and phase $\phi = 0$.

The total second moment $\langle \Delta B^2\rangle_t$ of a μSR spectrum with Gaussian smearing σ_g obtained by a multi-Gaussian fit contains three components as shown in

$$\langle \Delta B^2\rangle_t = \langle \Delta B^2\rangle + \sigma_{VD}^2 + \sigma_N^2, \tag{3.22}$$

where $\langle \Delta B^2\rangle$, σ_{VD}^2, and σ_N^2 are the second moments due to the internal field variation in the ideal FLL, the vortex disorder, and the nuclear depolarization, respectively. In order to obtain λ from the total second moment measured in real experiments, one determines σ_N above T_c and assumes that $\sigma_{VD}^2 \ll \langle \Delta B^2\rangle$ in Eq. (3.22), i.e. $\langle \Delta B^2\rangle_t \simeq \langle \Delta B^2\rangle + \sigma_N^2$ [142]. From the first and second moments of the individual Gaussians, one can calculate the total second moment $\langle \Delta B^2\rangle_t$ of the μSR spectrum using Eq. (3.9) (Note that in Eq. (3.9), the Gaussian smearing σ_g was not introduced , therefore, $\langle \Delta B^2\rangle$ of Eq. (3.9) is $\langle \Delta B^2\rangle_t$). One then determines $\langle \Delta B^2\rangle$ using Eq. (3.22). Finally, with Eq. (3.6), the magnetic penetration depth λ can readily be obtained.

Figure 3.7 shows the results for the penetration depth obtained by the second-moment method with $N =$ 1, 2, 3, 4 Gaussians. Note that a single Gaussian does not give reliable results; this is in agreement with earlier findings [135]. However, with increasing number of Gaussians N, the quality of the fits substantially improves. In order to fit the simulated data at 50 mT, at least 3 or better 4 Gaussians are required. For $N = 3$, there is a systematic deviation of about 10% of λ^{-2} from the real value (or 5% for λ), whereas for $N = 4$ the values of λ^{-2} are scattered by only a few percent about the real ones. For the data simulated at 0.5 T, even $N = 3$ Gaussians are sufficient to describe the local magnetic field distribution $P(B)$, and the values of λ^{-2} are systematically shifted by only a few percent. Fig. 3.8(a) shows an example of a real internal field distribution $P(B)$ ($\langle B\rangle = 0.5$ T, $T = 1$ K of Fig. 3.7) and the reconstructed $P(B)$ obtained from the analysis of the simulated μSR spectrum ($2{\times}10^7$ events) using a Gaussian fit with $N = 3$. It is obvious that three Gaussians describe the shape of the real $P(B)$ well. The largest systematic error in λ^{-2}, obtained by a multi-Gaussian fit, is observed at 5 T ($b = 0.24$). At such a high field ($\langle B\rangle \simeq B_{c2}/4$), the variation of the internal field is relatively small (see Fig. 3.5), and the Gaussian smearing

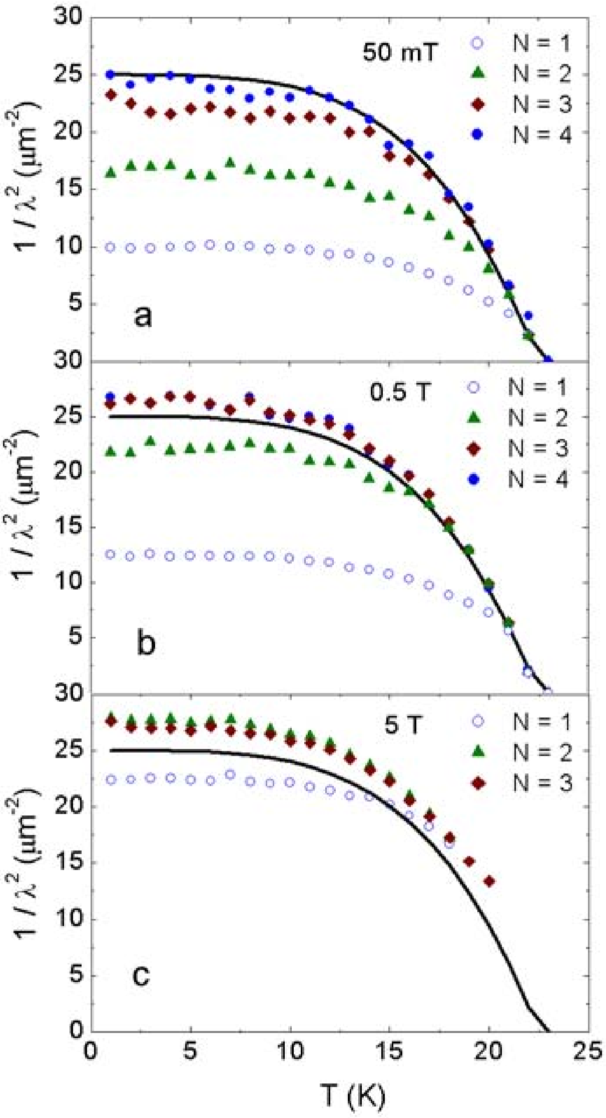

Figure 3.7: Fit results for λ^{-2} obtained by the second-moment method. The noisy spectra for the three different fields of 50 mT, 0.5, and 5 T were simulated by the NGL method as described in the text and then analyzed by a multi-Gaussian function with various numbers of Gaussians ($N = 1, 2, 3, 4$) as defined in Eq. (3.21). The black solid lines correspond to the real values of λ^{-2} used for the simulation.

σ_{VD} [cf. Eq. (3.22)] due to vortex disorder becomes essential. The second moment of this Gaussian smearing cannot be neglected and contributes considerably to the total second moment $\langle \Delta B^2 \rangle_t$ of $P(B)$. This leads to systematically higher values of λ^{-2} obtained by multi-Gaussian fits at high magnetic fields. Note, however, that there are two reasons why the contribution to the second moment due to vortex disorder is reduced with increasing magnetic field and consequently the systematic error in λ^{-2}. They are (1) at high fields $\sigma_{VD} \propto (1 - b)$, which was actually taken into account in the simulations of the μSR spectra and (2) vortex disorder is expected to decrease with increasing magnetic field, due to the strong repulsive interaction between the vortices at high fields (see e.g. Fig. 2 of Ref. [133]).

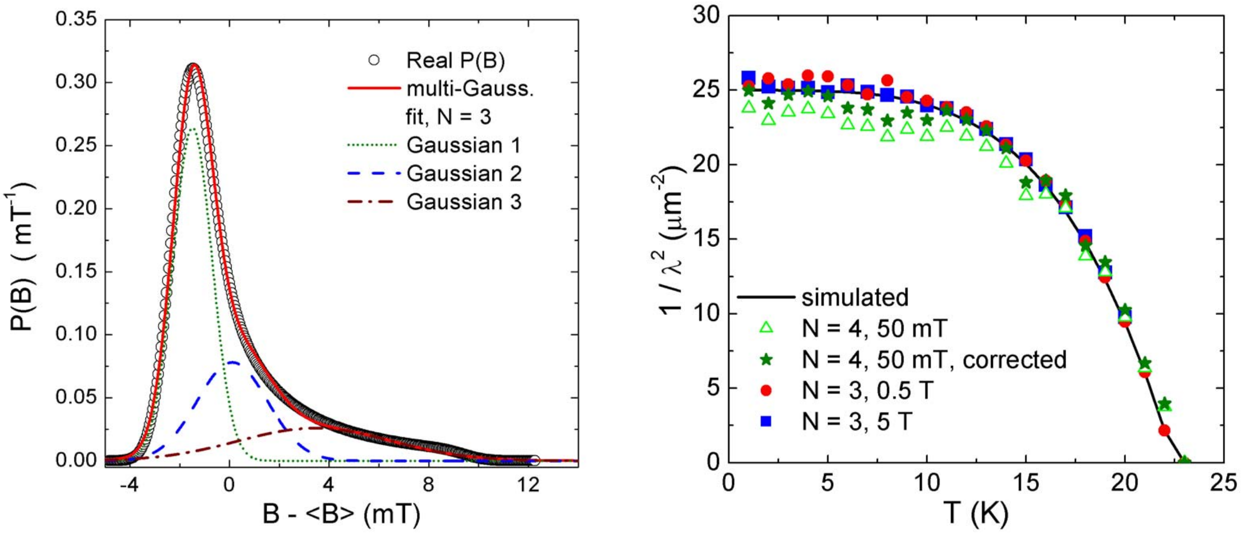

(a) Comparison of the real field distribution $P(B)$ (empty circles) simulated with the NGL model for parameters $\lambda = 200$ nm, $\xi = 4$ nm, $\langle B\rangle = 0.5$ T, $\sigma_g = 0.7$ mT (point at 1 K, $N = 3$ in Fig. 3.7b) with $P(B)$ obtained by a Gaussian fit with $N = 3$ (red line). The dotted, dashed, and dash-dotted lines represent individual Gaussian components used for the fit. It is obvious that a multi-Gaussian fit may well describe the real $P(B)$.

(b) Temperature dependence of $1/\lambda^2$ determined from $\langle \Delta B^2\rangle$, assuming that σ_{VD} is known as described in the text. Triangles: $N = 4$, 50 mT; stars: $N = 4$, 50 mT, corrected for finite $\kappa = 50$ (see text for explanation); circles: $N = 3$, 0.5 T; squares: $N = 3$, 5 T.

Figure 3.8: Fit by three Gaussians (a) and correction of $1/\lambda^2$ for σ_{VD} (b).

By means of a multi-Gaussian fit, it is not possible to separate $\langle \Delta B^2\rangle$ and σ_{VD} from the measured total second moment $\langle \Delta B^2\rangle_t$ [cf. Eq. (3.22)]. Assuming that $\sigma_{VD} = 0$ yields a lower limit for λ (upper limit for $1/\lambda^2$), as clearly demonstrated in Figs. 3.7(b) and 3.7(c) where the values of $1/\lambda^2$ are systematically too large. It is interesting to investigate what are the values of $1/\lambda^2$ are after correction with the real value of σ_{VD}. Fig. 3.8(b) shows some of the results of Fig. 3.7 after this correction. The corrected values of $1/\lambda^2$ are in good agreement with the real values (solid line in Fig. 3.8(b)), except for the data at 50 mT where a systematic deviation of about 5-10% is observed. One of the reasons for this deviation is that $\kappa = 50$ used in the simulations is not infinite. This implies that at 50 mT ($b \simeq 0.0024$) the parameter $C^{-1/2}$ in Eqs. (3.6) is about 5% smaller [133]. The stars in Fig. 3.8(b) represent the corrected values of $1/\lambda^2$ at 50 mT which are only about 3% systematically lower than the real values.

3.2.5 Test of the London model with Gaussian cut off (LG)

In order to test the reliability of the advanced methods described in Sec. 3.1, noisy μSR spectra were first simulated and then fit in a similar way to that used in the second-moment method. To avoid systematic errors in the fit results, it is important to analyze the data with the same model as used in the simulation. For these tests, the LG model was chosen,

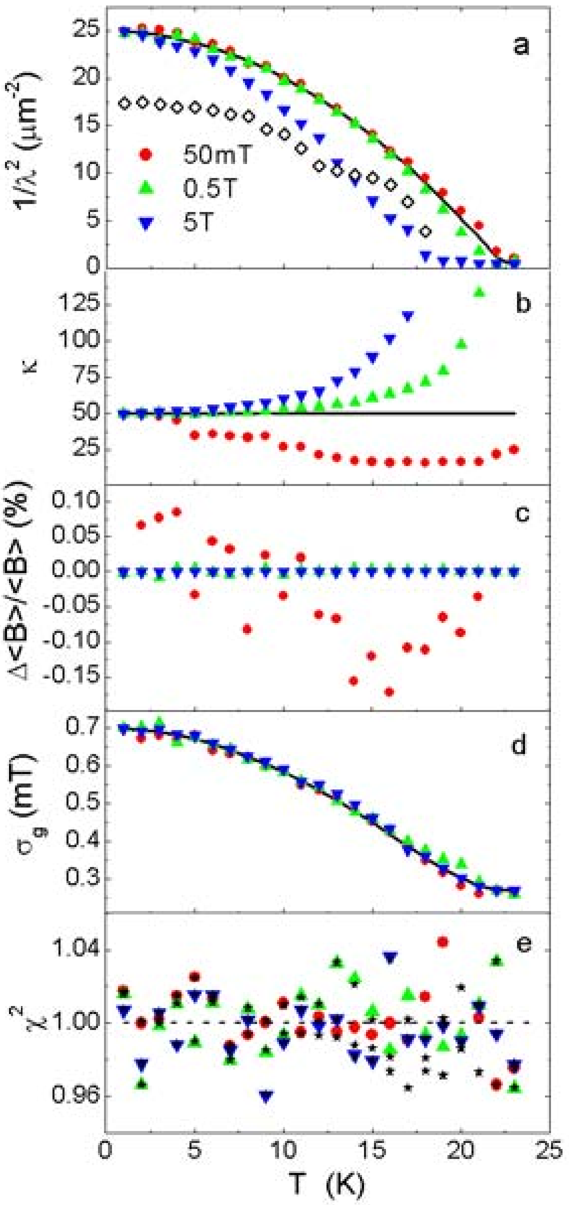

Figure 3.9: Summary of the fit results for the μSR spectra simulated by the LG model. The fitted values $1/\lambda^2$, κ, $\Delta\langle B\rangle/\langle B\rangle$, and σ_g as well as χ^2 are plotted as a function of temperature T for three different fields, 50 mT (circles), 0.5 T (up-triangles) and 5 T (down-triangles) for 20 million events. The parameters $1/\lambda^2$, κ, $\Delta\langle B\rangle/\langle B\rangle$, and σ_g were free during the fitting procedure. The solid lines correspond to the true values of the parameters. $\Delta\langle B\rangle/\langle B\rangle = (\langle B\rangle_{fit} - \langle B\rangle_{real})/\langle B\rangle_{real}$ denotes the relative deviation of the fitted value $\langle B\rangle_{fit}$ from the real $\langle B\rangle_{real}$. For comparison, χ^2 was also determined for the real values of the parameters (black stars). Empty diamonds in (a) shows possible fit result for $1/\lambda^2$ for 5 T data with extremely wrong initial parameters.

since it can approximate experimental data well in the whole range of fields (see Fig. 3.5). It is also the fastest to calculate and yields μSR spectra similar to the ones obtained by the NGL model. The temperature dependence of the penetration depth λ, coherence length

$\xi = \lambda/\kappa$, and σ_g for the simulated data is shown by solid black lines in Fig. 3.9. Again, the μSR spectra were simulated for three different mean fields $\langle B \rangle = 50$ mT, 0.5, and 5 T ($b = 0.0024$, 0.024, 0.24). As before, the mean field was assumed to be temperature independent. Statistics, asymmetry, and phase of the μSR time spectra were chosen to be $20 \cdot 10^6$, 0.2, and 0, respectively.

The fit results of the simulated μSR spectra with all the parameters free (except A and ϕ) are shown in Fig. 3.9. It is obvious that the fit results for λ and κ deviate substantially from the real values. A detailed analysis of the fitting procedure showed that the reasons for the large deviations seen in Fig. 3.9 were due to the following:
(1) At low fields (50 mT, $b \sim 0.001 - 0.01$), the fit result of λ is weakly dependent on the fit result of κ (or ξ).
(2) At high fields (5 T, $b \sim 0.1 - 1$), there is a strong correlation between λ and ξ obtained in the fit.
(3) The values of σ_g and $\langle B \rangle$ may be determined reasonably well from the fit of the μSR time spectra at any field b.

In Secs. 3.2.6 and 3.2.7, correlations between λ, ξ and σ_g were investigated which support the above conclusions.

3.2.6 Correlation between σ_g and λ^{-2} for small values of b

As shown in Fig. 3.3, with increasing Gaussian smearing σ_g, the characteristic fields of the internal magnetic field distribution $P(B)$ of the ideal FLL are gradually washed out, and $P(B)$ tends to become an asymmetric Gaussian-like distribution. Therefore, one expects some correlation between σ_g and the inverse square of the penetration depth $1/\lambda^2$ since both influence the second moment of the μSR spectrum. In order to show the possibility of extracting the real values of λ and σ_g from μSR spectra, the spectra were first simulated by the ML model, and then the goodness of fit χ^2 was calculated as a function of λ and σ_g with the other parameters fixed at their true values. Fig. 3.10(a) shows χ^2 as a function of λ with the other parameters fixed to their true values. It is evident that, with increasing σ_g, the error of λ extracted from the fit increases. Fig. 3.10(b) shows a contour plot of χ^2 as a function of λ and σ_g calculated for the case of extremely high $\kappa = 200$ and low field $b = 0.001$. Other parameters are set to values used for the analysis of simulated data (see Sec. 3.2.5), namely, $\lambda = 200$ nm, $\sigma_g = 0.75$, and 20 million events. From the figure, we conclude that λ^{-2} and σ_g are slightly correlated, but it is possible to extract both simultaneously if ξ is fixed.

3.2.7 Correlation between ξ and λ

For a low magnetic field, the dependence of the μSR spectrum on the coherence length ξ is very weak (see Fig. 3.3). But with an increasing field approaching B_{c2}, the shape of the spectrum becomes dependent, not only on the penetration depth λ, but also on ξ as well

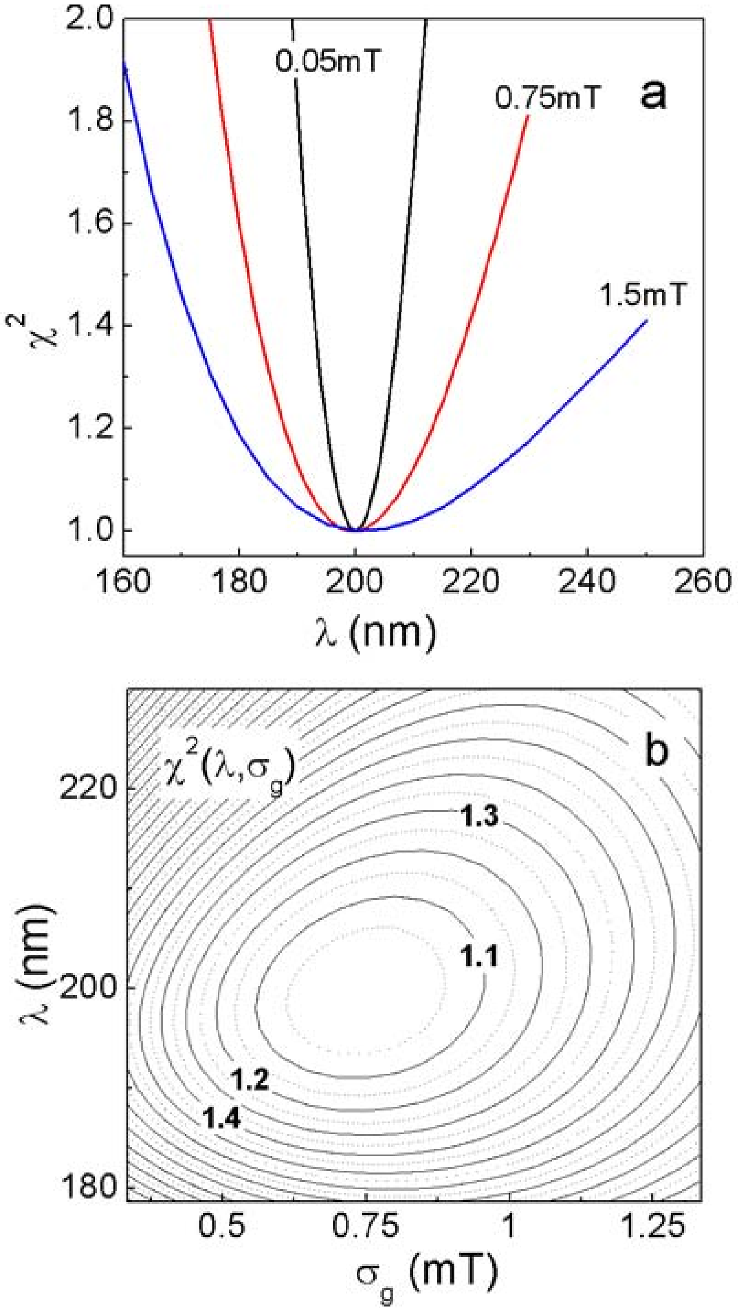

Figure 3.10: (a) χ^2 as a function of λ with the other parameters set to their true values. The following parameters were used for the μSR data simulation: $\lambda = 200$ nm, $\xi = 1$ nm, b $= 10^{-3}$, 20 million events, and $\sigma_g = 0.05$, 0.75, and 1.5 mT. (b) Contour plot of χ^2 as a function of λ and σ_g for the data simulated with $\lambda = 200$ nm, $\xi = 1$ nm, $b = 10^{-3}$, $\sigma_g = 0.75$, and 20 millions events. In both figures, the ML model was used for the calculations, and the statistically scattered minimal value of the χ^2 was normalized to 1.

(see Fig. 3.5). An increase of λ and/or ξ causes a decrease of the second moment and the characteristic fields. Therefore, it is expected that a decrease of λ is correlated with an increase of ξ in the fitting procedure and vice versa. So far, this problem was discussed previously only by Riseman *et al.* [117]. Here, this problem is studied in more detail. For

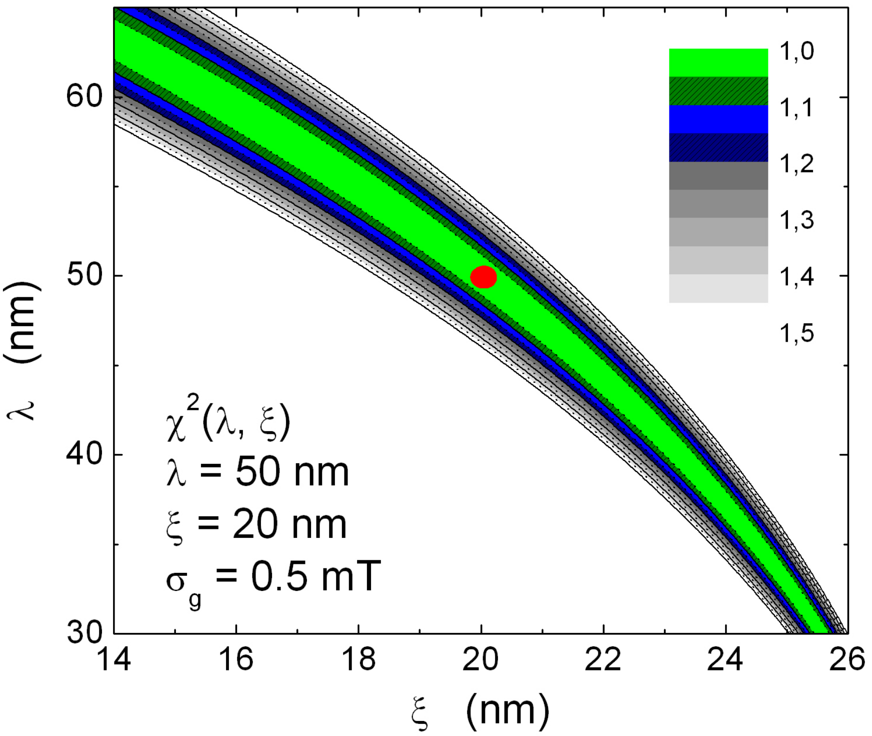

Figure 3.11: Contour plot of χ^2 as a function of λ and ξ for the data simulated with the parameters $\lambda = 50$ nm, $\xi = 20$ nm, $b = 0.5$, $\sigma_g = 0.5$ mT, and 20 million events as calculated by the NGL model. The fitted parameters λ and ξ exhibit a strong correlation, which is the reason for the pronounced systematic deviations of the fitted values of λ^{-2} and κ at 5 T from the real values displayed in Fig. 3.9. The statistically scattered minimal value of χ^2 is normalized to 1.

this purpose, χ^2 was determined for simulated μSR data as a function of λ and ξ at fixed applied field $\langle B \rangle = 0.5 B_{c2}$ and Gaussian smearing $\sigma_g = 0.5$ mT. The case of a relatively small $\kappa = 2.5$ ($\lambda = 50$ nm and $\xi = 20$ nm) was chosen for the data simulation since the relative volume of the vortex cores is large and therefore ξ may be more easily extracted from the fits. As before, the number of events was $20 \cdot 10^6$. The result of the analysis with the NGL model is shown in Fig. 3.11 where a contour plot of χ^2 as a function of λ and ξ with the other parameters fixed is displayed. There is indeed a strong correlation between λ and ξ. For $\lambda(\xi) \approx 58.68 + 2.14\xi - 0.127\xi^2$ where $\chi^2 \simeq 1$ is a minimum, the fits converge after a few hundred iterations. It should be noted that, for such a high reduced field $b = 0.5$ as used here for the analysis, the qualitative dependence of the characteristic fields δB_α on λ, ξ and $\langle B \rangle$ are independent of $\kappa = \lambda/\xi$ (see Fig. 3.3). Therefore, the correlation between λ and ξ shown in Fig. 3.11 also holds for any $\kappa = \lambda/\xi$.

In order to check whether there is a correlation between λ and ξ at other fields, similar contour plots were calculated for $b = 0.004$, 0.02 and 0.1. Figure 3.12 shows the result of this calculation. It is obvious that a substantial correlation remains at lower fields $b = 0.1$ and 0.02 as well, whereas at $b = 0.004$, χ^2 is practically independent on ξ. Therefore, in general,

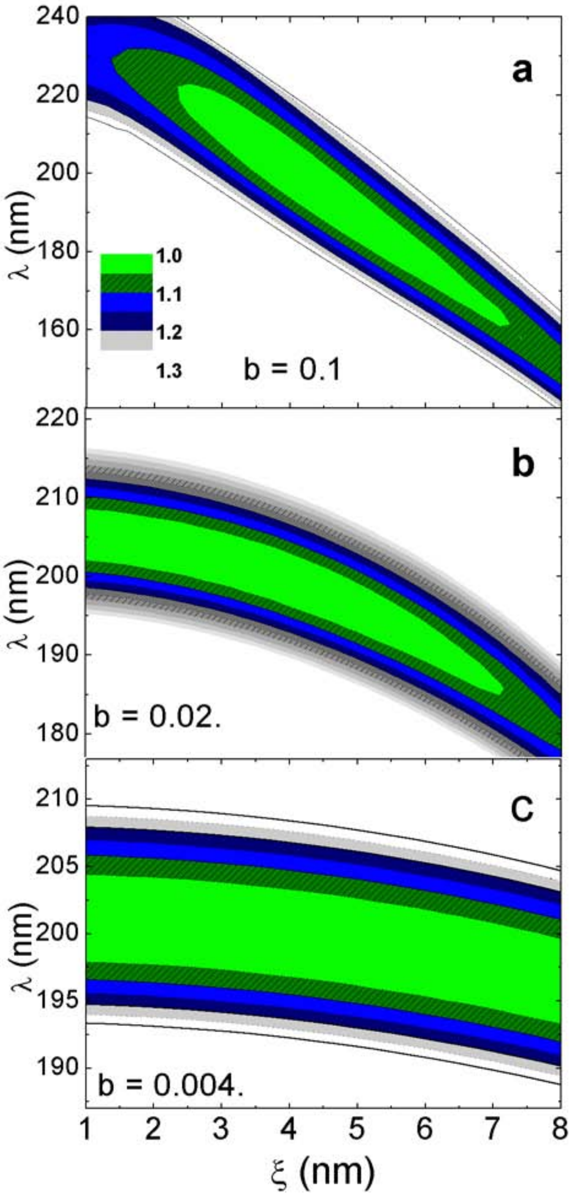

Figure 3.12: Contour plots of χ^2 as a function of λ and ξ for μSR spectra simulated with the parameters $\lambda = 200$ nm, $\xi = 4$ nm, $\sigma_g = 0.7$ mT, 20 million events, and $b = 0.004$, 0.02, and 0.1. The results in (a) were obtained by the NGL model, and those in (b) and (c) by the ML model. There is a strong correlation of the fitted values of λ and ξ for high ($b = 0.1$) and intermediate ($b = 0.02$) fields but nearly no correlation at low fields ($b = 0.004$). The statistically scattered minimal value of χ^2 is normalized to 1.

a simultaneous determination of ξ and λ from μSR spectra independent of the model used to describe the vortex state is not feasible without additional restrictions.

3.3 Related publication

Comparison of different methods for analyzing μSR line shapes in the vortex state of type-II superconductors
A. Maisuradze, R. Khasanov, A. Shengelaya, and H. Keller
J. Phys.: Condens. Matter **21**, 075701 (2009).

IOP Publishing Journal of Physics: Condensed Matter
J. Phys.: Condens. Matter **21** (2009) 075701 (15pp) doi:10.1088/0953-8984/21/7/075701

Comparison of different methods for analyzing μSR line shapes in the vortex state of type-II superconductors

A Maisuradze[1,2], **R Khasanov**[1,2], **A Shengelaya**[1,3] **and H Keller**[1]

[1] Physik-Institut der Universität Zürich, Winterthurerstrasse 190, CH-8057 Zürich, Switzerland
[2] Laboratory for Muon Spin Spectroscopy, Paul Scherrer Institut, CH-5232 Villigen PSI, Switzerland
[3] Physics Institute of Tbilisi State University, Chavchavadze 3, GE-0128 Tbilisi, Georgia

E-mail: alexander.maisuradze@psi.ch

Received 29 August 2008, in final form 21 December 2008
Published 19 January 2009
Online at stacks.iop.org/JPhysCM/21/075701

Abstract
A detailed analysis of muon-spin rotation (μSR) spectra in the vortex state of type-II superconductors using different theoretical models is presented. Analytical approximations of the London and Ginzburg–Landau (GL) models, as well as an exact solution of the GL model were used. The limits of the validity of these models and the reliability for extracting parameters such as the magnetic penetration depth λ and the coherence length ξ from the experimental μSR spectra were investigated. The analysis of the simulated μSR spectra showed that at high magnetic fields there is a strong correlation between λ and ξ obtained for any value of the Ginzburg–Landau parameter $\kappa = \lambda/\xi$. The smaller the applied magnetic field, the smaller the possibility of finding the correct value of ξ. A simultaneous determination of λ and ξ without any restrictions is very problematic, regardless of the model used to describe the vortex state. It was found that for extreme type-II superconductors and low magnetic fields, the fitted value of λ is practically independent of ξ. The second-moment method frequently used to analyze μSR spectra by means of a multi-component Gaussian fit generally yields reliable values of λ over the whole range of applied fields $H_{c1} \ll H \lesssim H_{c2}$ (H_{c1} and H_{c2} are the first and second critical fields, respectively). These results are also relevant for the interpretation of small-angle neutron scattering experiments on the vortex state in type-II superconductors.

(Some figures in this article are in colour only in the electronic version)

1. Introduction

The muon-spin rotation (μSR) technique is one of the most powerful and unique tools for studying the internal magnetic field distribution $P(B)$ associated with the vortex lattice in type-II superconductors (see e.g. [1–3]). In the vortex state for an applied magnetic field $H > H_{c1}$, or $B > 0$ (H_{c1} and B are the first critical field and the magnetic induction in a sample, respectively) [4] the energy of the surface separating normal and superconducting fractions of the sample becomes negative and the field penetrates the sample in the form of quantized flux lines, called vortices, each of them containing an elementary flux quantum ($\Phi_0 = h/2e \simeq 2.0678 \times 10^{-15}$ Wb) [5]. In the case of small pinning these vortices arrange themselves in a regular vortex lattice called a flux-line lattice (FLL) [5]. The distribution of the internal magnetic fields $P(B)$ inside the superconducting sample in the vortex state is uniquely determined by two characteristic lengths, the magnetic field penetration depth λ and the coherence length ξ. From μSR experiments, $P(B)$ profiles are obtained by performing a Fourier transformation of the μSR time spectra. There are different approaches for analyzing μSR data. Generally, the magnetic field penetration depth λ is determined from the second moment $\langle \Delta B^2 \rangle$ of the internal field distribution $P(B)$ [6–12]. For an isotropic extreme type-II superconductor ($\lambda \gg \xi$) it was shown that $\langle \Delta B^2 \rangle \propto \lambda^{-4}$ [13]. The more advanced approaches that allow one to obtain not only λ, but also the coherence length ξ require a theoretical model for the spatial variation of the internal magnetic field $B(\mathbf{r})$ ($\mathbf{r}$ is spatial coordinate). An essential requirement of the model is that it must account for the finite size of the vortex cores. So far, the internal magnetic field distribution $P(B)$ measured using μSR has been analyzed assuming analytical models for $B(\mathbf{r})$ based on London and Ginzburg–Landau (GL) theories. The London theory provides the simplest approach for modeling the FLL. Since London theory does not account for the finite size of the vortex cores, a cut-off factor derived from GL theory must be inserted into the analytical London expression for $B(\mathbf{r})$ to correct for the divergence of $B(\mathbf{r})$ in the vortex core [14, 3]. The GL theory has the spatial dependence of the order parameter built in and thus provides a phenomenological description of the magnetic field profile in the vortex core region. Abrikosov [5] predicted the vortex core state from a periodic solution of the GL equations near the second critical field $B_{c2} = \mu_0 H_{c2}$ and provided an approximate analytical solution of these equations for an isolated vortex for fields of the order of H_{c1}. Clem [15] proposed a variational method for solving the GL equations that was further extended by Hao *et al* [16]. A simplified version of this model for $\lambda/\xi \gg 1$ was developed by Yaouanc *et al* [14], and is often used in the literature [3].

The London and the GL models were widely applied to determine values of λ and ξ from measured μSR time spectra taken in the mixed state of type-II superconductors [17, 14, 18, 3, 19–31]. We should emphasize, however, that despite the broad usage, the limits of validity of these models and the reliability of the parameters extracted from the fits are not much discussed in the literature. The main purpose of the present paper is to address these basic questions. The paper is divided into two parts. In the first part we briefly describe the models often used for the analysis of μSR spectra: the London model with Gaussian cut-off (LG model), the modified London model (ML model), and the analytical Ginzburg–Landau model (AGL model). These models are compared with the most precise model based on the iterative method for solving the Ginzburg–Landau equations developed recently by Brandt [4], the so called numerical Ginzburg–Landau model (NGL model). $P(B)$ profiles for various sets of λ, ξ, and magnetic field B were first simulated by means of the NGL model and then analyzed within the framework of the LG, ML, and AGL models. For further discussions, it is convenient to define the reduced magnetic field $b = B/B_{c2}$. It was found that the ML model can be used *only* for low magnetic fields ($b \lesssim 0.1$), while both the AGL model and the LG model yield reliable results over almost the *whole* magnetic field range. However, the values of λ and ξ obtained by means of the AGL and the LG model deviate systematically from the initial parameters used for the simulated $P(B)$ profiles for magnetic fields in the range $0.01 \lesssim b \leqslant 1$. It was also shown that for $b \lesssim 0.01$ the $P(B)$ profiles do not depend on the coherence length ξ. In the second part of the paper we present a systematic analysis of simulated μSR time spectra (with typical statistics used in real μSR experiments) by means of the LG model. Over the whole field range ($0 < b \leqslant 1$) and for any values of the Ginzburg–Landau parameter $\kappa = \lambda/\xi$ there is a strong correlation between the values of λ and ξ determined from the fit. This implies that an analysis of μSR data using this approach, without taking into account these correlations, may lead to substantial errors in the determination of the absolute values of λ and ξ, and even may result in unphysical dependences of λ and ξ on magnetic field and temperature. In addition, the second-moment method applied to a multiple-Gaussian fit was tested in order to check how reliably the penetration depth λ can be determined by this method. In particular, the influence of the number of Gaussians used in the multi-Gaussian fit on the quality of the fit was investigated. For typical statistics used in the experiment and practically over the whole field range ($0 < b \lesssim 1$), the second-moment method applied to a multi-Gaussian fit may provide correct values for λ within a few per cent.

The paper is organized as follows. In section 2 various theoretical models used to analyze μSR data are briefly described. The dependence of the magnetic field distribution $P(B)$ on λ, ξ, b, and the Gaussian smearing parameter σ_g, as calculated within the LG model, is discussed in section 3. In section 4 we compare the results obtained by means of the models described in section 2 for the case of an extreme type-II superconductor ($\kappa = \lambda/\xi \gg 1$). Section 5 comprises the studies of the simulated μSR data. The simulated μSR spectra were analyzed by means of the various models described in section 2 in order to search for possible correlations between the parameters, such as λ, ξ, and σ_g. The conclusions follow in section 6.

2. Models for data analysis

As mentioned in section 1, the simplest and the most widely used approach for analyzing μSR data is based on the relation between the magnetic penetration depth λ and the second moment $\langle \Delta B^2 \rangle$ of the internal field distribution $P_{id}(B)$ of the ideal FLL [13, 4, 32]:

$$\lambda^{-4} = C \langle \Delta B^2 \rangle. \tag{1}$$

Here, C is the proportionality coefficient depending on the value of the reduced magnetic field $b = \langle B \rangle / B_{c2}$ ($\langle B \rangle$ is the first moment of $P_{id}(B)$) and the Ginzburg–Landau parameter κ [13, 4, 32]. In order to estimate $\langle \Delta B^2 \rangle$ one often assumes that $P_{id}(B)$ is a sum of N Gaussian distributions (generally, $N = 1, 2, 3$) [33, 34]:

$$P_{id}(B) = \frac{\gamma_\mu}{\sqrt{2\pi}(A_1 + \cdots + A_N)} \times \sum_{i=1}^{N} \frac{A_i}{\sigma_i} \exp[(B - B_i)^2 / 2(\sigma_i/\gamma_\mu)^2], \tag{2}$$

where A_i, B_i, and σ_i/γ_μ are the weight factor, the first moment, and the standard deviation of the ith Gaussian component, respectively. $\gamma_\mu = 2\pi \times 135.5342$ MHz T^{-1} is the muon gyromagnetic ratio. The first and second moment of $P_{id}(B)$ are then readily obtained [33, 34]:

$$\langle B \rangle = \sum_{i=1}^{N} \frac{A_i B_i}{A_1 + \cdots + A_N}, \tag{3}$$

and

$$\langle \Delta B^2 \rangle = \sum_{i=1}^{N} \frac{A_i}{A_1+\cdots+A_N}\left[(\sigma_i/\gamma_\mu)^2 + [B_i - \langle B\rangle]^2\right]. \tag{4}$$

With modern computers it became possible to develop models that allow us to calculate $P_{\mathrm{id}}(B)$ for a FLL as a function of various parameters, such as magnetic penetration depth, coherence length, applied magnetic field, and FLL geometry (rectangular or hexagonal) [35, 17, 3, 4]. The London models (with different cut-off factors) provide the simplest and fastest way to calculate $P_{\mathrm{id}}(B)$ for the analysis of μSR data for $\kappa \gg 1$ [3]. Better approximations of $P_{\mathrm{id}}(B)$ for small values of κ and fields closer to B_{c2} can be obtained using the AGL model [16, 14]. Strictly speaking, Ginzburg–Landau theory is only valid in the neighborhood of the phase boundary $T_c(B)$ of a type-II superconductor. However, it is generally assumed that Ginzburg–Landau models are also good approximations for any field and temperature. The results obtained using the NGL model correspond to the minimum of the Ginzburg–Landau free energy, whereas other models described in this paper are just approximations to the NGL model. Therefore, the NGL model will be used as a reference for comparison with the AGL, ML, and LG models. A relatively simple method for calculating $P_{\mathrm{id}}(B)$ within the framework of the NGL model was proposed by Brandt [36, 4].

In the LG, ML, AGL, and NGL approximations the spatial distribution of the magnetic field in the mixed state of a type-II superconductor is described using the Fourier expansion:

$$B(\mathbf{r}) = \langle B\rangle \sum_{\mathbf{G}} \exp(-\mathrm{i}\mathbf{G}\mathbf{r})\, B_{\mathbf{G}}(\lambda, \xi). \tag{5}$$

Here, $\mathbf{r}$ is the vector coordinate in a plane perpendicular to the applied field. The origin of the coordinate system is in the center of a vortex core (see e.g. [29]), $\mathbf{G} = 4\pi/\sqrt{3}a(m\sqrt{3}/2, n + m/2)$ are the reciprocal lattice vectors for the hexagonal FLL, a is the intervortex distance, $B_{\mathbf{G}}$ are the Fourier components, and m, n are integer numbers. For the LG model the Fourier components $B_{\mathbf{G}}$ are [35, 3]

$$B_{\mathbf{G}} = \frac{\mathrm{e}^{-\xi^2G^2/2}}{1+G^2\lambda^2}. \tag{6}$$

For the ML model the Fourier components $B_{\mathbf{G}}$ are given by [17, 3]

$$B_{\mathbf{G}} = \frac{\mathrm{e}^{-\xi^2G^2/2(1-b)}}{1+G^2\lambda^2/(1-b)}, \tag{7}$$

For the AGL model the Fourier components $B_{\mathbf{G}}$ are [16, 14]

$$B_{\mathbf{G}} = \frac{\Phi_0}{S}\,\frac{f_\infty K_1[\frac{\xi_v}{\lambda}(f_\infty^2+\lambda^2G^2)^{1/2}]}{(f_\infty^2+\lambda^2G^2)^{1/2}K_1(\frac{\xi_v}{\lambda}f_\infty)}, \tag{8}$$

where $f_\infty = 1 - b^4$, and

$$\xi_v = \xi\left(\sqrt{2} - \frac{0.75}{\kappa}\right)(1+b^4)^{1/2}[1-2b(1-b)^2]^{1/2}.$$

Here, $K_1(x)$ is the modified Bessel function. For applied magnetic fields $H \gg H_{c1}$ the relation $\mu_0 H \simeq \langle B\rangle$ holds [36]. Finally, for the NGL model no analytical solution for the Fourier components $B_{\mathbf{G}}$ exists. They are determined numerically [36, 4].

From the known spatial distribution of the magnetic field $B(\mathbf{r})$ in the mixed state one can extract the internal magnetic field distribution $P_{\mathrm{id}}(B)$ for the ideal FLL by means of the following equation:

$$P_{\mathrm{id}}(B) = \frac{\int \delta(B-B')\,\mathrm{d}A(B')}{\int \mathrm{d}A(B')}, \tag{9}$$

where $\mathrm{d}A(B')$ is the elementary area of the FLL with a field B' inside, and the integration is over a quarter of the FLL unit cell [29]. In order to take into account possible random deviations of the flux core positions from their ideal ones (vortex disorder) and/or possible broadening of the μSR spectra due to nuclear depolarization, one may convolute the ideal distribution $P_{\mathrm{id}}(B)$ with a Gaussian distribution [35]:

$$P(B) = \frac{1}{\sqrt{2\pi}\sigma_{\mathrm{g}}}\int P_{\mathrm{id}}(B')\exp\left[-\frac{1}{2}\left(\frac{B-B'}{\sigma_{\mathrm{g}}}\right)^2\right]\mathrm{d}B', \tag{10}$$

where σ_{g} is the width of the Gaussian distribution. The relation between σ_{g}, vortex disorder, and nuclear depolarization is described in section 3.4.

The μSR time spectra can be further simulated by performing the Fourier transform of $P(B)$ convoluted with the Gaussian function given in equation (10):

$$\tilde{P}(t) = A\mathrm{e}^{\mathrm{i}\phi}\int P(B)\mathrm{e}^{\mathrm{i}\gamma_\mu Bt}\,\mathrm{d}B, \tag{11}$$

where A and ϕ are the initial asymmetry and the phase of the μSR time spectra, respectively. For the calculations of the spatial magnetic field distribution $B(\mathbf{r})$ in the FLL 31 × 31 Fourier components of the magnetic field and the reciprocal vector $\mathbf{G}$ were used. This allows one to calculate the second moment of $P(B)$ with a precision of better than 10^{-6}. The integral in equation (9) was calculated numerically over a quarter of the FLL unit cell, divided into approximately 100 × 100 equal pixels, depending on the mean magnetic field $\langle B\rangle$ (see figure 1 of [29]).

Equations (5)–(8) are only valid for isotropic superconductors or superconductors with axial symmetry with the external magnetic field applied along the symmetry axis. In the present study we mostly concentrate on the case of extreme type-II superconductors ($\kappa \gg 1$), such as the cuprate high temperature superconductors. Since the qualitative behavior of $P_{\mathrm{id}}(B)$ as a function of various parameters is essentially the same for a hexagonal and a square FFL, we will consider here only the hexagonal case.

In figure 1 we plot the spatial distribution of the magnetic field $B(\mathbf{r})$ in the mixed state and the corresponding local magnetic field distribution $P_{\mathrm{id}}(B)$ for $\lambda = 50$ nm, $\xi = 20$ nm, and $\langle B\rangle = 0.3B_{c2} \simeq 246.8$ mT, as determined by the NGL model. The ideal FLL has three characteristic fields: (i) the maximal field $B_{\max}$ corresponds to the field in the vortex core, (ii) the field at the peak of $P_{\mathrm{id}}(B)$ is the saddle point field B_{sad} (located in the middle between neighboring

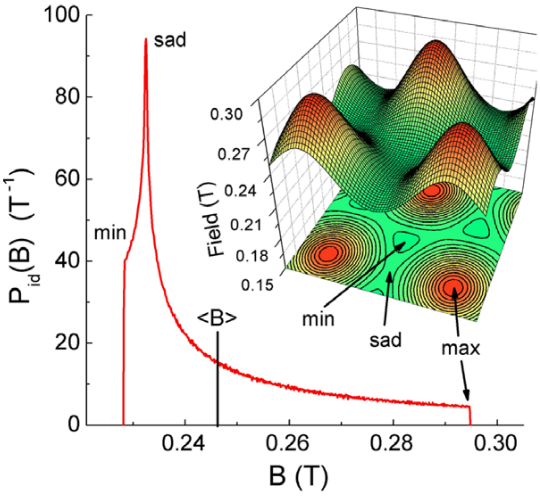

Figure 1. Example of a spatial distribution of the magnetic field $B(\mathbf{r})$ and the corresponding local magnetic field distribution $P_{\mathrm{id}}(B)$ for an ideal hexagonal FLL determined by the NGL method. The parameters used for the calculations are $\lambda = 50$ nm, $\xi = 20$ nm, and $\langle B\rangle = 0.3B_{\mathrm{c2}} \simeq 246.8$ mT, and intervortex distance $a = 69.5$ nm.

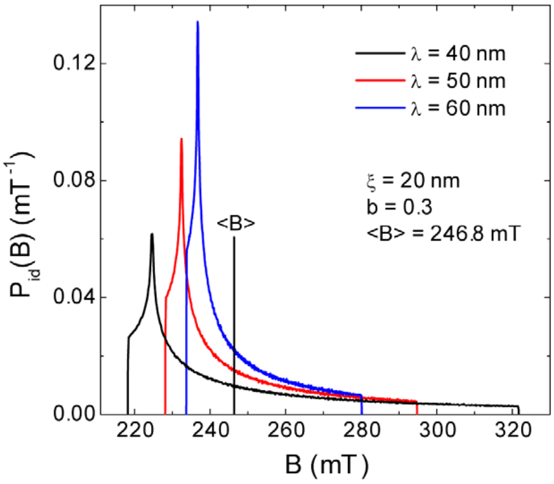

Figure 2. Local magnetic field distribution $P_{\mathrm{id}}(B)$ for an ideal hexagonal FLL obtained using the NGL model for different values of λ, at fixed ξ and applied field $B_{\mathrm{app}} \simeq \langle B\rangle$. The curves are normalized so that $\int P_{\mathrm{id}}(B)\,\mathrm{d}B = 1$. Note that the shape of $P_{\mathrm{id}}(B)$ strongly depends on λ.

vortices), and (iii) the minimal field $B_{\min}$ is in the center of the triangle of vortices forming the hexagonal FLL[4]. Instead of the full local magnetic field distribution $P_{\mathrm{id}}(B)$ we will use these characteristic fields to discuss the dependence of the shape of $P_{\mathrm{id}}(B)$ on different parameters.

3. Dependence of $P(B)$ on λ, ξ, $\langle B\rangle$, and σ_{g}

In this section we concentrate on the analysis of the shape of $P(B)$ given in equation (10) as a function of penetration depth λ (section 3.1), coherence length ξ (section 3.2), mean magnetic field $\langle B\rangle$ (section 3.3), and Gaussian smearing width σ_{g} (section 3.4).

3.1. Dependence of $P_{id}(B)$ on λ

In figure 2 we show examples of the magnetic field distribution $P_{\mathrm{id}}(B)$ for different values of the magnetic penetration depth λ at constant mean field $\langle B\rangle = 0.3B_{\mathrm{c2}} = 246.8$ mT and coherence length $\xi = 20$ nm, as calculated using the NGL model. The region between the minimal and the mean field $\langle B\rangle$ is most important, because the high field tail is usually below the noise level of experimental μSR spectra and is generally not observed, especially at low fields and for $\kappa \gg 1$. Our calculations show that the differences between the characteristic fields and the mean field $\langle B\rangle$ are proportional to $1/\lambda^2$. This is in full agreement with the results of Sidorenko *et al* [38] who obtained for applied fields $H_{\mathrm{c1}} \ll H \ll H_{\mathrm{c2}}$ and $\kappa \gg 1$ (in this case $\langle B\rangle \simeq \mu_0 H$) in the London approximation the following expressions:

$$\delta B_{\min} = B_{\min} - \langle B\rangle = -0.79(\Phi_0/4\pi\lambda^2)\ln 2, \qquad (12)$$

$$\delta B_{\mathrm{sad}} = B_{\mathrm{sad}} - \langle B\rangle = -\tfrac{2}{3}(\Phi_0/4\pi\lambda^2)\ln 2, \qquad (13)$$

$$\delta B_{\max} = B_{\max} - \langle B\rangle = 2(\Phi_0/4\pi\lambda^2)\ln\frac{a}{2\sqrt{2}K\xi}. \qquad (14)$$

Here, a is the intervortex distance, and $K = K(1/\sqrt{3}) \simeq 1.926$ is the complete elliptic integral of the first kind [38]. Hereafter, for convenience the quantities $\delta B_{\min}$, δB_{sad}, and $\delta B_{\max}$ defined above are denoted as characteristic fields as well. From figure 2 and the pronounced dependence of the characteristic fields on $1/\lambda^2$ it is evident that the μSR time spectra strongly depend on λ. Therefore, it should be possible to extract reliable values of λ from experimental μSR data.

3.2. Dependence of $P_{id}(B)$ on ξ

Figure 3 shows the ξ dependence of the characteristic fields δB_α (α = min, sad, max) normalized to $\Phi_0/4\pi\lambda^2$ (cf equations (12)–(14)) for a set of different mean fields $\langle B\rangle$, as obtained using the LG model. All the characteristic fields δB_α disappear at $\xi \geqslant (\Phi_0/2\pi\langle B\rangle)^{1/2}$ (Φ_0 is the flux quantum), where superconductivity vanishes. Below a certain value of ξ the characteristic fields $\delta B_{\min}$ and δB_{sad} are independent of ξ, whereas $\delta B_{\max}$ still depends on ξ. However, in real μSR experiments $\delta B_{\max}$ cannot be determined out of the noise level at low $\langle B\rangle$. Therefore, at these low values of ξ μSR spectra are practically independent of ξ. In order to get a feeling for what this means for cuprate superconductors we assume $\xi \simeq 3$ nm, a typical value of ξ for cuprates below $T_{\mathrm{c}}/2$. In this case the shape of $P_{\mathrm{id}}(B)$ is almost independent of ξ for fields $\langle B\rangle \leqslant 0.3$ T, where $\delta B_{\min}$ and δB_{sad} saturate (see figure 3). It is thus difficult to find the correct value of ξ at low magnetic fields. At higher fields the shape of $P_{\mathrm{id}}(B)$ strongly depends on ξ. Note that in figure 3 the curves corresponding to the smallest field ($\langle B\rangle = 0.01$ T) exhibit slightly smaller saturation values

---

[4] At high fields and low temperatures the minimal and the saddle points are exchanged and the magnetic field distribution around the vortex core has a conical shape. See [37] and [35].

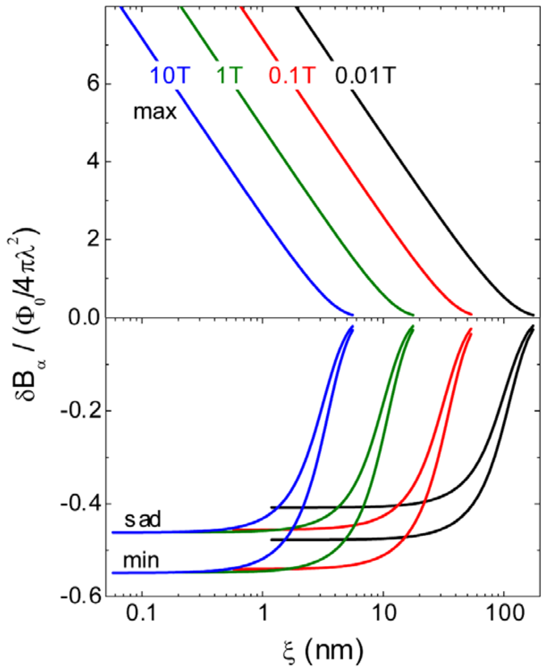

Figure 3. ξ dependence of the characteristic fields δB_α (α = min, sad, max) normalized to $\Phi_0/4\pi\lambda^2$ for a set of different applied magnetic fields ($B_{\rm app} \simeq \langle B\rangle = 0.01, 0.1, 1, 10$ T) as obtained using the LG model. Note that there is a critical value of ξ below which $\delta B_{\rm min}$ and $\delta B_{\rm sad}$ are practically independent of ξ. This critical value depends on $\langle B\rangle$.

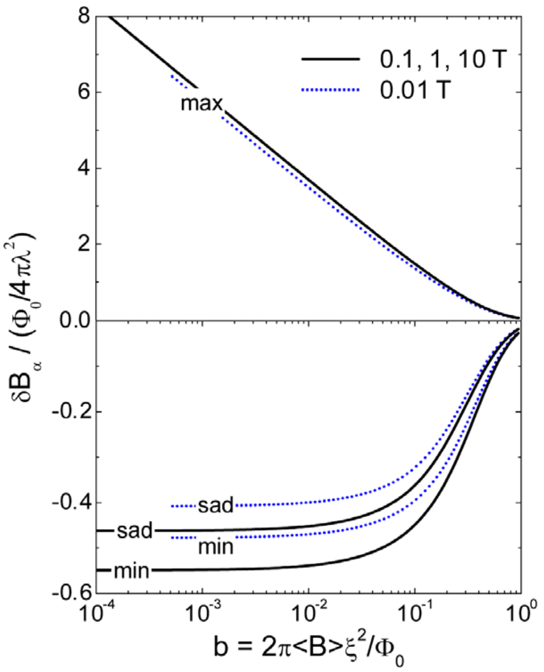

Figure 4. Characteristic fields δB_α (α = min, sad, max) of figure 3 plotted as a function of the reduced field $b = \langle B\rangle/B_{\rm c2}(\xi)$ ($B_{\rm c2}(\xi) = \Phi_0/2\pi\xi^2$) at $\langle B\rangle = 0.1$, 1, and 10 T (black solid line), and at 0.01 T (blue dotted line). Note that all the curves $\delta B_\alpha(\xi)$ of figure 3, at $\langle B\rangle = 0.1$, 1, 10 T merge to single curves $\delta B_\alpha(b)$.

of the characteristic fields $\delta B_{\rm min}$ and $\delta B_{\rm sad}$ than for the higher fields. The reason for this is discussed in section 3.3.

As shown by Brandt [36, 4] the ideal internal field distribution $P_{\rm id}(B)$ may be expressed using normalized parameters, depending only on $\kappa = \lambda/\xi$ and $b = \langle B\rangle/B_{\rm c2}$. In a similar way we can plot the curves in figure 3 not as a function of ξ, but as a function of $b = \langle B\rangle/B_{\rm c2}$, where $B_{\rm c2}(\xi) = \Phi_0/2\pi\xi^2$ (the relation obtained from Ginzburg–Landau theory). This plot is shown in figure 4. All the curves of figure 3, except the one for the smallest field $\langle B\rangle = 0.01$ T, fall on the same line.

3.3. Field dependence of $P_{id}(B)$

Before we discuss the dependence of the characteristic fields δB_α (α = min, sad, max) on various parameters, it is useful to define the minimal value of the reduced field $b_{\rm min} = B_{\rm c1}/B_{\rm c2} \simeq \ln\kappa/2\kappa^2$ which is needed to form a regular FLL. This field corresponds to the limit below which the vortices can be considered as well separated and noninteracting.

Figure 5 shows δB_α (normalized to $\Phi_0/4\pi\lambda^2$) as a function of the reduced magnetic field b for different values of κ, as calculated using the LG model. The arrows at $\delta B_{\rm sad}$ correspond to $b_{\rm min}(\kappa)$. This figure looks very similar to figure 4 and represents actually its generalization. It shows how δB_α depends on all three parameters λ, ξ, $\langle B\rangle$, and not only δB_α as a function of $\langle B\rangle$. Since figure 5 demonstrates the dependence of δB_α on all the parameters it is the basis of all further discussions. At high values of b, the characteristic fields $\delta B_\alpha(\langle B\rangle)$ and $\delta B_\alpha(\xi^2)$ coincide, but at lower fields they deviate substantially (dependence of δB_α on a parameter x means that all other parameters, except x, are fixed). The reason for this is obvious. For $b \to 0$ at constant ξ or $B_{\rm c2}$ the intervortex distance a increases, and $\langle B\rangle$, $\delta B_{\rm min}(b)$, and $\delta B_{\rm sad}(b)$ tend to zero as well. This is the reason for the smaller saturation values of δB_α at the lowest field $\langle B\rangle = 0.01$ T in figure 3. However, in the case of the ξ dependence, when $b \to 0$ at constant field $\langle B\rangle$, only the vortex core size is reduced, and the intervortex distance a does not change. This does not have much influence on the internal magnetic field distribution $P_{\rm id}(B)$ for $\kappa \gg 1$ (see figure 5). When κ is reduced, the deviation of $\delta B_\alpha(\langle B\rangle)$ from $\delta B_\alpha(\langle B\rangle)_{\kappa=\infty}$ starts at higher values of b. For small values of κ the characteristic fields $\delta B_\alpha(\langle B\rangle)$ do not even reach saturated values as in the case of high κ and small b. Despite the similarity of $\delta B_\alpha(\langle B\rangle)$ and $\delta B_\alpha(\xi^2)$, the mean field $\langle B\rangle$ can easily be extracted from the fit (unlike ξ), since it defines the oscillation frequency of the μSR time spectrum.

3.4. Dependence of $P(B)$ on σ_g

In reality the internal magnetic field distribution in the mixed state of a type-II superconductor is influenced by several factors, which generally lead to an additional broadening of $P_{\rm id}(B)$. (i) The FLL is never ideal, but disordered by random pinning effects of the vortex cores. (ii) For powder samples of anisotropic superconductors—such as the layered cuprate

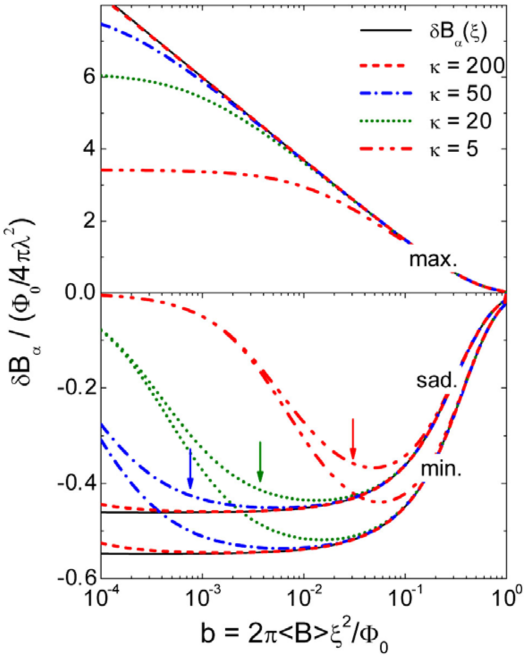

Figure 5. Characteristic fields δB_α (α = min, sad, max) calculated using the LG model as a function of the reduced field b (dashed, dotted and dash–dotted lines) for different values of κ. The black solid lines represent the curves $\delta B_\alpha(\xi)$ shown in figure 4 for $\langle B\rangle = 0.1$, 1, and 10 T. The arrows indicate the values of $b_{\min}$ at which $\langle B\rangle = B_{c1}$.

superconductors—the grains usually have random shapes, and therefore have anisotropic superconducting properties and demagnetization effects play a role [33]. (iii) The sample may contain magnetic nuclear moments or paramagnetic impurities. Vortex disorder and nuclear broadening can be taken into account by convoluting the ideal internal field distribution $P_{\mathrm{id}}(B)$ with a Gaussian distribution of width (see equation (10)) [35, 17, 39]

$$\sigma_{\mathrm{g}} = \sqrt{\sigma_{\mathrm{VD}}^2 + \sigma_{\mathrm{N}}^2}, \tag{15}$$

where σ_{VD} and σ_{N} are the contributions to the Gaussian broadening of $P_{\mathrm{id}}(B)$ due to vortex disorder and nuclear depolarization, respectively[5]. For $\kappa \gg 1$ the standard deviation of the vortex core positions from the ideal positions in the FLL $\langle s^2\rangle^{1/2}$ is related to σ_{VD} by the following equation [17]:

$$\sigma_{\mathrm{VD}} \propto \lambda^{-2}(1-b)\frac{\langle s^2\rangle^{1/2}}{a}. \tag{16}$$

Here $b = \langle B\rangle/B_{c2}$, and a is the intervortex distance.

Figure 6 shows examples of $P(B)$ for $\lambda = 200$ nm, $\xi = 4$ nm, $\langle B\rangle = 0.1$ T, and for various values of σ_{g}, calculated by means of the LG model. It is obvious that with increasing

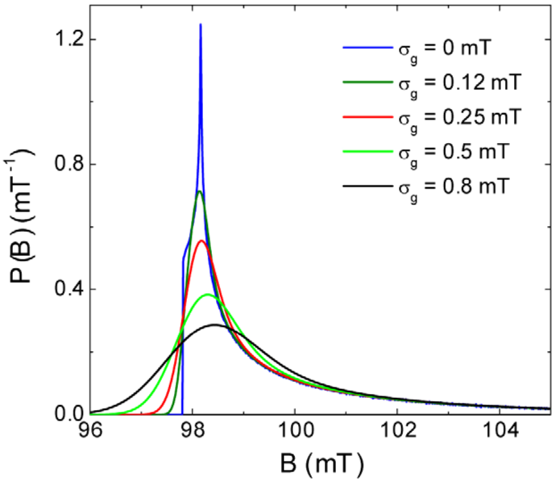

Figure 6. Change of the local magnetic field distribution $P_{\mathrm{id}}(B)$ for an ideal FLL after convolution with a Gaussian distribution of various widths σ_{g}. The following parameters were used to generate $P_{\mathrm{id}}(B)$ with the LG model: $\lambda = 200$ nm, $\xi = 4$ nm, and $\langle B\rangle = 100$ mT.

degree of disorder the Van Hove singularities in the ideal internal field distribution $P_{\mathrm{id}}(B)$ are smeared out. Note that the low field part of $P_{\mathrm{id}}(B)$ is mainly truncated by the Gaussian smearing, whereas the high field tail is nearly unaffected.

4. Comparison of different models

In this section the different models (LG, ML, AGL, and NGL) discussed in this work are compared. For this purpose the NGL model is used as a reference model for describing the mixed state of a type-II superconductor. In section 2 we showed that the characteristic fields δB_α for $\kappa \gg 1$ may be represented by single curves (see figure 5). Figure 7 shows the characteristic fields δB_α as a function of the reduced magnetic field $b = \langle B\rangle/B_{c2}$ in the limit of $\kappa \to \infty$ as calculated using the LG, ML, AGL, and NGL models. For small b values $\delta B_{\min}(b)$ and $\delta B_{\mathrm{sad}}(b)$ coincide for all models. Deviations of the AGL and LG models from the NGL model appear above $b \approx 0.01$. Although the AGL and LG models may fit well the μSR spectra simulated using the NGL model, the fitted values of ξ may deviate substantially from the *real values* for reduced magnetic fields $b \gtrsim 10^{-2}$. This systematic deviation increases with increasing magnetic field. For the LG model, in contrast to the AGL model, the systematic errors even change sign with increasing magnetic field. One should note that for $\kappa > 5$ there is no advantage of using the AGL model instead of the LG model. Of all the models the ML model approximates best the NGL model up to about $b \simeq 0.1$, in agreement with previous results of Brandt [13]. However, at higher fields this model substantially deviates from the NGL model. The ML model has often been used to analyze experimental data for $b > 0.1$ [3, 29]. We found that μSR spectra simulated using the NGL model in the range $b = 0.1$–1 may well be fitted with the ML model. But for $b > 0.1$ the values of ξ extracted from the simulated μSR spectra are artificially reduced compared to the real values of ξ (see figure 7). For

---

[5] For powder samples with a Gaussian distribution of the first moments $\langle B\rangle$ due to Gaussian distribution of demagnetization factors N one may add an additional term $\sigma^2_{\langle B\rangle}$ to equation (15).

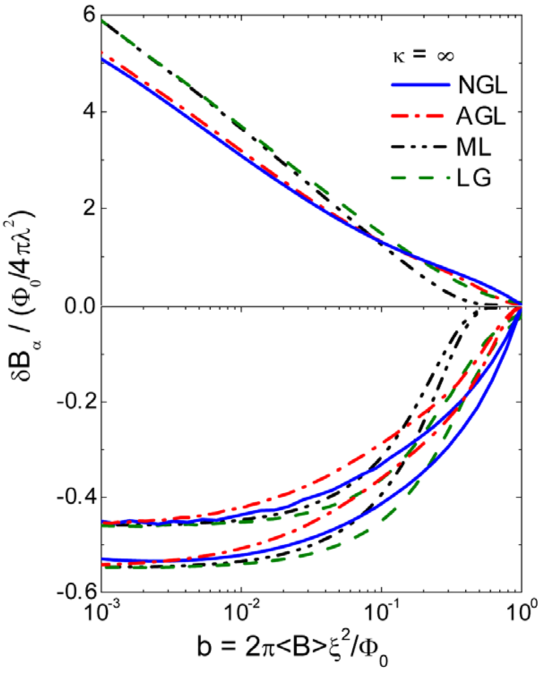

Figure 7. Characteristic fields δB_α (α = min, sad, max) as a function of the reduced field $b = 2\pi\langle B\rangle\xi^2/\Phi_0$ for $\kappa = \infty$, as calculated using the LG, ML, AGL, and NGL models.

smaller values of κ, the characteristic fields δB_α for the ML, AGL, and NGL models behave similarly to those of the LG model (see figure 5). Namely, for high reduced fields b all the curves with different values of κ coincide. The smaller κ, the higher the reduced field b when they start to deviate from the curves shown in figure 7. The only exception is for the AGL model, for which for $\kappa \leqslant 5$ the curves become closer to the NGL curves. Here we should mention that our results obtained with the NGL model are in full agreement with the calculations of Brandt [4].

5. Simulation and fitting of μSR spectra

In order to check the conclusions we reached in the previous sections 'experimentally', μSR time spectra with known parameters ($\langle B\rangle, \lambda, \xi, \sigma_g$) were simulated using the LG and NGL models. For the simulation of the μSR experiment a transverse field (TF) configuration with two positron detectors D1 and D2 located on opposite sides of the sample was used. The number of positrons detected by the detector D1 at time $t_i = i\Delta t$ is $N_1(t_i)\Delta t$ ($i = 1, 2, \ldots, 8000$; Δt was chosen to be 1.25 ns, corresponding to a typical time resolution for the GPS spectrometer at the Paul Scherrer Institute, Switzerland). This positron count number obeys Poisson statistics, and the standard deviation is simply given by $\sqrt{N_1(t_i)\Delta t}$. In the ideal case of no noise, the detector D1 would detect the signal $n_1(t_i) = n_0 \mathrm{e}^{-t_i/\tau_\mu}[1 + P(t_i)]$, where n_0 is a constant depending on the number of muons detected (statistics) and the time interval Δt, $\tau_\mu = 2.197\,019(21)$ μs is the muon lifetime, and $P(t_i)$ is the noiseless μSR time signal (see equation (11)) to which noise has to be added. The signal monitored by detector D1 can be simulated using the equation $N_1(t_i) = n_1(t_i) + \sqrt{n_1(t_i)}g_i$, where g_i is a random number generator obeying Gaussian statistics with standard deviation and variance equal to 1. A similar signal but with opposite phase is registered by detector D2. In analogy to real μSR experiments one can calculate the asymmetry [1, 3] $A(t_i) = [N_1(t_i) - N_2(t_i)]/[N_1(t_i) + N_2(t_i)]$, yielding $P(t_i)$ with 'experimental noise'. The μSR time spectra were simulated according to the procedure described above with total statistics of 20 million events, a value typically used in real experiments.

The simulated μSR time spectra were then analyzed as follows.

1. The μSR spectra simulated using the NGL model were analyzed by the second-moment (SM) method.
2. The μSR spectra simulated using the LG model were analyzed using a fitting procedure based on the LG model.

According to the discussions in the previous sections the following important questions emerge.

1. How reliable is the second moment obtained using a multi-Gaussian fit of the μSR spectra (see equation (17)) and the value of the penetration depth λ extracted from the second moment?
2. Is there a correlation between σ_g and $1/\lambda^2$, since both of them influence the second moment of the μSR spectrum?
3. Is it possible to extract reliable values of ξ from μSR spectra at low magnetic fields $b \simeq 10^{-3}$?
4. Is there a correlation between λ and ξ at high fields (since for $b \approx 0.1$–0.9 both parameters strongly influence the characteristic fields δB_α)?

5.1. *Test of the second-moment method*

In this section the second-moment (SM) method is tested by analyzing μSR time spectra simulated using the NGL model with well defined parameters ($\langle B\rangle, \lambda, \xi, \sigma_g$). The SM method is theoretically well described in the literature [13, 38, 4] and was extensively used to extract the magnetic penetration depths of extreme type-II superconductors from μSR spectra [6–12]. In the framework of this method the μSR time spectra are usually fitted to a sum of N Gaussian components [33, 34]:

$$P(t) = \sum_{i=1}^{N} A_i \exp(-\sigma_i^2 t^2/2)\cos(\gamma_\mu B_i t + \phi). \qquad (17)$$

Here ϕ is initial phase of the muon beam, and A_i, σ_i, and B_i are the asymmetry, the relaxation rate, and the first moment of the ith Gaussian component, respectively. From the fit parameters A_i, σ_i, and B_i one readily obtains the first and the second moment of $P(B)$ from equations (3) and (4), respectively. Using equation (1) one finds the penetration depth λ. Here a serious question arises: How reliable is the value of λ obtained by the SM method using a multi-Gaussian fit? In order to investigate this question μSR time spectra were simulated using the NGL model for an extreme type-II superconductor (such as the cuprate superconductors) with a Ginzburg–Landau parameter $\kappa = 50 \gg 1$. The temperature dependence of λ was assumed to follow the relation (two-fluid model) $\lambda(T)^{-2}/\lambda(0)^{-2} = [1-(T/T_c)^4]$ with $T_c = 22.5$ K and $\lambda(0) = 200$ nm (zero-temperature penetration depth). This approximately corresponds to the temperature dependence of λ in the strong-coupling BCS case [40]. In the first step we assume that there is no vortex disorder ($\sigma_{VD} = 0$) and no nuclear depolarization ($\sigma_N = 0$) present (cf equation (15)). The simulations were performed for three different magnetic fields: $\langle B\rangle = 0.05$, 0.5, and 5 T.[6] This corresponds to the reduced fields $b = 0.0024$, 0.024, and 0.24, an extremely small, an intermediate, and a high magnetic field, respectively (see figure 5). Since B_{c2} is decreasing with increasing temperature ($1/\xi^2 \propto B_{c2}$; $1/\xi^2 \propto 1/\lambda^2$ at constant κ), the analysis of the μSR spectra for $B = 5$ T makes sense only up to 21 K where $B_{c2}(21\ \text{K}) \approx \langle B\rangle$ and superconductivity disappears. Noisy μSR time spectra were simulated using the parameters λ, ξ, and $\langle B\rangle$ as described above. For the technical parameters the following typical values were used: statistics 20×10^6, asymmetry $A = 0.2$, and phase $\phi = 0$.

For the analysis of the simulated μSR spectra, $P(t)$ in equation (17) was approximated by a sum of $N = 1, 2, 3, 4, 5$ Gaussians in order to check the reliability of the result obtained using a multi-Gaussian fit. The number of Gaussians N determines the quality of the fit. N should be increased from 1 until χ^2 (normalized to the degrees of freedom) is close to 1 within statistical scattering. The total asymmetry $A = \sum_{i=1}^{N} A_i$ and the phase ϕ of $P(t)$ in equation (17) were assumed to be known and were fixed in the fitting procedure. According to our experience, in order to reduce the scattering of the fitted values of the second moment, one should fix the asymmetries A_i of the individual Gaussians to their average values obtained using a fit with all parameters free. From the first and the second moments of the individual Gaussians one can calculate the second moment $\langle\Delta B^2\rangle$ of the μSR spectrum using equation (4), which corresponds to the second moment of $P_{id}(B)$ of an ideal FLL. The magnetic penetration depth λ is readily obtained from $\langle\Delta B^2\rangle$ with equation (1). The result of the analysis of the simulated μSR time spectra for an ideal FLL is shown in figure 8. For the 0.05 T data the finite value of $\kappa = 50$ was taken into account in the coefficient C in equation (1) [4]. One can see that the smaller the field, the greater the number of Gaussians N needed to describe the spectra. Whereas for 5 T $N = 2, 3$ Gaussians are sufficient for reproducing the spectra, $N = 4$ and $N = 5$ are required for 0.5 and 0.05 T, respectively. Note that the scattering of the data points increases with increasing number of Gaussians N. Although at 0.05 T the fitted values of $1/\lambda^2$ deviate systematically from the real values by a few per cent, the qualitative behavior of $1/\lambda^2(T)$ is the same. As will be shown below by adding a Gaussian smearing σ_g to the μSR spectra, the scattering is reduced, and a smaller number of Gaussians N are needed to describe the spectra. Figure 9 demonstrates how the local magnetic field distribution $P_{id}(B)$ for an ideal FLL can be approximated by $N = 5$ Gaussians. Although not all the details of $P_{id}(B)$ are reproduced, the overall agreement is good, in particular the second moment.

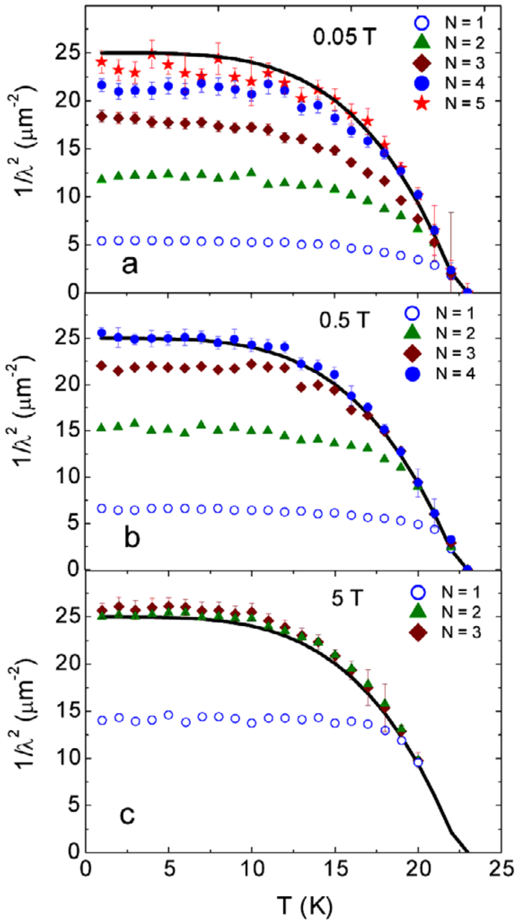

Figure 8. Fit results for λ^{-2} obtained by the second-moment method. The noisy spectra for the three different fields of 0.05, 0.5, and 5 T were simulated using the NGL method for an ideal FLL as described in the text, and then analyzed using a multi-Gaussian function with different number of Gaussians ($N = 1, 2, 3, 4, 5$) as defined in equation (17). The black solid lines correspond to the real values of λ^{-2} used for the simulation.

In order to test the second-moment method under more realistic conditions one should add a Gaussian smearing σ_g to the μSR spectra (cf equation (10)). According to equation (15), we assume for the further discussions that σ_g is composed of two components: $\sigma_g = (\sigma_{VD}^2 + \sigma_N^2)^{1/2}$, where σ_{VD} denotes the temperature dependent smearing due to vortex disorder, and σ_N is the temperature independent smearing due to nuclear depolarization (cf equation (16)). For a constant vortex disorder $\langle s^2\rangle^{1/2}/a = \text{const.}$ (rigid vortex lattice) and reduced field b, the relation $\sigma_{VD} \propto 1/\lambda^2$ holds. As is obvious from equation (16), for $\langle B\rangle = 5$ T the term $(1-b) = 0.76$ substantially deviates from unity and has to be taken into account in the simulation of μSR data.

For the simulations of the smeared μSR spectra the following values for single-crystal $La_{1.83}Sr_{0.17}CuO_{4-\delta}$ were

---

[6] In a real μSR experiment with a time binning $\Delta t = 1.25$ ns the maximal possible field for a measurement is 2.95 T (this corresponds to two binnings per precession period). At higher fields the asymmetry of the signal drops. In our simulations, unlike in experiments, we do not integrate the positron counts within the time interval Δt, but simulate the detector counts at $t_i = i\Delta t$. For this reason it is possible to simulate and fit μSR data at higher fields due to the stroboscopic effect. In this case the absolute value of the real field is the fitted field plus $N\times2.95$ T, where N is a positive integer number.

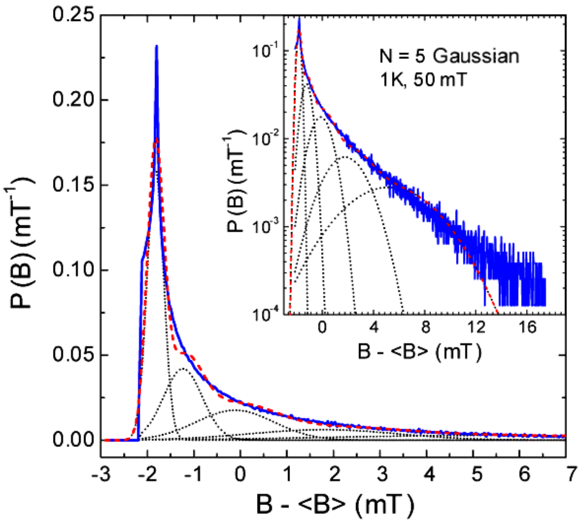

Figure 9. Comparison of the ideal field distribution $P_{\rm id}(B)$ simulated using the NGL model at 0.5 T and 1 K (blue solid line) with $P(B)$ obtained using a Gaussian fit with $N = 5$ (red dashed line). The five individual Gaussian components used for the fit are also shown (black dotted lines). The inset shows the same plot but on a semi-logarithmic scale.

used: $\sigma_{\rm VD} = \beta/\lambda^2$, $\beta = 2.585 \times 10^4$ (mT nm^2) and $\sigma_{\rm N} = \sigma_{\rm Cu} = 0.27$ mT [41]. Noisy μSR time spectra were simulated using the parameters λ, ξ, $\langle B\rangle$, and $\sigma_{\rm g}$ as described above. For the technical parameters the following typical values were used: statistics 20×10^6, asymmetry $A = 0.2$, and phase $\phi = 0$.

The total second moment $\langle \Delta B^2\rangle_{\rm t}$ of a μSR spectrum with Gaussian smearing $\sigma_{\rm g}$ obtained using a multi-Gaussian fit contains three components:

$$\langle \Delta B^2\rangle_{\rm t} = \langle \Delta B^2\rangle + \sigma_{\rm VD}^2 + \sigma_{\rm N}^2, \qquad (18)$$

where $\langle \Delta B^2\rangle$, $\sigma_{\rm VD}^2$, and $\sigma_{\rm N}^2$ are the second moments due to the internal field variation in the ideal FLL, the vortex disorder, and the nuclear depolarization, respectively. In order to obtain λ from the total second moment measured in real experiments one determines $\sigma_{\rm N}$ above $T_{\rm c}$, and assumes that $\sigma_{\rm VD}^2 \ll \langle \Delta B^2\rangle$ in equation (18), i.e. $\langle \Delta B^2\rangle_{\rm t} \simeq \langle \Delta B^2\rangle + \sigma_{\rm N}^2$ [42]. From the first and the second moments of the individual Gaussians one can calculate the total second moment $\langle \Delta B^2\rangle_{\rm t}$ of the μSR spectrum using equation (4) (note that in equation (4) $\langle \Delta B^2\rangle$ has to be replaced by $\langle \Delta B^2\rangle_{\rm t}$ for the case $\sigma_{\rm g} \neq 0$). By means of equations (18) and (1) the magnetic penetration depth λ then is readily obtained. Figure 10 shows the results for the penetration depth obtained by the second-moment method with $N = 1, 2, 3, 4$ Gaussians. Note that a single Gaussian does not give reliable results in agreement with earlier findings [33]. However, with increasing number of Gaussians N the quality of the fits substantially improves. In order to fit the simulated data at 0.05 T at least three or, better, four Gaussians are required. For $N = 3$ there is a systematic deviation of about 10% of λ^{-2} from the real value (or 5% for λ), whereas for $N = 4$ the values of λ^{-2} are scattered within a few per cent around the real ones. For the data simulated at 0.5 T even $N = 3$ Gaussians are sufficient for describing the local magnetic field distribution $P(B)$, and the values of λ^{-2} are systematically shifted only within a few per cent. Figure 11 shows an example of a real internal field distribution $P(B)$ ($\langle B\rangle = 0.5$ T, $T = 1$ K of figure 10) and the reconstructed $P(B)$ obtained from the analysis of the simulated μSR spectrum (2×10^7 statistics) using a Gaussian fit with $N = 3$. It is obvious that three Gaussians describe well the shape of the real $P(B)$. The largest systematic error in λ^{-2} obtained using a multi-Gaussian fit is observed at 5 T ($b = 0.24$). At such a high field ($\langle B\rangle \simeq B_{\rm c2}/4$) the variation of the internal field is relatively small (see figure 7), and the Gaussian smearing $\sigma_{\rm VD}$ (cf equation (18)) due to vortex disorder becomes essential. The second moment of this Gaussian smearing cannot be neglected and considerably contributes to the total second moment $\langle \Delta B^2\rangle_{\rm t}$ of $P(B)$. This leads to systematically higher values of λ^{-2} obtained using multi-Gaussian fits at high magnetic fields. Note, however,

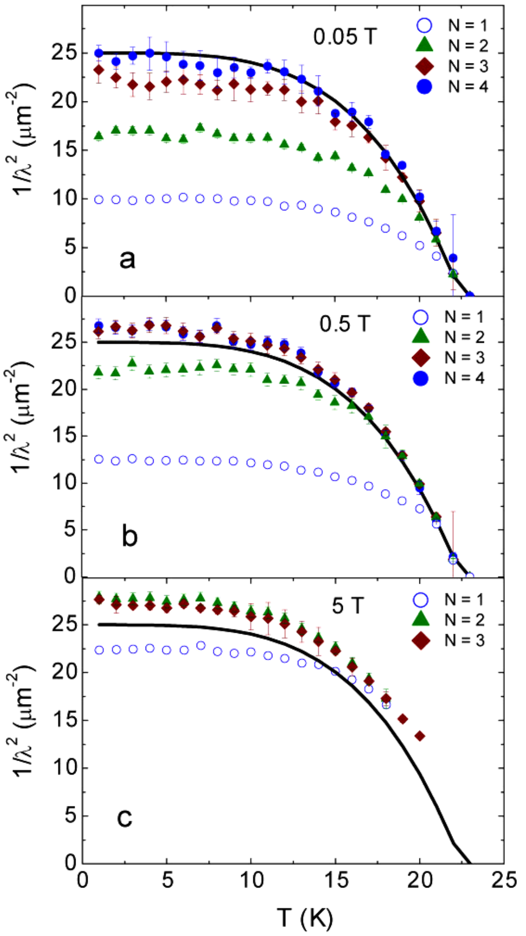

Figure 10. Fit results for λ^{-2} obtained by the second-moment method. The noisy spectra for the three different fields of 0.05, 0.5, and 5 T were simulated using the NGL method including Gaussian smearing $\sigma_{\rm g}$ as described in the text, and then analyzed using a multi-Gaussian function with different numbers of Gaussians ($N = 1, 2, 3, 4$), as defined in equation (17). The black solid lines correspond to the real values of λ^{-2} used for the simulation.

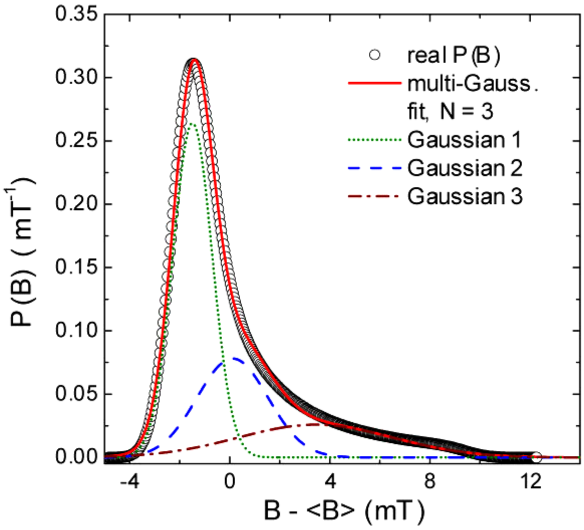

Figure 11. Comparison of the real field distribution $P(B)$ (empty circles) simulated using the NGL model for parameters $\lambda = 200$ nm, $\xi = 4$ nm, $\langle B\rangle = 0.5$ T, $\sigma_g = 0.7$ mT (the data point at $T = 1$ K for $N = 3$ in figure 10(b)) with $P(B)$ obtained using a Gaussian fit with $N = 3$ (red solid line). The dotted, dashed, and dash–dotted lines represent individual Gaussian components used for the fit. It is obvious that a multi-Gaussian fit may well describe the real $P(B)$.

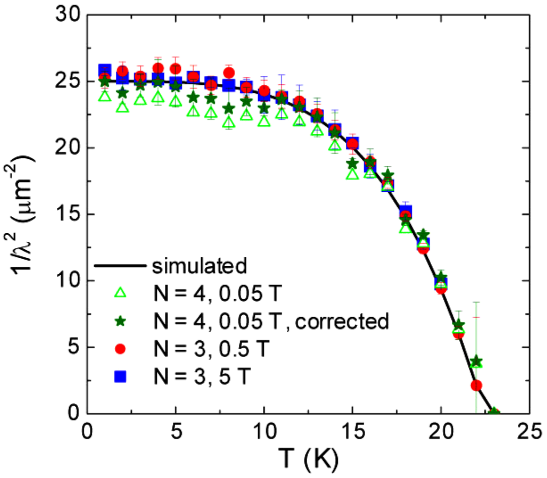

Figure 12. Temperature dependence of $1/\lambda^2$ determined from $\langle\Delta B^2\rangle$, assuming that σ_{VD} is known as described in the text. Triangles: $N = 4$, 0.05 T; stars: $N = 4$, 0.05 T, corrected for finite $\kappa = 50$ (see the text for an explanation); circles: $N = 3$, 0.5 T; squares: $N = 3$, 5 T.

that there are two reasons why the contribution to the second moment due to vortex disorder is reduced with increasing magnetic field, and consequently the systematic error in λ^{-2}. (1) At high fields $\sigma_{VD} \propto (1 - b)$ (cf equation (16)), which was taken into account in the simulations of the μSR spectra. (2) Vortex disorder, $\langle s^2\rangle^{1/2}/a$, is expected to decrease with increasing magnetic field, because of the strong repulsive interaction between the vortices at high fields (see e.g. [4]).

By means of a multi-Gaussian fit it is not possible to separate $\langle\Delta B^2\rangle$ and σ_{VD} from the measured total second moment $\langle\Delta B^2\rangle_t$ (cf equation (18)). Assuming that $\sigma_{VD} = 0$ yields a lower limit for λ (upper limit for $1/\lambda^2$), as clearly demonstrated in figures 10(b) and (c) where the values of $1/\lambda^2$ are systematically too large. It is interesting to investigate what the values of $1/\lambda^2$ are after correction with the real value of σ_{VD}. For this purpose we write equation (16) in the form $\sigma_{VD} = \beta\lambda^{-2}$ and with the help of equations (1) and (18) we obtain

$$\lambda^{-2} = [C/(1+\epsilon)]^{1/2}[\langle\Delta B^2\rangle_t - \sigma_N^2]^{1/2}, \qquad (19)$$

where $\epsilon = C\beta^2$ is the correction due to vortex disorder. The values of $1/\lambda^2$ plotted in figure 10 were obtained with $\epsilon = 0$ (no vortex disorder correction). Figure 12 shows some of the results of figure 10 after correcting the values of $1/\lambda^2$ with the values of $\epsilon_{T=0} = 0.050, 0.073$, and 0.155 for 0.05 T, 0.5 T, and 5 T, respectively (ϵ is temperature dependent, since $C(b(T), \kappa)$ is temperature dependent). The corrected values of $1/\lambda^2$ are in good agreement with the real values (solid line in figure 12), except for the data at 0.05 T where a systematic deviation of about 5–10% is observed. One of the reasons for this deviation is that $\kappa = 50$ used in the simulations is not infinite. This implies that at 0.05 T ($b \simeq 0.0024$) the parameter $C^{-1/2}$ in equations (1) and (19) is about 5% smaller [4]. The stars in figure 12 represent the corrected values of $1/\lambda^2$ at 0.05 T, which are only about 3% systematically lower than the real values.

5.2. Test of the London model with Gaussian cut-off (LG)

In order to test the reliability of the advanced methods described in section 2 we first simulated noisy μSR spectra and then fitted them like with the second-moment method. To avoid systematic errors in the fit results it is important to analyze the data using the same model as they were simulated. Here we present results for the LG model, since it can approximate experimental data well over the whole field range (see figure 7). Similar results are also obtained with all other models. The temperature dependence of the penetration depth λ was assumed to follow the relation $\lambda^{-2}(T)/\lambda^{-2}(0) = [1 - (T/T_c)^2]$ with $\lambda(0) = 200$ nm and $T_c = 22.5$ K. The Ginzburg–Landau parameter $\kappa = 50$, and Gaussian smearing $\sigma_g(T) = (\sigma_{VD}^2(T) + \sigma_N^2)^{1/2}$ [$\sigma_{VD} \propto 1/\lambda^2(T)$] was chosen, to be the same as in section 5.1. Again the μSR spectra were simulated for three different mean fields $\langle B\rangle = 0.05$, 0.5, and 5 T ($b = 0.0024, 0.024, 0.24$). As before the mean field was assumed to be temperature independent. The statistics, asymmetry, and phase of the μSR time spectra were chosen to be 20×10^6, 0.2, and 0, respectively.

The results of the fits of the simulated μSR spectra with all the parameters free (except A and ϕ) are shown in figure 13. Phase ϕ and asymmetry A were assumed to be known and were fixed to their real values. In order to exclude any artificial influence on the fitting procedure we performed the fits in automatic mode. This means that with increasing temperature the fit results for temperature T_i were used as initial parameters for the next temperature T_{i+1}. For T_1 (lowest temperature) the

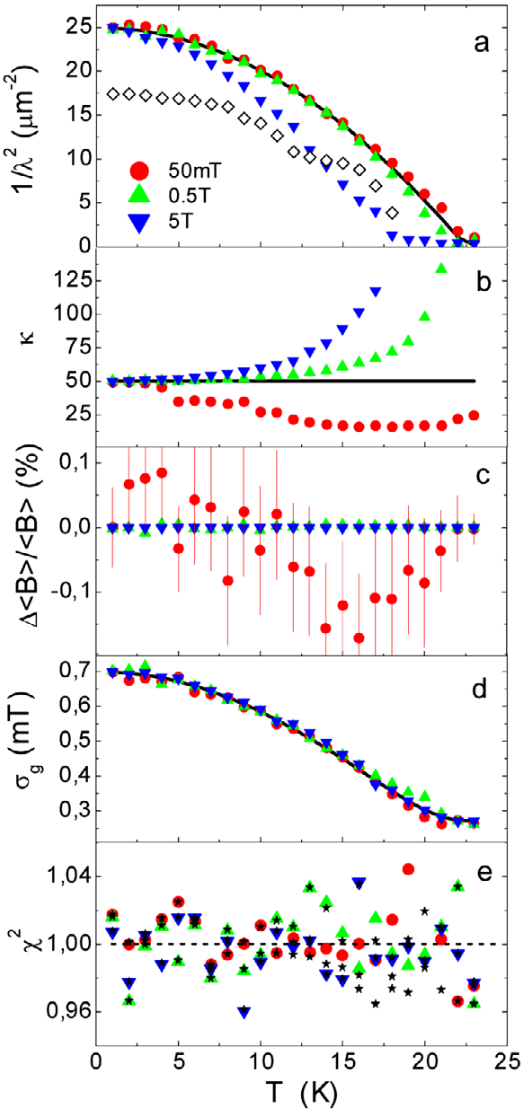

Figure 13. Summary of the fit results for the μSR spectra simulated using the LG model. The fitted values $1/\lambda^2$, κ, $\Delta\langle B\rangle/\langle B\rangle$, and σ_g, as well as χ^2, are plotted as a function of temperature T for three different fields 0.05 T (circles), 0.5 T (upward-pointing triangles), and 5 T (downward-pointing triangles) for 20 million statistics. The parameters $1/\lambda^2$, κ, $\Delta\langle B\rangle/\langle B\rangle$, and σ_g were free during the fitting procedure. The solid lines correspond to the true values of the parameters. $\Delta\langle B\rangle/\langle B\rangle = (\langle B\rangle_{\mathrm{fit}} - \langle B\rangle_{\mathrm{real}})/\langle B\rangle_{\mathrm{real}}$ denotes the relative deviation of the fitted value $\langle B\rangle_{\mathrm{fit}}$ from the real $\langle B\rangle_{\mathrm{real}}$. For comparison χ^2 was also determined for the real values of the parameters (black stars). The black empty diamonds in (a) show a possible fit result for $1/\lambda^2$ at 5 T with extremely wrong initial parameters. Note that the error bars of $1/\lambda^2$, as calculated using the fitting program (the function 'fit' of the MATLAB program was used), are within the point size ($\simeq$2%).

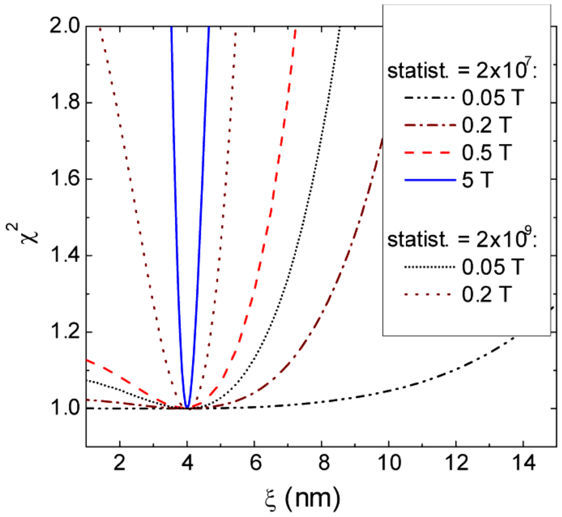

Figure 14. χ^2 as a function of ξ for the μSR spectra simulated using the LG model with 20 million counts, $\langle B\rangle = 0.05$, 0.2, 0.5, and 5 T, $\lambda = 200$ nm, $\xi = 4$ nm, and $\sigma_g = 0.7$ mT. For comparison $\chi^2(\xi)$ is also shown for the higher statistics of 2000 million at $\langle B\rangle = 0.05$ and 0.2 T. The statistically scattered minimal value of χ^2 was normalized to 1. Note that the dependence of χ^2 on ξ at low fields is weak.

correct initial parameters were used. As shown in figure 13 for λ^{-2} we got good results at low fields; however there are substantial systematic deviations for κ. At the highest field there are substantial systematic deviations of the fitted values for both λ and κ, although the goodness of fit χ^2 for these fits is comparable to those for the correct parameters (figure 13). The values of χ^2 weighted and normalized to the degrees of freedom ($\approx$8000) scatter around 1 within 0.04, as expected for the present degrees of freedom. The black stars in figure 13 denote χ^2 for the true values of the parameters for comparison. From all the fitted parameters, the values obtained for κ deviate most from the real ones for all the fields. In order to check the reason for this strong deviation for κ at 0.05 T, the fit was performed using different initial parameters. For λ, $\langle B\rangle$, and σ_g correct values within a few per cent were obtained, whereas ξ was found to be in the range 2–13 nm with a very good value of χ^2. The dependence of χ^2 on ξ for different fields and statistics is demonstrated in figure 14. It is evident that at low fields and 20 million statistics the quality of the fit is practically independent of ξ over a very broad range. For the 5 T data not only κ but also λ substantially deviates from the real value (see figure 13). The good agreement at low temperatures is misleading, since it is only due to the correct initial parameters that we set for the lowest temperature. The empty black diamonds in figure 13(a) show the fit result for intentionally extremely wrong starting parameters. In real measurements one never knows the optimal starting parameters. We performed fits of the 5 T data at $T = 1$ K with different starting values of λ, ξ, $\langle B\rangle$, and σ_g. It was found that for $\langle B\rangle$ and σ_g one obtains values close to the real ones; however, for λ and ξ this is not the case. Figure 15 shows the variation of the values of λ and ξ during the fitting process. The starting values of λ and ξ are indicated by number $\boxed{1}$. The numbers $\boxed{2}$, $\boxed{3}$, …, $\boxed{10}$ indicate the values of λ and ξ after each five fitting iterations. The maximal number of fitting iterations was not restricted. However, 50 iterations were usually sufficient, and the fit was terminated when the relative changes of all the parameters during the iteration were

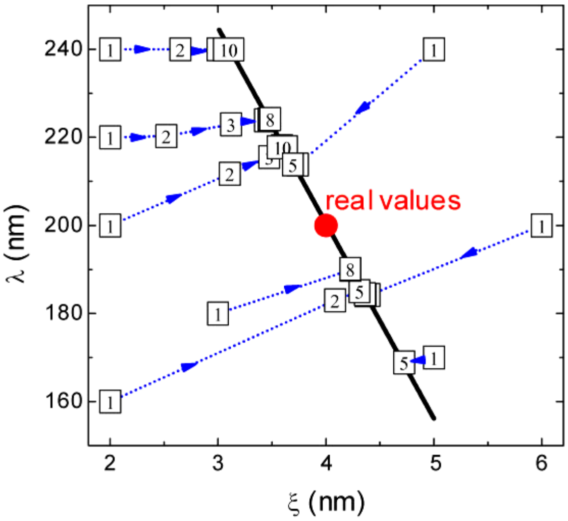

Figure 15. Visualization of the fitting process of the simulated μSR spectrum for the parameters $\lambda = 200$ nm, $\xi = 4$ nm, $\langle B\rangle = 5$ T, $\sigma_g = 0.7$ mT using the LG model. Number $\boxed{1}$ indicates the starting values for λ and ξ. The numbers $\boxed{2}, \boxed{3}, \ldots, \boxed{10}$ denote the values of λ and ξ after each five iterations of the fitting process. The fit was terminated when relative changes of all the parameters were less than 10^{-6}. The solid line shows the points in the λ versus ξ plane where the fit is finally converging. Note that the fit results for the other parameters $\langle B\rangle$ and σ_g are close to the real ones, independently of the starting values.

less than 10^{-6}. The final results of the fit eventually correspond to local minima of χ^2. The fit converges on a certain $\lambda = \lambda(\xi)$ curve denoted by the black line in figure 15, indicating a possible correlation between λ and ξ at high fields. Therefore, we can conclude that the determination of a reliable value of ξ is problematic at low fields as expected (see figure 3). At higher fields not only the value of ξ, but also the value of λ may systematically deviate from the real value. However, at low fields reliable values of $\langle B\rangle$, σ_g, and λ may presumably be well determined from fits with the advanced models.

The next step for improving the fitting procedure is to restrict some parameters. On the basis of the results obtained from the free parameter fits we conclude that a good candidate for restriction is ξ, especially at low fields. One can fix κ in order to relate ξ to λ via $\xi = \lambda/\kappa$ and let the other parameters λ, $\langle B\rangle$, and σ_g be free. This is also reasonable from a theoretical point of view. In the BSC approximation κ does not change substantially with temperature in the weak-coupling limit [43]. The results of the fits with the only restricted parameter κ (i.e., ξ was calculated with $\xi = \lambda/\kappa$) are shown in figure 16. It is obvious that the fits are excellent and all the parameters are very close to the real ones with only small statistical scattering.

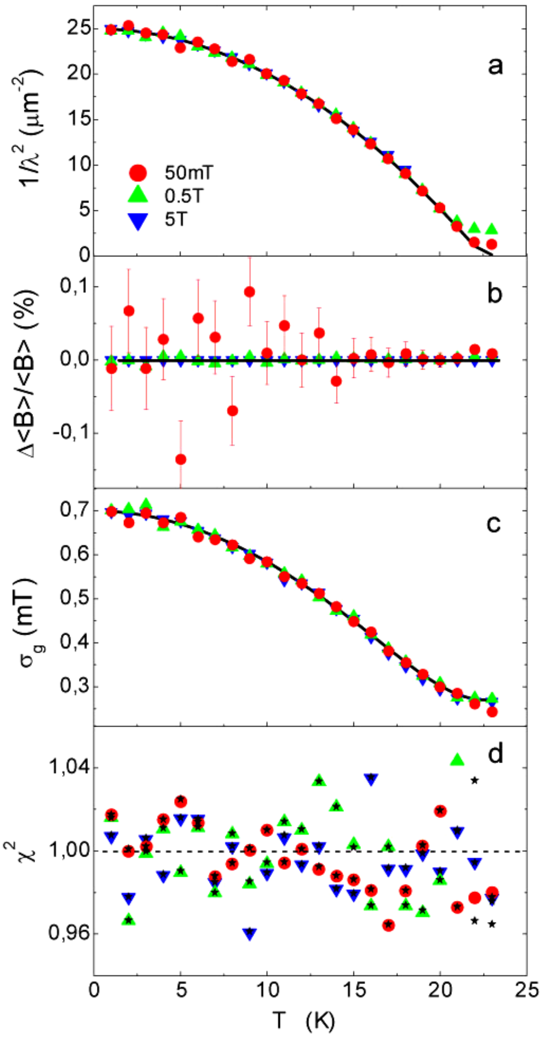

Figure 16. Summary of the fit results for the μSR spectra simulated using the LG model. The fitted values $1/\lambda^2$, $\Delta\langle B\rangle/\langle B\rangle$, and σ_g, as well as χ^2, are plotted as a function of temperature T for three different fields 0.05 T (circles), 0.5 T (upward-pointing triangles), and 5 T (downward-pointing triangles) for 20 million statistics. The parameters $1/\lambda^2$, $\Delta\langle B\rangle/\langle B\rangle$, and σ_g were free during the fitting procedure, whereas κ was fixed at the real value. The solid lines correspond to the true values of the parameters. $\Delta\langle B\rangle/\langle B\rangle = (\langle B\rangle_{\mathrm{fit}} - \langle B\rangle_{\mathrm{real}})/\langle B\rangle_{\mathrm{real}}$ is the relative deviation of the fitted value $\langle B\rangle_{\mathrm{fit}}$ from the real one $\langle B\rangle_{\mathrm{real}}$. For comparison χ^2 was also determined for the real values of the parameters (black stars).

5.3. Correlation between σ_g and λ^{-2} for small values of b

As shown in figure 6, with increasing Gaussian smearing σ_g the characteristic fields of the internal magnetic field distribution $P_{\mathrm{id}}(B)$ of the ideal FLL are gradually washed out, and $P(B)$ tends to become an asymmetric Gaussian-like distribution. Therefore, one expects some correlation between σ_g and the inverse square of the penetration depth $1/\lambda^2$, since both of them influence the second moment of the μSR spectrum. In order to show the possibility of extracting the real values of λ and σ_g from μSR spectra, we simulated μSR data using the ML model and then calculated the goodness of fit χ^2 as a function of λ and σ_g with the other parameters fixed to their true values. Figure 17(a) shows χ^2 as a function of λ with the other parameters fixed to their true values. For the simulated data the following parameters were used: $\lambda_0 = 200$ nm,

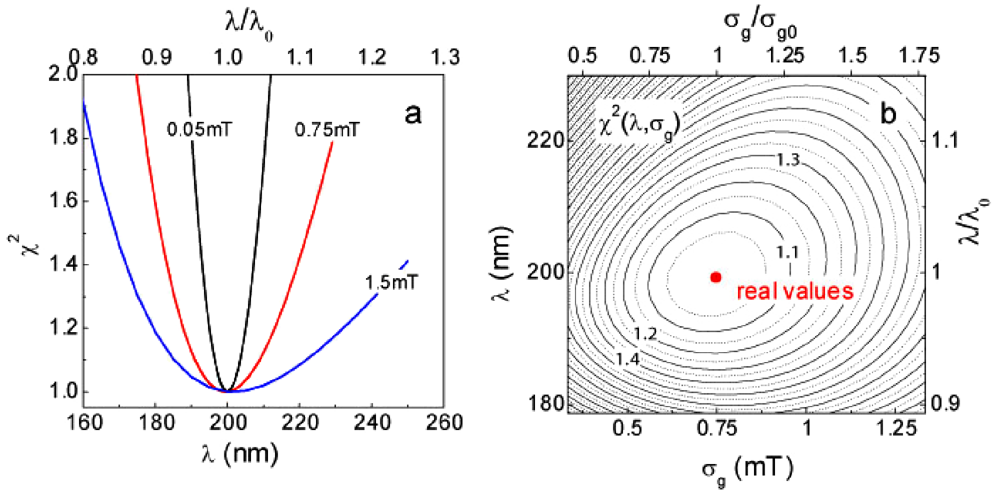

Figure 17. (a) χ^2 as a function of λ with the other parameters set to the true values. The following parameters were used for the μSR data simulation: $\lambda_0 = 200$ nm, $\xi_0 = 1$ nm, $b_0 = 10^{-3}$, 20 million statistics, and $\sigma_{g0} = 0.05$, 0.75, and 1.5 mT. (b) Contour plot of χ^2 as a function of λ and σ_g for the data simulated using $\lambda_0 = 200$ nm, $\xi_0 = 1$ nm, $b_0 = 10^{-3}$, $\sigma_{g0} = 0.75$, and 20 million counts (red point). In both figures the ML model was used for the calculations, and the statistically scattered minimal value of the χ^2 was normalized to 1. The real values of λ and ξ are indicated by the red point.

$\xi_0 = 1$ nm, $b_0 = 10^{-3}$, $\sigma_{g0} = 0.05$, 0.75, 1.5 mT, and 20 million counts. It is evident that with increasing σ_{g0} the error of λ extracted from the fit increases. Figure 17(b) shows a contour plot of χ^2 as a function of λ and σ_g calculated for data with $\lambda_0 = 200$ nm, $\xi_0 = 1$ nm, $b_0 = 10^{-3}$, $\sigma_{g0} = 0.75$, and 20 million statistics. This approximately corresponds to the case that we analyzed before. From the figure we conclude that λ^{-2} and σ_g are slightly correlated, but it is possible to extract them simultaneously if ξ is fixed. This agrees well with the results of the analysis performed in section 5.2.

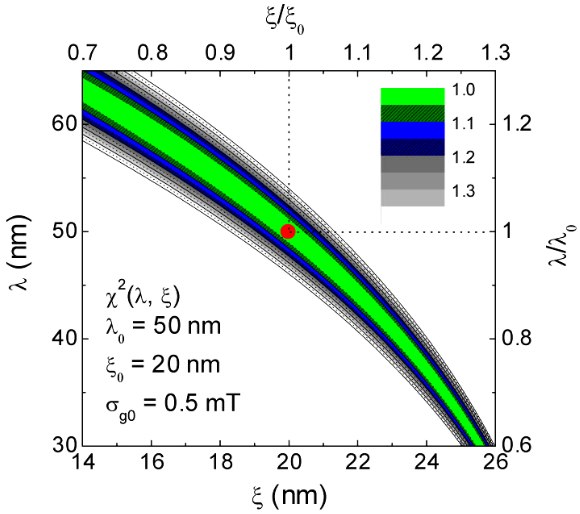

Figure 18. Contour plot of χ^2 as a function of λ and ξ for the data simulated using parameters $\lambda_0 = 50$ nm, $\xi_0 = 20$ nm, $b_0 = 0.5$, $\sigma_{g0} = 0.5$ mT, and 20 million counts, calculated using the NGL model. The fitted parameters λ and ξ exhibit a strong correlation, which is the reason for the pronounced systematic deviations of the fitted values of λ^{-2} and κ at 5 T from the real values displayed in figure 13. The statistically scattered minimal value of χ^2 is normalized to 1. The real values of λ and ξ are indicated by the red point.

5.4. Correlation between ξ and λ

For low magnetic fields the dependence of the μSR spectrum on the coherence length ξ is very weak (see figure 14). But with field increasing towards B_{c2} the shape of the spectrum becomes dependent not only on the penetration depth λ, but also on ξ (see figure 7). An increase of λ and/or ξ causes a decrease of the second moment and the characteristic fields. Therefore, it is expected that a decrease of λ is correlated with an increase of ξ in the fitting procedure and vice versa. So far, to our knowledge, this problem has been discussed previously only by Riseman *et al* [17]. Here we study this problem in more detail. For this procedure we determined χ^2 for simulated μSR data as a function of λ and ξ at fixed $\langle B\rangle_0 = 0.5B_{c2}$ and Gaussian smearing $\sigma_{g0} = 0.5$ mT. We have chosen the case of a relatively small $\kappa_0 = 2.5$ ($\lambda_0 = 50$ nm and $\xi_0 = 20$ nm) for the data simulation, since the relative volume of the vortex cores is large, and therefore it is easier to extract ξ from the fits. As before, the statistics were 20×10^6. The result of the analysis with the NGL model is shown in figure 18, where a contour plot of χ^2 as a function of λ and ξ with the other parameters fixed is displayed. There is indeed a strong correlation between λ and ξ. For $\lambda(\xi) \approx 58.68 + 2.14\xi - 0.127\xi^2$, where $\chi^2 \simeq 1$ is minimal, the fits converge after a few hundred iterations. Tests showed that for different starting parameters the fits were converging in the correlated region of $\xi = 14$–24 nm and $\lambda \approx 36$–63 nm. This region lies within the interval of $\chi^2 < 1.05$ (see figure 18). It should be noted that for such a high reduced field $b = 0.5$ as was used here for the analysis, the qualitative dependences of the characteristic fields δB_α on λ, ξ, and $\langle B\rangle$ are independent of $\kappa = \lambda/\xi$ (see figure 5). Therefore the qualitative behavior of the contour plot of $\chi^2(\lambda/\lambda_0, \xi/\xi_0)$ in figure 18 is independent of $\kappa_0 = \lambda_0/\xi_0$ for any $\kappa_0 > 5$.

The situation could be improved for fields $b \simeq 10^{-2}$ where the minimal and saddle point fields slightly depend on ξ (see figure 7), and on the other hand the maximal field is not very large and still depends on ξ. However, with decreasing field, the vortex core volume substantially reduces which is disadvantageous for the data analysis as discussed above. Figure 19 shows a similar contour plot of $\chi^2(\lambda, \xi)$ for noisy data simulated using the NGL and ML models with parameters $\lambda_0 = 200$ nm, $\xi_0 = 4$ nm ($\kappa_0 = 50$), $\sigma_{g0} = 0.7$ mT, 20 million statistics, and $b_0 = 0.004$, 0.02, and 0.1. This corresponds approximately to the analysis of the simulated data that we discussed before. There is a substantial correlation between λ and ξ at all fields. For $b_0 = 0.1$ the analysis yields $\xi = 4(1)$ nm (correlated with λ), for $b_0 = 0.02$ only an upper limit of $\xi \simeq 5$ nm can be given, and for $b_0 = 0.004$ (0.082 T) the fit is practically independent of ξ at 20 million statistics. However, at unrealistically high statistics the dependence of χ^2 on λ and ξ becomes stronger (see figure 14), and the precision of the parameters extracted from the fit increases as the square root of the statistics. Another way of solving this problem was proposed by Riseman *et al* [17]: by simultaneously fitting several spectra measured at different fields with common values of the parameters λ and ξ. This has two advantages. (1) It effectively increases the statistics. (2) Since the correlation curve $\lambda(\xi)$ changes their slope with field (see figure 19), the total contour graph of $\chi^2(\lambda, \xi)$ will shrink, allowing a determination of the correct parameters. For example in the case of a high value of κ and extremely small field b, one can determine the correct value of λ (independently of the value of ξ), and with the known value of λ it is possible to evaluate a reliable value of ξ at high field by means of the correlation curve $\xi(\lambda)$. This procedure can be justified at least for conventional superconductors. Recently, Landau and Keller [32] reanalyzed μSR data for various conventional superconductors and convincingly demonstrated that in many cases type-II superconductors can be described by a field independent penetration depth. The present results are also relevant for the interpretation of small-angle neutron scattering (SANS) experiments in the mixed phase of type-II superconductors, since the strong correlation between λ and ξ is also present in Fourier components of the FLL [44].

We can conclude that in general a simultaneous determination of ξ and λ from μSR spectra without additional restrictions is not easy, regardless of the model used to describe the vortex state. At high κ and low fields there is practically no dependence of the spectra on ξ, and at high fields ξ is strongly correlated with λ. As demonstrated in figures 3, 5, and 7 this is independent of the value of κ and the model used. It is important to add that in our analysis of the μSR data using the advanced models, we used the same model for the simulations and the analysis, which reduces systematic errors to a minimum. In practice, there is often no adequate model for the description of the experimental μSR spectra, as for instance for unconventional superconductors such as the cuprate superconductors. In this case additional difficulties in the data analysis are expected. In the analysis of the μSR spectra in section 5 we did not consider background signals arising from impurity fractions/phases in the sample and/or from muons stopping in the sample holder or other parts of the spectrometer. These background signals may be a hidden source of uncertainties in the determination of reliable parameters from μSR spectra. The introduction of additional fit parameters in the advanced models should be done only with great care, since already the existing minimal set of parameters of the models are, in general, difficult to extract.

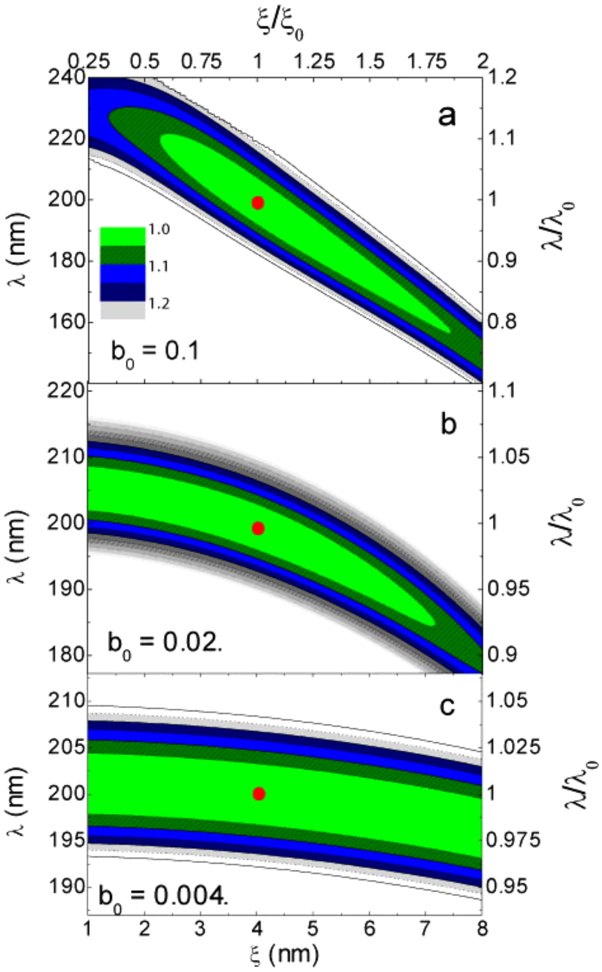

Figure 19. Contour plots of χ^2 as a function of λ and ξ for μSR spectra simulated using the parameters $\lambda_0 = 200$ nm, $\xi_0 = 4$ nm, $\sigma_{g0} = 0.7$ mT, 20 million counts, and $b_0 = 0.004$, 0.02, and 0.1. The results in (a) were obtained using the NGL model, and those in (b) and (c) were obtained using the ML model. There is a strong correlation of the fitted values of λ and ξ for high ($b_0 = 0.1$) and intermediate ($b_0 = 0.02$) fields, but nearly no correlation at low fields ($b_0 = 0.004$). The statistically scattered minimal value of χ^2 is normalized to 1. The real values of λ and ξ are indicated by the red point.

6. Conclusions

We performed an analysis of the line shape of μSR spectra of type-II superconductors in the mixed state simulated using four different models frequently adopted: (1) the modified London model (ML), (2) the London model with Gaussian cut-off (LG), (3) the analytical Ginzburg–Landau (AGL), and (4) the numerical Ginzburg–Landau (NGL) model. The dependence of the line shape on the penetration depth λ, the coherence length ξ, the applied magnetic field B, and the Gaussian smearing parameter σ_g is in agreement with previous studies [35, 38, 4]. It is discussed under what conditions these models can be used to describe the vortex state in extreme type-II superconductors. As a result, the ML model can be applied for fields $b = B/B_{c2} \leqslant 0.1$ (B_{c2} is the second critical field). On the other hand, the AGL and LG models can be applied over the whole range of fields, but in the range $b \simeq 10^{-2}$–1 they systematically deviate from the NGL model. It was shown that at low fields $b \leqslant 10^{-3}$ there is practically no dependence of the line shape on ξ. However, with increasing field, there is a strong dependence of the line shape on both λ and ξ, but the strong correlation between them makes it almost impossible to determine λ and ξ simultaneously. This is independent of $\kappa = \lambda/\xi$ and the model used. Additional restrictions for ξ (or λ) are needed to get rid of this correlation for reasonable statistics. Furthermore, it was shown that it is possible to determine λ and σ_g simultaneously, provided that ξ is fixed and the correlation between them is not too strong. In addition, it was demonstrated that the second-moment method (SM), frequently used for μSR data analysis, may yield reliable values for λ (within a few per cent) over whole field range $0 < b \lesssim 1$, provided that the vortex lattice disorder is not substantial. A multiple-Gaussian fit may give reliable values for the second moment and may approximate well the local magnetic field distribution in a type-II superconductor. In order to substantiate these conclusions made above, we performed virtual experiments by generating noisy μSR spectra with known parameters. The results of a comprehensive analysis of these μSR spectra are in full agreement with the conclusions drawn above.

Acknowledgments

We would like to acknowledge E H Brandt and I L Landau for valuable discussions. This work was partly supported by the Swiss National Science Foundation, the K Alex Müller Foundation, and the SCOPES GRANT No. IB7420-110784.

References

[1] Schenck A 1985 *Muon Spin Rotation Spectroscopy: Principles and Applications in Solid State Physics* (Bristol: Hilger)

[2] Dalmas De Réotier P and Yaouanc A 1997 *J. Phys.: Condens. Matter* **9** 9113

[3] Sonier J E, Brewer J H and Kiefl R F 2000 *Rev. Mod. Phys.* **72** 769
Sonier J E 2007 *Rep. Prog. Phys.* **70** 1717–55

[4] Brandt E H 2003 *Phys. Rev.* B **68** 054506

[5] Abrikosov A A 1950 *Zh. Eksp. Teor. Fiz.* **32** 1064

[6] Aeppli G, Cava R J, Ansaldo E J, Brewer J H, Kreitzman S R, Luke G M, Noakes D R and Kiefl R F 1978 *Phys. Rev.* B **35** 7129

[7] Harshman D R *et al* 1987 *Phys. Rev.* B **36** 2386

[8] Uemura Y J *et al* 1988 *Phys. Rev.* B **38** 909

[9] Pümpin B *et al* 1990 *Phys. Rev.* B **42** 8019

[10] Zimmermann P *et al* 1995 *Phys. Rev.* B **52** 541

[11] Aegerter C M and Lee S L 1997 *Appl. Magn. Reson.* **13** 75

[12] Lee S L 1999 *Muon Science* ed S L Lee, S H Kilcoyne and R Cywinski (Bristol: Institute of Physics Publishing) p 149

[13] Brandt E H 1988 *Phys. Rev.* B **37** 2349

[14] Yaouanc A, Dalmas de Réotier P and Brandt E H 1997 *Phys. Rev.* B **55** 11107

[15] Clem J R 1975 *J. Low Temp. Phys.* **18** 427

[16] Hao Z, Clem J R, McElfresh M W, Civale L, Malozemoff A P and Holtzberg F 1991 *Phys. Rev.* B **43** 2844

[17] Riseman T M *et al* 1995 *Phys. Rev.* B **52** 10569

[18] Yamashita A, Ishii K, Yokoo T, Akimitsu J, Hedo M, Inada Y, Onuki Y, Yamamoto E, Haga Y and Kadono R 1997 *Phys. Rev. Lett.* **79** 3771

[19] Miller R I, Kiefl R F, Brewer J H, Chakhalian J, Dunsiger S, Morris G D, Sonier J E and MacFarlane W A 2000 *Phys. Rev. Lett.* **85** 1540

[20] Ohishi K *et al* 2000 *Physica* B **289/290** 377

[21] Kadono R *et al* 2001 *Phys. Rev.* B **63** 224520

[22] Price A N, Miller R I, Kiefl R F, Chakhalian J A, Dunsiger S R, Morris G D, Sonier J E and Canfield P C 2002 *Phys. Rev.* B **65** 214520

[23] Ohishi K *et al* 2002 *Phys. Rev.* B **65** 140505(R)

[24] Miller R I, Kiefl R F, Brewer J H, Chakhalian J C, Dunsiger S, Price A N, Bonn D A, Hardy W H, Liang R and Sonier J E 2003 *Physica* B **326** 296

[25] Sonier J E, Callaghan F D, Miller R I, Boaknin E, Taillefer L, Kiefl R F, Brewer J H, Poon K F and Brewer J D 2004 *Phys. Rev. Lett.* **93** 017002

[26] Serventi S, Allodi G, De Renzi R, Guidi G, Romanó L, Manfrinetti P, Palenzona A, Niedermayer Ch, Amato A and Baines Ch 2004 *Phys. Rev. Lett.* **93** 217003

[27] Sonier J E 2004 *J. Phys.: Condens. Matter* **16** S4499

[28] Callaghan F D, Laulajainen M, Kaiser C V and Sonier J E 2005 *Phys. Rev. Lett.* **95** 197001

[29] Laulajainen M, Callaghan F D, Kaiser C V and Sonier J E 2006 *Phys. Rev.* B **74** 054511

[30] Salman Z *et al* 2007 *Phys. Rev. Lett.* **98** 167001

[31] Sonier J E *et al* 2007 *Phys. Rev.* B **76** 134518

[32] Landau I L and Keller H 2007 *Physica* C **466** 131

[33] Weber M *et al* 1993 *Phys. Rev.* B **48** 13022

[34] Khasanov R, Shengelaya A, Maisuradze A, La Mattina F, Bussmann-Holder A, Keller H and Müller K A 2007 *Phys. Rev. Lett.* **98** 057007

[35] Brandt E H 1977 *J. Low Temp. Phys.* **26** 709
Brandt E H 1988 *J. Low Temp. Phys.* **73** 355

[36] Brandt E H 1997 *Phys. Rev. Lett.* **78** 2208

[37] Delrieu J M 1972 *J. Low Temp. Phys.* **6** 197

[38] Sidorenko A D, Smilga V P and Fesenko V I 1990 *Hyperfine Interact.* **63** 49

[39] Dalmas de Réotier P, Gubbens P C M and Yaouanc A 2004 *J. Phys.: Condens. Matter* **16** S4687

[40] Tinkham M 1996 *Introduction to Superconductivity* 2nd edn (New York: McGraw-Hill)
Pümpin B *et al* 1990 *J. Less-Common Met.* **164/65** 994

[41] Maisuradze A *et al* 2008 unpublished

[42] Khasanov R, Landau I L, Baines C, La Mattina F, Maisuradze A, Togano K and Keller H 2006 *Phys. Rev.* B **73** 214528

[43] Rainer D and Usadel K D 1974 *Phys. Rev.* B **9** 2409

[44] Chang J, Mesot J, Gilardi R, Kohlbrecher J, Drew A J, Divakar U, Lister S J, Lee S L, Brown S P, Charalambous D, Forgan E M, Dewhurst C D, Cubitt R, Momono N and Oda M 2006 *Physica* B **385/386** 35

Chapter 4

Conclusions

Conclusions and outlook

In the first part of this thesis, the whole phase diagram of $Y_{0.98}Yb_{0.02}Ba_2Cu_3O_x$ as a function of doping x was investigated by means of the Yb^{3+} EPR probe. In addition, a few other cuprates were investigated for comparison. Yb^{3+} proved to be a very suitable probe for studying superconductivity due to the simplicity of its spin Hamiltonian, the absence of low-lying levels and its ability to couple, not only to carriers, but also to the lattice, since it has a nonzero orbital momentum. It is very important that it occupies a site between the superconducting CuO_2 layers in $Y_{0.98}Yb_{0.02}Ba_2Cu_3O_x$, $Bi_2Sr_2Ca_{1-x}Yb_xCu_2O_8$, and $Sr_{0.9}La_{0.08}Yb_{0.02}CuO_2$ which makes it possible to study the physics taking place in these layers. One of the main results is the clarification of relaxation mechanisms of rare earth (RE) elements in $YBa_2Cu_3O_x$ and $Sr_{0.9}La_{0.08}Yb_{0.02}CuO_2$ superconductors. It was found that there are two dominant contributions to the relaxation of Yb^{3+}, namely, the electronic (Korringa) and the phononic one. The electronic contribution is proportional to the doping of carriers, and the phononic part is doping independent and is dominated by the Raman mechanism of phonons with an energy $\simeq 500(50)$ K. By comparing the relaxation rates of $Y_{0.98}Yb_{0.02}Ba_2Cu_3O_x$ and $Y_{0.98}Yb_{0.02}Ba_2Cu_3O_x$:Zn, we were able for the first time to extract the electronic relaxation across the superconducting transition as shown in Figs. 2.7(a) and 2.8. Concerning the phononic part of the relaxation, the phonon responsible for the relaxation was not identified. Possible candidates are an optical phonon mode or a mode related to the Jahn-Teller (JT) fluctuations of the Cu spin. It was shown that there exist a few planar optical modes with this energy, namely, the in-plane bending and the out-of-plane B_{1g} modes. On the other hand, a possible JT fluctuation frequency is also expected at this energy. Note that a model of the phonon density of states (PDOS) describing the relaxation could be different from that used for the calculation of the specific heat and may well fail to describe the PDOS measured by neutron spectroscopy [50]. The planar-phonon mode observed by EPR-relaxation measurements coincides nicely with the phonon peak of neutron PDOS measurements at 44 meV. In order to clarify its nature, further investigations are necessary.

Further, an interesting study was performed on $Y_{0.98}Yb_{0.02}Ba_2Cu_3O_x$ for $x \simeq 6.4$, where a antiferromagnetic (AF) to superconducting (SC) phase transition takes place. In recent years, this region of the phase diagram has attracted much attention and was investigated by μSR and neutron spectroscopy. There exist contradictory reports on the AF-to-SC phase transition of $YBa_2Cu_3O_x$. In some reports, it was claimed that the sample is homogeneous in the vicinity of the AF-to-SC phase transition and that superconductivity develops gradually from the fluctuating AF ground state. In others, it was concluded that the $\mathrm{YBa_2Cu_3O}_x$ system in this region is separated into a magnetic and a superconducting phase. Yb^{3+} EPR is a sensitive tool for the investigations of phase transitions. Experimentally, it was found that the Yb^{3+} EPR signal changes drastically across the AF-to-SC phase transition. Within a certain range in the vicinity of the AF-to-SC phase boundary, the superconducting and the magnetic phases coexist. Distinct EPR signals originating from each of these phases are observed. We were able to deduce the volume fractions of the two phases as a function of temperature and doping. The broad signal observed in EPR corresponds to the central mode of the Cu-spin fluctuations observed by means of neutrons and allows an estimate of the central-mode frequency of $\nu_{fluct} \simeq 7.4$ GHz. The observation of two spatially separated phases which are probably arranged in a stripe-like geometry implies that the SC and the AF order parameters have a different origin and presumably compete with each other.

In the second part of the thesis, an analysis of the line shape of μSR spectra of type-II superconductors in the mixed state simulated by four common models was performed. These models are (1) the modified London (ML) model, (2) the London model with Gaussian cut-off (LG), (3) the analytical Ginzburg-Landau (AGL) model, and (4) the numerical Ginzburg-Landau (NGL) model. The shape of the local field distribution as a function of penetration depth λ, coherence length ξ, vortex-lattice disorder, and nuclear depolarization for each of these models was thoroughly investigated. Limitations and systematic deviations of the ML, the LG, and the AGL models as compared with the NGL model were discussed. Substantial limitations were found in the ability to extract simultaneously λ and ξ from these models due to the strong correlation between these parameters. However, these models can fit the data properly by assuming a fixed relation between λ and ξ. In addition, it was demonstrated that the second moment (SM) method, frequently used for μSR data analysis, may yield reliable values for λ (within a few percent) in the whole range of the applied field $H_{c1} \ll H \lesssim H_{c2}$ (H_{c1} and H_{c2} are the first and the second critical field, respectively), provided that the vortex-lattice disorder is not substantial. A multiple-Gaussian fit can give reliable values for the SM and good approximations of the local magnetic field distribution in a type-II superconductor. In order to substantiate these findings, we performed virtual experiments by generating noisy μSR spectra with known parameters. The results of a comprehensive analysis of these μSR spectra are in full agreement with our conclusions. Special software was developed for this project which allows analysis as well as simulation of μSR spectra. The program is built around the commercial MatLab software. The various procedures have been documented in a User's Manual. It is hoped that this software will be useful for future μSR investigations.

Acknowledgements

I would like to acknowledge all who have contributed to the completion of this thesis.

I would like to express my deep gratitude to Hugo Keller for giving me the opportunity to work in his group on one of the most interesting field in modern solid-state physics, namely, the field of superconductivity. During my work in this group, I obtained very valuable experience in experimental physics and the technique of magnetic resonance. I am grateful for his support. His ideas on μSR helped to improve the second part of this thesis.

My very special thanks goes to Alexander Shengelaya for his support, his supervision and for his guidance in introducing me to the physics of HTS and the application of the magnetic resonance technique to this subject. The first part of this thesis is basically the result of investigations based on his interesting ideas concerning HTS. These years of working with him were very pleasant, interesting and fruitful in science as well as in our personal relationship.

I am very grateful to Boris Ivanovich Kochelaev for his theoretical support in the EPR studies. Discussions with him helped in deepening my understanding of the physics of superconductivity and paramagnetic resonance. Numerous stories about science and life during lunch brakes with him and with A. Shengelaya were always humorous and pleasant.

It was a great honor for me to work in the group where one of its members, Karl Alex Müller, was the discoverer of HTS and who received the Nobel prize for this discovery. My occasional discussions with him were always very interesting.

I would like to thank Joseph Roos for his help and advice on technical problems in the laboratory and for the many interesting discussions we had. If I needed anything, he was always the right person to ask. I am also grateful to Mihael Mali for many interesting discussions and for his numerous suggestions.

To the kings of μSR, Rustem Khasanov and Dimitry Eshchenko, belong my grateful acknowledgements for the nice times we had during μSR beam time and for introducing me to the details of working with the μSR spectrometer. I am especially thankful to Rustem Khasanov for his important remarks regarding the second part of this thesis. Frequent and interesting discussions of the various μSR related papers substantially contributed to my

knowledge of μSR as applied to HTS. I am also grateful to Prof. Ilia Savić for the pleasant times we spent during the μSR beam times.

My work would have been impossible without the colleagues of our group, namely, Fabio La Mattina, Simon Strässle, Stephen Weyeneth, Bastian Wojek, Stefan Kohout, Daniele Di Castro, Petra Häfliger, Björn Graneli, Urs Mosele and Clemens Duttwyler. The warm and friendly atmosphere in our group was very important during my work. Our discussions on seemingly simple things in physics helped in a deeper understanding of the subject. I am very grateful to Simon Strässle, Stephen Weyeneth for correcting my English. ”A” or ”The”, that was the question, and they always knew the answer. I am grateful to all these people for the pleasant years we spent together, especially to my officemate Fabio from Palermo for the very fruitful discussions on EPR which we had.

I am very grateful to Ekaterina Pomjakushina and Kazimirz Conder for the high quality samples which they provided for my work. Although I sometimes had doubts about the sample quality, I was wrong and their samples were always much better than I might have prepared myself.

I am thankful to Vladimir Ivanshin for the nice time and numerous discussions about life and EPR which we had during his short visits.

I am grateful to Walter Fässler, Kurt Bösiger, Peter Soland, Karoly Szeker and Ticiano Crudelli for their help in solving various technical problems.

I would like to thank members of other groups at the Physik-Institute who are not listed here. The friendly and warm relation to these people was very important.

I would like to thank the Swiss National Foundation and Physik-Institut for financing my PhD project.

Last but not at least, I would like to thank Ralph Pixley for his help in correcting the English of my thesis, for the many hours he spent reading it and for the tips he gave me on how to write in ”Pix” English. Thanks to his critical and professional view, this thesis became more understandable for physicist not familiar with the magnetic resonance techniques.

Appendix A

Crystal field splitting of Yb^{3+}

Although a critical reader might think that it is extremely simple and completely straightforward to calculate the crystal-field splitting, I decided to include this description for several reasons. First, knowledge about the ground state and first excited states of an ion is one of the most important things needed before beginning an investigation. For a student reading this manuscript, it will be interesting and useful to know how the crystal-field splitting of the "Hund's unperturbed state[1]" is calculated . For other rare earths, it is completely similar. The crystal field of Yb^{3+} for orthorombic symmetry can be expressed by the equation [44]:

$$\mathcal{H}_{CEF} = \sum_{n=1}^{3} \sum_{m=0}^{n} B_{2n}^{2m} \hat{O}_{2n}^{2m} \tag{A.1}$$

where B_{2n}^{2m} are the crystal-electric-field (CEF) parameters, and $\hat{O}_{2n}^{2m}$ are the Stevens operators [5, 144, 145] which have the following form:

$$\hat{O}_{20} = 3\hat{J}_z^2 - \hat{J}(\hat{J}+1), \tag{A.2}$$

$$\hat{O}_{22} = 1/2(\hat{J}_+^2 + \hat{J}_-^2), \tag{A.3}$$

$$\hat{O}_{40} = 35\hat{J}_z^4 - 30\hat{J}(\hat{J}+1)\hat{J}_z^2 + 25\hat{J}_z^2 - 6\hat{J}(\hat{J}+1) + 3\hat{J}^2(\hat{J}+1)^2, \tag{A.4}$$

$$\hat{O}_{42} = 1/4[(7\hat{J}_z^2 - J(J+1) - 5)(\hat{J}_+^2 + J_-^2) + (\hat{J}_+^2 + J_-^2)(7\hat{J}_z^2 - J(J+1) - 5)(\hat{J}_+^2 + J_-^2)], \tag{A.5}$$

$$\hat{O}_{44} = \frac{1}{2}(\hat{J}_+^4 + \hat{J}_-^4), \tag{A.6}$$

$$\begin{aligned} \hat{O}_{60} = {} & 231\hat{J}_z^6 - 315\hat{J}(\hat{J}+1)\hat{J}_z^4 + 735\hat{J}_z^4 + 105\hat{J}^2(\hat{J}+1)^2 J_z^2 \\ & - 525\hat{J}(\hat{J}+1)\hat{J}_z^2 + 294\hat{J}_z^2 - 5\hat{J}^3(\hat{J}+1)^3 + 40\hat{J}^2(\hat{J}+1)^2 - 60\hat{J}(\hat{J}+1), \end{aligned} \tag{A.7}$$

$$\begin{aligned} \hat{O}_{62} = {} & 1/4((33\hat{J}_z^4 - 18J(J+1)\hat{J}_z^2 - 123\hat{J}_z^2 + J^2(J+1)^2 + 10J(J+1) + 102)(\hat{J}_+^2 + \hat{J}_-^2) + \\ & (\hat{J}_+^2 + \hat{J}_-^2)(33\hat{J}_z^4 - 18J(J+1)\hat{J}_z^2 - 123\hat{J}_z^2 + J^2(J+1)^2 + 10J(J+1) + 102)), \end{aligned} \tag{A.8}$$

$$\hat{O}_{64} = \frac{1}{4}[(11\hat{J}_z^2 - \hat{J}(\hat{J}+1) - 38)(\hat{J}_+^4 + \hat{J}_-^4) + (\hat{J}_+^4 + \hat{J}_-^4)(11\hat{J}_z^2 - \hat{J}(\hat{J}+1) - 38)], \tag{A.9}$$

$$\hat{O}_{66} = 1/2(\hat{J}_+^6 + \hat{J}_-^6). \tag{A.10}$$

---

[1] Here is meant the ground state of an isolated rare-earth ion such as Yb^{3+} according to Hund's rules

Here, $J = 7/2$, $\hat{J}_z$ is an operator corresponding to the z-component of the magnetic moment, $\hat{J}_+ = \hat{J}_x + i\hat{J}_y$ and $\hat{J}_- = \hat{J}_x - i\hat{J}_y$ are the raising and lowering operators that have the following effect on the spin component of the wave function:

$$\hat{J}_+|J, J_z\rangle = \sqrt{J(J+1) - J_z(J_z+1)}|J, J_z{+}1\rangle, \qquad \hat{J}_-|J, J_z\rangle = \sqrt{J(J+1) - J_z(J_z-1)}|J, J_z{-}1\rangle.$$

This operator increases (reduces) the quantum number J_z of a wave function. If one takes into account that the basic set of wave functions (vectors) $|J, J_z\rangle$ are orthogonal and normalized, then the matrix elements $\langle J, J_z'|\hat{J}_+|J, J_z\rangle$ and $\langle J, J_z'|\hat{J}_-|J, J_z\rangle$ $(J_z, J_z' = -7/2, -5/2, ..., 7/2)$ of these operators are

$$\langle J, J_z'|\hat{J}_+|J, J_z\rangle = \begin{cases} 0, & \text{if} J_z' \neq J_z + 1 \\ \sqrt{J(J+1) - J_z(J_z+1)}, & \text{if} J_z' = J_z + 1 \end{cases}$$

$$\langle J, J_z'|\hat{J}_-|J, J_z\rangle = \begin{cases} 0, & \text{if} J_z' \neq J_z - 1 \\ \sqrt{J(J+1) - J_z(J_z-1)}, & \text{if} J_z' = J_z - 1 \end{cases}$$

Therefore, for $J = 7/2$, the operators $\hat{J}_z$, $\hat{J}_+$ and $\hat{J}_-$ have the following matrix form:

$$\hat{J}_z = \begin{pmatrix} -7/2 & 0 & 0 & 0 & 0 & 0 & 0 & 0 \\ 0 & -5/2 & 0 & 0 & 0 & 0 & 0 & 0 \\ 0 & 0 & -3/2 & 0 & 0 & 0 & 0 & 0 \\ 0 & 0 & 0 & -1/2 & 0 & 0 & 0 & 0 \\ 0 & 0 & 0 & 0 & 1/2 & 0 & 0 & 0 \\ 0 & 0 & 0 & 0 & 0 & 3/2 & 0 & 0 \\ 0 & 0 & 0 & 0 & 0 & 0 & 5/2 & 0 \\ 0 & 0 & 0 & 0 & 0 & 0 & 0 & 7/2 \end{pmatrix}$$

$$\hat{J}_+ = \begin{pmatrix} 0 & 0 & 0 & 0 & 0 & 0 & 0 & 0 \\ 2.646 & 0 & 0 & 0 & 0 & 0 & 0 & 0 \\ 0 & 3.464 & 0 & 0 & 0 & 0 & 0 & 0 \\ 0 & 0 & 3.873 & 0 & 0 & 0 & 0 & 0 \\ 0 & 0 & 0 & 4 & 0 & 0 & 0 & 0 \\ 0 & 0 & 0 & 0 & 3.873 & 0 & 0 & 0 \\ 0 & 0 & 0 & 0 & 0 & 3.464 & 0 & 0 \\ 0 & 0 & 0 & 0 & 0 & 0 & 2.646 & 0 \end{pmatrix}$$

$$\hat{J}_- = \begin{pmatrix} 0 & 2.646 & 0 & 0 & 0 & 0 & 0 & 0 \\ 0 & 0 & 3.464 & 0 & 0 & 0 & 0 & 0 \\ 0 & 0 & 0 & 3.873 & 0 & 0 & 0 & 0 \\ 0 & 0 & 0 & 0 & 4 & 0 & 0 & 0 \\ 0 & 0 & 0 & 0 & 0 & 3.873 & 0 & 0 \\ 0 & 0 & 0 & 0 & 0 & 0 & 3.464 & 0 \\ 0 & 0 & 0 & 0 & 0 & 0 & 0 & 2.646 \\ 0 & 0 & 0 & 0 & 0 & 0 & 0 & 0 \end{pmatrix}$$

In order to get the matrix form of the Hamiltonian according to Eq. (A.1), one needs to calculate the matrices for the operators $\hat{O}_{20} - \hat{O}_{66}$ according to the equations (A.2)-(A.10) and then determine the coefficients B_{2n}^{2m} from an experiment. These coefficients obtained from neutron scattering experiment by Guillaume *at al.* [44] as expressed in meV are

$$\begin{gathered} B_2^0 = 0.18; \qquad B_2^2 = 0.063; \\ B_4^0 = 0.056; \qquad B_4^2 = -0.014; \qquad B_4^4 = -0.2587; \\ B_6^0 = 6.6 \cdot 10^{-4}; \quad B_6^2 = -9.24 \cdot 10^{-5}; \quad B_6^4 = 1.62 \cdot 10^{-2}; \quad B_6^6 = 0.99 \cdot 10^{-4}; \end{gathered}$$

If one puts these parameters into Eq. (A.1) and performs the proper calculations, one obtains the following hamiltonian:

$$\mathcal{H} = \begin{pmatrix} 28.132 & 0 & -1.687 & 0 & -1.092 & 0 & 0.0943 & 0 \\ 0 & -47.298 & 0 & 0.3389 & 0 & -38.688 & 0 & 0.0943 \\ -1.687 & 0 & -4.216 & 0 & 1.729 & 0 & -38.688 & 0 \\ 0 & 0.339 & 0 & 23.382 & 0 & 1.729 & 0 & -1.092 \\ -1.092 & 0 & 1.729 & 0 & 23.382 & 0 & 0.339 & 0 \\ 0 & -38.688 & 0 & 1.729 & 0 & -4.216 & 0 & -1.687 \\ 0.00943 & 0 & -38.688 & 0 & 0.339 & 0 & -47.298 & 0 \\ 0 & 0.0943 & 0 & -1.092 & 0 & -1.687 & 0 & 28.132 \end{pmatrix}.$$

Diagonalization of this matrix (for instance by the function `eig` in MatLab) gives the following eigenvalues for the four doublets (in meV):

$$\begin{aligned} E_1 &= -70.058; \qquad & E_2 &= 18.046; \\ E_3 &= 23.325; \qquad & E_4 &= 28.688. \end{aligned} \tag{A.11}$$

The energies obtained for ground state and the first three excited states in the $J = 7/2$ multiplet by this method are $E_1 = -70.058$ meV, $\Delta_1 = E_2 - E_1 = 88.1$, $\Delta_2 = E_3 - E_1 = 93.4$ and $\Delta_3 = E_3 - E_1 = 98.7$ meV, respectively. The eigenvalues are in good agreement with the results of Ref. [44] and do not depend on the algorithm used for the diagonalization; however, the eigenvectors obtained numerically by the standard MatLab program are slightly dependent on the algorithm employed but are close to those reported by Guillaume *at al.* [44].

Bibliography

[1] J.G. Bednorz and K.A. Müller, Z. Phys. B - Condensed Matter **64**, 189 (1986).

[2] J. Bardeen, L.N. Cooper, and J.R. Schrieffer, Phys. Rev. **108**, 1175 (1957).

[3] "Superconductivity in Comples Systems", Editors: K.A. Müller and A. Bussmann-Holder, *Springer-Verlag Berlin Heidelberg (2005)* .

[4] B.I. Kochelaev, A.M. Safina, A. Shengelaya, H. Keller, K.A. Müller, and K. Conder, Mod. Phys. Lett. B **17**, 415 (2003).

[5] A. Abragam and B. Bleaney, "Electron Paramagnetic Resonance of Transition Ions" *Clarendon Press, Oxford, (1970).*

[6] V.L. Ginzburg, Rev. Mod. Phys. **76**, 981 (2004).

[7] A. Schenck, "Muon Spin Rotation Spectroscopy: Principles and Applications in Solid State Physics" *Adam Hilger, Bristol, England (1985).*

[8] P.D. De Réotier and A. Yaouanc J. Phys.: Condens. Matter **9**, 9113 (1997).

[9] Diploma work of Urs Mosele in Physik-Institut of University of Zürich, Switzerland (2007).

[10] Robert Schrieffer, "Theory of Superconductivity", *W.A. BENJAMIN INC. New York 10016 (1964).*

[11] C.A. Reynolds, B. Serin, W.H. Wright, and L.B. Nesbitt, Phys. Rev. **78**, 487 (1950); E. Maxwell, Phys. Rev. **78**, 477 (1950).

[12] N.F. Mott, Philosophical Magazine **6**, 287 (1961).

[13] Charles P. Poole Jr., Electron Spin Resonance, "A Comprehensive Treatise on Experimental Techniques", *DOVER PUBLICATIONS, INC. Mineola, New York, (1996).*

[14] A. Abragam, "Principles of Nuclear Magnetism", *Oxford science publications, (1989).*

[15] J.R. Pilbrow, "Transition Ion Electron Paramagnetic Resonance", *Clarendon Press, Oxford, (1990).*

[16] S.J. Blundell, Contemporary Physics **77**, 175 (1999).

[17] A.A. Abrikosov, Zh. Eksp. Teor. Fiz. **32**, 1064 (1950).

[18] J. Mesot and A. Furrer, J. Supercond. **10**, 623 (1997).

[19] A.T. Boothroyd, Phys. Rev. B **64**, 066501 (2001).

[20] S.W. Lovesey and U. Staub, Phys. Rev. B **64**, 066502 (2001).

[21] U. Walter, S. Fahy, A. Zettl, S.G. Louie, M.L. Cohen, P. Tejedor, and A.M. Stacy, Phys. Rev. B **36**, 8899 (1987).

[22] G. Amoretti, R. Caciuffo, P. Santini, O. Francescangeli, E.A. Goremychkin, R. Osborn, G. Calestani, M. Sparpaglione, and L. Bonoldi, Physica C **221**, 227 (1994).

[23] A.T. Boothroyd, A. Mukherjee, and A.P. Murani, Phys. Rev. Lett. **77**, 1600 (1996).

[24] J. Mesot, G. Bottger, H. Mutka, and A. Furrer, Europhys. Lett. **44**, 498 (1998).

[25] U. Staub, M. Gutmann, F. Fauth, and W. Kagunya, J. Phys.: Condens. Matter **11**, L59 (1999).

[26] S.W. Lovesey and U. Staub, Phys. Rev. B **61**, 9130 (2000).

[27] M. Roepke, E. Holland-Moritz, B. Biichner, H. Berg, R.E. Lechner, S. Longeville, J. Fitter, R. Kahn, G. Coddens, and M. Ferrand, Phys. Rev. B **60**, 9793 (1999).

[28] S.E. Barnes, Adv. Phys. **30**, 801 (1981).

[29] L. Kan, S. Elschner, and B. Elschner, Solid State Commun. **79**, 61 (1991).

[30] M.V. Eremin, I.N. Kurkin, M.P. Rodionova, I.H. Salihov, and L.R. Tagirov, Supercond. Phys. Chem. Techn. (Russia) **4**, 716 (1991).

[31] I.N. Kurkin, I.Kh. Salikhov, L.L. Sedov, M.A. Teplov, and R.Sh. Zhdanov, JETP **76**, 657 (1993).

[32] H. Shimizu, K. Fujiwara, and K. Hatada, Physica C **288**, 190 (1997).

[33] H. Shimizu, K. Fujiwara, and K. Hatada, Physica C **299**, 169 (1998).

[34] V.A. Ivanshin, M.R. Gafurov, I.N. Kurkin, S.P. Kurzin, A. Shengelaya, H. Keller, and M. Gutmann, Physica C **307**, 61 (1998).

[35] L.K. Aminov, V.A. Ivanshin, I.N. Kurkin, M.R. Gafurov, I.Kh. Salikhov, H. Keller, and M. Gutmann, Physica C **349**, 30 (2001).

[36] M.R. Gafurov, I.N. Kurkin, and S.P. Kurzin, Supercond. Sci. Technol. **18**, 1183 (2005).

[37] V. Likodimos, N. Guskos, H. Gamari-Seale, A. Koufoudakis, M. Wabia, J. Typek, and H. Fuks, Phys. Rev. B **54**, 12342 (1996).

[38] V. Likodimos, N. Guskos, J. Typek, and M. Wabia, Eur. Phys. J. B **24**, 143 (2001).

[39] M.R. Gafurov, V.A. Ivanshin, I.N. Kurkin, M.P. Rodionova, H. Keller, M. Gutmann, U. Staub, Journ. Magn. Reson. **161**, 210 (2003).

[40] D.E. Farrell, B.S. Chandrasekhar, M.R. DeGuire, M.M. Fang, V.G. Kogan, J.R. Clem, and D.K. Finnemore, Phys. Rev. B **36**, 4025 (1987).

[41] G. Shirane, J. Als-Nielsen, M. Nielsen, J.M. Tranquada, H. Chou, S. Shamoto, and M. Sato, Phys. Rev. B **41**, 6547 (1990).

[42] Stephen Blundell, "Magnetizm in Condensed Matter“, *OXFORD University Press (2001).*

[43] A. Kutuzov and B.I. Kochelaev (to be published)

[44] M. Guillaume, P. Allenspach, J. Mesot, U. Staub, A. Furrer, R. Osborn, A.D. Taylor, F. Stucki, and P. Unternahrer, Solid State Commun. **81**, 999 (1992).

[45] J. Sichelschmidt, B. Elschner, A. Loidl, and B.I. Kochelaev, Phys. Rev. B **51**, 9199 (1995).

[46] V. Likodimos, N. Guskos, H. Gamari-Seale, A. Koufoudakis, M. Wabia, J. Typek, and H. Fuks, Phys. Rev. B **54**, 12342 (1996).

[47] R.N. de Mesquita, J.H. Castilho, G.E. Barberis, C. Rettori, I. Torriani, O.F. de Lima, S. Gama, R.F. Jardim, M.C. Terrile, H. Basso, and O.R. Nascimento, Phys. Rev. B **39**, 6694 (1989).

[48] S.A. Dodds, J. Sanny, R. Orbach, Phys. Rev. B **18**, 1016 (1978).

[49] S. von Molnar, A. Torressen, D. Kaiser, F. Holtzberg, and T. Penney, Phys. Rev. B **37**, 3762 (1988).

[50] M. Arai, K. Yamada, Y. Hidaka, S. Itoh, Z.A. Bowden, A.D. Taylor, and Y. Endoh, Phys. Rev. Lett. **69**, 359 (1992).

[51] B.I. Kochelaev, JETP **10**, 171 (1960).

[52] Chao-Yuan Huang, Phys. Rev. **154**, 215 (1967).

[53] L. Pintschovius, W. Reichardt, M. Kläser, T. Wolf, and H.V. Löhneysen, Phys. Rev. Lett. **89**, 037002 (2002); M. Opel, R. Hackl, T.P. Devereaux, A. Virosztek, A. Zawadowski, A. Erb, E. Walker, H. Berger, and L. Forró, Phys. Rev. B **60**, 9836 (1999).

[54] U. Höchli and K.A. Müller Phys. Rev. Lett. **12**, 730 (1964); U. Höchli, K.A. Müller, and P. Wysling Phys. Letters **15**, 1 (1965).

[55] K.A. Müller, Proceedings of the XIVth Colloque Ampére Ljubljana, 6-11 September 1966, "Magnetic resonance and relaxation“, pp 192-208, *Amsterdam: North-Holland publishing company (1967).*

[56] A. Pöppl, G. Völkel, J. Hoentsch, S. Orlinski, and A. Klöpperpieper, Chem. Phys. Lett. **224**, 233 (1994); G. Völkel, W. Brunner, and H.-E. Müller, Ferroelectrics **78**, 267 (1988).

[57] P.C. Hammel, M. Takigawa, R.H. Heffner, Z. Fisk, and K.C. Ott, Phys. Rev. Lett. **63**, 1992 (1989).

[58] Y. Kitaoka, S. Hiramatsu, T. Kondo, and K. Asayama, J. Phys. Soc. Jpn. **57**, 30 (1988).

[59] Magnetic Resonance of Phase Transitions, edited by Frank J. Owens, Charles P. Poole jr., and Horacio A. Farach, *ACADEMIC PRESS, INC. (LODNOD) LTD (1979)*; C.H. Pennington and C.P. Slichter, in "Physical Properties of High Temperature Superconductors II“, edited by D.M. Ginsberg *World Scientific, New Jersey (1990).*

[60] A. Shengelaya, M. Bruun, B.I. Kochelaev, A. Safina, K. Conder, and K.A. Müller Phys. Rev. Lett. **93**, 017001 (2004).

[61] S.A. Kivelson and I.P. Bindloss, Rev. Mod. Phys. B **75**, 1201 (2003).

[62] Yoichi Ando, Kouji Segawa, Seiki Komiya, and A. N. Lavrov, Phys. Rev. Lett. **88**, 137005 (2002).

[63] H.A. Mook, Pengcheng Dai, and F. Dogan, Phys. Rev. Lett. **88**, 097004 (2002).

[64] K.M. Lang, V. Madhavan, J.E. Hoffman, E.W. Hudson, H. Eisaki, S. Uchida, J.C. Davis, Nature **415**, 412 (2002).

[65] C. Howald, H. Eisaki, N. Kaneko, M. Greven, and A. Kapitulnik, Phys. Rev. B **67**, 014533 (2003).

[66] J.A. Bonetti, D.S. Caplan, D.J. Van Harlingen, M.B. Weissman, arXiv:cond-mat/0403231v1 (2008).

[67] N.E. Alexeevskii, A.V. Mitin, V.I. Nizhankovskii, I.A. Garifullin, N.N. Garifyanov, G.G. Khaliullin, E.P. Khlybov, B.I. Kochelaev, and L.R. Tagirov, J. Low Temp. Phys. **77**, 87 (1989).

[68] C. Bucci, R. De Renzi, G. Guidi, G. Allodi, and F. Licci, Hyperfine Interactions **105**, 71 (1997).

[69] K. Tagaya and T. Yokoo, J. Magn. Magn. Mater. **210**, 203 (2000).

[70] Y.K. Du, G.C. Che, S.L. Jia, and Z.X. Zhao, *J. Solid State Chem.* **112**, 406 (1994).

[71] V. Likodimos, N. Guskos, M. Wabia, and J.Typek, Phys. Rev. B **58**, 8244 (1998).

[72] J.H. Van Vleck, Phys. Rev. **74**, 1168 (1948).

[73] B. Roessli, P. Allenspach, P. Fischer, J. Mesot, U. Staub, H. Maletta, P. Brüesch, C. Ritter, and A.W. Hewat, Physica B **180&181**, 396 (1992); J.A. Hodges, P. Bouville, P. Imbert, and G. Jéhanno, Hiperfine Interactions **90**, 187 (1994).

[74] S. Simizu, G.H. Bellesis, J. Lukin, S.A. Friedberg, H.S. Lessure, S.M. Fine, and M. Greenblatt, Phys. Rev. B **39**, 9099 (1989).

[75] M.D. Kemple and H.J. Stapleton, Phys. Rev. B **5**, 1668 (1972).

[76] P.W. Anderson and P.R. Weiss, Rev. Mod. Phys. **25**, 269 (1953); R. Kubo and K. Tomita, J. Phys. Soc. Jpn. **9**, 888 (1954).

[77] A. Abragam and G. Goldman, "Nuclear magnetizm: order and disorder“, *Oxford: Clarendon Press (1982).*

[78] M.A. Garstens, L.S. Singer, and A.H. Ryan, Phys. Rev. **96**, 53 (1954); M.A. Garsents and J.I. Kaplan, Phys. Rev. **99**, 459 (1955).

[79] N. Bloembergen and S. Wang, Phys. Rev. **93**, 72 (1954) ; A.G. Anderson and A.G. Redfield, Phys. Rev. **116**, 583 (1959).

[80] A.N. Lavrov and V.F. Gantmakher, Phys. Usp. **69**, 223 (1998).

[81] J.W. Loram, J. Luo, J.R. Cooper, W.Y. Liang, and J.L. Tallon, J. Phys. Chem. Solids **62**, 59 (2001).

[82] M. Sutherland, S.Y. Li, D.G. Hawthorn, R.W. Hill, F. Ronning, M.A. Tanatar, J. Paglione, H. Zhang, L. Taillefer, J. DeBenedictis, R. Liang, D.A. Bonn, and W.N. Hardy, Phys. Rev. Lett. **94**, 147004 (2005).

[83] X.F. Sun, K. Segawa, and Y. Ando, Phys. Rev. B **72**, 100502(R) (2005).

[84] S. Sanna, G. Allodi, G. Concas, A.D. Hillier, and R. De Renzi, Phys. Rev. Lett. **93**, 207001 (2004).

[85] C. Stock, W.J. Buyers, Z. Yamani, C.L. Broholm, J.H. Chung, Z. Tun, R. Liang, D. Bonn, W.N. Hardy, and R.J. Birgenau, Phys. Rev. B **73**, 100504(R) (2006).

[86] I.M. Fita, R. Puzniak, W. Paszkowicz, A. Wisniewski, N.A. Doroshenko, and V.P. Dyakonov, Phys. Rev. B **66**, 014519 (2002).

[87] J.D. Jorgensen, S. Pei, P. Lightfoot, H. Shi, A.P. Paulikas, and B.W. Veal, Physsica C **167**, 571 (1990).

[88] H. Claus, S. Yang, A.P. Paulikas, J.W. Downey, and B.W. Veal, Physsica C **171**, 205 (1990).

[89] K. Conder, Matter. Sci. Eng. **R32**, 41 (2001).

[90] Y. Ando, S. Komiya, K. Segawa, S. Ono, and Y Kurita, Phys. Rev. Lett. **93**, 267001 (2004).

[91] Mun-Seog Kim, C.U. Jung, J.Y. Kim, Jae-Hyuk Choi, and Sung-Ik Lee, Solid State Commun. **123**, 17 (2002).

[92] T. Siegrist, S.M. Zahurak, D.W. Murphy, and R.S. Roth, Nature **334**, 231 (1988).

[93] M.G. Smith, A. Manthiran, J. Zhou, J.B. Goodenough, and J.T. Markert, Nature **351**, 549 (1991).

[94] C.U. Jung, J.Y. Kim, Mun-Seog Kim, Min-Seok Park, Heon-Jung Kim, Y. Yao, S.Y. Lee, and Sung-Ik Lee, Physica C **366**, 299 (2002).

[95] N. Ikeda, Z. Hiroi, M. Azuma, M. Takano, and Y. Bando, Physica C **210**, 367 (1993).

[96] Z.Y. Liu, H.H. Wen, L. Shan, H.P. Yang, X.F. Lu, and H. Gao, Europhys. Lett., **69**(2), 263 (2005).

[97] G.V.M. Williams, R. Dupree, A. Howes, S. Krämer, H.J. Trodahl, C.U. Jung, Min-Seok Park, and Sung-Ik Lee, Phys. Rev. B **65**, 224520 (2002).

[98] A. Shengelaya, R. Khasanov, D.G. Eshchenko, D.Di Castro, I.M. Savić, M.S. Park, K.H. Kim, Sung-Ik Lee, K.A. Müller, and H. Keller, Phys. Rev. Lett. **94**, 127001 (2005).

[99] C. Rettori, D. Rao, S. Oseroff, G. Amoretti, Z. Fisk, S.-W. Cheong, D. Vier, S Schultz, M. Tovar, R.D. Zysler, and J.E. Schirber, Phys. Rev. B **47**, 8156 (1993).

[100] R.D. Zysler, M. Tovar, C. Rettori, D. Rao, H. Shore, S.B. Oseroff, D.C. Vier, S Schultz, Z. Fisk, and S-W. Cheong, Phys. Rev. B **44**, 9467 (1991).

[101] K.R. Lea, M.J.M. Leask, and W.P. Wolf, J. Phys. Chem. Solids **23**, 1381 (1962).

[102] C. Rettori, D. Rao, S. Oseroff, R.D. Zysler, M. Tovar, Z. Fisk, S.-W. Cheong, S. Schultz, and D.C. Vier, Phys. Rev. B **44**, 826 (1991).

[103] F. Mehran, K.W.H. Stevens, and T.S. Plaskett, Phys. Rev. B **20**, 1817 (1979); F. Mehran, K.W.H. Stevens, and F. Holtzberg, Phys. Rev. B **17**, 3707 (1978).

[104] B.I. Kochelaev, J. Sichelschmidt, B. Elschner, W. Lemor, and A. Loidl, Phys. Rev. Lett. **79**, 4274 (1997).

[105] J.E. Sonier, J.H. Brewer, and R.F. Kiefl, Rev. Mod. Phys. **72**, 769 (2000).

[106] M. Tinkham, "Introduction to Superconductivity", *Krieger Publishing company, Malabar, Florida (1975).*

[107] Charles P. Poole Jr., Horacio A. Farach, and Richard J. Creswick, "Superconductivity", *Academic Press Limited, London (1995).*

[108] L.P. Gor'kov, JETP **9**, 1364 (1959).

[109] G. Aeppli, R.J. Cava, E.J. Ansaldo, J.H. Brewer, S.R. Kreitzman, G.M. Luke, D.R. Naokes, and R.F. Kiefl, Phys. Rev. B **35**, 7129 (1987).

[110] D.R. Harshman, G. Aeppli, E.J. Ansaldo, B. Batlogg, J.H. Brewer, J.F. Carolan, R.J. Cava, and M. Celio, Phys. Rev. B **36**, 2386 (1987).

[111] Y.J. Uemura, V.J. Emery, A.R. Moodenbaugh, M. Suenaga, D.C. Jonston, A.J. Jacobson, J.T. Lewandowski, J.H. Brewer, R.F. Kiefl, S.R. Kreitzman, G.M. Luke, T. Riseman, C.E. Stronach, W.J. Klossler, J.R. Kempton, X.H. Yu, D. Opie, and H.E. Schone, Phys. Rev. B **38**, 909 (1988).

[112] B. Pümpin, H. Keller, W. Kündig, W. Odermatt, I.M. Savić, J.W. Schneider, H. Simmler, P. Zimmerman, E. Kaldis, S. Rusiecki, Y. Maeno, and C. Rossel, Phys. Rev. B **42**, 8019 (1990).

[113] P. Zimmermann, H. Keller, S.L. Lee, I.M. Savić, M. Warden, D. Zech, R. Cubitt, E.M. Forgan, E. Kaldis, J. Karpinski, and C. Krüger, Phys. Rev. B **52**, 541 (1995).

[114] C.M. Aegerter and S.L. Lee, Appl. Magn. Reson. **13**, 75 (1997).

[115] S.L. Lee, in "Muon Science", editors: S.L. Lee, S.H. Kilcoyne, and R. Cywinski; p. 149, *IOP Bristol and Philadelphia (1999).*

[116] E.H. Brandt, Phys. Rev. B **37**, 2349 (1988).

[117] T.M. Riseman, J.H. Brewer, K.H. Chow, W.N. Hardy, R.F. Kiefl, S.R. Kreitzman, R. Liang, W.A. MacFarlane, P. Mendels, G.D. Morris, J. Rammer, J.W. Schneider, C. Niedermayer, and S.L. Lee, Phys. Rev. B **52**, 10569 (1995).

[118] A. Yaouanc, P. Dalmas de Réotier, and E.H. Brandt, Phys. Rev. B **55**, 11107 (1997).

[119] A. Yamashita, K. Ishii, T. Yokoo, J. Akimitsu, M. Hedo, Y. Inada, Y. Onuki, E. Yamamoto, Y. Haga, and R. Kadono, Phys. Rev. Lett. **79**, 3771 (1997).

[120] R.I. Miller, R.F. Kiefl, J.H. Brewer, J. Chakhalian, S. Dunsiger, G.D. Morris, J.E. Sonier, and W.A. MacFarlane, Phys. Rev. Lett. **85**, 1540 (2000).

[121] K. Ohishi, K. Kakuta, J. Akimitsu, W. Higemoto, R. Kadono, R.I. Miller, A.N. Price, R.F. Kiefl, J.E. Sonier, M. Nohara, H. Suzuki, and H. Takagi, Physica B **289-290**, 377 (2000).

[122] R. Kadono, W. Higemoto, A. Koda, K. Ohishi, T. Yokoo, J. Akimitsu, M. Hedo, Y. Inada, Y. Onuki, E. Yamamoto, and Y. Haga, Phys. Rev. B **63**, 224520 (2001).

[123] A.N. Price, R.I. Miller, R.F. Kiefl, J.A. Chakhalian, S.R. Dunsiger, G.D. Morris, J.E. Sonier, and P.C. Canfield, Phys. Rev. B **65**, 214520 (2002).

[124] K. Ohishi, K. Kakuta, J. Akimitsu, W. Higemoto, R. Kadono, J.E. Sonier, A.N. Price, R.I. Miller, R.F. Kiefl, M. Nohara, H. Suzuki, and H. Takagi, Phys. Rev. B **65**, 140505 (2001).

[125] R.I. Miller, R.F. Kiefl, J.H. Brewer, J.C. Chakhalian, S. Dunsiger, A.N. Price, D.A. Bonn, W.H. Hardy, R. Liang, and J.E. Sonier, Physica B **326**, 296 (2003).

[126] J.E. Sonier, F.D. Callaghan, R.I. Miller, E. Boaknin, L. Taillefer, R.F. Kiefl, J.H. Brewer, K.F. Poon, and J.D. Brewer, Phys. Rev. Lett. **93**, 017002 (2004).

[127] S. Serventi, G. Allodi, R. De Renzi, G. Guidi, L. Romanó, P. Manfrinetti, A. Palenzona, Ch. Niedermayer, A. Amato, and Ch. Baines, Phys. Rev. Lett. **93**, 217003 (2004).

[128] J.E. Sonier, J. Physics: Condens. Matter **16**, S4499 (2004).

[129] F.D. Callaghan, M. Laulajainen, C.V. Kaiser, and J.E. Sonier, Phys. Rev. Lett. **95**, 197001 (2005).

[130] M. Laulajainen, F.D. Callaghan, C.V. Kaiser, and J.E. Sonier, Phys. Rev. B **74**, 054511 (2006).

[131] Z. Salman, D. Wang, K.H. Chow, M.D. Hossian, S.R. Kreitzman, T.A. Keeler, C.D.P. Levy, W.A. MacFarlane, R.I. Miller, G.D. Morris, T.J. Parolin, H. Saadaoui, M. Smadella, and R.F. Kiefl, Phys. Rev. Lett. **98**, 167001 (2007).

[132] J.E. Sonier, S.A. Sabok-Sayr, F.D. Callaghan, C.V. Kaiser, V. Pacradouni, J.H. Brewer, S.L. Stubbs, W.N. Hardy, D.A. Bonn, R. Liang, and W.A. Atkinson, Phys. Rev. B **76**, 134518 (2007).

[133] E.H. Brandt, Phys. Rev. B **68**, 054506 (2003).

[134] I.L. Landau and H. Keller, Physica C **466**, 131 (2007).

[135] M. Weber, A. Amato, F.N. Gygax, A. Schenk, H. Maletta, V.N. Duginov, V.G. Grebinnik, A.B. Lazarev, V.G. Olshevsky, V.Yu. Pomjakushin, S.N. Shilov, B.F. Kirillov, A.V. Pirogov, A.N. Ponomarev, V.G. Storchak, S. Kapusta, and J. Bock, Phys. Rev. B **48**, 13022 (1993).

[136] R. Khasanov, A. Shengelaya, A. Maisuradze, F. La Mattina, A. Bussman-Holder, H. Keller, and K.A. Müller, Phys. Rev. Lett. **98**, 057007 (2007).

[137] E.H. Brandt, J. Low Temp. Phys. **26**, 709 (1977); **73**, 355 (1988).

[138] Z. Hao, J.R. Clem, M.W. McElfresh, L. Civale, A.P. Malozemoff, and F. Holtzberg, Phys. Rev. B **43**, 2844 (1991).

[139] E.H. Brandt, Phys. Rev. Lett. **78**, 2208 (1997).

[140] At high fields and low temperatures the minimal and the saddle points are exchanged and the magnetic field distribution around the vortex core has a conical shape. See J.M. Delrieu, J. Low Temp. Phys. **6**, 197 (1972); and Ref. [137].

[141] In a real μSR experiment with a time binning of 1.25 ns the maximal possible field for a measurement is 2.95 T (corresponds to two binnings per precession period). Hovewer, since we are not technically restricted, it is still possible to simulate and fit μSR data at higher fields due to the stroboscopic effect. In this case the absolute value of the real field is the fitted field plus N·2.95 T, where N is any integer number.

[142] R. Khasanov, I.L. Landau, C. Baines, F. La Mattina, A. Maisuradze, K. Togano, and H. Keller, Phys. Rev. B **73**, 214528 (2006).

[143] D. Rainer and K.D. Usadel, Phys. Rev. B **9**, 2409 (1974).

[144] K.W.H. Stevens, Proc. Phys. Soc. (London) **A65**, 209 (1952).

[145] S.A. Altschuler and B.M. Kosyrev, "Paramagnetische Electronenresonanz“, *B.G. TEUBNER VERLAGSGESELLSCHAFT, Leipzig (1963).*

[146] D.R. Noakes, J.H. Brewer, D.R. Harshman, E.J. Ansaldo, and C.Y. Huang, Phys. Rev. B **35**, 6597 (1987).

Curriculum Vitae

Personal Data

Name	Alexander Maisuradze
Date of birth	5 June 1978
Place of birth	Rustavi, Georgia
Citizenship	Georgia
Languages	Georgian (native, written and spoken)
	English (proficient, written and spoken)
	Russian (proficient, written and spoken)
	German (advanced, written and spoken)

Education and Experience

2004–2008	Physik-Institut der Universität Zürich; Assistant;
	Dissertation under Prof. Dr. H. Keller and Prof. Dr. A. Shengelaya
2002	Master degree in physics
1999	Bachelor degree in physics
1995–2004	Tbilisi State University, Tbilisi, Georgia;
1984–1995	Studied in school, Rustavi, Georgia.

List of lecturers whose courses and seminars I have attended

H. Keller

P. Meier

E. Morentzoni

List of Publications

1. Probing the Yb^{3+} spin relaxation in $Y_{0.98}Yb_{0.02}Ba_2Cu_3O_x$ by electron paramagnetic resonance
   A. Maisuradze, A. Shengelaya, B.I. Kochelaev, E. Pomjakushina, K. Conder, H. Keller, and K.A. Müller
   Phys. Rev. B **79**, 054519 (2009).

2. Comparison of different methods for analyzing μSR line shapes in the vortex state of type-II superconductors
   A. Maisuradze, R. Khasanov, A. Shengelaya, and H. Keller
   J. Phys.: Condens. Matter **21**, 075701 (2009).

3. Correlation between the transition temperature and the superfluid density in BCS superconductor NbB_{2+x}
   R. Khasanov, A. Shengelaya, A. Maisuradze, D. Di Castro, R. Escamilla, and H. Keller
   Phys. Rev. B **77**, 064506 (2008).

4. Mixed order parameter symmetries in cuprate superconductors
   A. Bussmann-Holder, R. Khasanov, A. Shengelaya, A. Maisuradze, F. La Mattina, H. Keller, and K. A. Müller
   EPL **77**, 27002 (2007).

5. Experimental Evidence for Two Gaps in the High-Temperature $La_{1.83}Sr_{0.17}CuO_4$ Superconductor
   R. Khasanov, A. Shengelaya, A. Maisuradze, F. La Mattina, A. Bussmann-Holder, H. Keller, and K. A. Müller
   Phys. Rev. Lett. **98**, 057007 (2007).

6. Muon-spin-rotation measurements of the penetration depth in Li_2Pd_3B
   R. Khasanov, I. L. Landau, C. Baines, F. La Mattina, A. Maisuradze, K. Togano, and H. Keller
   Phys. Rev. B **73**, 214528 (2006) .

7. Magnetic penetration depth in $RbOs_2O_6$ studied by muon spin rotation
   R. Khasanov, D. G. Eshchenko, D. Di Castro, A. Shengelaya, F. La Mattina, A.

Maisuradze, C. Baines, H. Luetkens, J. Karpinski, S. M. Kazakov, and H. Keller
Phys. Rev. B **72**, 104504 (2005).

8. Pressure Effects on the Transition Temperature and the Magnetic Field Penetration Depth in the Pyrochlore Superconductor $RbOs_2O_6$
R. Khasanov, D.G. Eshchenko, J. Karpinski, S.M. Kazakov, N.D. Zhigadlo, R. Bratsch, D. Gavillet, D. Di Castro, A. Shengelaya, F. La Mattina, A. Maisuradze, C. Baines, and H. Keller
Phys. Rev. Lett. **93**, 157004 (2004).